

THE UNIVERSITY
OF ADELAIDE
AUSTRALIA

Investigation of External Acoustic Loadings on a Launch Vehicle Fairing During Lift-off

Mir Md. Maruf Morshed

Supervisors:

Professor Colin H. Hansen

Associate Professor Anthony C. Zander

**School of Mechanical Engineering
University of Adelaide
South Australia 5005
AUSTRALIA**

*Dissertation Submitted for the Award of the Degree of Doctor of Philosophy on the 19th
May, 2008. Qualified on the 26th August, 2008.*

This page intentionally contains only this sentence.

Abstract

During the lift-off of a launch vehicle, the acoustic pressure fluctuations caused by the engine exhaust gases produce high noise levels inside the cavity of the fairing and can damage the payload inside the fairing. Hence reducing the noise transmitted into the payload bay is an important area of research. Work presented in this thesis investigates the external acoustic pressure excitations on the fairing of a launch vehicle during the lift-off acoustic environment. In particular, it investigates the external sound pressure levels in the low frequency range from 50Hz to 400Hz, on the fairing during the lift-off of a launch vehicle.

This study establishes theoretical and numerical models for the prediction of external sound pressure loading on composite structures representing launch vehicles, such as a large composite cylinder referred to as a Boeing cylinder and a Representative Small Launch Vehicle Fairing (RSLVF). To predict the external sound pressure loading, various incident wave conditions were investigated, including incident plane waves, oblique plane waves and oblique plane waves with random phases that strike the circumference of the composite structures.

For the theoretical model, both the incident and scattered sound pressure fields due to incident plane waves; perpendicular to an idealised long cylinder were investigated. The results show that the scattered sound pressure field plays a major role in determining the total circumferential sound pressure field at the surface of the cylinder and cannot be ignored for the launch case.

Abstract

The theoretical model was developed further for a point source, line source and oblique incident waves, and modified to determine the incident, scattered and total sound pressure fields away from the cylinder. The approach developed overcomes some limitations of previous analytical derivations.

An experiment was undertaken to determine the sound pressure patterns at the surface of a cylinder at various frequencies due to a point source positioned at a finite distance from the cylinder surface. The experimental work confirmed the accuracy of the theoretical model for a point source at a finite distance from the cylinder.

The Boundary Element Method (BEM), approach was used for the numerical investigation of the acoustic loadings. The numerical analysis was developed for various acoustic loading conditions and verified with the theoretical results, which showed that the numerical and theoretical models agree well. Both models were extended to a Boeing composite cylinder and an RSLVF for various acoustic loading conditions.

The complex acoustic environment generated during the lift-off of a launch vehicle was investigated and used as a basis for the acoustic loading on an RSLVF. To predict the acoustic excitations on an RSLVF, two different source allocation techniques were investigated, which considered acoustic sources along the rocket engine exhaust flow. The investigations were conducted both numerically and analytically. Both results agree well and show that it is possible to predict the acoustic loads on the fairing numerically and analytically.

Statement of Originality

To the best of my knowledge and belief, all the material presented in this thesis, except where otherwise referenced, is my own original work, and has not been published previously for the award of any other degree or diploma in any university. If accepted for the award of the degree of Doctor of Philosophy, I consent that this thesis be made available for loan and photocopying.

Mir Md. Maruf Morshed

Date:

Acknowledgement

I would like to acknowledge the efforts of all the people who have made a contribution toward this thesis. Many thanks to my parents, Mir Md. Morshed Ali and Shahana Morshed, who encouraged my mathematical and scientific interests from an early age, made many sacrifices to ensure I received a good education and to their financial support for this study. I would also like to thank my brother Mir Md. Mahmud Morshed and his wife Amy Louise Morshed, for their valuable support while finishing.

I am especially grateful to Professor Colin H. Hansen and Associate Professor Anthony C. Zander, for their supervision and support throughout the entire research. Without their direction and guidance, this thesis would most likely never have been completed. Thanks also to Karen Adams for her contribution to the writing corrections made to this thesis. I would also like to thank Dr Rick Morgans, Dr Carl Q. Howard and Dr Xun Li, for all of their discussions and advice. I am indebted to Silvio De Ieso, Norio Itsumi, Philip Schmidt, Joel Walker and Richard Pateman, for all their help with the design and construction of the electronics and experimental apparatus.

Finally, I would like to express my gratitude to Patricia Anderson, International Student Centre Manager, who handled my visa status during the stay in Australia.

This dissertation is dedicated to all of my family members, especially to my sister Maisha Tasnim and to brother's son who is my little nephew Mir Md. Zebediah Morshed.

Contents

Abstract	iii
Statement of Originality	v
Acknowledgements	vi
Contents	vii
List of Tables	xi
List of Figures	xiii
Glossary of Symbols	xxvii
1. Introduction	1
1.1 Introduction and Significance	1
1.2 Objectives of the Study	2
1.3 Contributions of the Study	3
1.4 Overview of the Thesis	4
2. Literature Review	8
2.1 Introduction	8
2.2 Scope	8
2.3 Underlying Theory and Analytical Models for Acoustic Loading	9
2.4 Launch Acoustic Environments and Prediction Techniques	13
2.5 Solutions to Minimize the Acoustic Loads	16
2.6 Numerical Analysis Techniques	19
2.7 Current Gaps in Knowledge	21
3. Sound Pressure at the Surface of a Cylinder Due to Incident Plane Waves	23
3.1 Introduction	23
3.2 Background Theory	23
3.3 Plane Wave Pressure at the Surface of a Cylinder	25
3.3.1 Incident Sound Pressure	26
3.3.2 Scattered Sound Pressure	30
3.3.3 Total Sound Pressure	38
3.3.4 Discussion	46
3.4 Other Theoretical Approaches and Comparison with the Current Approach	46

3.5 Conclusions	52
4. Pressure at Any Location from a Cylinder in the Sound Field Due to Normal Incident Plane Waves	54
4.1 Introduction	54
4.2 Pressure at Any Location in the Sound Field	55
4.2.1 Incident Sound Pressure Field	55
4.2.2 Scattered Sound Pressure Field	58
4.2.3 Total Sound Pressure Field	67
4.3 Comparison with Previous Work	69
4.3.1 Sound Pressure Field	72
4.3.2 Sound Intensity Field	77
4.3.2.1 Case I (Short Wavelength)	77
4.3.2.2 Case II and III (Medium and Large Wavelength)	81
4.4 Conclusions	84
5. Sound Pressure at the Surface of a Cylinder Due to a Point Source and Line Source	85
5.1 Introduction	85
5.2 <i>Green's</i> Function	86
5.3 Monopole or Point Source	86
5.4 Sound Pressure Due to a Point Source	86
5.5 Sound Pressure Due to a Point Source Location Inclined with Respect to the Cylinder Coordinates	91
5.6 Sound Pressure Due to a Line Source	95
5.7 Conclusions	99
6. Experimental Work	101
6.1 Introduction	101
6.2 Experimental Arrangement	101
6.3 Experimental Results and Discussion	103
6.4 Comparison between Analytical and Experimental Results	107
6.5 Conclusions	113
7. Sound Pressure Field Due to Obliquely Incident Waves on a Boeing Cylinder and an RSLVF	114
7.1 Introduction	114
7.2 Method to Determine the Sound Pressure Due to Obliquely Incident Waves on a cylinder	115
7.3 Application of the Method to a Boeing Cylinder	119

7.4 Application of the Method to a Launch Fairing	122
7.5 Conclusions	129
8. Numerical Calculations of the Sound Pressure Field	131
8.1 Introduction	131
8.2 Boundary Integral Formulation of <i>Helmholtz Equation</i>	132
8.3 Reduced Integral Formulation for Scattering Problem	135
8.4 Numerical Implementation	136
8.5 Verifications of Open BEM (Boundary Element Method)	137
8.5.1 Verifications of 2D BEM	137
8.5.2 Verifications of 3D BEM	153
8.5.3 Concluding Remarks	166
8.6 Application of BEM Analysis to a Boeing Cylinder	166
8.6.1 2D BEM Results	167
8.6.2 3D BEM Results	171
8.6.2.1 Sound Pressure Due to Incident Plane Waves	172
8.6.2.2 Sound Pressure Due to a Point Source	176
8.6.2.3 Sound Pressure Due to a Line Source	178
8.7 Application of BEM Analysis to an RSLVF	181
8.7.1 Sound Pressure Due to Incident Plane Waves	183
8.7.2 Sound Pressure Due to a Point Source	189
8.7.3 Sound Pressure Due to a Line Source	191
8.8 Conclusions	194
9. Prediction of Acoustic Loads on the Fairing During Lift-off of a Launch Vehicle	196
9.1 Introduction	196
9.2 Estimation of the Rocket Engine Exhaust Noise	198
9.3 Geometry Under Consideration to Predict the Acoustic Loads	201
9.4 Prediction of Acoustic Loads Using the Unique Source Allocation Method	203
9.4.1 Prediction Formulations	203
9.4.2 Acoustic Loadings on the Fairing	208
9.4.2.1 Analytical Results	210
9.4.2.2 Numerical Results	213
9.5 Prediction of Acoustic Loads Using the Non-Unique Source Allocation Method	222
9.5.1 Prediction Formulations	222
9.5.2 Acoustic Loadings on the Fairing	226
9.5.2.1 Analytical Results	229

Contents

9.5.2.2 Numerical Results	232
9.6 Conclusions	239
10. Summary and Conclusions	241
10.1 Summary	241
10.2 Conclusions	246
10.3 Recommendations for Future Works	248
A. Bessel's Differential Equation	250
A.1 Bessel Function of the First Kind (J_m)	250
A.2 Bessel Function of the Second Kind (N_m)	251
A.3 Bessel Function of the Third Kind (H_m)	252
B. Values of Phase Angle γ_m and Coefficient A_m	262
C. Wronskian Relationship	266
D. Corrections in the Real-time theory presented by Friot <i>et al.</i>, (2004)	267
E. Rocket Engine Noise Prediction Comparison with Gierke Method	268
References	269

List of Tables

3.1	Total number of terms required in equation (3.18) for various values of ka .	45
4.1	Complex incident sound pressure at various distances for $ka = 5$.	57
4.2	Comparison between the asymptotic values using equation (4.11) and the exact computational values using MATLAB of the out going <i>Hankel function</i> , $H_m(kr)$.	74
4.3	Values of λ and ka for the three cases examined.	77
4.4	Total number of terms required in the series calculation in equation (4.4), for scattered sound intensity.	84
5.1	Arbitrary strengths for fifteen point sources.	98
6.1	Physical parameters of the experimental setup.	102
6.2	Descriptions of the applied parameters in the experiment.	104
7.1	Boeing cylinder physical properties (Hansen <i>et al.</i> , 2001a).	120
7.2	RSLVF physical dimensions.	122
7.3	Approximate parameters of four slices.	122
9.1	Rocket engine operating and exit parameters. [Data taken from Mayes <i>et al.</i> (1959)]	198
9.2	Details of the 10 sources. (All the data given here for engine 'E'; overall acoustic power level, $L_w = 56.28$ dB; speed of sound and density in air at $T = 1000^\circ\text{C}$ is 715.49 m/s and 0.28 kg/m^3 respectively.)	209
9.3	Details of 10 sources using the non-unique source allocation method (all the data presented here for engine 'E'). Core length, $x_t = 5.15\text{m}$; Overall acoustic power level of the rocket engine, $L_w = 56.28$ dB; Length of each segments, $\Delta x = 1\text{m}$. [Data estimated from Figure 12, presented in NASA-SP-8072 (1971)]	227
9.4	Estimated relative sound power level for ten sources for each 1/3 octave band centre frequency from 50Hz to 400Hz, using the non-unique source allocation method (all the data presented here for engine 'E'). Core length, $x_t = 5.15\text{m}$; Overall acoustic power level of the rocket engine, $L_w = 56.28$ dB; Speed of sound in the exhaust flow, $a_e = 715.49$ m/s ; Length of each segments, $\Delta x = 1\text{m}$. [Data estimated from Figure 13, presented in NASA-SP-8072 (1971)]	228
9.5	Calculated acoustic power level for 10 sources corresponding to 10 segments for each 1/3 octave band centre frequency from 50Hz to 400Hz, using the non-unique source allocation method (all the data presented here for engine 'E'). Core length, $x_t = 5.15\text{m}$; Overall acoustic power level, $L_w = 56.28$ dB; Speed of sound in the exhaust flow, $a_e = 715.49$ m/s ; Length of each segments, $\Delta x = 1\text{m}$.	228
9.6	Calculated source strength for 10 sources corresponding to 10 segments for each 1/3 octave band centre frequency from 50Hz to 400Hz, using the non-unique source allocation method (all the data presented here for engine 'E'). Core length, $x_t = 5.15\text{m}$; Overall acoustic power level, $L_w = 56.28$ dB; Length of each segments, $\Delta x = 1\text{m}$; speed of sound and density in air at $T = 1000^\circ\text{C}$ is 715.49 m/s and 0.28 kg/m^3 respectively.	229

A.1	Values of cylindrical <i>Bessel functions</i> calculated using MATLAB for $ka = 1$.	254
A.2	Values of cylindrical <i>Bessel functions</i> calculated using MATLAB for $ka = 3$.	255
A.3	Values of cylindrical <i>Bessel functions</i> calculated using MATLAB for $ka = 5$.	256
A.4	Values of cylindrical <i>Bessel functions</i> calculated using MATLAB for $ka = 10$.	257
A.5	Values of cylindrical <i>Bessel functions</i> calculated using MATLAB for $ka = 15$.	258
A.6	Values of cylindrical <i>Bessel functions</i> calculated using MATLAB for $ka = 20$.	259
A.7	Values of cylindrical <i>Bessel functions</i> calculated using MATLAB for $ka = 25$.	260
A.8	Values of cylindrical <i>Bessel functions</i> calculated using MATLAB for $ka = 30$.	261
B.1	Values of γ_m and A_m calculated using MATLAB for $ka = 1$ and 3 .	262
B.2	Values of γ_m and A_m calculated using MATLAB for $ka = 5$ and 10 .	263
B.3	Values of γ_m and A_m calculated using MATLAB for $ka = 15$ and 20 .	264
B.4	Values of γ_m and A_m calculated using MATLAB for $ka = 25$ and 30 .	265

List of Figures

3.1	Geometry of the cylindrical external problem.	26
3.2	Two-dimensional incident plane waves travelling normal to the cylinder axis (positive z axis is out of page).	27
3.3	Incident sound pressure distributions at the surface of a cylinder of radius a , for $ka = 5$ and $M = 1, 2, 3, 4, 5, 6$ and 7 respectively, assuming that no distortion of sound waves occurs due to the presence of the cylinder. [Incident pressure magnitude $P^0 = 1 \text{ Pa}$]	29
3.4	Incident sound pressure distributions at the surface of a cylinder of radius a , for $ka = 5$ and $M = 7, 8, 9, 10, 11$ and 12 respectively, assuming that no distortion of sound waves occurs due to the presence of the cylinder. [Incident pressure magnitude $P^0 = 1 \text{ Pa}$]	30
3.5	Scattered sound pressure distributions at the surface of a cylinder of radius a , for $ka = 5$ and $M = 1, 2, 3, 4, 5, 6$ and 7 respectively. [Incident pressure magnitude $P^0 = 1 \text{ Pa}$]	34
3.6	Scattered sound pressure distributions at the surface of a cylinder of radius a , for $ka = 5$ and $M = 7, 8, 9, 10, 11$ and 12 respectively. [Incident pressure magnitude $P^0 = 1 \text{ Pa}$]	34
3.7(a-h)	Directivity pattern of the scattered sound pressure at the surface of a cylinder of radius a , for various values of ka . The arrows in the figures indicate the direction of incident waves. [Incident pressure magnitude $P^0 = 1 \text{ Pa}$]	36
3.8	Scattered sound pressure as a function of azimuthal angle, ϕ_i , for values of $ka = 1$ and 3 respectively. [Incident pressure magnitude $P^0 = 1 \text{ Pa}$]	36
3.9	Scattered sound pressure as a function of azimuthal angle, ϕ_i , for values of $ka = 5$ and 10 respectively. [Incident pressure magnitude $P^0 = 1 \text{ Pa}$]	37
3.10	Scattered sound pressure as function of azimuthal angle, ϕ_i , for values of $ka = 15$ and 20 respectively. [Incident pressure magnitude $P^0 = 1 \text{ Pa}$]	37
3.11	Scattered sound pressure as function of azimuthal angle, ϕ_i , for values of $ka = 25$ and 30 respectively. [Incident pressure magnitude $P^0 = 1 \text{ Pa}$]	38
3.12(a-h)	Directivity pattern of the total sound pressure at the surface of a cylinder of radius a , for various values of ka . The arrows in the figures show the incident wave direction. [Reference pressure $20\mu\text{Pa}$ and incident pressure magnitude $P^0 = 1 \text{ Pa}$]	41
3.13	Total sound pressure as a function of azimuthal angle, ϕ_i , at the surface of a cylinder of radius a , for values of $ka = 1$ and 3 respectively. [Reference pressure $20\mu\text{Pa}$ and incident pressure magnitude $P^0 = 1 \text{ Pa}$]	41
3.14	Total sound pressure as a function of azimuthal angle, ϕ_i , at the surface of a cylinder of radius a , for values of $ka = 5$ and 10 respectively. [Reference pressure $20\mu\text{Pa}$ and incident pressure magnitude $P^0 = 1 \text{ Pa}$]	42

3.15	Total sound pressure as a function of azimuthal angle, ϕ_i , at the surface of a cylinder of radius a , for values of $ka = 15$ and 20 respectively. [Reference pressure $20\mu\text{Pa}$ and incident pressure magnitude $P^0 = 1 \text{ Pa}$]	42
3.16	Total sound pressure as a function of azimuthal angle, ϕ_i , at the surface of a cylinder of radius a , for values of $ka = 25$ and 30 respectively.[Reference pressure $20\mu\text{Pa}$ and incident pressure magnitude $P^0 = 1 \text{ Pa}$]	43
3.17(a)	Characteristic behavior of γ_m as a function of m , for values of $ka = 1, 3, 5$ and 10 respectively.	43
3.17(b)	Characteristic behavior of γ_m as a function of m , for values of $ka = 15, 20, 25$ and 30 respectively.	44
3.18(a)	Characteristic behavior of A_m as a function of m , for values of $ka = 1, 3, 5$ and 10 respectively.	44
3.18(b)	Characteristic behavior of A_m as a function of m , for values of $ka = 15, 20, 25$ and 30 respectively.	45
3.19	Scattered sound pressure comparison between results obtained at the surface of a cylinder of radius a using equations (3.11) and (3.20), for $ka = 5$. To calculate scattered sound pressure at the surface of the cylinder use ' $r = a$ ' in equation (3.20). [Incident pressure magnitude $P^0 = 1 \text{ Pa}$]	47
3.20	Total sound pressure comparison between results obtained at the surface of a cylinder of radius a using equations (3.18) and (3.21), for $ka = 5$. [Reference pressure $20\mu\text{Pa}$, incident pressure magnitude $P^0 = 1 \text{ Pa}$]	48
3.21	Total sound pressure comparison between results obtained at the surface of a cylinder of radius a using equations (3.18) and (3.24), for $ka = 5$. [Reference pressure $20\mu\text{Pa}$ and incident pressure magnitude $P^0 = 1 \text{ Pa}$]	50
3.22	Total sound pressure comparison between results obtained at the surface of a cylinder of radius a using equations (3.26) and (3.18), for $ka = 5$. [Reference pressure $20\mu\text{Pa}$ and incident pressure magnitude $P^0 = 1 \text{ Pa}$]	51
4.1	Incident plane waves travelling normal to the cylinder axis z (z axis is out of page).	56
4.2	Directivity patterns of the scattered sound pressure at various distances from the origin of a cylinder of radius a , for $ka = 5$. [Incident pressure magnitude $P^0 = 1 \text{ Pa}$]	60
4.3	Directivity patterns of the scattered sound pressure at a distance of $r = 5a$ from the origin of a cylinder of radius a , for values of $ka = 1, 3$ and 5 respectively. [Incident pressure magnitude $P^0 = 1 \text{ Pa}$]	61
4.4	Scattered sound pressure variation as a function of azimuthal angle, ϕ_i , at a distance of $r = 5a$ from the origin of a cylinder of radius a , for values of $ka = 1, 3$ and 5 respectively. [Incident pressure magnitude $P^0 = 1 \text{ Pa}$]	61
4.5(a)	Directivity pattern of the scattered sound pressure at a distance of $r = 5a$ (five times the cylinder radius) from the origin of a cylinder of radius a , for $ka = 10$. [Incident pressure	

	magnitude $P^0 = 1 \text{ Pa}$]	62
4.5(b)	Directivity pattern of the scattered sound pressure at a distance of $r = 5a$ (five times the cylinder radius) from the origin of a cylinder of radius a , for $ka = 15$. [Incident pressure magnitude $P^0 = 1 \text{ Pa}$]	62
4.5(c)	Directivity pattern of the scattered sound pressure at a distance of $r = 5a$ (five times the cylinder radius) from the origin of a cylinder of radius a , for $ka = 20$. [Incident pressure magnitude $P^0 = 1 \text{ Pa}$]	63
4.5(d)	Directivity pattern of the scattered sound pressure at a distance of $r = 5a$ (five times the cylinder radius) from the origin of a cylinder of radius a , for $ka = 25$. [Incident pressure magnitude $P^0 = 1 \text{ Pa}$]	63
4.5(e)	Directivity pattern of the scattered sound pressure at a distance of $r = 5a$ (five times the cylinder radius) from the origin of a cylinder of radius a , for $ka = 30$. [Incident pressure magnitude $P^0 = 1 \text{ Pa}$]	64
4.6(a)	Scattered sound pressure variation as a function of azimuthal angle, ϕ_i , at a distance of $r = 5a$ (five times the cylinder radius) from the origin of a cylinder of radius a , for $ka = 10$. [Incident pressure magnitude $P^0 = 1 \text{ Pa}$]	64
4.6(b)	Scattered sound pressure variation as a function of azimuthal angle, ϕ_i , at a distance of $r = 5a$ (five times the cylinder radius) from the origin of a cylinder of radius a , for $ka = 15$. [Incident pressure magnitude $P^0 = 1 \text{ Pa}$]	65
4.6(c)	Scattered sound pressure variation as a function of azimuthal angle, ϕ_i , at a distance of $r = 5a$ (five times the cylinder radius) from the origin of a cylinder of radius a , for $ka = 20$. [Incident pressure magnitude $P^0 = 1 \text{ Pa}$]	65
4.6(d)	Scattered sound pressure variation as a function of azimuthal angle, ϕ_i , at a distance of $r = 5a$ (five times the cylinder radius) from the origin of a cylinder of radius a , for $ka = 25$. [Incident pressure magnitude $P^0 = 1 \text{ Pa}$]	66
4.6(e)	Scattered sound pressure variation as a function of azimuthal angle, ϕ_i , at a distance of $r = 5a$ (five times the cylinder radius) from the origin of a cylinder of radius a , for $ka = 30$. [Incident pressure magnitude $P^0 = 1 \text{ Pa}$]	66
4.7(a)	Directivity pattern of the total sound pressure of a cylinder of radius a at various distances, for $ka = 1$. [Reference pressure $20\mu\text{Pa}$ and incident pressure magnitude $P^0 = 1 \text{ Pa}$]	68
4.7(b)	Directivity pattern of the total sound pressure of a cylinder of radius a at various distances, for $ka = 3$. [Reference pressure $20\mu\text{Pa}$ and incident pressure magnitude $P^0 = 1 \text{ Pa}$]	68
4.7(c)	Directivity pattern of the total sound pressure of a cylinder of radius a at various distances, for $ka = 5$. [Reference pressure $20\mu\text{Pa}$ and incident pressure magnitude $P^0 = 1 \text{ Pa}$]	69

4.8(a)	Scattered sound pressure comparison between results obtained at a distance of $5a$ (five times the cylinder radius) in the sound field from the origin of a cylinder of radius a , using equations (4.3) and (3.20), for $ka = 5$. [Incident pressure magnitude $P^0 = 1 \text{ Pa}$]	70
4.8(b)	Total sound pressure comparison between results obtained at a distance $5a$ (five times the cylinder radius) in the sound field from the origin of a cylinder of radius a , using equations (4.5) and (3.21), for $ka = 5$. [Reference pressure $20 \mu\text{Pa}$ and incident pressure magnitude $P^0 = 1 \text{ Pa}$]	70
4.9(a)	Scattered sound pressure comparison between results obtained using equations (4.3) and (4.7), for $ka = 5$ and $r = 57a$. [Incident pressure magnitude $P^0 = 1 \text{ Pa}$]	75
4.9(b)	Scattered sound pressure comparison between results obtained using equations (4.3) and (4.7), for $ka = 5$ and $r = 5a$. [Incident pressure magnitude $P^0 = 1 \text{ Pa}$]	75
4.9(c)	Scattered sound pressure comparison between results obtained using equations (4.3) and (4.7), for $ka = 5$ and $r = 2a$. [Incident pressure magnitude $P^0 = 1 \text{ Pa}$]	76
4.9(d)	Scattered sound pressure comparison between results obtained using equations (4.3) and (4.7), for $ka = 5$ and $r = 1.2a$. [Incident pressure magnitude $P^0 = 1 \text{ Pa}$]	76
4.10	Directivity patterns of the scattered sound intensity at a distance of $r = 57a$ from the origin of a cylinder of radius a , for $ka = 5$ and $M = 5$. The red (dash line) and black (solid line) lines show the current and the previous (Morse, 1936; Morse & Ingard, 1986) results respectively. [Incident pressure magnitude $P^0 = 1 \text{ Pa}$]	79
4.11	Directivity pattern of the scattered sound intensity at a distance of $r = 57a$ from the origin of a cylinder of radius a , for $ka = 5$ and $M = 12$. [Incident pressure magnitude $P^0 = 1 \text{ Pa}$]	80
4.12	Directivity pattern of the scattered sound intensity at a distance of $r = 57a$ from the origin of a cylinder of radius a , for $ka = 5$ and $M = 17$. [Incident pressure magnitude $P^0 = 1 \text{ Pa}$]	80
4.13	Scattered sound intensity fluctuations with various azimuthal angle at a distance of $r = 57a$ from the origin of a cylinder of radius a , for $ka = 5$ and $M = 12$. [Incident pressure magnitude $P^0 = 1 \text{ Pa}$]	81
4.14	Directivity patterns of the scattered sound intensity at a distance of $r = 57a$ from the origin of a cylinder of radius a , for $ka = 3$ and $M = 8$. The red (dash line) and black (solid line) lines show the current and the previous (Morse, 1936; Morse & Ingard, 1986) results respectively. [Incident pressure magnitude $P^0 = 1 \text{ Pa}$]	82
4.15	Directivity patterns of the scattered sound intensity at a distance of $r = 57a$ from the origin of a cylinder of radius a , for $ka = 1$ and $M = 6$. The red (dash line) and black (solid line) lines show the current and the previous (Morse, 1936; Morse & Ingard, 1986) results respectively. [Incident pressure magnitude $P^0 = 1 \text{ Pa}$]	83
4.16	Scattered sound intensity with various azimuthal angles at a distance of $r = 57a$ from a cylinder of radius a , for $ka = 3$ and $ka = 1$. [Incident pressure magnitude $P^0 = 1 \text{ Pa}$]	83
5.1	Geometry of the sound pressure field due to a point source for two-dimensional	

coordinate axes.	87
5.2 Total sound pressure at the surface of a cylinder of radius $a = 1.23\text{m}$ (Boeing cylinder radius), calculated using equations (3.18) and (5.5), for $ka = 5$ and $r' = -3a$. [Source strength, $Q_s = 1+i \text{ m}^3/\text{s}$ and reference pressure $20\mu\text{Pa}$]	89
5.3 Total sound pressure at the surface of a cylinder of radius $a = 1.23\text{m}$ (Boeing cylinder radius), due to a point source positioned at various distances from the origin of the cylinder, for $ka = 5$. [Source strength, $Q_s = 1+i \text{ m}^3/\text{s}$ and reference pressure $20\mu\text{Pa}$]	90
5.4 Directivity patterns of the total sound pressure at the surface of a cylinder of radius $a = 1.23\text{m}$ (Boeing cylinder radius), due to a point source placed at various distances from the origin of the cylinder, for $ka = 5$. [Source strength, $Q_s = 1+i \text{ m}^3/\text{s}$ and reference pressure $20\mu\text{Pa}$]	90
5.5 Geometry of the inclined point source for two-dimensional cylinder coordinate axes.	91
5.6(a-h) Directivity patterns of the total sound pressure due to inclined incident waves for various values of ka at the surface of a cylinder of radius $a = 1.23\text{m}$ (Boeing cylinder radius). The source of strength $Q_s = 1+i \text{ m}^3/\text{s}$ is placed at an angle $\beta = \pi/3$ from the x axis (see Figure 5.5) and at a distance of $r' = -3a$ from the origin of the cylinder. [Reference pressure $20\mu\text{Pa}$]	93
5.7(a-h) Directivity patterns of the scattered sound pressure due to inclined incident waves for various values of ka at the surface of a cylinder of radius $a = 1.23\text{m}$ (Boeing cylinder radius). The source of strength $Q_s = 1+i \text{ m}^3/\text{s}$ is placed at an angle $\beta = \pi/3$ from the x axis (see Figure 5.5) and at a distance of $r' = -3a$ from the origin of the cylinder.	95
5.8 Geometry of the line source for two-dimensional cylinder coordinate axes.	95
5.9 Directivity pattern of the total sound pressure at the surface of a cylinder of radius $a = 1.23\text{m}$ (Boeing cylinder radius) due to a line source of different arbitrary amplitudes and phases (see table 5.1), for $ka = 5$. [Reference pressure $20\mu\text{Pa}$]	98
5.10 Directivity pattern of the total sound pressure at the surface of a cylinder of radius $a = 1.23\text{m}$ (Boeing cylinder radius) due to a line source of different arbitrary amplitudes and phases (see Table 5.1) with distributed frequencies from 50 Hz to 400Hz. [Reference pressure $20\mu\text{Pa}$]	99
6.1 (a) Picture of the experimental setup inside the anechoic chamber, (b) picture showing the placement of the microphone inside the experimental cylinder.	102
6.2 Relative sound pressure at the surface of the experimental cylinder, for $f = 700 \text{ Hz}$ and $ka = 0.73$.	105
6.3 Relative sound pressure at the surface of the experimental cylinder, for $f = 1.5 \text{ kHz}$ and $ka = 1.57$.	105
6.4 Relative sound pressure at the surface of the experimental cylinder, for $f = 3 \text{ kHz}$ and $ka = 3.13$.	106
6.5 Relative sound pressure at the surface of the experimental cylinder, for $f = 5 \text{ kHz}$ and $ka = 5.22$.	106
6.6 Comparison between the experimental and normalised analytical results for relative sound pressure at the surface of the experimental cylinder, for $f = 700 \text{ Hz}$ and $ka = 0.73$.	109
6.7 Comparison between the experimental and normalised analytical results for relative sound pressure at the surface of the experimental cylinder, for $f = 1.5 \text{ kHz}$ and $ka = 1.57$.	109
6.8 Comparison between the experimental and normalised analytical results for relative sound	

pressure at the surface of the experimental cylinder, for $f = 3$ kHz and $ka = 3.13$.	110
6.9 Comparison between the experimental and normalised analytical results for relative sound pressure at the surface of the experimental cylinder, for $f = 5$ kHz and $ka = 5.22$.	110
6.10 Sound pressure directivity comparison between the experimental and normalised analytical results at the surface of the experimental cylinder, for $f = 700$ Hz and $ka = 0.73$.	111
6.11 Sound pressure directivity comparison between the experimental and normalised analytical results at the surface of the experimental cylinder, for $f = 1.5$ kHz and $ka = 1.57$.	111
6.12 Sound pressure directivity comparison between the experimental and normalised analytical results at the surface of the experimental cylinder, for $f = 3$ kHz and $ka = 3.13$.	112
6.13 Sound pressure directivity comparison between the experimental and normalised analytical results at the surface of the experimental cylinder, for $f = 5$ kHz and $ka = 5.22$.	112
7.1 Geometry of obliquely incident waves for three-dimensional cylinder coordinate axes.	116
7.2 Total sound pressure at the surface of a cylinder of radius $a = 1.23$ m, for various heights, z , along the cylinder for $ka = 5$. The point source of complex strength of $Q_s = 1 + i$ m ³ /s, is placed at a distance of $r' = -5a$ (five times the cylinder radius) from the cylinder axis at $z = 0$. [Reference pressure 20 μ Pa]	118
7.3 Total sound pressure distributions as a function of circumferential angles at various frequencies from 50Hz to 125Hz in the middle ($z = 1.395$ m) of the Boeing cylinder. The point source of complex strength of $Q_s = 1 + i$ m ³ /s, is placed at a distance of $r' = -5a$ from the cylinder axis at $z = 0$. [Reference pressure 20 μ Pa]	121
7.4 Total sound pressure distributions as a function of circumferential angles at various frequencies from 160Hz to 400Hz in the middle ($z = 1.395$ m) of the Boeing cylinder. The point source of complex strength of $Q_s = 1 + i$ m ³ /s, is placed at a distance of $r' = -5a$ from the cylinder axis at $z = 0$. [Reference pressure 20 μ Pa]	121
7.5 RSLVF cross-section and modelled different sections.	123
7.6(a) Total circumferential sound pressure at various frequencies from 50Hz to 125 Hz at the surface of slice one of the RSLVF. The point source of complex strength of $Q_s = 1 + i$ m ³ /s, is placed at a distance of $r' = -5$ m from the RSLVF axis at $z = 0$. [Reference pressure 20 μ Pa]	125
7.6(b) Total circumferential sound pressure at various frequencies from 160Hz to 400 Hz at the surface of slice one of the RSLVF. The point source of complex strength of $Q_s = 1 + i$ m ³ /s, is placed at a distance of $r' = -5$ m from the RSLVF axis at $z = 0$. [Reference pressure 20 μ Pa]	125
7.7(a) Total circumferential sound pressure at various frequencies from 50Hz to 125 Hz at the surface of slice two of the RSLVF. The point source of complex strength of $Q_s = 1 + i$ m ³ /s, is placed at a distance of $r' = -5$ m from the RSLVF axis at $z = 0$. [Reference pressure 20 μ Pa]	126
7.7(b) Total circumferential sound pressure at various frequencies from 160Hz to 400 Hz at the surface of slice two of the RSLVF. The point source of complex strength of $Q_s = 1 + i$ m ³ /s, is placed at a distance of $r' = -5$ m from the RSLVF axis at $z = 0$. [Reference pressure 20 μ Pa]	126

7.8(a)	Total circumferential sound pressure at various frequencies from 50Hz to 125 Hz at the surface of slice three of the RSLVF. The point source of complex strength of $Q_s = 1 + i$ m ³ /s, is placed at a distance of $r' = -5$ m from the RSLVF axis at $z = 0$. [Reference pressure 20 μ Pa]	127
7.8(b)	Total circumferential sound pressure at various frequencies from 160Hz to 400 Hz at the surface of slice three of the RSLVF. The point source of complex strength of $Q_s = 1 + i$ m ³ /s, is placed at a distance of $r' = -5$ m from the RSLVF axis at $z = 0$. [Reference pressure 20 μ Pa]	127
7.9(a)	Total circumferential sound pressure at various frequencies from 50Hz to 125 Hz at the surface of slice four of the RSLVF. The point source of complex strength of $Q_s = 1 + i$ m ³ /s, is placed at a distance of $r' = -5$ m from the RSLVF axis at $z = 0$. [Reference pressure 20 μ Pa]	128
7.9(b)	Total circumferential sound pressure at various frequencies from 160Hz to 400 Hz at the surface of slice four of the RSLVF. The point source of complex strength of $Q_s = 1 + i$ m ³ /s, is placed at a distance of $r' = -5$ m from the RSLVF axis at $z = 0$. [Reference pressure 20 μ Pa]	128
8.1	Geometry of the exterior boundary problem.	133
8.2	2D BEM surface discretization of a cylinder of radius a , contains 40 elements and 80 nodes on the surface. X and Y represents the coordinates of the cylinder respectively.	138
8.3(a)	Total sound pressure comparison between the analytical and 2D BEM results at the surface of a cylinder of radius a , for incident plane waves travelling from left to right, for $ka = 1$. [Reference pressure 20 μ Pa and incident pressure magnitude $P^O = 1$ Pa]	139
8.3(b)	Total sound pressure comparison between the analytical and 2D BEM results at the surface of a cylinder of radius a , for incident plane waves travelling from left to right, for $ka = 5$. [Reference pressure 20 μ Pa and incident pressure magnitude $P^O = 1$ Pa]	140
8.3 (c)	Total sound pressure comparison between the analytical and 2D BEM results at the surface of a cylinder of radius a , for incident plane waves travelling from left to right, for $ka = 10$. [Reference pressure 20 μ Pa and incident pressure magnitude $P^O = 1$ Pa]	140
8.3(d)	Total sound pressure comparison between the analytical and 2D BEM results at the surface of a cylinder of radius a , for incident plane waves travelling from left to right, for $ka = 15$. [Reference pressure 20 μ Pa and incident pressure magnitude $P^O = 1$ Pa]	141
8.4	Total sound pressure comparison between the analytical and 2D BEM results at the surface of a cylinder of radius a , for incident plane waves travelling from left to right, for $ka = 16$. [Reference pressure 20 μ Pa and incident pressure magnitude $P^O = 1$ Pa]	141
8.5	Total sound pressure comparison between the analytical and 2D BEM results at the surface of a cylinder of radius a , for incident plane waves travelling from left to right, for $ka = 20$. [Reference pressure 20 μ Pa and incident pressure magnitude $P^O = 1$ Pa]	142
8.6	Comparisons between the experimental, analytical and 2D BEM results for pressure at the surface of the experimental cylinder of radius 0.057m, for $f = 700$ Hz and $ka = 0.73$	144
8.7	Comparisons between the experimental, analytical and 2D BEM results for pressure at the surface of the experimental cylinder of radius 0.057m, for $f = 1.5$ kHz and $ka = 1.57$.	144
8.8	Comparisons between the experimental, analytical and 2D BEM results for pressure at the surface of the experimental cylinder of radius 0.057m, for $f = 3$ kHz and $ka = 3.13$.	145

8.9	Comparisons between the experimental, analytical and 2D BEM results for pressure at the surface of the experimental cylinder of radius 0.057m, for $f = 5$ kHz and $ka = 5.22$.	145
8.10	Total sound pressure comparison between the analytical and 2D BEM results for a line source of 15 point sources of arbitrary amplitudes and phases (see Table 5.1 in Chapter 5) placed on the negative X axis for $ka = 5$. The radius of the cylinder is 0.057m. [Reference pressure $20\mu\text{Pa}$]	147
8.11(a)	Scattered sound pressure comparison between the analytical and 2D BEM results at a distance of $5a$ (five times the cylinder radius) from the origin of a cylinder of radius a , for incident plane waves travelling from left to right, for $ka = 5$. [Incident pressure amplitude $P^o = 1 \text{ Pa}$]	149
8.11(b)	Scattered sound pressure comparison between the analytical and 2D BEM results at a distance of $5a$ (five times the cylinder radius) from the origin of a cylinder of radius a , for incident plane waves travelling from left to right, for $ka = 10$. [Incident pressure amplitude $P^o = 1 \text{ Pa}$]	149
8.11(c)	Scattered sound pressure comparison between the analytical and 2D BEM results at a distance of $5a$ (five times the cylinder radius) from the origin of a cylinder of radius a , for incident plane waves travelling from left to right, for $ka = 15$. [Incident pressure amplitude $P^o = 1 \text{ Pa}$]	150
8.12(a)	Total sound pressure comparison between the analytical and 2D BEM results at a distance of $5a$ (five times the cylinder radius) from the origin of a cylinder of radius a , for incident plane waves travelling from left to right, for $ka = 5$. [Reference pressure $20\mu\text{Pa}$ and incident pressure amplitude $P^o = 1 \text{ Pa}$]	150
8.12(b)	Total sound pressure comparison between the analytical and 2D BEM results at a distance of $5a$ (five times the cylinder radius) from the origin of a cylinder of radius a , for incident plane waves travelling from left to right, for $ka = 10$. [Reference pressure $20\mu\text{Pa}$ and incident pressure amplitude $P^o = 1 \text{ Pa}$]	151
8.12(c)	Total sound pressure comparison between the analytical and 2D BEM results at a distance of $5a$ (five times the cylinder radius) from the origin of a cylinder of radius a , for incident plane waves travelling from left to right, for $ka = 15$. [Reference pressure $20\mu\text{Pa}$ and incident pressure amplitude $P^o = 1 \text{ Pa}$]	151
8.13	Scattered sound pressure comparison between the analytical and 2D BEM results at a distance of $5a$ (five times the cylinder radius) from the origin of a cylinder of radius a , for incident plane waves travelling from left to right, for $ka = 20$. [Incident pressure amplitude $P^o = 1 \text{ Pa}$]	152
8.14	Total sound pressure comparison between the analytical and 2D BEM results at a distance of $5a$ (five times the cylinder radius) from the origin of a cylinder of radius a , for incident plane waves travelling from left to right, for $ka = 20$. [Reference pressure $20\mu\text{Pa}$ and incident pressure amplitude $P^o = 1 \text{ Pa}$]	152
8.15(a)	8-node quadratic element.	153
8.15(b)	FEA model of the experimental cylinder.	153
8.16	BEM model of the experimental cylinder showing the surface elements and nodes.	154
8.17(a-d)	Numerical results of the total sound pressure distribution at the surface of the experimental cylinder, for plane waves incident on the front face, for $f = 1.5$ kHz and $ka = 1.57$. The green circles show the circumferential nodes at the middle of the cylinder.	

	[Reference pressure $20\mu\text{Pa}$ and incident pressure magnitude $P^o = 1 \text{ Pa}$]	155
8.18	Total sound pressure comparison between the analytical and 3D BEM results calculated on the circumferential nodes at the middle ($z = 0.75\text{m}$, see Figures 8.17a and 8.17b) of the experimental cylinder, for plane waves incident on the front face, for $f = 1.5\text{kHz}$ and $ka = 1.57$. [Reference pressure $20\mu\text{Pa}$ and incident pressure magnitude $P^o = 1 \text{ Pa}$]	156
8.19(a-b)	Numerical results of the total sound pressure distribution at the surface of the extended cylinder, for plane waves incident on the front face, for $f = 1.5 \text{ kHz}$ and $ka = 1.57$. The green circles show the circumferential nodes at the middle of the cylinder. [Reference pressure $20\mu\text{Pa}$ and incident pressure magnitude $P^o = 1 \text{ Pa}$]	156
8.20	Total sound pressure comparison between the analytical and 3D BEM results calculated on the circumferential nodes at the middle ($z = 2.5\text{m}$, see Figures 8.19a and 8.19b) of the extended cylinder of length 5m, for plane waves incident on the front face, for $f = 1.5\text{kHz}$ and $ka = 1.57$. [Reference pressure $20\mu\text{Pa}$ and incident pressure magnitude $P^o = 1 \text{ Pa}$]	157
8.21(a-d)	Numerical results of the total sound pressure distribution at the surface of the extended cylinder of length 5m, for plane waves incident on the front face, for $ka = 1$, and 5 respectively. [Reference pressure $20\mu\text{Pa}$ and incident pressure magnitude $P^o = 1 \text{ Pa}$]	159
8.22	Total Sound pressure comparison between the analytical and 3D BEM results calculated on the circumferential nodes at the middle ($z = 2.5\text{m}$, see Figures 8.19a and 8.19b) of the extended cylinder of length 5m, for plane waves incident on the front face, for $ka = 1$. [Reference pressure $20\mu\text{Pa}$ and incident pressure magnitude $P^o = 1 \text{ Pa}$]	159
8.23	Total sound pressure comparison between the analytical and 3D BEM results calculated on the circumferential nodes at the middle ($z = 2.5\text{m}$, see Figures 8.19a and 8.19b) of the extended cylinder of length 5m, for plane waves incident on the front face, for $ka = 5$. [Reference pressure $20\mu\text{Pa}$ and incident pressure magnitude $P^o = 1 \text{ Pa}$]	160
8.24(a-b)	Numerical results of the total sound pressure distribution at the surface of the extended cylinder of length 5m, for plane waves incident on the front face, for $ka = 6$. [Reference pressure $20\mu\text{Pa}$ and incident pressure magnitude $P^o = 1 \text{ Pa}$]	160
8.25	Total sound pressure comparison between the analytical and 3D BEM results calculated on the circumferential nodes at the middle ($z = 2.5\text{m}$, see Figures 8.19a and 8.19b) of the extended cylinder of length 5m, for plane waves incident on the front face, for $ka = 6$. [Reference pressure $20\mu\text{Pa}$ and incident pressure magnitude $P^o = 1 \text{ Pa}$]	161
8.26(a-b)	Numerical results of the total sound pressure distribution at the surface of the extended cylinder of length 5m and radius 0.057m , due to a point source of $f = 1.5 \text{ kHz}$ and $ka = 1.57$ is placed at a location of $X = -4.1\text{m}$, $Y = 0\text{m}$ and $Z = 0\text{m}$ (consider Figure 7.1 for the source geometry). The green circles show the circumferential nodes at a height of $z = 1.39\text{m}$ of the cylinder. [Reference pressure $20\mu\text{Pa}$]	162
8.27	Total sound pressure comparison between the analytical and 3D BEM results calculated on the circumferential nodes at a height of $z = 1.39\text{m}$ (see Figures 8.26a and 8.26b) of the extended cylinder of length 5m and radius 0.057m , due to a point source of $f = 1.5 \text{ kHz}$ and $ka = 1.57$ is placed at a location of $X = -4.1\text{m}$, $Y = 0\text{m}$ and $Z = 0\text{m}$ (consider Figure 7.1 for the source geometry). [Reference pressure $20\mu\text{Pa}$]	163
8.28	3D arrangement of a line source.	164
8.29(a-b)	Numerical results of the total sound pressure distribution at the surface of the extended	

cylinder of length 5m and radius 0.057m, due to a line source of 15 point sources of arbitrary amplitudes and phases (Table 5.1 was used) placed on the negative X axis, for $f = 1.5\text{kHz}$ and $ka = 1.57$. [Reference pressure $20\mu\text{Pa}$]	165
8.30 Total sound pressure comparison between the 3D BEM and analytical results calculated on the circumferential nodes at the middle ($z = 2.5\text{m}$, see Figures 8.19a and 8.19b) of the extended cylinder of length 5m and radius 0.057m, due to a line source of 15 point sources of arbitrary amplitudes and phases (Table 5.1 was used) placed on the negative X axis, for $f = 1.5\text{kHz}$ and $ka = 1.566$. [Reference pressure $20\mu\text{Pa}$]	165
8.31(a-j) 2D BEM results showing the scattered and total pressure fields around the Boeing cylinder, for plane waves incident from the left, for different values of ka . The scales for the scattered and total pressures are (Pa) and (dB) respectively. [Incident pressure magnitude $P^o = 1\text{ Pa}$ and reference pressure $20\mu\text{Pa}$]	169
8.32 Total sound pressure comparison between the 2D BEM and analytical results at the surface of the Boeing cylinder, for a point source is placed at $X = -20D\text{ m}$ and $Y = 0\text{m}$, for $ka = 5$. [Diameter of the cylinder is $D = 2.46\text{m}$ and reference pressure $20\mu\text{Pa}$]	170
8.33 Total sound pressure comparison between the 2D BEM and analytical results at the surface of the Boeing cylinder, for a line source of 15 point sources of arbitrary amplitudes and phases (see Table 5.1) placed on the negative X axis, for $ka = 5$. [Reference pressure $20\mu\text{Pa}$]	170
8.34 FEA model of the Boeing cylinder.	171
8.35 Boeing cylinder geometry showing the surface elements and nodes. The green circles are showing the positions of the circumferential nodes (60 nodes) at a height of $z = 1.67\text{m}$ of the cylinder.	171
8.36(a-h) Numerical results for the total sound pressure distribution at the surface of the Boeing cylinder due to incident plane waves on the front face for various values of ka . [Reference pressure $20\mu\text{Pa}$ and incident pressure magnitude $P^o = 1\text{ Pa}$]	174
8.37 Total sound pressure calculated using BEM on the circumferential nodes (60 nodes) at a height of $z = 1.67\text{m}$ (see Figure 8.35) of the Boeing cylinder, for incident plane waves on the front face, for various values of ka . [Reference pressure $20\mu\text{Pa}$ and incident pressure magnitude $P^o = 1\text{ Pa}$]	174
8.38 Total sound pressure comparison between the 3D BEM and analytical results calculated on the circumferential nodes at a height of $z = 1.67\text{m}$ (see Figure 8.35) of the Boeing cylinder, for plane incident waves on the front face, for $ka = 8$. [Reference pressure $20\mu\text{Pa}$ and incident pressure magnitude $P^o = 1\text{ Pa}$]	175
8.39(a-b) Numerical results for the sound pressure distribution at the surface of the Boeing cylinder due to incident plane waves on the front face, for $ka = 10$. [Reference pressure $20\mu\text{Pa}$ and incident pressure magnitude $P^o = 1\text{ Pa}$]	175
8.40 Total sound pressure comparisons between the 3D BEM and analytical results calculated on 60 circumferential nodes at a height of $z = 1.67\text{m}$ (see Figure 8.35) of the Boeing cylinder, for plane incident waves on the front face, for $ka = 10$. [Reference pressure $20\mu\text{Pa}$ and incident pressure magnitude $P^o = 1\text{ Pa}$]	176
8.41(a-b) Numerical results for the total sound pressure distribution at the surface of the Boeing cylinder due to a point source of 250Hz placed at $X = -20D\text{ m}$, $Y = 0\text{m}$ and $Z = 0\text{m}$ (see Figure 7.1 for the source geometry). [Diameter of the cylinder, $D = 2.46\text{m}$ and reference pressure $20\mu\text{Pa}$]	177

8.42	Total sound pressure comparison between the 3D BEM and analytical results calculated on the circumferential nodes (60 nodes) at a height of $z = 1.67\text{m}$ on the Boeing cylinder, due to a point source of 250Hz placed at $X = -20D\text{ m}$, $Y = 0\text{m}$ and $Z = 0\text{m}$ (see Figure 7.1 for the source geometry). [Diameter of the cylinder, $D = 2.46\text{m}$, and reference pressure $20\mu\text{Pa}$]	177
8.43(a-b)	Numerical results for the total sound pressure distribution at the surface of the Boeing cylinder, due to a line source of fifteen point sources (see Figure 8.28 for the line source geometry) of arbitrary amplitudes (see Table 5.1), placed on the negative X axis. Each source generated a frequency of 250Hz. [Reference pressure $20\mu\text{Pa}$]	179
8.44	Total sound pressure comparison between the BEM and analytical results calculated on the circumferential nodes at a height of $z = 1.67\text{m}$ on the Boeing cylinder, due to a line source of fifteen point sources (see Figure 8.28 for the line source geometry) of arbitrary amplitudes (see Table 5.1), placed on the negative X axis at the bottom of the Boeing cylinder. Each source generated a frequency of 250Hz. [Reference pressure $20\mu\text{Pa}$]	180
8.45(a-b)	Numerical results for the total sound pressure distribution at the surface of the Boeing cylinder, due to a line source of varying frequencies corresponding to one-third-octave centre frequencies from 50Hz to 315Hz. Arbitrary strengths given in Table 5.1 were used for each point source. [Reference pressure $20\mu\text{Pa}$]	180
8.46	Total sound pressure comparison between the BEM and analytical results calculated on the circumferential nodes at a height of $z = 1.67\text{m}$ on the Boeing cylinder, due to a line source of nine point sources (see Figure 8.28 for the line source geometry) of varying frequencies corresponding to one-third octave centre frequencies from 50Hz to 315Hz, placed on the negative X axis at the bottom of the Boeing cylinder. Arbitrary strengths given in Table 5.1 were used for each point source. [Reference pressure $20\mu\text{Pa}$]	181
8.47	FEA model of an RSLVF	182
8.48	RSLVF surface elements and nodes. Geometry imported into the Open BEM. The blue circles show the circumferential nodes at a height of $z = 2.065\text{m}$ on the RSLVF.	182
8.49(a-t)	Numerical results for the sound pressure distribution at the surface of the RSLVF for plane waves incident on the front face at various 1/3-octave band centre frequencies from 50Hz to 400Hz. [Reference pressure $20\mu\text{Pa}$ and incident pressure magnitude $P^O = 1\text{ Pa}$]	187
8.50	Total sound pressure calculated using BEM on the circumferential nodes at a height of $z = 2.065\text{m}$ (see Figure 8.48) on the RSLVF, for plane waves incident on the front face, for various 1/3-octave band centre frequencies from 50Hz to 100Hz. [Reference pressure $20\mu\text{Pa}$ and incident pressure magnitude $P^O = 1\text{ Pa}$]	187
8.51	Total sound pressure calculated using BEM on the circumferential nodes at a height of $z = 2.065\text{m}$ (see Figure 8.48) on the RSLVF, for plane waves incident on the front face, for various 1/3-octave band centre frequencies from 125Hz to 200Hz. [Reference pressure $20\mu\text{Pa}$ and incident pressure magnitude $P^O = 1\text{ Pa}$]	188
8.52	Total sound pressure calculated using BEM on the circumferential nodes at a height of $z = 2.065\text{m}$ (see Figure 8.48) on the RSLVF, for plane waves incident on the front face, for various 1/3-octave band centre frequencies from 250Hz to 400Hz. [Reference pressure $20\mu\text{Pa}$ and incident pressure magnitude $P^O = 1\text{ Pa}$]	188
8.53	Total sound pressure comparison between the BEM and analytical results calculated on the circumferential nodes at a height of $z = 2.065\text{m}$ (see Figure 8.48) on the RSLVF, for plane waves incident on the front face, for 1/3-octave band centre frequency of 400Hz. [Reference pressure $20\mu\text{Pa}$ and incident pressure magnitude $P^O = 1\text{ Pa}$]	189

8.54(a-b)	Numerical results for the sound pressure distribution at the surface of the RSLVF, due to a point source (see Figure 7.1 for the point source geometry) of 50Hz located at $X = -20D$ m (Diameter, $D = 1.266$ m, see Figure 7.5), $Y = 0$ m and $Z = 0$ m. [Reference pressure $20\mu\text{Pa}$]	190
8.55	Total sound pressure comparison between the 3D BEM and analytical results calculated on the circumferential nodes at a height of $z = 2.065$ m (see Figure 8.48) on the RSLVF, for a point source of 50Hz located at $X = -20D$ m (Diameter, $D = 1.266$ m, see Figure 7.5), $Y = 0$ m and $Z = 0$ m. [Reference pressure $20\mu\text{Pa}$]	190
8.56(a-b)	Numerical results for the total sound pressure distribution at the surface of the RSLVF, due to a line source of fifteen point sources (see Figure 8.28 for the line source geometry) of arbitrary amplitudes (see Table 5.1) placed on the negative X axis. Each source generated a frequency of 50Hz. [Reference pressure $20\mu\text{Pa}$]	192
8.57(a-b)	Numerical results for the total sound pressure distribution at the surface of the RSLVF, due to a line source consisting of ten point sources of varying frequencies corresponding to one-third-octave band centre frequencies from 50Hz to 400Hz. Arbitrary strengths given in Table 5.1 were used for each point source. [Reference pressure $20\mu\text{Pa}$]	192
8.58	Total sound pressure comparison between the 3D BEM and analytical results calculated on the circumferential nodes at a height of $z = 2.065$ m (see Figure 8.48) on the RSLVF, for a line source consisting of fifteen point sources (see Figure 8.28 for the line source geometry) of arbitrary amplitudes (see Table 5.1) placed on the negative X axis. Each source generated a frequency of 50Hz. [Reference pressure $20\mu\text{Pa}$]	193
8.59	Total sound pressure comparison between the 3D BEM and analytical results calculated on the circumferential nodes at a height of $z = 2.065$ m on the RSLVF, due to a line source consisting of ten point sources (see Figure 8.28 for the line source geometry) of varying frequencies corresponding to one-third octave band centre frequencies from 50Hz to 400Hz, placed on the negative X axis at the bottom of the RSLVF. Arbitrary strengths given in Table 5.1 were used for each point source. [Reference pressure $20\mu\text{Pa}$]	193
9.1	Overall acoustic power levels for various rocket engines 'A' to 'F'.	200
9.2	Core lengths for various chemical rocket engines 'A' to 'F'.	200
9.3	Geometry of source locations relative to the vehicle and flow axis.	202
9.4	Estimated relative sound power levels for each one-third-octave band centre frequency from 50Hz to 400Hz. [Data estimated from Figure 5, presented in NASA-SP-8072 (1971)]	205
9.5	Estimated source locations for each one-third-octave band centre frequency from 50Hz to 400Hz. [Data estimated from Figure 14, presented in NASA-SP-8072 (1971)]	205
9.6	Calculated sound power levels at each one-third-octave bandwidth from 50Hz to 400Hz.	206
9.7	Simple directivity curve is used in calculations. [Data estimated from Figure 10, presented in NASA-SP-8072 (1971)]	206
9.8	Analytically calculated sound pressure levels at the surface of section two (see Figure 7.5 in Chapter 7) at a height of $z = 2.17$ m from the bottom face of the RSLVF, using the unique source allocation method, for an equivalent single point source for each one-third-octave band centre frequency from 50Hz to 100Hz. For the equivalent point source location at each frequency see Table 9.2. [$x_1 = 15D_e$, $x_2 = 5D_e$ and reference pressure $20\mu\text{Pa}$]	211
9.9	Analytically calculated sound pressure levels at the surface of section two (see Figure 7.5 in Chapter 7) at a height of $z = 2.17$ m from the bottom face of the RSLVF, using the unique source allocation method, for an equivalent single point source for each one-third-	

octave band centre frequency from 125Hz to 200Hz. For the equivalent point source location at each frequency see Table 9.2. [$x_1 = 15D_e$, $x_2 = 5D_e$ and reference pressure $20\mu\text{Pa}$]	211
9.10 Analytically calculated sound pressure levels at the surface of section two (see Figure 7.5 in Chapter 7) at a height of $z = 2.17\text{m}$ from the bottom face of the RSLVF, using the unique source allocation method, for an equivalent single point source for each one-third-octave band centre frequency from 250Hz to 400Hz. For the equivalent point source location at each frequency see Table 9.2. [$x_1 = 15D_e$, $x_2 = 5D_e$ and reference pressure $20\mu\text{Pa}$]	212
9.11 Analytically calculated overall sound pressure level at the surface of section two (see Figure 7.5 in Chapter 7) at a height of $z = 2.17\text{m}$ from the bottom face of the RSLVF, using the unique source allocation method, for the entire spectrum of one-third-octave band centre frequency range from 50Hz to 400Hz. For the equivalent point source location at each frequency see Table 9.2. [$x_1 = 15D_e$, $x_2 = 5D_e$ and reference pressure $20\mu\text{Pa}$]	212
9.12 Analytically calculated directivity pattern of the overall sound pressure level at the surface of section two (see Figure 7.5 in Chapter 7) at a height of $z = 2.17\text{m}$ from the bottom face of the RSLVF, using the unique source allocation method, for the entire spectrum of one-third-octave band centre frequency range from 50Hz to 400Hz. For the equivalent point source location at each frequency see Table 9.2. [$x_1 = 15D_e$, $x_2 = 5D_e$ and reference pressure $20\mu\text{Pa}$]	213
9.13 (a-t) Numerically calculated sound pressure excitation at the surface of the RSLVF using the unique source allocation method, for various one-third-octave band centre frequencies from 50Hz to 400Hz. For the equivalent point source location at each frequency see Table 9.2. [$x_1 = 15D_e$, $x_2 = 5D_e$ and reference pressure $20\mu\text{Pa}$]	219
9.14 (a-b) Numerically calculated overall sound pressure excitation at the surface of the RSLVF using the unique source allocation method, for the entire spectrum of one-third-octave band centre frequency range from 50Hz to 400Hz. For the equivalent point source location at each frequency see Table 9.2. [$x_1 = 15D_e$, $x_2 = 5D_e$ and reference pressure $20\mu\text{Pa}$]	219
9.15 Numerically calculated sound pressure levels on the circumferential nodes at a height of $z = 2.17\text{m}$ from the bottom face of the RSLVF, using the unique source allocation method, for various one-third-octave centre frequencies from 50Hz to 100Hz. For the equivalent point source location at each frequency see Table 9.2. [$x_1 = 15D_e$, $x_2 = 5D_e$ and reference pressure $20\mu\text{Pa}$]	220
9.16 Numerically calculated sound pressure levels on the circumferential nodes at a height of $z = 2.17\text{m}$ from the bottom face of the RSLVF, using the unique source allocation method, for various one-third-octave centre frequencies from 125Hz to 200Hz. For the equivalent point source location at each frequency see Table 9.2. [$x_1 = 15D_e$, $x_2 = 5D_e$ and reference pressure $20\mu\text{Pa}$]	220
9.17 Numerically calculated sound pressure levels on the circumferential nodes at a height of $z = 2.17\text{m}$ from the bottom face of the RSLVF, using the unique source allocation method, for various one-third-octave centre frequencies from 250Hz to 400Hz. For the equivalent point source location at each frequency see Table 9.2. [$x_1 = 15D_e$, $x_2 = 5D_e$ and reference pressure $20\mu\text{Pa}$]	221
9.18 Comparison of the overall sound pressure level between the numerical and analytical results calculated on the circumferential nodes at a height of $z = 2.17\text{m}$ from the bottom of the RSLVF, using the unique source allocation method, for the entire spectrum of one-	

third-octave band centre frequency range from 50Hz to 400Hz. For the equivalent point source location at each frequency see Table 9.2. [$x_1 = 15D_e$, $x_2 = 5D_e$ and reference pressure $20\mu\text{Pa}$]	221
9.19 Analytically calculated overall sound pressure level at the circumferential surface of section two (see Figure 7.5) at a height of $z = 2.17\text{m}$ from the bottom face of the RSLVF, using the non-unique source allocation method, for a line source of 10 individual point sources along the exhaust flow (see Figure 9.3), for each one-third-octave band centre frequency from 50Hz to 100Hz. The data used for the analytical calculation for each point source are given in Tables 9.3, 9.4, 9.5 and 9.6. [$x_1 = 15D_e$, $x_2 = 5D_e$ and reference pressure $20\mu\text{Pa}$]	231
9.20 Analytically calculated overall sound pressure level at the circumferential surface of section two (see Figure 7.5) at a height of $z = 2.17\text{m}$ from the bottom face of the RSLVF, using the non-unique source allocation method, for a line source of 10 individual point sources along the exhaust flow (see Figure 9.3), for each one-third-octave band centre frequency from 125Hz to 200Hz. The data used for the analytical calculation for each point source are given in Tables 9.3, 9.4, 9.5 and 9.6. [$x_1 = 15D_e$, $x_2 = 5D_e$ and reference pressure $20\mu\text{Pa}$]	231
9.21 Analytically calculated overall sound pressure level at the circumferential surface of section two (see Figure 7.5) at a height of $z = 2.17\text{m}$ from the bottom face of the RSLVF, using the non-unique source allocation method, for a line source of 10 individual point sources along the exhaust flow (see Figure 9.3), for each one-third-octave band centre frequency from 250Hz to 400Hz. The data used for the analytical calculation for each point source are given in Tables 9.3, 9.4, 9.5 and 9.6. [$x_1 = 15D_e$, $x_2 = 5D_e$ and reference pressure $20\mu\text{Pa}$]	232
9.22 (a-t) Numerically calculated sound pressure excitation at the surface of the RSLVF at various one-third-octave band centre frequencies from 50Hz to 400Hz, using the non-unique source allocation method. The data used for the numerical calculation for each point source are given in Tables 9.3, 9.4, 9.5 and 9.6. [$x_1 = 15D_e$, $x_2 = 5D_e$ and reference pressure $20\mu\text{Pa}$]	237
9.23 Numerically calculated sound pressure levels on the circumferential nodes at a height of $z = 2.17\text{m}$ from the bottom face of the RSLVF at various one-third-octave centre frequencies from 50Hz to 100Hz, using the non-unique source allocation method. The data used for the numerical calculation for each point source are given in Tables 9.3, 9.4, 9.5 and 9.6. [$x_1 = 15D_e$, $x_2 = 5D_e$ and reference pressure $20\mu\text{Pa}$]	237
9.24 Numerically calculated sound pressure levels on the circumferential nodes at a height of $z = 2.17\text{m}$ from the bottom face of the RSLVF at various one-third-octave centre frequencies from 125Hz to 200Hz, using the non-unique source allocation method. The data used for the numerical calculation for each point source are given in Tables 9.3, 9.4, 9.5 and 9.6. [$x_1 = 15D_e$, $x_2 = 5D_e$ and reference pressure $20\mu\text{Pa}$]	238
9.25 Numerically calculated sound pressure levels on the circumferential nodes at a height of $z = 2.17\text{m}$ from the bottom face of the RSLVF at various one-third-octave centre frequencies from 250Hz to 400Hz, using the non-unique source allocation method. The data used for the numerical calculation for each point source are given in Tables 9.3, 9.4, 9.5 and 9.6. [$x_1 = 15D_e$, $x_2 = 5D_e$ and reference pressure $20\mu\text{Pa}$]	238
A1 Characteristic behavior of <i>Bessel functions of the first kind</i> of order 0, and 1 with respect to the argument z .	251
A2 Characteristic behavior of <i>Bessel functions of the second kind</i> of order 0 and 1 with respect to the argument z .	252

Glossary of Symbols

a	Radius of a cylinder
a	Observation point
a_e	Speed of sound in the exhaust flow
A_m	Coefficients [defined by equations (3.16)]
b	Distance between two point sources [see Figure (5.8)]; also, frequency band (Ch.9)
c	Speed of sound
$C(q)$	Solid angle from volume V [defined by equations (8.7)]
d	Distance between the nearest source and the cylinder surface [see Figure (5.8)]
D_e	Nozzle exit diameter
E_m^i	Amplitudes of the incident waves [see equation (3.22)]
E_m^o	Amplitudes of the outgoing waves [see equations (3.22), (3.26) and (3.27)]
f	Frequency of sound
F	Driving force in the medium (Ch.3); also, thrust of the rocket engine (Ch.9)
$G(a/r'), G(r_p, r_q)$	
$G(R)$	Acoustic Green's function [see equations (5.1), (5.2) and (8.1)]
H_m	Bessel function of the 3 rd kind or Hankel function
H_{m+1}	Hankel Function of $(m+1)$ th order
H_{m-1}	Hankel Function of $(m-1)$ th order
$H_m^1(z)$	Hankel function for incoming waves [defined by equation (A.5)]
$H_m^2(z)$	Hankel function for outgoing waves [defined by equation (A.6)]
H'_m	Derivatives of the Hankel function of m th order
H'_0	Derivatives of the Hankel function of 0th order
H_1	Derivatives of the Hankel function of first order
$I^s(r, k, \phi_i)$	Scattered sound intensity as a function of radial distance r , wavelength k and azimuthal angle ϕ_i [defined by equation (4.4)]
J_m	Bessel function of the first kind of m th order
J'_m	Derivatives of the m th order Bessel function
J_{m+1}	Bessel function of $(m+1)$ th order
J_{m-1}	Bessel function of $(m-1)$ th order
J'_0	Derivatives of the 0th order Bessel function
J_1	Bessel function of first order

k	Wave number
L	Length of a cylinder
L_{p,b,ϕ_i}	Sound pressure level at a frequency band b of interest [defined by equation (9.8)]
L_{p,OA,ϕ_i}	Overall sound pressure level [defined by equation (9.9)]
$L_{p,\text{seg},b,\phi_i}$	Sound pressure level corresponding to each segment at a frequency band b of interest [defined by equation (9.14)]
$L_{p,\text{OA,seg},b,\phi_i}$	Overall sound pressure level over the entire segments of the exhaust flow at a frequency band b of interest [defined by equation (9.15)]
L_w	Overall acoustic power level [defined by equation (9.2)]
$L_{w,b}$	Acoustic power level at a frequency band b of interest [defined by equation (9.5)]
$L_{w,\text{seg}}$	Overall acoustic power level of exhaust flow segments [defined by equation (9.10)]
$L_{w,\text{seg},b}$	Acoustic power level of exhaust flow segments at a frequency band b of interest [defined by equation (9.11)]
n	Number of the point sources (Chs.5, 7); also, number of nozzles (Ch.9)
N	Total number of point sources (Ch.5); also, number of surface elements (Ch.8)
$N_i(\xi)$	Element shape functions [see equation (8.11)]
N_m	Bessel function of the 2 nd kind or Neumann function
N'_m	Derivatives of the m th order Neumann function
N_{m+1}	Neumann function of the $(m+1)$ th order
N_{m-1}	Neumann function of the $(m-1)$ th order
N'_0	Derivatives of the 0th order Neumann function
N_1	Neumann function of first order
$p(a, \phi_i)$	Resultant pressure as a function of cylinder radius a and azimuthal angle ϕ_i [defined by equations (3.21) and (3.24)]
p_a	Resultant sound pressure at the surface of a cylinder [defined by equation (3.26)]
p^i	Incident wave pressure [see equation (3.7)]
P	Acoustic pressure
$P(p), P(r_p)$	Acoustic pressure at a point p (Ch.8)
$P(p), P_i(p)$	Constant nodal pressure on a point p ; also, constant nodal pressure for i th elements [see equations (8.9) and (8.10)]
P_o	Equilibrium pressure in the medium
$P_{s\infty}(r, \phi)$	Scattered sound pressure as a function of radial distance r and azimuthal angle ϕ [defined by equation (3.20)]
P^i	Incident wave pressure [defined by equation (7.1)]
$P^i(a, k, \phi_i)$	Incident wave pressure as a function of cylinder radius a , wave number k and azimuthal angle ϕ_i [defined by equation (3.10)]

$P^i(r, k, \phi_i)$	Incident sound pressure as a function of radial distance r , wave number k and azimuthal angle ϕ_i [defined by equation (4.1)]
P^s, p_s	Scattered sound pressure
$P^s(a, k, \phi_i)$	Scattered sound pressure as a function of cylinder radius a , wave number k and azimuthal angle ϕ_i [defined by equation (3.11)]
$P^s(r, k, \phi_i)$	Scattered pressure as a function of radial distance r , wave number k and azimuthal angle ϕ_i [defined by equation (4.3)]
$P^I(q)$	Incident acoustic pressure at point q (Ch.8)
P_f^I	Incident acoustic pressure on the field points [see equation (8.18)]
$P_a^t(a, k, \phi_i)$	Total sound pressure as a function of cylinder radius a , wave number k and azimuthal angle ϕ_i [defined by equation (3.18)]
$P_a^t(R_i, k, a, \phi_i, Q_s)$	Total sound pressure at the surface of a cylinder due to a point source [defined by equation (5.5)]
$P'(R_i)$	Spatially dependent factor [defined by equation (5.4)]
$Q_s, Q_{s,b}, Q_{s,seg,b}$	Source strength [see equations (5.4), (9.7) and (9.13)]
r_n	Distance between the origin of the cylinder to the n th number of point sources [defined by equation (5.6)]
r_p	Distance to integration point on the boundary from the centre of the body (Ch.8)
r_q	Distance to point q from the centre of the body (Ch.8)
r'	Source distance [see equation (5.1)]
R	Distance between a point source and observation point [see equation (5.2)]; also, oblique resultant distance between a point source and an observation point [defined by equation (7.3)]
R_i	Distances between a point source and i th number of observation points [see equations (5.3) and (7.4)]
R'	Distance between a point source and an projected observation point [see Figure (7.1); also, defined by equation (7.2)]
S	Boundary surface (Ch.8)
t	Time
\mathbf{u}	Directional particle velocity
$u(p), u_n(r_p)$	Outward normal particle velocity at a point p (Ch.8)
U_e	Fully expanded exit velocity
W_b	Acoustic power of a source at a frequency band b of interest [defined by equation (9.6)]
$W_{seg,b}$	Acoustic power of a source corresponding to a segment of exhaust flow at a frequency band b of interest [defined by equation (9.12)]
x	Distance travelled by sound waves along the x -axis; also, node position along the x coordinate (Ch.8)

x_t	Core length
y	node position along the y coordinate (Ch.8)
z	Cylinder axis
ω	Angular frequency
β	Elevation angle
γ	Specific heat ratio
γ_m	Phase angles for m th order
ϕ_i	Azimuthal or circumferential angle
ψ, ψ_s	Velocity potential
$\psi_m^s(a, k, \phi_i)$	Velocity potential as a function of cylinder radius a , wavelength k and azimuthal angle ϕ_i [defined by equation (4.2)]
λ	Wavelength
ρ	Density of air in the exhaust flow
ρ_o	Equilibrium density in the fluid
$\delta(a - r'), \delta(r_p - r_q)$	Dirac delta function [see equations (5.1) and (8.1)]
Γ	Gamma function [defined by equation (A.3)]
ε_m	Constant terms used in the equations
∇	Laplacian operator or differential operator
Δx	Length of exhaust flow slices
Δf_b	Bandwidth of the frequency band, b

Chapter 1

Introduction

1.1 Introduction and Significance

During the launch of space vehicles, there is a large external excitation generated by acoustic and structural vibration. This is due to acoustic pressure fluctuations on the vehicle fairing caused by the engine exhaust gases. This external excitation drives the fairing structure and produces large acoustic pressure fluctuations inside the fairing cavity. The acoustic pressure fluctuations not only produce high noise levels inside the cavity but also cause damage such as structural fatigue, and damage to, or destruction of, the payload inside the fairing. This is an important problem because one trend of the aerospace industry is to use composite materials for the construction of launch vehicle fairings. The use of these materials has resulted in large-scale weight reductions of launch vehicles, but one of its potential disadvantages is the increase of noise transmission with a resulting increase in acoustic levels inside the fairing.

The present study forms part of a large collaboration between the School of Mechanical Engineering at the University of Adelaide and the Air Force Research Lab at Kirtland AFB, New Mexico, which focuses on developing analytical and numerical tools for noise reduction treatment. The ultimate goal of the project is to reduce the noise levels transmitted into the interior cavity of a real launch vehicle fairing using Passive Vibro Acoustic Devices (PVADs). Such devices integrate acoustic and vibration absorbers

(Tuned Mass Dampers, TMDs) to reduce the interior noise levels by absorbing both acoustic and structural energy. An important part of the present work is the prediction of the acoustic loading on the external fairing surface as a result of rocket motor noise during launch.

1.2 Objectives of the Study

The work in this thesis focuses on the investigation of both incident and scattered sound pressure fields and their effect on the external acoustic loading on a large composite cylinder and Representative Small Launch Vehicle Fairing (RSLVF). Specific objectives are to:

- investigate the theoretical model of the sound field resulting from incident plane waves that strike normal to the circumference of a cylinder;
- develop a theoretical model for the sound field due to normal incident waves from a point source and a line source incident on the surface of a cylinder;
- develop a theoretical model for the sound field due to oblique incident waves from a point source and a line source incident on the surface of a cylinder;
- investigate potential numerical analyses and build numerical models to predict the sound field as a result of normal and oblique incident waves from various idealised sources (plane waves, point source and line source) incident on a large composite cylinder and an RSLVF;

(The large composite cylinder analysed here was constructed by Boeing Company for the US Air Force and tested extensively by the Vibration and Acoustic Laboratories at Virginia Tech in the USA.)

- investigate and obtain numerical descriptions for the launch vehicle lift-off acoustic

environment;

- build an analytical and numerical model to describe the lift-off acoustic environment for a rocket fairing;
- apply both analytical and numerical models to an RSLVF to estimate the external acoustic loading under actual launch conditions.

1.3 Contributions of the Study

The contributions of this study are outlined as follows

- A suitable analytical form is developed to calculate the total circumferential sound pressure field at the surface of a cylinder, as a result of incident plane waves that strike normal to the circumference of the cylinder. This form has the advantage that it can consider both incident and scattered sound pressure fields at the same time, with no need to calculate them separately unless required, thus reducing the calculation time. Also, it converges for all values of the argument ka (k is wave number and a is radius of a cylinder).
- An analytical model is developed to calculate the scattered and total sound pressure fields at any position relative to a cylinder in a sound field, resulting from incident plane waves that strike normal to the circumference of the cylinder. This new model has overcome the near-field and far-field limitations, and is applicable for any position in the sound field for any frequency of interest.
- A theoretical method is developed that can take into account the type of noise source and its position at a finite distance from a cylinder, to calculate the circumferential sound pressure field at the cylinder surface. This method is

developed further for a line source.

- A theoretical method is developed which predicts the circumferential sound pressure field at the surface of a cylinder; due to oblique incident waves from a point source and line source.
- A full investigation is conducted for the external acoustic loading of an RSLVF using the Boundary Element Method (BEM) approach. Various acoustic loading conditions are investigated, including the effect due to reflecting surface of the RSLVF, and the results presented in this are new and not available in the published literature as far as the author knows.

1.4 Overview of the Thesis

This thesis presents the results of an investigation into the external acoustic loading of a launch vehicle fairing structure resulting from rocket engine exhaust noise during lift-off.

The intention is that the work serves as a basis for further investigations directed at reducing noise levels inside a rocket fairing structure. As the work described here represents only an initial investigation, the cylinder and fairing walls are modelled as rigid for the purpose of determining the external acoustic loading. Hence, the effect of secondary radiation due to vibration of the flexible cylinder and fairing walls or absorption of energy due to their damping behaviour has not been taken into account. Also the non-linear effects of high sound pressure levels on the acoustic loading have been ignored in this study for simplicity. These would be the subject of an extended investigation.

The thesis consists of five parts:

- Literature review, Chapter 2.

- Theory, Chapters 3, 4, 5 and 7.
- Experimental work, Chapter 6.
- Numerical analysis, Chapters 8 and 9.
- Conclusions and future work, Chapter 10.

In Chapter 2, a literature review is presented which describes the previous work in the areas relevant to this thesis. The gaps in the current knowledge are also discussed.

Prior to investigating the acoustic loading on a rocket fairing, it was necessary to evaluate and verify the available theory, which predicts the circumferential sound pressure field at the surface of a cylinder. Chapter 3 is concerned with the theory for predicting the circumferential sound pressure field at the surface of a cylinder. The theoretical model used in that chapter predicts the circumferential sound pressure field due to incident plane waves striking normal to a cylinder of infinite length and is based on previous work by Morse (1936), Morse & Feshbach (1953b) and Morse & Ingard (1986). Both incident pressure and scattered pressure fields were investigated theoretically. The concepts were then used to produce a suitable theoretical form to calculate the total circumferential sound pressure field at the surface of a cylinder. The results from the current work were also compared with those from previous work (Morse, 1936; Morse & Feshbach, 1953b; Morse & Ingard, 1986; Junger & Feit, 1993) and demonstrate the improvements obtained using the model developed here.

In particular, it has been observed that in previous work (Morse, 1936; Morse & Feshbach, 1953b; Morse & Ingard, 1986) the mathematical expressions do not give results that converge to a solution for the scattered and total sound pressure fields in the near-field of a

cylinder for the case of incident plane waves striking normal to a cylinder of infinite length. The use of asymptotic forms and the limits of the argument kr (k is wave number and r is radial distance of the observation point in the sound field from a cylinder) in the mathematical expressions are the main reasons for these problems. This is described in more detail in Chapter 4, where a suitable analytical model is also developed that overcomes the limitations. The analytical model presented in Chapter 4, is suitable for both near-field and far-field calculations of the scattered and total sound pressure fields of a cylinder. However, the current model has also been compared with Junger & Feit (1993). The comparisons show that there are no significant differences between the results obtained using the current derivations and those using Junger & Feit (1993).

The theoretical method developed in Chapter 5 predicts the circumferential sound pressure field at the surface of a cylinder due to a point source positioned at a finite distance from the cylinder. The method was further developed for a line source. The work presented here shows that it is possible to predict the sound pressure field at the surface of a cylinder by identifying the source position and strength. This was not possible using results from previous work by Morse (1936), Morse & Feshbach (1953b), Morse & Ingard (1986) and Junger & Feit (1993).

In Chapter 6, an experiment is described which used a PVC cylinder to verify that the theoretical method developed in Chapter 5 can predict the sound pressure field at the surface of the cylinder for a source positioned at a finite distance from the cylinder.

For the actual acoustic loading of a rocket fairing, the prediction method needs to account for oblique incident waves that strike the circumference of the fairing. Therefore, a

theoretical method is developed in Chapter 7, which predicts the circumferential pressure field due to oblique incident waves from a point source and line source. The method is applied to a composite Boeing cylinder and RSLVF for the prediction of acoustic loads on the surface of each model.

A numerical analysis is described in Chapter 8, which used the Boundary Element Method (BEM) technique to predict the sound pressure field at the surface. The technique was used to verify the theoretical predictions made in Chapters 3, 4, 5, 6 and 7. It was also used to investigate various more complex acoustic loading conditions for a composite Boeing cylinder and RSLVF, for which both analytical and numerical results are presented.

In Chapter 9, the complex acoustic environment generated during the lift-off of a launch vehicle is investigated. The work presented here was based on NASA-SP-8072 (1971), a space vehicle design criteria document. Two different source allocation techniques were investigated separately for calculating the acoustic loading on an RSLVF. The investigations were conducted both analytically and numerically for each technique and are described separately.

Finally, some conclusions on the analytical and numerical results presented in this thesis are outlined in Chapter 10. Recommendations for future work are also given.

Chapter 2

Literature Review

2.1 Introduction

Researchers who are investigating the problem of reducing the noise levels inside the payload fairing of a launch vehicle face the problem of finding a suitable representation that can describe the launch environment for the purposes of determining the acoustic loading on the payload fairing. The launch environment during lift-off of a space vehicle can be explained briefly as “the noise generated from the rocket boosters and exhaust gases. It is deflected to one or two sides depending on the type of deflector used; is reflected by the launch platform and re-injected into the payload fairing (Howard *et al.*, 2003a)”. Although analyses exist for predicting the acoustic pressure on the surface of a simple cylinder, no one theory exists that can fully describe the noise injection into the fairing of a launch vehicle from the rocket boosters. Thus, little literature was found which was related to the main objective of the current work. The literature review presented here is mostly concerned with the theoretical and numerical methods that have been used and modified in this thesis to model the launch acoustic conditions. Other work that has been reviewed is concerned with describing the launch environments. In addition, a few papers concerned with the acoustic loading of a payload fairing have also been reviewed.

2.2 Scope

The literature review addresses the following topics which are relevant for acoustic loading

on a payload fairing:

Underlying Theory and Analytical Models for Acoustic Loading: A review is undertaken of existing theories for predicting the external sound pressure excitation at the surface of a cylinder due to incident plane waves that strike normal to the circumference of a cylinder of infinite length. A review of models is also undertaken for predicting the scattered and total sound pressure fields at locations in the acoustic domain due to incident plane waves that strike normal to the circumference of a cylinder of infinite length. The limitations of currently available theories are discussed.

Launch Acoustic Environments and Prediction Techniques: This part of the review concerns the environment that creates acoustic loads on a launch vehicle fairing during launch. Several launch noise prediction techniques are reviewed. The possibility of using these techniques to predict the acoustic loads on the fairing is discussed.

Solutions to Minimize the Acoustic Loads: Here, publications directed at reducing the interior noise levels of a launch vehicle fairing are reviewed.

Numerical Analysis Techniques: A Boundary Element Method (BEM) technique has been used in the present work to calculate the external acoustic loading. Previous BEM work relevant to this application is reviewed in this section.

2.3 Underlying Theory and Analytical Models for Acoustic Loading

The prediction of the acoustic loading at the surface of rocket fairings is challenging because of the complexity of the fairing geometry. The incident waves that strike the

circumference of the fairing produce complicated patterns of scattered waves, which make the problem even more complex. However, for simplicity, the majority of the previous analytical investigations of external acoustic loading have been conducted using a cylindrical geometry. Estève & Johnson (2000a, 2000b) and Johnson *et al.* (2001) have used a theoretical model of an infinite cylinder to determine the external acoustic pressure loading. They combined wave propagation in two component planes to determine the acoustic loading resulting from plane waves impinging on the cylinder at an arbitrary elevation angle. Gardonio *et al.* (2001) have also used a similar approach to determine the response of a cylinder which is externally excited by plane acoustic waves.

The theoretical models (Estève & Johnson 2000a, 2000b; Gardonio *et al.* 2001; Johnson *et al.* 2001) are based on Morse & Ingard (1986). Similar theoretical derivations can also be found in Morse (1936) and Morse & Feshbach (1953b). The theoretical models assume that the cylinder is infinite in length, and is excited by plane waves that strike perpendicular to the circumference of the cylinder from a particular direction.

The incident sound pressure is determined at different positions on the surface of the cylinder assuming that no distortion of sound waves occurs by the cylinder. The scattered sound pressure can be determined taking into account the distortion of the incident waves by the cylinder, which produces the scattered waves. The scattered waves spread out in all directions from the surface of the cylinder. The characteristics of the scattered wave field are strongly related to the circumferential length of the cylinder and the wavelength of the waves that impinge on the cylinder. These scattered waves can be added to the incident waves analytically to determine the total effect, in terms of the total sound pressure at

various points on the surface of the cylinder. The authors (Morse, 1936, Ch. 7, pp-266; Morse & Ingard, 1986, Ch. 8, pp-405) have presented an analytical derivation that determines the total sound pressure by adding the incident and scattered sound pressures. This model has been used in many applications, such as Potter (1966), to analyse the acoustic pressure loading, including the effects of scattering on the Saturn S-IC vehicle. To determine the acoustic pressure correlation on the vehicle, all the cross terms between the two signals from two point sources have been completely omitted by Potter (1966), which leads to significant errors in his work. Moreover, the governing derivation used by Morse (1936), Potter (1966) and Morse & Ingard (1986) may be partially suitable for analysing the total sound pressure including the radiation effects from a cylinder, but not suitable at all for determining the scattering effects for a hard cylindrical wall. This limitation may be due to the form of the governing derivation, which does not satisfy the boundary condition for scattering from a hard cylindrical wall.

Other analyses for scattering from an infinite cylinder can be found in Junger & Feit (1993, Ch.10, pp-322). They derived expressions for the incident sound pressure and the scattered sound pressure analytically, then added these to produce a suitable analytical form for the total sound pressure. The analyses are very similar to those of Morse (1936) and Morse & Ingard (1986). Nye (2003) used a similar approach to analyse electromagnetic waves incident on a circular cylinder, including the effect of scattering. Friot & Bordier (2004) have also used similar derivations to analyse the performance of an active noise control strategy, referred to as a “real-time control strategy”, for a cylinder including the effect of scattering. The expressions given by Morse (1936, Ch. 7, pp-266), Morse & Ingard (1986, Ch. 8, pp-405), Judger & Feit (1993, Ch.10, pp-322), Nye (2003) and Friot & Bordier

(2004) are suitable for plane waves, where the source position is assumed to be at an infinite distance from the cylinder, but completely unsuitable for a point source positioned at a finite distance from the cylinder or a line source. Junger & Feit (1993) have also derived a simplified analytical model to determine the total sound pressure at the surface of a cylinder using the *Wronskian* formula for *Bessel functions*. The simplified analysis using the *Wronskian* formula is useful to determine the total sound pressure at the surface of the cylinder, but it is unable to determine the sound pressure at any other location in the sound field, since there is no scope in that analytical model to account for the radial distance from the cylinder.

The determination of the scattered and total sound pressures at locations in the sound field due to incident plane waves on a cylinder may be of importance in many areas of acoustics, especially in underwater acoustics, to detect a submerged hard cylindrical structure. Descriptions of the theoretical analyses relevant to this problem can be found in Morse & Ingard (1986, Ch. 8, pp-402). However the analyses are only suitable for determining the scattered sound pressure and intensity, due to normal incident plane waves that strike perpendicular to the circumference of the cylinder, at a very large distance from the cylinder. This is because the governing equations require low and high frequency or large distance approximations to determine the amplitude of the scattered waves and phase angle between the incident and scattered waves at the surface of a cylinder. However it is not clear how far the distance needs to be for convergence of the analytical solutions. What is certain is that if the distance is very close to the cylinder, the analytical solutions will completely fail to produce the required results due to their divergent behaviour. Therefore, it is worthwhile to make an effort to construct a suitable analytical form to overcome those shortcomings.

2.4 Launch Acoustic Environments and Prediction Techniques

Severe acoustic loading, which occurs during the flight mission of a launch vehicle, is often responsible for damage to the payload inside the fairing compartment. The launch acoustic levels are estimated to be about 160dB and this can damage the sensitive parts of some payloads (Margasahayam & Caimi, 1999; Rogerio *et al.*, 2002). The acoustic loads reach their maximum under the fairing during take-off (Elias, 2000). These acoustic loads are primarily generated by the large propulsion motors and associated high velocity exhaust gases (Morgan *et al.*, 1961; NASA PN PD-ED-1259, 1996). Such very severe acoustic loadings, reflected by the launch platform and re-injected into the payload compartment, cause extreme pressure loadings on the launch vehicle fairing (Rogerio *et al.*, 2002). The pressure loadings are mainly due to two waves: (a) ignition overpressure (IOP) that comes from the inlet of the exhaust duct and propagates along the launch vehicle and (b) duct overpressure (DOP) that comes from the outlet of the exhaust duct and impinges the launch vehicle laterally (Chemoul, 1999). The pressure loadings are affected by parameters such as vehicle configuration, altitude, velocity, flow geometry, nozzle exit flow parameters, deflector configurations and interaction of flow turbulence with the deflector surfaces (NASA-SP-8072, 1971).

Fluctuating pressure loads can cause vibration of launch vehicle structural components over a broad frequency range, from 20Hz to 10,000Hz and above (NASA PN PD-ED-1259, 1996). Eldred *et al.* stated that in the sub-audible frequency range, the fundamental vehicle vibration modes are not strongly excited because the vehicle dimensions are relatively small compared to the wavelength of the very low frequency noise. However, in the higher frequency range from 100Hz to 10,000Hz, most of the vehicle dimensions are

no longer smaller than the acoustic wavelength; hence, much of the acoustic energy incident on the vehicle is absorbed, particularly at the resonance frequencies of the vehicle's outer surface and its substructures. This causes considerable vibration response of the vehicle surface and substructures, and this vibration is transmitted mechanically throughout the vehicle equipment and internal structures (Eldred *et al.*, 1961).

The excessive vibration can cause structural fatigue of the internal components and supporting hardware, lightweight exterior structures and lightweight spacecraft structures (NASA-SP-8072, 1971). Therefore, the prediction of acoustic loads impinging on the launch vehicle is essential from the design point of view to provide sufficient information for the development of the dynamic design of the vehicle shape, for the vibro-acoustic test of the hardware design and for the reduction of noise levels inside the cavity.

The prediction of acoustic loads on the payload fairing generated by the propulsion devices requires the use of analytical methods to identify the acoustic sources and the spectrum of the acoustic loads. Currently used analytical methods are based on experimental data and are strongly related to various parameters such as propulsion system configurations, nozzle configurations and exhaust flow configurations. Different parameters may produce different acoustic loading results.

For many years researchers have been trying to develop a suitable analytical methodology for the prediction of acoustic loads on launch vehicles, based on different sub-scale or full-scale tests of supersonic and subsonic engine exhaust jet flows. For example, Mayes *et al.* (1959) conducted near-field and far-field noise surveys on straight horizontal solid fuel rocket engines for a range of nozzle exit pressures, with the influence of the launch pad

excluded. The measurements were presented for a 1,500-pound-thrust engine and for several 5,000-pound-thrust engines for which the nozzle exit flow conditions varied widely. From the near-field measurements in the one-third-octave band frequency range from 5Hz to 2.5kHz; the apparent source of noise was found to be approximately 20 diameters downstream of the nozzle exit. The far-field measurements showed that the maximum overall noise levels for all engines occur between 30° to 45° from the axis of the flow.

Tedrick (1964) conducted acoustical measurements of clustered and single-nozzle rocket engines, and discussed the characteristics of near-field and far-field noise fields. Also, experimental results for various types of rocket engines, including exhaust flow configurations, and broad discussions can be found in a wide range of literature, including Lassiter & Heitkotter (1954), Cole *et al.* (1957), Eldred *et al.* (1961) and Morgan *et al.* (1961). Based on several experimental models, Franken *et al.* (1960), Morgan *et al.* (1961) and Potter & Crocker (1966) proposed an extensive empirical prediction methodology to calculate the near-field and far-field noise produced by jet and rocket flows, including the deflected flow from various types of exhaust deflectors. Recently, Mel'nikov *et al.* (1999) and Dumnov *et al.* (2000) investigated empirical techniques to define the maximum acoustic loads on the fairing on the basis of flight and experimental model data. In their work, the interaction of the jet flow with the launch pad was extensively studied to determine the acoustic noise using empirical techniques. Using as a basis, experimental and theoretical studies, Dementjev *et al.* (1999) developed a semi-empirical technique to determine the acoustic noise due to the interaction of supersonic high temperature jets with different shaped deflectors. All the aforementioned empirical techniques require a

considerable amount of experimental data and this is one of their major shortcomings. Standard empirical methodologies as discussed above and recommended implementation practices are outlined in NASA-SP-8072 (1971), a space vehicle design criteria document, which is used in the current work described in this thesis to determine the acoustic loading on the launch vehicle fairing.

Two different source allocation techniques have been proposed in NASA-SP-8072 (1971), based on experimental data for chemical rockets and generalized sound spectrum levels. The first technique assumes a unique source location along the exhaust flow in each frequency band, whereas the second technique assumes that the noise in each frequency band is generated throughout the exhaust flow. Although both techniques predict the acoustic loads at a specified point on the launch vehicle, the effects of scattering of the sound waves from the launch vehicle surface were completely omitted from the analysis using either technique. Part of the work undertaken in this thesis is concerned with the effect of scattering by a large composite cylinder that represents the launch vehicle. The concept of scattering is then incorporated with the source allocation techniques to determine acoustic loading on the launch vehicle fairing.

2.5 Solutions to Minimize the Acoustic Loads

Several techniques that have been proposed in NASA-SP-8072 (1971) to reduce the severe acoustic loads during lift-off include:

- the deflection angle of the engine exhaust gases through the deflector should be kept as small as possible.
- the exhaust flow should be deflected through a covered bucket or tunnel to provide

shielding from direct radiation from the deflected flow.

- the deflector and vehicle stand should be designed properly to eliminate large reflective surfaces turned toward the vehicle.
- water should be injected into the deflector near the nozzle.
- acoustic-attenuation padding should be placed over sensitive areas of the vehicle.

Water injection systems and launch pad geometry were extensively examined in order to reduce the acoustic pressure levels inside the payload fairing of the Ariane 5 launcher during different flights. Two test campaigns were conducted by ONERA (Office National d'Etudes et de Recherches Aérospatiales) at the MARTEL test facility to improve the acoustic environment of the Ariane 5 launcher during lift-off. Gély *et al.* (2000) reported that the first test was concerned with the optimisation of the water injection systems using a new pipe spray system at the inlets of the solid rocket booster (SRB) flues. The improved water injection system was implemented during the V503 flight and only 5dB of noise attenuation was achieved on the fairing wall compared with the V502 flight.

A second test campaign was conducted to modify the launch pad for the V504 flight. It was observed during the V503 flight that the maximum acoustic noise levels occurred when the launcher altitude was from 10m to 20m. A source localization technique (analyzing the signals from a microphone array fitted on the launcher) was performed in the 31.5 Hz octave band to identify the sources at those altitudes, and this showed that the acoustic sources appear to be located at the SRB flue outlets. Hence, the SRB lateral flues were extended by 30m just before the V504 flight. Noise attenuation of around 5dB on the fairing and around 10dB inside the fairing was achieved for the V504 flight.

Elias (2000) explained the source localization method and compared the localization results between the V503 and V504 flights at different altitudes in the 63Hz octave band. The source localization method on flight V503 found the following results (Elias, 2000):

- A dominant acoustic source appears in the middle of the central flue when the vehicle altitude is 0m;
- The dominant acoustic sources appear at the exit of the side flues with a secondary source in the middle of the central flue when the launcher altitude is 9m (this configuration of sources appear for all the altitudes between 0 and 30m);
- The source structure becomes more complex when the launcher altitude is 57m, due to the jet's impingement on the launch pad and acoustic reflections from the launch pad.

The author also reported that to treat the sources at the exit of the side flues, the flue ducts had been extended by 30m (aforementioned) and the source localization technique of the V504 flight showed that at all altitudes between 0 and 30m the sources at the lateral flue outlets had completely disappeared. However, the results also showed that at an altitude of 57m, the lengthened flue ducts were not effective because the jet flues impinge on the launch pad and produce a more complex source pattern (Elias, 2000). It seems that modification of the launch pad configurations and several water injection systems cannot significantly attenuate the acoustic noise levels due to the launch pad source. In particular, the low frequency noise source still appeared on the launch pad, which injected acoustic energy into the payload compartment. In addition, high frequency noise was also found to be transmitting into the payload cavity. Therefore, to attenuate significantly the low and high frequency noise levels, it was concluded that additional noise protection is required for the fairing compartment. However, before applying noise control treatment or before

being able to estimate with capable accuracy, the attenuation of any noise control treatment, it is essential to be able to accurately estimate the external acoustic excitation on a launch vehicle fairing during launch, and as this has so far not been modelled accurately either analytically or numerically, it is the main focus of this thesis.

2.6 Numerical Analysis Techniques

As described in section 2.3, if the problem geometry and the boundary conditions are simple, the external acoustic pressure loading on a cylindrical object may generally be determined using analytical expressions (Morse, 1936; Morse & Feshbach, 1953b; Morse & Ingard, 1986; Junger & Feit, 1993). However, for complex geometry, such as a launch fairing structure, it may not be possible to obtain a solution for the external acoustic pressure excitation because of the complicated wave reflections and diffractions caused by the complex geometry. This is one of the major shortcomings of the governing equations approach (Morse, 1936; Morse & Feshbach, 1953b; Morse & Ingard, 1986; Junger & Feit, 1993). Hence, a discrete element approximation such as Finite Element Analysis (FEA) or the Boundary Element Method (BEM), sometimes also known as Boundary Element Analysis (BEA), may be used as an alternative.

Finite element analysis has been used extensively in the past (Hansen *et al.*, 2000a, 2000b, 2001a, 2001b; Howard *et al.*, 2003a, 2003b, 2004) for problems involving scattered and radiated sound fields coupled with the structural response of the scatterers or radiators. For example, finite element models and modal analyses were used to analyse the coupled structural, acoustical and Passive Vibro Acoustic Devices (PVADs) response of a composite cylinder and an Representative Small Launch Vehicle Fairing (RSLVF) in previous work

(Hansen *et al.*, 2000a, 2000b, 2001a, 2001b; Howard *et al.*, 2003a, 2003b, 2004).

However, in the absence of data describing the actual exterior noise field, a simple uniform external acoustic loading only was used in their work.

The use of BEM is based on the *Helmholtz integral equation* (HIE) and has been used in the past for the solution of interior and exterior acoustic radiation and scattering problems (Cunefare & Gary, 1989). For problems related to the scattering from a rigid body, the integral equation can be modelled using the *Neumann condition* (the particle velocity normal to the boundary surface is zero) at the boundary (Kleinman *et al.*, 1988). Moreover, *Sommerfeld's* radiation condition of the radiating surface is automatically satisfied for the exterior infinite problem domain (Hwang & Chang, 1991). Basically, the integration relies on discrete boundary elements; hence the discretization is only needed on the boundary surface; in contrast, FEA requires discretization everywhere in the entire domain of the problem (Hwang & Chang, 1991). Therefore, fewer nodes are required for meshing the boundary surface than needed for meshing the entire problem domain. This is one of the major advantages of BEM over FEA and it often results in less computational time to solve interior and exterior acoustic problems.

One limitation of the BEM method is that it fails to give reliable results when the frequency reaches a characteristic frequency (also known as an *eigenfrequency*), since the system of equations becomes ill-conditioned at that frequency (Francis, 1993). Although this non-uniqueness problem generally appears for a few frequencies in the mid to high frequency range, it is a completely mathematical problem and has no physical meaning (Seybert & Rengarajan, 1987).

Another problem with the BEM technique is that it is sensitive to computational node points where the boundary conditions are applied. So, any incorrect placement of the node location can produce an unreliable result (Epstein & Bliss, 1997). In spite of the problems mentioned above, the BEM approach seems a suitable alternative in the low frequency range and is applicable for the current study, which is concerned with determining the amplitude of incident and scattered waves of a launch vehicle fairing impacted by plane waves or waves originating from point or line sources.

2.7 Current Gaps in Knowledge

A cylindrical geometry for which theoretical analyses are available has been used in previously reported work for theoretical investigations of external acoustic loading (Potter, 1966; Fuller, 1986, 1989; Junger & Feit, 1993; Estève & Johnson, 2000a, 2000b; Gardonio *et al.*, 2001; Johnson *et al.*, 2001; Nye, 2003; Friot & Bordier, 2004). However, all of these previous analyses are based on analyses presented by Morse (1936), Morse & Feshbach (1953b) and Morse & Ingard (1986). In their analyses at least one or two of the following shortcomings are present, which are:

- a) the analytical solutions of the governing equations are limited to high or low frequency approximations, or the diameter of the cylinder compared to wavelength.
- b) the governing equations require that the source position be assumed to be at an infinite distance from the cylinder and they are not able to model either the source position being located at a finite distance from the cylinder or the source strength.
- c) although *Green's function* has been used in the governing equations to express the source position, this approach is not able to consider the oblique distance between the

source and the cylinder for three-dimensional acoustic loading.

An alternative approach must be sought to overcome the aforementioned limitations of previously published work concerned with acoustic loading on a cylinder, which can be extended to estimate the acoustic loading on a launch vehicle fairing during launch.

No published work could be found that provides the overall theoretical solutions for estimating the acoustic loading on a launch vehicle fairing during launch. The work closest to this problem is outlined in NASA-SP-8072 (1971), a space vehicle design criteria document, which provides two empirical methods to determine the acoustic loading on a launch vehicle fairing due to acoustic sources located along the engine exhaust flow. Although the empirical methodologies predict the acoustic loads at a specified point on the launch vehicle, the effects of scattering of the sound waves from the launch vehicle surface were omitted. Malbeque *et al.* (1987) also considered the empirical technique to analyse the scattering of incident acoustic waves by the surface of the Ariane IV space launcher, using boundary integral methods. However, the analyses examined the sound field in the vicinity of the launcher rather than at the launcher surface.

The work undertaken in this thesis addresses the gaps identified above by developing theoretical and numerical analyses to predict the external sound field pressure incident on a large composite cylinder and a Representative Small Launch Vehicle Fairing (RSLVF), as a result of normal and oblique incident waves from various idealised sources (plane waves, point source and line source). The work also extends the empirical methodologies developed by NASA-SP-8072 (1971) to include the effect of scattered waves from a hard walled RSLVF surface. This study only considered the linear features of sound on acoustic loading. The non-linear features of sound on acoustic loading could be of interest for future investigation.

Chapter 3

Sound Pressure at the Surface of a Cylinder Due to Incident Plane Waves

3.1 Introduction

Prior to investigating the acoustic loading on a rocket fairing structure, it is important to verify numerical approaches by analysing the acoustic response of a cylinder for which theoretical analyses are available. The work presented in this chapter is concerned with theoretical analyses to predict the sound pressure at the surface of a cylinder of infinite length.

As discussed in the previous chapter, there are some theoretical approaches available in the literature to determine the sound pressure at the surface of a cylinder. It was decided to use the derivations given by Morse (1936), Morse & Feshbech (1953b) and Morse & Ingard (1986), as a basis for the current approach. The work presented here develops a suitable theoretical framework and also compares the results with the derivations given by Junger & Feit (1993).

3.2 Background Theory

In a homogeneous, inviscid, compressible medium, the space and time dependent propagation of sound waves can be derived by the second order wave equation

$$\nabla^2 P = \frac{1}{c^2} \left(\frac{\partial^2 P}{\partial t^2} \right); \quad (3.1)$$

which is a linear equation, where the *Laplacian operator* (∇^2) represents the source or sink of a vector field (for this case it is the vector field of air particle velocity). Note that in equation (3.1), P is a scalar acoustic pressure field. It is convenient to derive equation (3.1) in terms of velocity potential, ψ to avoid confusion between the scalar and vector product. The relation between the pressure gradient and the velocity potential gradient is

$$\nabla P = -\rho_o \frac{\partial}{\partial t} (\nabla \psi), \quad (3.2)$$

and

$$\mathbf{u} = \nabla \psi, \quad (3.3)$$

where \mathbf{u} is the vector particle velocity. The direction of gradient is orthogonal (normal) to every tangent vector on the curved boundary surface. That is $\partial \psi / \partial n = 0$; where n is the normal to the boundary surface. For a more detailed explanation see O'Neil (1995). Substituting equation (3.3) into (3.1) and integrating with respect to time, t , it can be shown that the velocity potential, ψ also satisfies the wave equation (Morse & Ingard, 1986; Kinsler *et al.*, 1982)

$$\nabla^2 \psi = \frac{1}{c^2} \left(\frac{\partial^2 \psi}{\partial t^2} \right), \quad (3.4)$$

where the speed of sound, $c = \sqrt{\gamma P_o / \rho_o}$; ρ_o is the equilibrium density in the fluid and γ

is the specific heat ratio. The above equation is both space and time dependent. If the wave motion is sinusoidal in its time dependence, the term depending only on time of the form $e^{-i\omega t}$ (the minus notation has been chosen using Morse (1936), Morse & Feshbach (1953b)

and Morse & Ingard (1986), and for comparison with their results) can be omitted, where $\omega=2\pi f$ is the angular frequency, and equation (3.4) is reduced to the well-known *Helmholtz equation* (Morse & Feshbach, 1953a)

$$\nabla^2\psi + k^2\psi = 0 , \quad (3.5)$$

where $k=\omega/c$ is defined as the wave number. Equation (3.5) is said to be a homogeneous *Helmholtz equation*. If there are external forces acting within, outside or on the boundary surface, the equation becomes inhomogeneous. The inhomogeneous *Helmholtz equation* can be written as (Morse & Feshbach, 1953a)

$$\nabla^2\psi + k^2\psi = -4\pi F , \quad (3.6)$$

where F is the driving force and is a function of space, and non-zero in the inhomogeneous case. If F is zero, the equation returns to the homogeneous *Helmholtz equation*, equation (3.5). The quantities F and k are both known but the field ψ is unknown. The first step is to find ψ and produce an equivalent equation similar to equation (3.6) to determine the sound pressure at the surface of a cylinder.

3.3 Plane Wave Pressure at the Surface of a Cylinder

To predict the overall external sound pressure at the surface of a cylinder, it is necessary to consider the pressures due to both incident and scattered waves; the latter occur due to the reflection of waves from the surface. As shown in Figure 3.1, the incident waves impinge on the surface of the cylinder and in addition to that there are scattered waves, which usually spread out from the surface of the cylinder. The total external sound pressure at the surface of a cylinder is the superposition of these two waves:

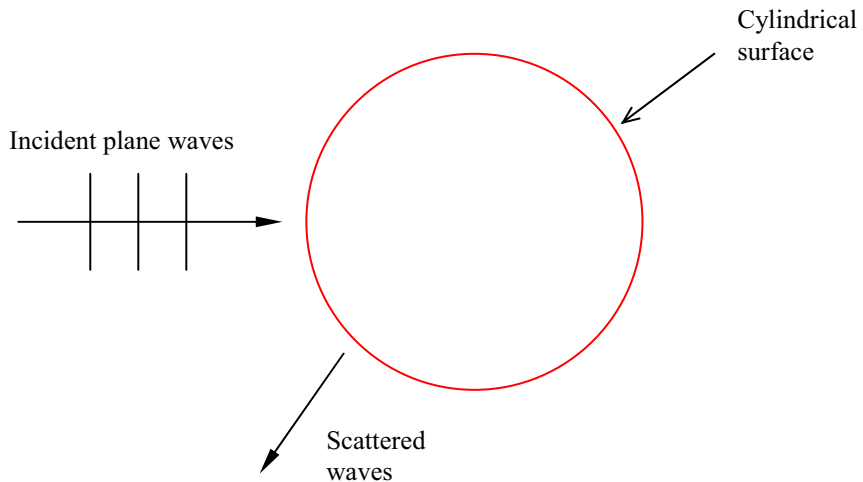


Figure 3.1: Geometry of the cylindrical external problem.

- (a) Incident sound pressure, denoted by P^i ; and
- (b) Scattered sound pressure, denoted by P^s .

In this instance, to calculate the total sound pressure at the surface of a cylinder the following assumptions have been made:

- (a) the incident waves are plane waves;
- (b) the cylinder is infinite in length; and
- (c) the cylinder wall is hard so that all of the scattered waves proceed outward from the surface.

3.3.1 Incident Sound Pressure

If all the plane waves are travelling normal to the cylinder axis z and positive x direction as shown in Figure 3.2 (the directions $\phi=180^\circ$ and $\phi=0^\circ$ from the positive x axis will be considered as the front and back of the cylinder respectively), then the incident sound

pressure can be expressed by the well-known plane wave equation

$$P^i = P^o e^{-i(\omega t - kx)}, \quad (3.7)$$

where P^o is the incident wave amplitude and k is the wavenumber. Equation (3.7) can be reduced by omitting the time dependent part for simplicity and can be written in terms of polar coordinates as follows:

$$P^i(a, k, \phi_i) = P^o e^{ikx} = P^o e^{ik(a \cos \phi_i)}, \quad (3.8)$$

where the incident sound pressure is a function of the incident wave amplitude, cylinder radius a , wave number k and azimuthal angle ϕ_i .

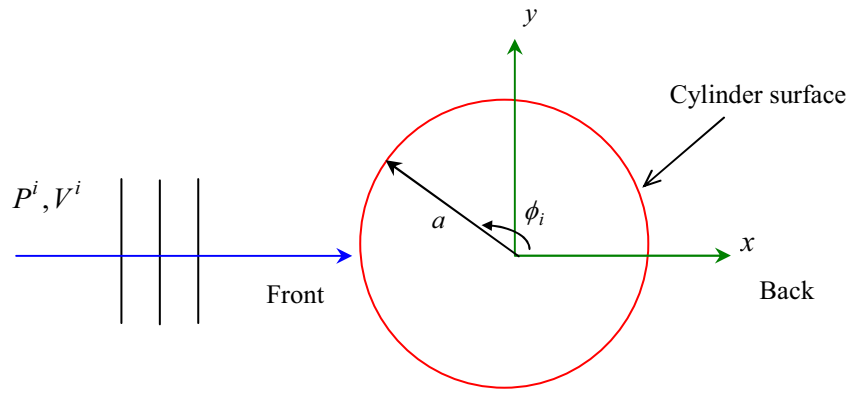


Figure 3.2: Two-dimensional incident plane waves travelling normal to the cylinder axis (positive z axis is out of page).

Referring to Figure 3.2, the incident pressure expressed in equation (3.8) can be written in terms of cylindrical waves assuming that no distortion of sound waves occurs due to the cylinder as follows (Morse & Feshbach, 1953b):

$$P^i(a, k, \phi_i) = P^o \sum_{m=0}^{\infty} \varepsilon_m i^m \cos(m\phi_i) J_m(ka). \quad (3.9)$$

The distortion of sound waves by the cylinder will be taken into account later in the expression for scattered pressure. An approximation to the above equation (3.9) is

$$P^i(a, k, \phi_i) = P^o \sum_{m=0}^{M-1} \varepsilon_m i^m \cos(m\phi_i) J_m(ka), \quad (3.10)$$

where the plane waves are travelling from left to right assuming that the source is at an infinite distance, m and M are the term number and total number of terms required in the series summation respectively, $\varepsilon_m = 1$ if $m=0$ and 2 if $m > 0$, and J_m is a *Bessel function of the first kind* of m th order for variable coefficients k and a . For more explanation about J_m , see *Appendix A*. The values of J_m calculated using MATLAB are also provided in Tables A.1 to A.8 in *Appendix A* for various values of ka . The values of J_m corresponding to the values of $m = 0, 1$ and 2 have been verified with Abramowitz & Stegun (1965, Table 9.1). The incident sound pressure distributions calculated using equation (3.10) at the surface of a cylinder of radius a , corresponding to different values of M , are shown in Figures 3.3 and 3.4 respectively for $ka = 5$. Note that the incident sound pressure distributions are different for different values of M and become almost equal in magnitude around the cylinder once a certain value of M has been reached using a relative accuracy of $1e^{-7}$ between the summation of each term. More clearly, the circular incident sound pressure pattern corresponding to the value of $M = 12$ shown in Figure 3.4 satisfies the undisturbed incident sound pressure distribution across the circumference of a cylinder, since it is assumed that no distortion of sound waves occurs due to the presence of the cylinder.

For convenience, it is necessary to explain the reason that results presented in Figures 3.3 and 3.4 are only given up to values of $M = 12$. It has been found that the coefficient A_m (which satisfies the boundary condition for the hard walled cylinder and is defined in

equation 3.16) and phase angle γ_m (the angle between the incident and scattered waves and is defined in equation 3.17) which determine the total circumferential sound pressure at the surface of a cylinder, and tend to zero as the value of m increases (which is explained detail later in Section 3.3.3). This trend means that after a certain value of M in equation (3.10) there will be negligible contribution from additional terms to the total circumferential sound pressure at the surface of a cylinder. Therefore, for the case $ka = 5$, the results presented in Figures 3.3 and 3.4 correspond to values of M up to $M = 12$, where it can be seen that the expected uniform pressure distribution around the cylinder is achieved. However, it can be concluded from the results that the value of M required in the sum in equation (3.10) to achieve the requirement of uniform undisturbed incident sound pressure distribution across the circumference of a cylinder, depends on the value of ka .

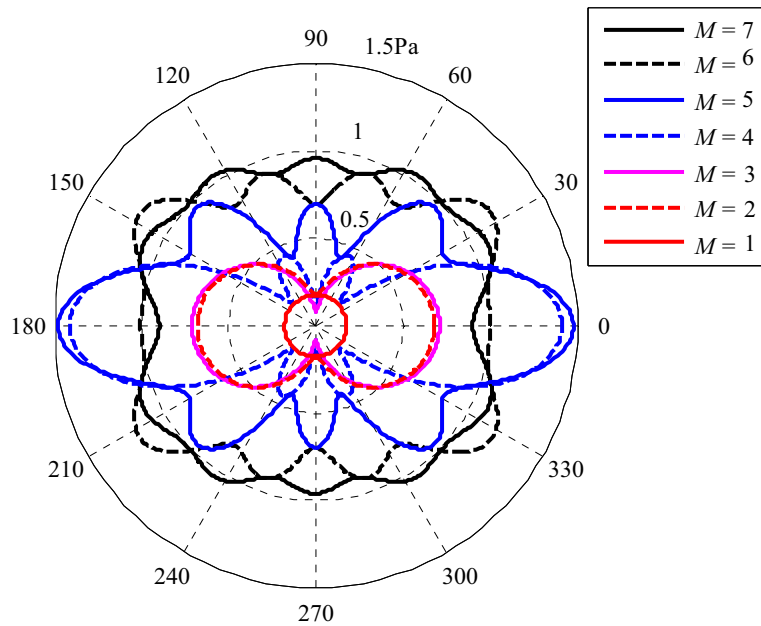


Figure 3.3: Incident sound pressure distributions at the surface of a cylinder of radius a , for $ka = 5$ and $M = 1, 2, 3, 4, 5, 6$ and 7 respectively, assuming that no distortion of sound waves occurs due to the presence of the cylinder. [Incident pressure magnitude $P^o = 1 \text{ Pa}$]

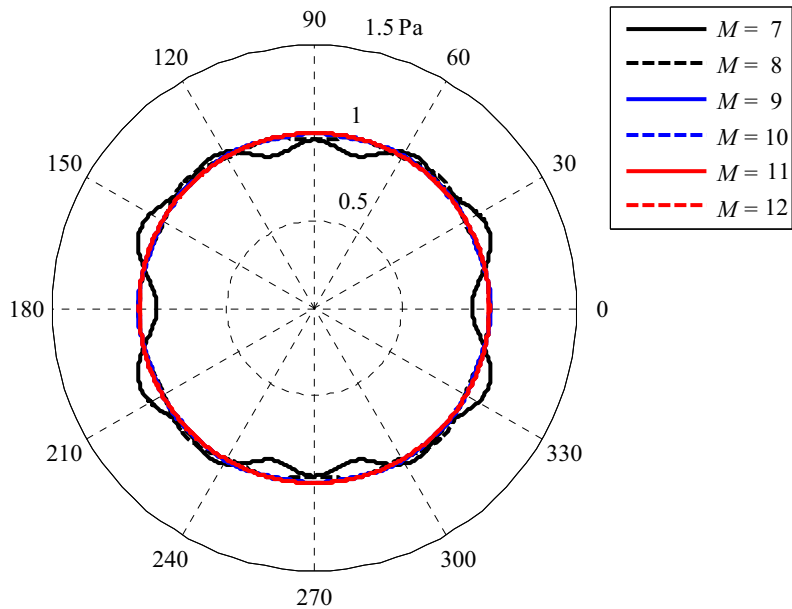


Figure 3.4: Incident sound pressure distributions at the surface of a cylinder of radius a , for $ka = 5$ and $M = 7, 8, 9, 10, 11$ and 12 respectively, assuming that no distortion of sound waves occurs due to the presence of the cylinder. [Incident pressure magnitude $P^o = 1$ Pa]

3.3.2 Scattered Sound Pressure

To predict the scattered sound pressure, the distortion of sound waves due to the presence of the cylinder needs to be taken into account because it distorts the sound waves at the surface. The cylinder can be simulated as a source, where all the waves travel outwards from its surface, since the boundary is hard. The scattered sound pressure P^s can then be calculated as a function of cylinder radius a , wave number k and azimuthal angle ϕ_i as follows (Morse, 1936; Morse & Ingard, 1986):

$$P^s(a, k, \phi_i) = -P^o \sum_{m=0}^{M-1} A_m \cos(m\phi_i) H_m(ka), \quad (3.11)$$

where $H_m(ka)$ is the *Hankel function* or *Bessel function of the third kind* of m th order

and M is the total number of terms required in the series summation. The *Hankel function* is the combination of *Bessel functions of the first and second kind* (also called *Neumann function*, N_m) respectively. For more explanation about N_m and H_m see *Appendix A*. Values of N_m calculated using MATLAB are also given in Tables A1 to A8 in *Appendix A* for various values of ka . The values of N_m corresponding to the values of $m = 0, 1$ and 2 have been verified with Abramowitz & Stegun (1965, Table 9.1). The combination of J_m and N_m ensures that all the waves are going outwards from the surface and can be expressed in the form for outgoing waves

$$H_m(ka) = J_m(ka) + iN_m(ka). \quad (3.12)$$

According to the recurrence relations the derivatives of the m th order *Bessel function of the first kind* can be written as (Agrest & Maksimov, 1971):

$$\begin{aligned} J'_0(ka) &= -J_1(ka) && \text{when } m = 0, \\ 2J'_m(ka) &= J_{m-1}(ka) - J_{m+1}(ka) && \text{when } m > 0. \end{aligned} \quad (3.13)$$

Again the *Neumann function*, N_m , satisfies the same recurrence relations as the *Bessel function of the first kind* as shown in equation (3.13) and can be written as

$$\begin{aligned} N'_0(ka) &= -N_1(ka) && \text{when } m = 0, \\ 2N'_m(ka) &= N_{m-1}(ka) - N_{m+1}(ka) && \text{when } m > 0. \end{aligned} \quad (3.14)$$

From equation (3.13) and (3.14) it can be easily shown that the *Hankel function* also satisfies the same recurrence relations, which are:

$$H'_0(ka) = -H_1(ka) \quad \text{when } m = 0,$$

$$2H'_m(ka) = \{J_{m-1}(ka) - J_{m+1}(ka) + i[N_{m-1}(ka) - N_{m+1}(ka)]\}$$

$$= H_{m-1}(ka) - H_{m+1}(ka) \quad \text{when } m > 0. \quad (3.15)$$

To calculate the scattered sound pressure using equation (3.11), it is necessary to determine the coefficients, A_m , which satisfy the hard wall boundary condition at the surface by making $U^i + U^s = 0$, where U^i and U^s are the incident and scattered velocity respectively.

The coefficients A_m can be determined as follows (Morse & Ingard, 1986):

$$\begin{aligned} A_0 &= \varepsilon_0 i e^{-i\gamma_0} \sin \gamma_0 & \text{when } m = 0, \\ A_m &= \varepsilon_m i^{m+1} e^{-i\gamma_m} \sin \gamma_m & \text{when } m > 0. \end{aligned} \quad (3.16)$$

In equation (3.16) the sine and $e^{-i\gamma_m}$ term have been chosen to ensure the correct combination of the incident and scattered waves and the phase angles, γ_m , can be defined depending on the values of m as follows (Morse, 1936; Morse & Ingard, 1986):

$$\begin{aligned} \tan \gamma_0 &= - \frac{J_1(ka)}{N_1(ka)} & \text{when } m = 0 \\ \tan \gamma_m &= - \frac{J'_m(ka)}{N'_m(ka)} & \text{when } m > 0. \end{aligned} \quad (3.17)$$

The values of A_m and γ_m are given in Tables B1 to B4 in *Appendix B* for various values of ka . After solving all of these equations, the scattered sound pressure distributions calculated using equation (3.11) at the surface of a cylinder of radius a , corresponding to different values of M using a relative accuracy of $1e^{-7}$ between the summation of each term, are shown in Figures 3.5 and 3.6 respectively for $ka = 5$. Increasing M above $M = 12$ has a negligible effect on the results. This is because the coefficient A_m (which satisfies the boundary condition for the hard walled cylinder and is defined in equation 3.16) and phase angle γ_m (the angle between the incident and scattered waves and is defined in equation 3.17), both tend to zero as the value of m

increases. The final result corresponding to the value of $M=12$ presented in Figure 3.6, shows that the scattered sound pressure distribution at the surface of the cylinder fluctuates compared with the incident pressure shown in Figure 3.4. The reason for this variation in amplitude is that waves are diffracted around the two sides of the cylinder in the clockwise and anti-clockwise directions. When one wave travels a distance which is an odd number of half wavelengths more than the distance travelled by the other, there is destructive interference. When they travel the same distance or an integer number of wavelengths, there is reinforcement and a peak results.

The directivity patterns of the scattered sound pressure calculated using equation (3.11) for various values of ka at the surface of a cylinder of radius a are shown in the polar Figures 3.7(a-h) respectively. The arrows in the figures indicate the direction of incident waves. The scattered sound pressure fluctuations at the surface of a cylinder of radius a calculated using equation (3.11) with various azimuthal angles for various values of ka are shown more clearly in the Cartesian Figures 3.8 to 3.11 respectively. From the results, it is interesting to see that the scattered wave amplitude is relatively smoothly varying in the region from approximately 100° to 260° at the front face of the cylinder and varies more aggressively in the regions from approximately 0° to 100° and 260° to 360° of the cylinder. The reason has been discussed in the preceding paragraph and is a result of positive and/or negative interference of the two diffracted waves travelling around the two sides of the cylinder. At the back of the cylinder; where $\phi_i = 0^\circ$, the scattered wave pressure has a peak for values of ka up to 5. When ka increases (for the cases shown $ka \geq 10$), the wavelengths become much shorter than those of $ka \leq 5$, compared with the cylinder circumference. This increases the amount of interference of the diffracted waves at the back of the cylinder, resulting in an increase in the number of scattered peaks at the back of the cylinder.

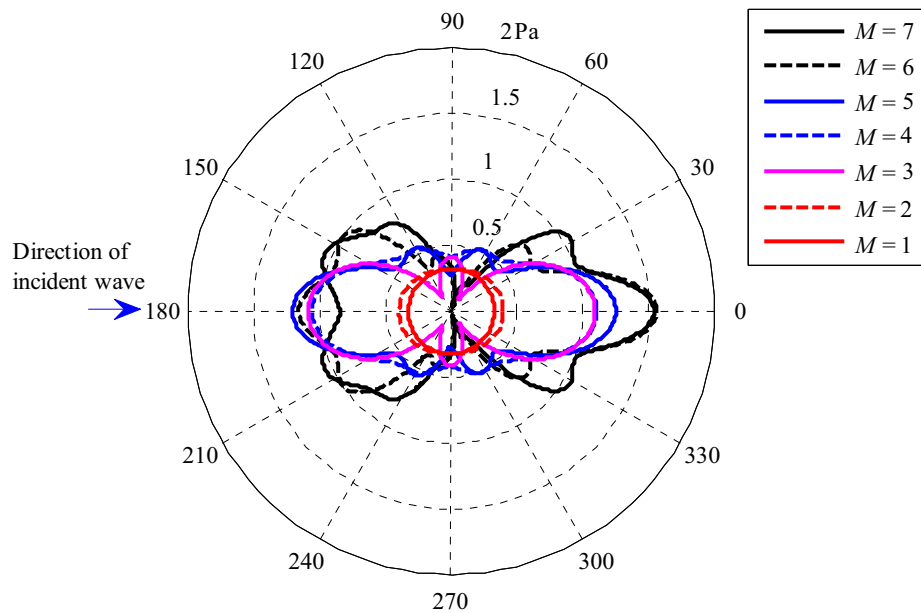


Figure 3.5: Scattered sound pressure distributions at the surface of a cylinder of radius a , for $ka = 5$ and $M = 1, 2, 3, 4, 5, 6$ and 7 respectively. [Incident pressure magnitude $P^0 = 1$ Pa]

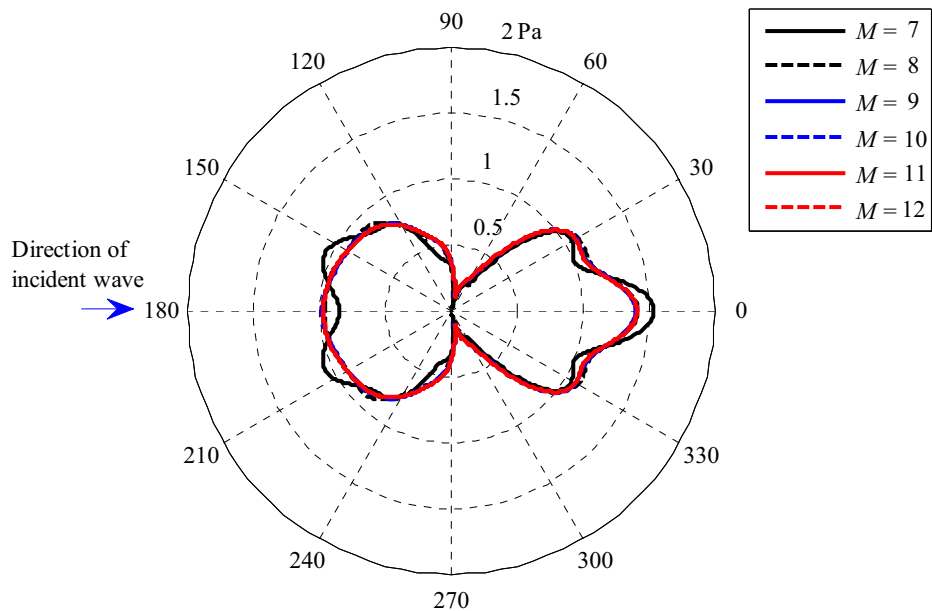
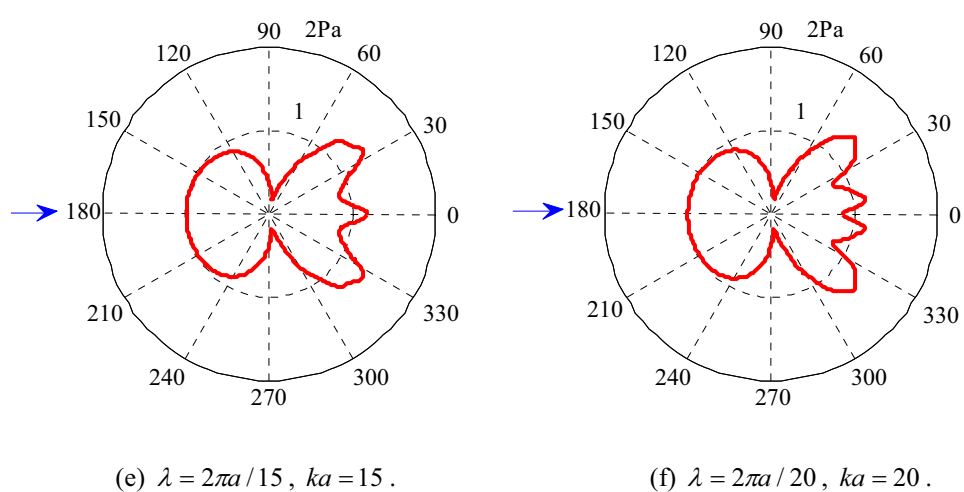
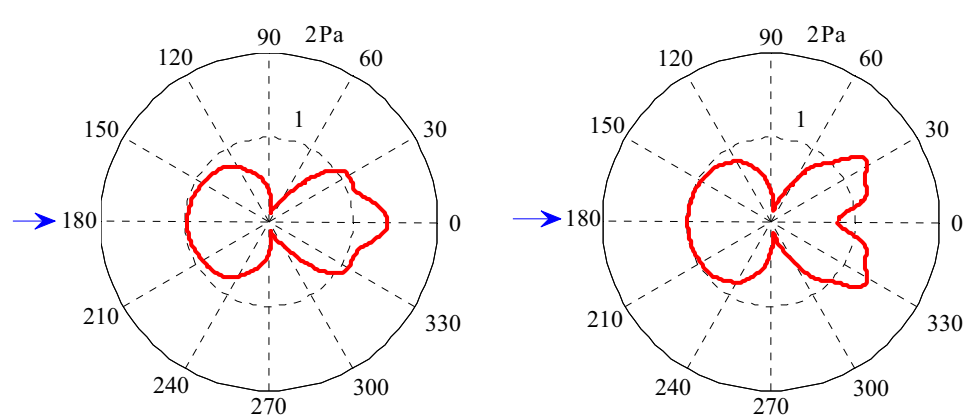
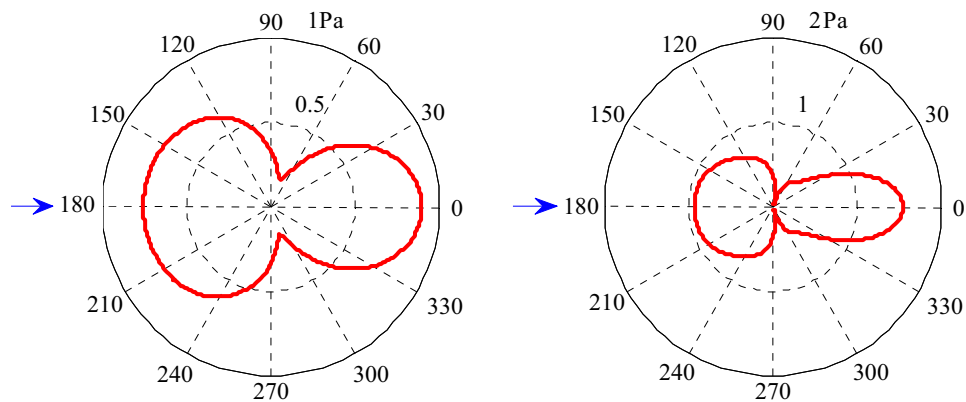
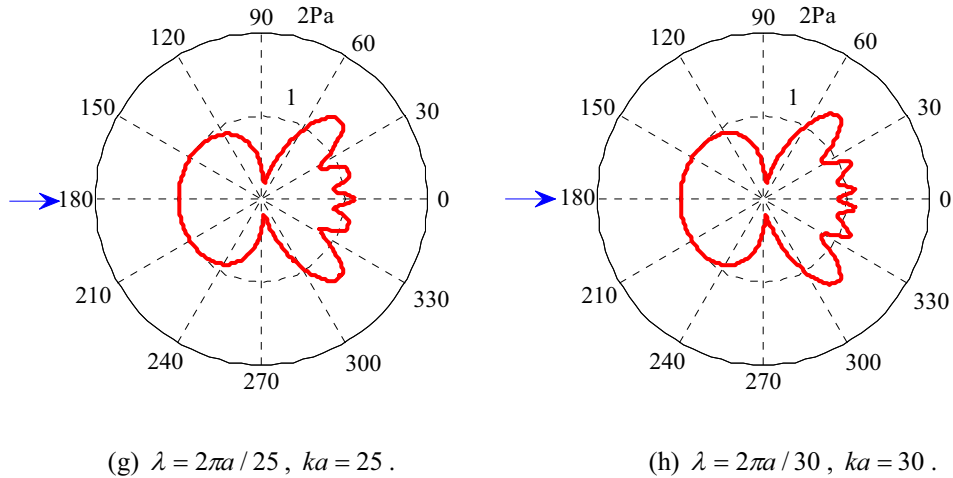


Figure 3.6: Scattered sound pressure distributions at the surface of a cylinder of radius a , for $ka = 5$ and $M = 7, 8, 9, 10, 11$ and 12 respectively. [Incident pressure magnitude $P^0 = 1$ Pa]





Figures 3.7 (a-h): Directivity pattern of the scattered sound pressure at the surface of a cylinder of radius a , for various values of ka . The arrows in the figures indicate the direction of incident waves. [Incident pressure magnitude $P^o = 1$ Pa]

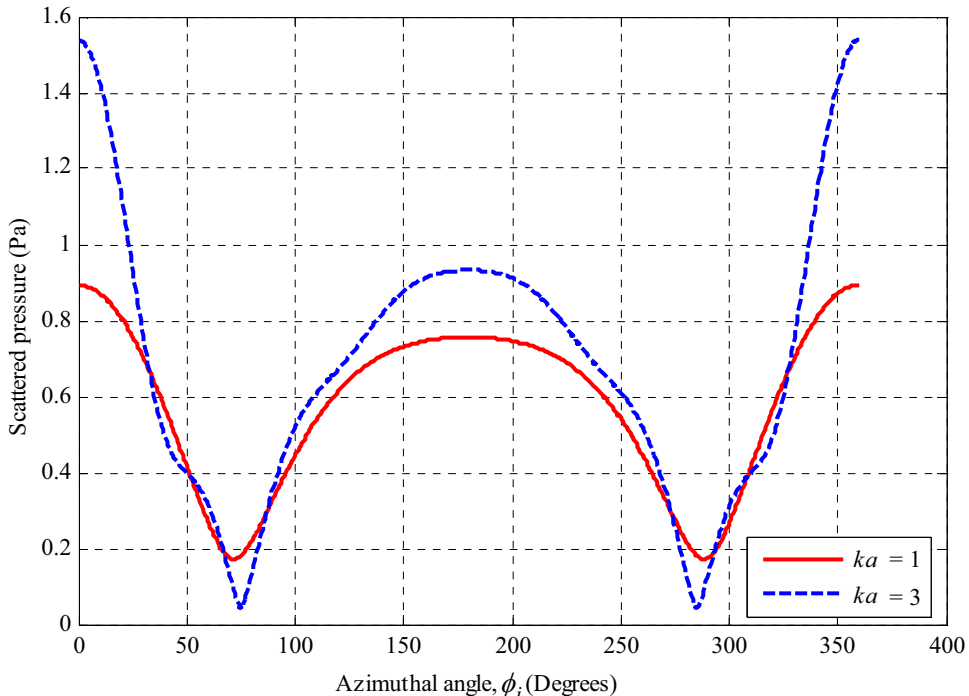


Figure 3.8: Scattered sound pressure as a function of azimuthal angle, ϕ_i , for values of $ka = 1$ and 3 respectively. [Incident pressure magnitude $P^o = 1$ Pa]

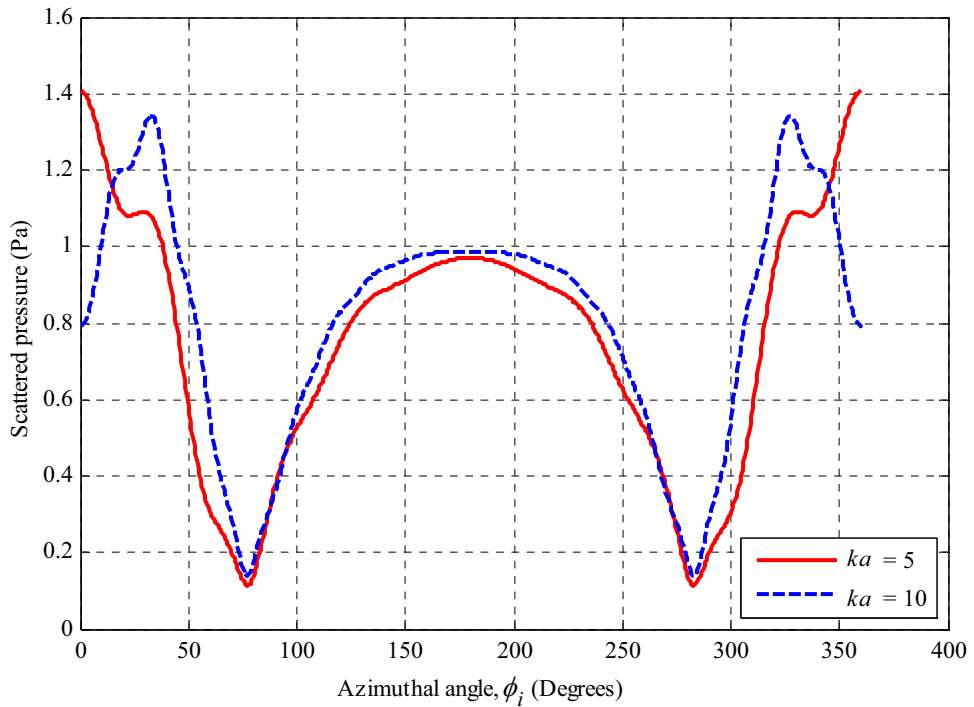


Figure 3.9: Scattered sound pressure as a function of azimuthal angle, ϕ_i , for values of $ka = 5$ and 10 respectively. [Incident pressure magnitude $P^o = 1$ Pa]

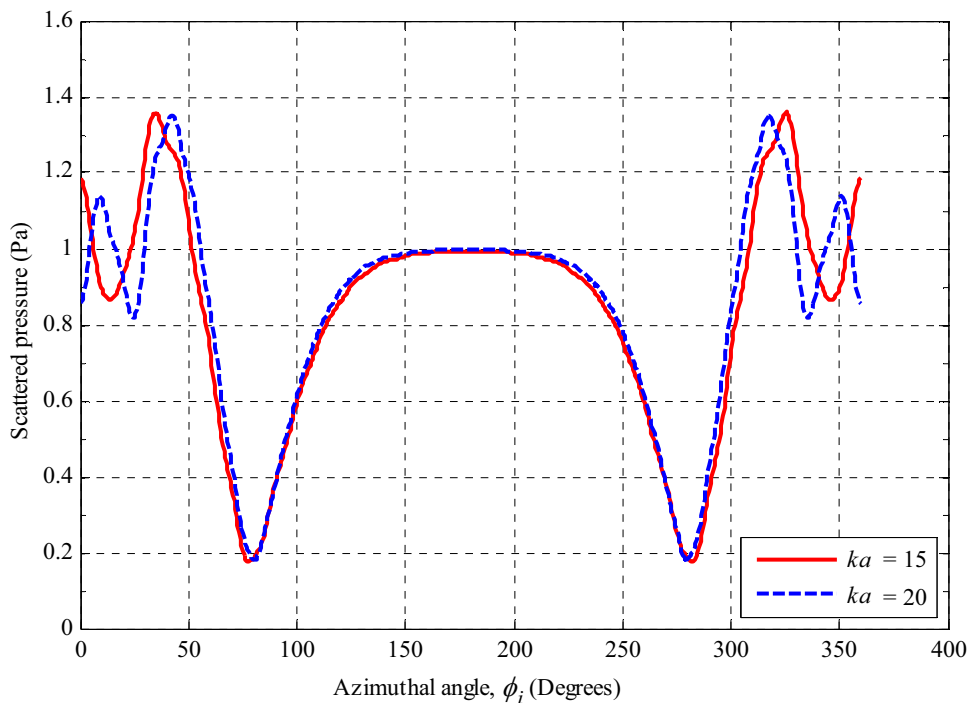


Figure 3.10: Scattered sound pressure as function of azimuthal angle, ϕ_i , for values of $ka = 15$ and 20 respectively. [Incident pressure magnitude $P^o = 1$ Pa]

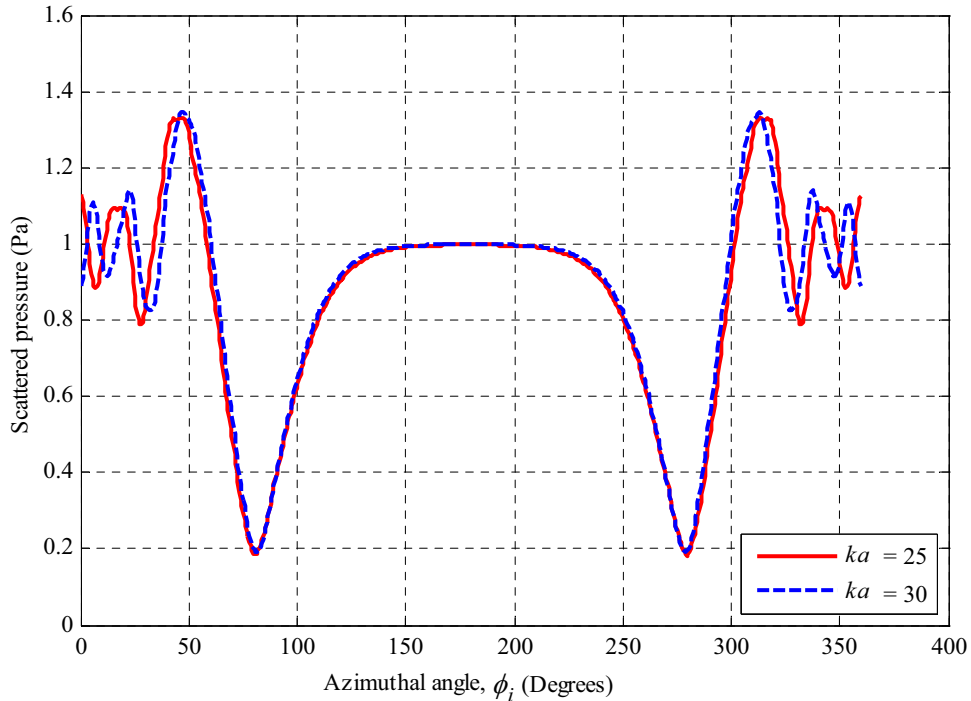


Figure 3.11: Scattered sound pressure as function of azimuthal angle, ϕ_i , for values of $ka = 25$ and 30 respectively. [Incident pressure magnitude $P^o = 1$ Pa]

3.3.3 Total Sound Pressure

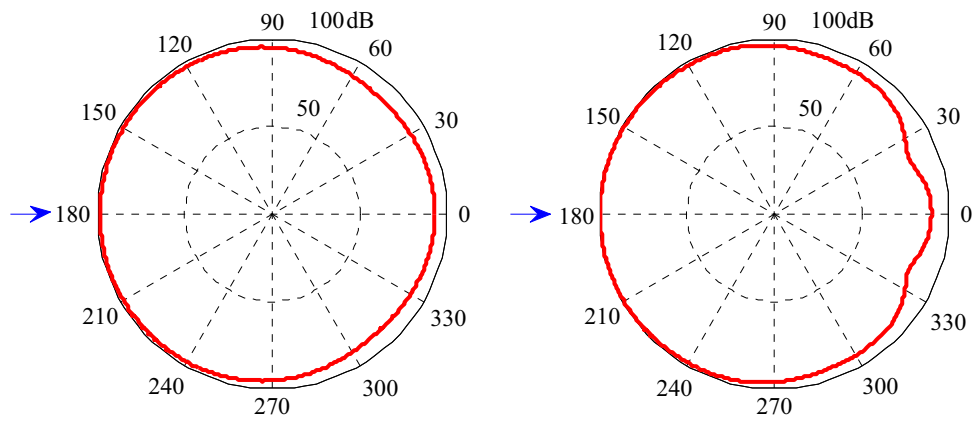
The total sound pressure at the surface of a cylinder due to both incident and scattered waves can be calculated by simply adding equations (3.10) and (3.11), and it can be written in the following form

$$\begin{aligned}
 P_a^t(a, k, \phi_i) &= P^i(a, k, \phi_i) + P^s(a, k, \phi_i) \\
 &= P^o \sum_{m=0}^{M-1} \varepsilon_m i^m \cos(m\phi_i) [J_m(ka) - i e^{-i\gamma_m} \sin \gamma_m H_m(ka)], \quad (3.18)
 \end{aligned}$$

which gives the total sound pressure at the surface of a cylinder directly. The directivity patterns of the total sound pressure at the surface of a cylinder for various values of ka are shown individually in the polar Figures 3.12 (a-h) respectively. The arrows in the figures

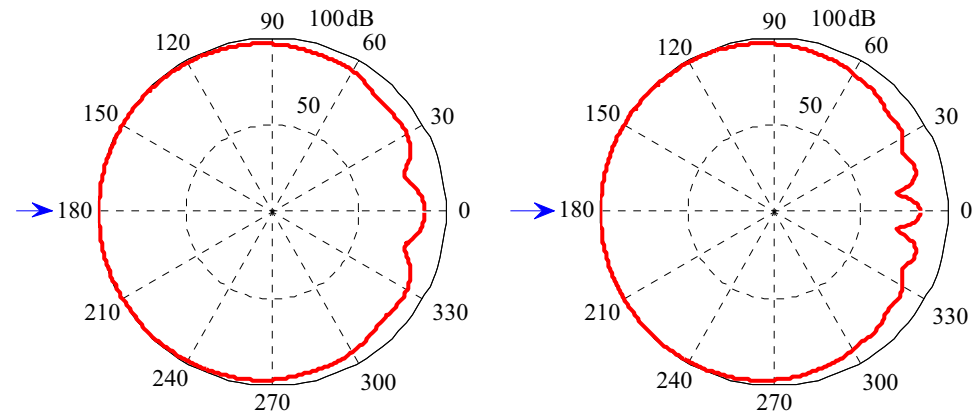
show the incident wave direction. The total sound pressure fluctuations as a function of azimuthal angle at the surface of a cylinder for various values of ka are shown more clearly in the cartesian Figures 3.13 to 3.16 respectively. From these results it can be seen that the total sound pressure amplitude is relatively smoothly varying at the front ($\phi = 180^\circ$) of the cylinder and varies more aggressively at the back ($\phi = 0^\circ$) of the cylinder. It is also interesting to see that the sound pressure fluctuations increase at the back of the cylinder as the value of ka increases. The reason is that when ka increases, the interference pattern between the two diffracted waves travelling around the two sides of the cylinder becomes more complex and this increases the scattered sound pressure fluctuations at the back of the cylinder (see Figures 3.7(a-h) and 3.8 to 3.11).

While the sum in equation (3.18) is theoretically an infinite sum, in practice there are a finite number of terms required for acceptable accuracy. The number of terms required for acceptable accuracy increases as ka increases as will be shown. Figures 3.17(a-b) and 3.18(a-b) show the characteristic behaviours of γ_m and A_m with respect to m for various values of ka . It is interesting to see that as the frequency increases, the values of M required in the sum increases in order for γ_m and A_m to become infinitesimally small (that is $1e^{-7}$). The values of γ_m and A_m are given in Tables B1 to B4 in *Appendix B* for various values of ka . The total number of terms M required in equation (3.18) to determine the total sound pressure at the surface of a cylinder to an accuracy of $1e^{-7}$ are reported in Table 3.1 for various values of ka .



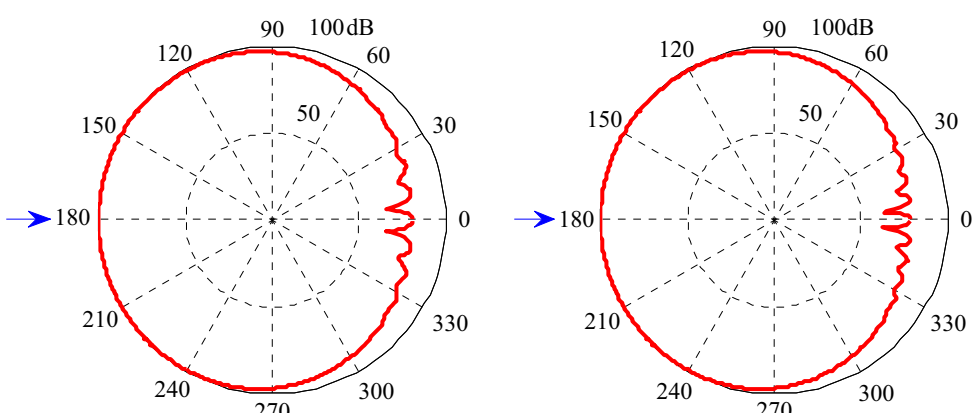
(a) $\lambda = 2\pi a$, $ka = 1$.

(b) $\lambda = 2\pi a / 3$, $ka = 3$.



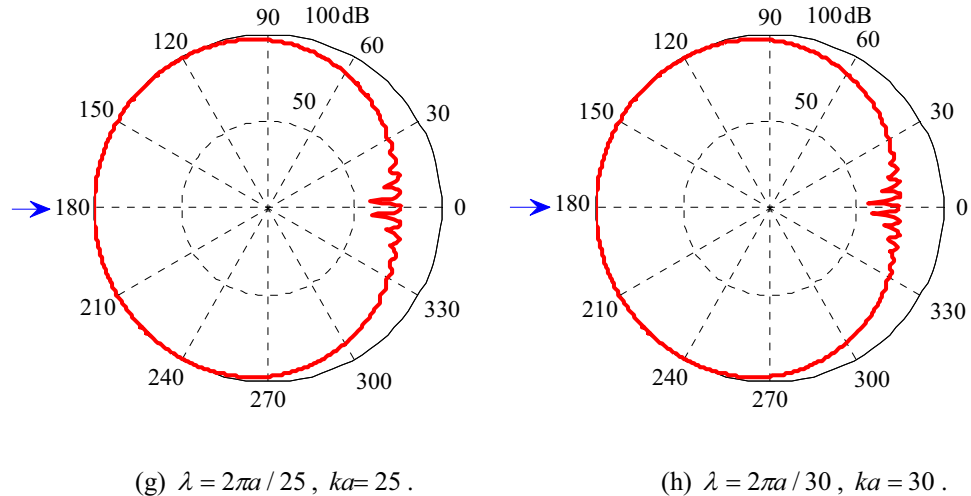
(c) $\lambda = 2\pi a / 5$, $ka = 5$.

(d) $\lambda = 2\pi a / 10$, $ka = 10$.



(e) $\lambda = 2\pi a / 15$, $ka = 15$.

(f) $\lambda = 2\pi a / 20$, $ka = 20$.



Figures 3.12(a-h): Directivity pattern of the total sound pressure at the surface of a cylinder of radius a , for various values of ka . The arrows in the figures show the incident wave direction. [Reference pressure $20\mu\text{Pa}$ and incident pressure magnitude $P^o = 1\text{ Pa}$]

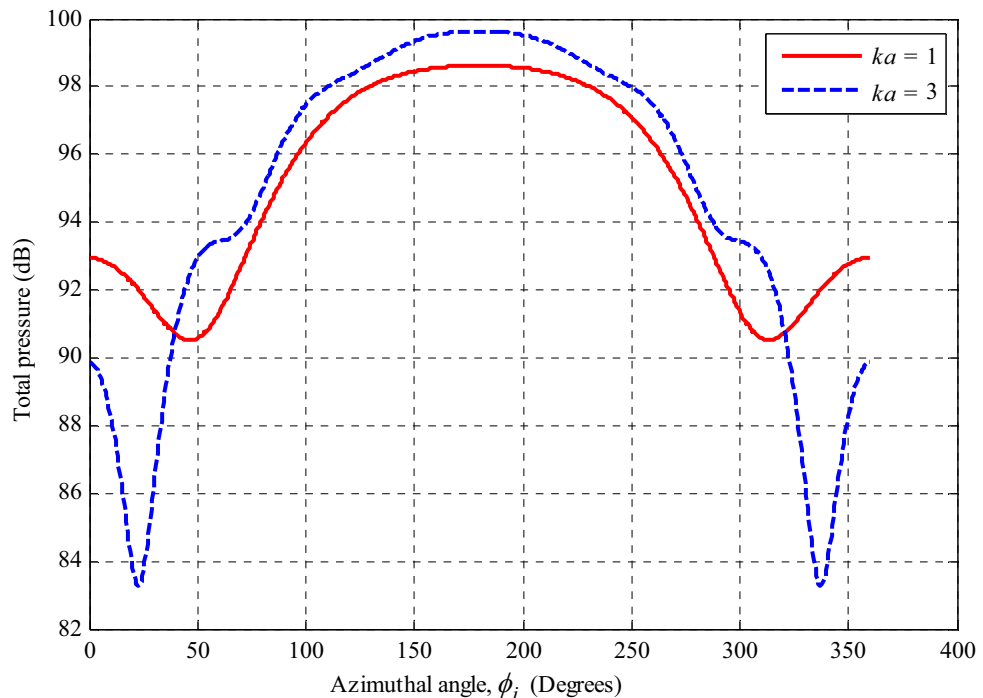


Figure 3.13: Total sound pressure as a function of azimuthal angle, ϕ_i , at the surface of a cylinder of radius a , for values of $ka = 1$ and 3 respectively. [Reference pressure $20\mu\text{Pa}$ and incident pressure magnitude $P^o = 1\text{ Pa}$]

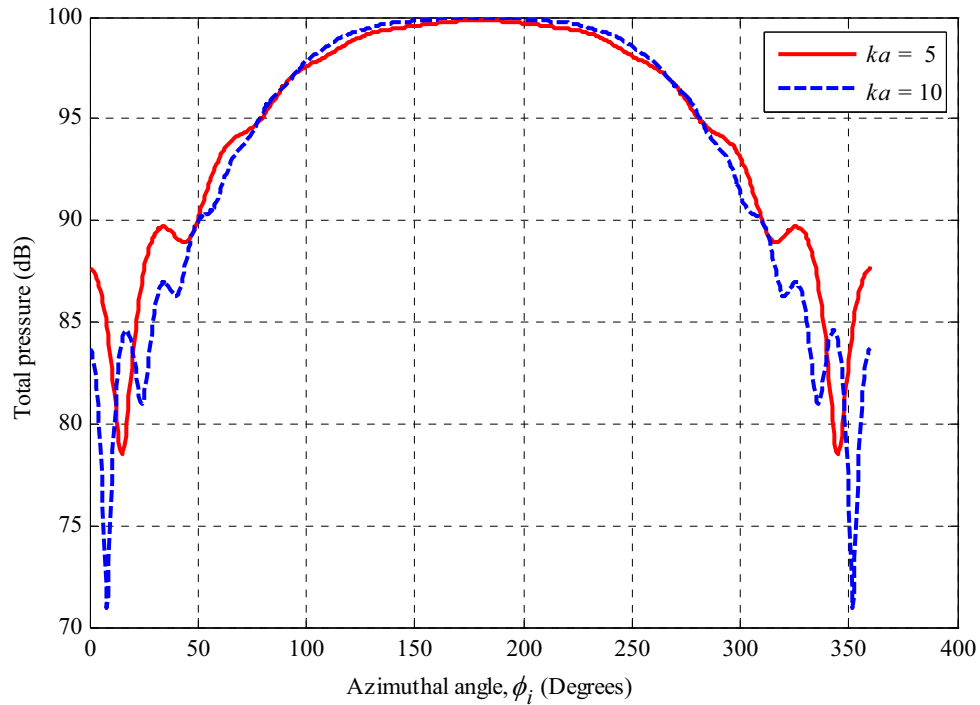


Figure 3.14: Total sound pressure as a function of azimuthal angle, ϕ_i , at the surface of a cylinder of radius a , for values of $ka = 5$ and 10 respectively. [Reference pressure $20\mu\text{Pa}$ and incident pressure magnitude $P^O = 1 \text{ Pa}$]

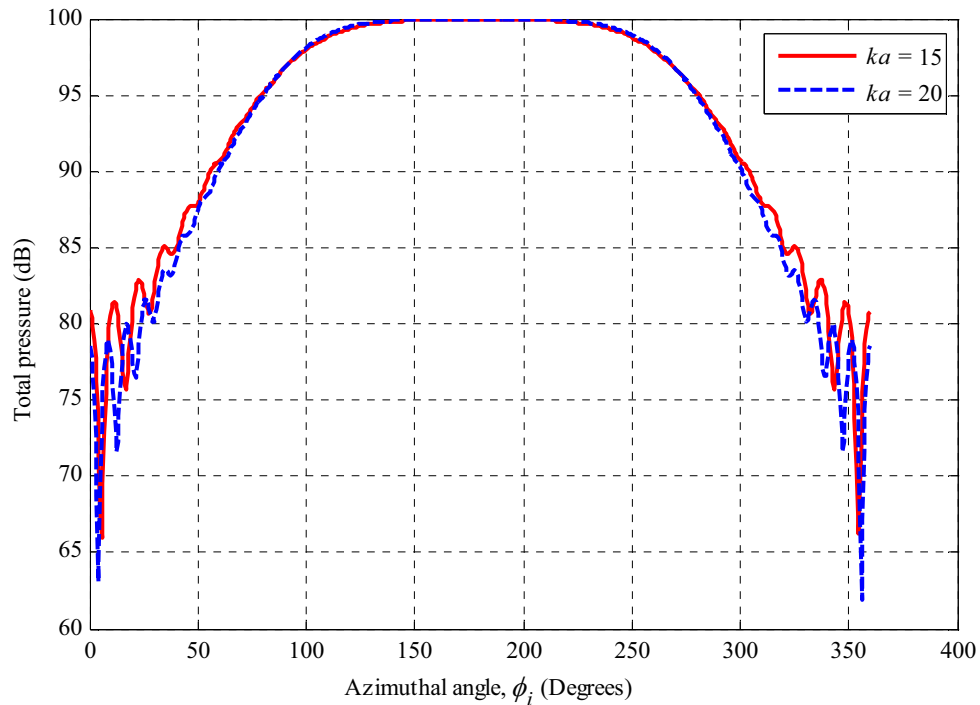


Figure 3.15: Total sound pressure as a function of azimuthal angle, ϕ_i , at the surface of a cylinder of radius a , for values of $ka = 15$ and 20 respectively. [Reference pressure $20\mu\text{Pa}$ and incident pressure magnitude $P^O = 1 \text{ Pa}$]

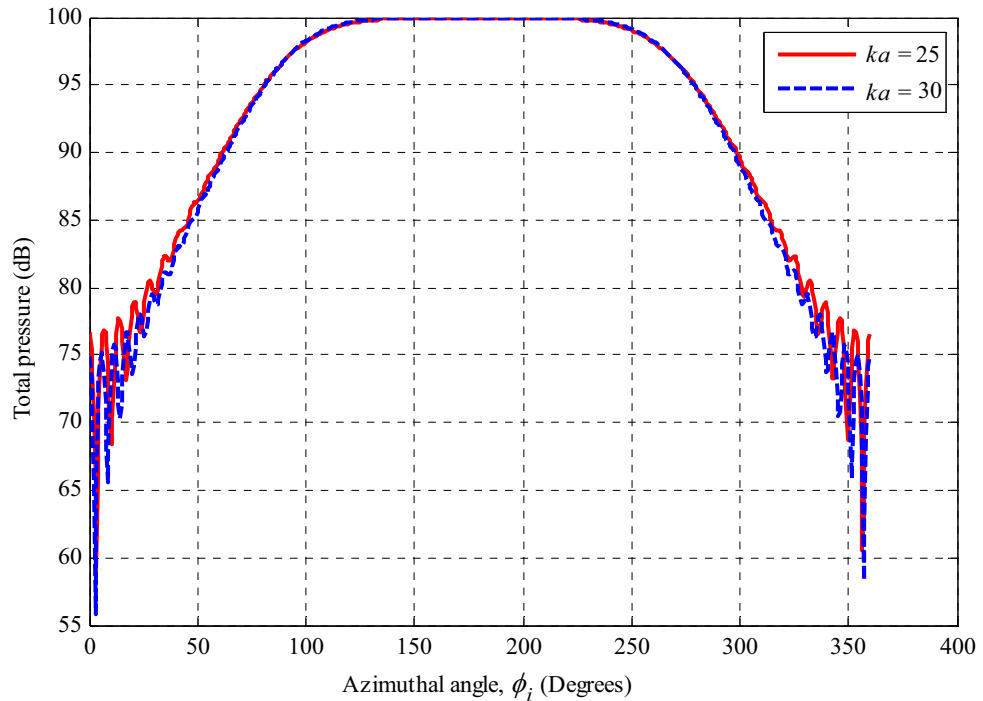


Figure 3.16: Total sound pressure as a function of azimuthal angle, ϕ_i , at the surface of a cylinder of radius a , for values of $ka = 25$ and 30 respectively.[Reference pressure $20\mu\text{Pa}$ and incident pressure magnitude $P^O = 1 \text{ Pa}$]

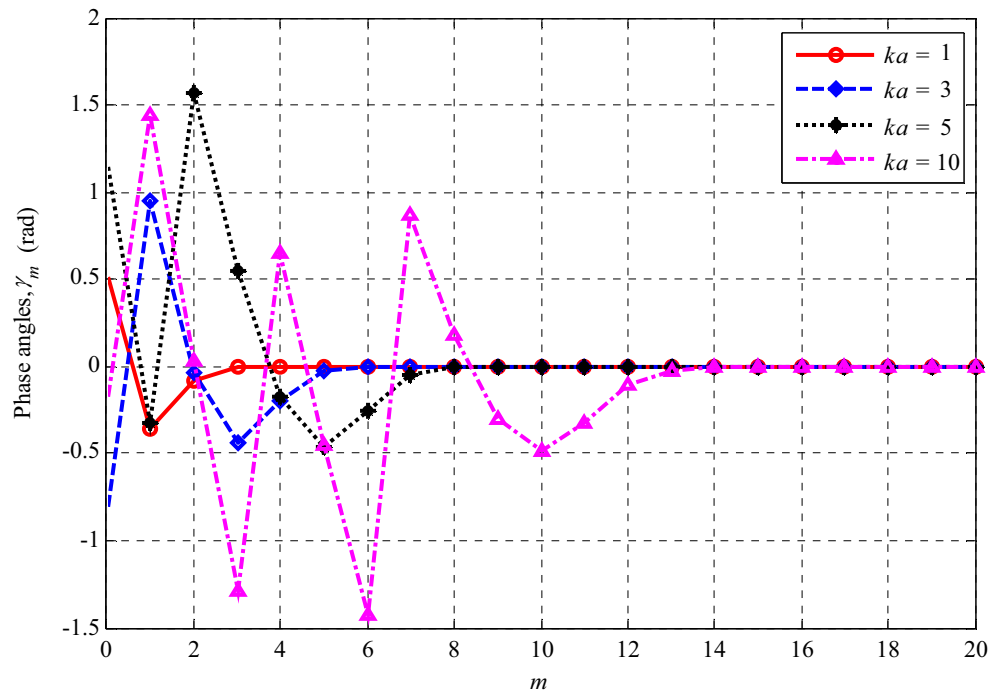


Figure 3.17(a): Characteristic behavior of γ_m as a function of m , for values of $ka = 1, 3, 5$ and 10 respectively.

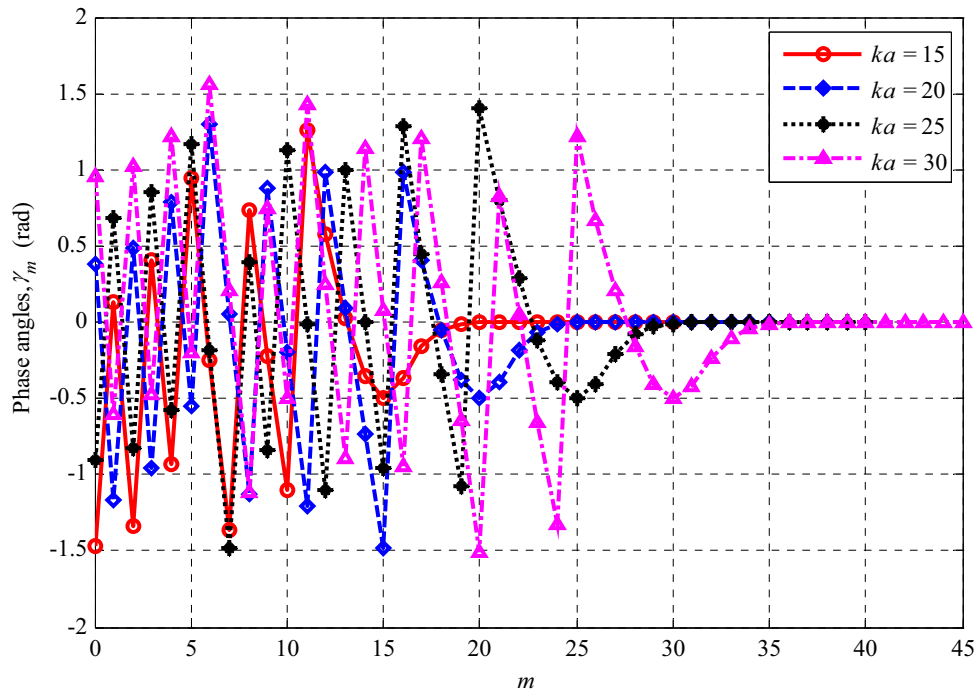


Figure 3.17(b): Characteristic behavior of γ_m as a function of m , for values of $ka = 15, 20, 25$ and 30 respectively.

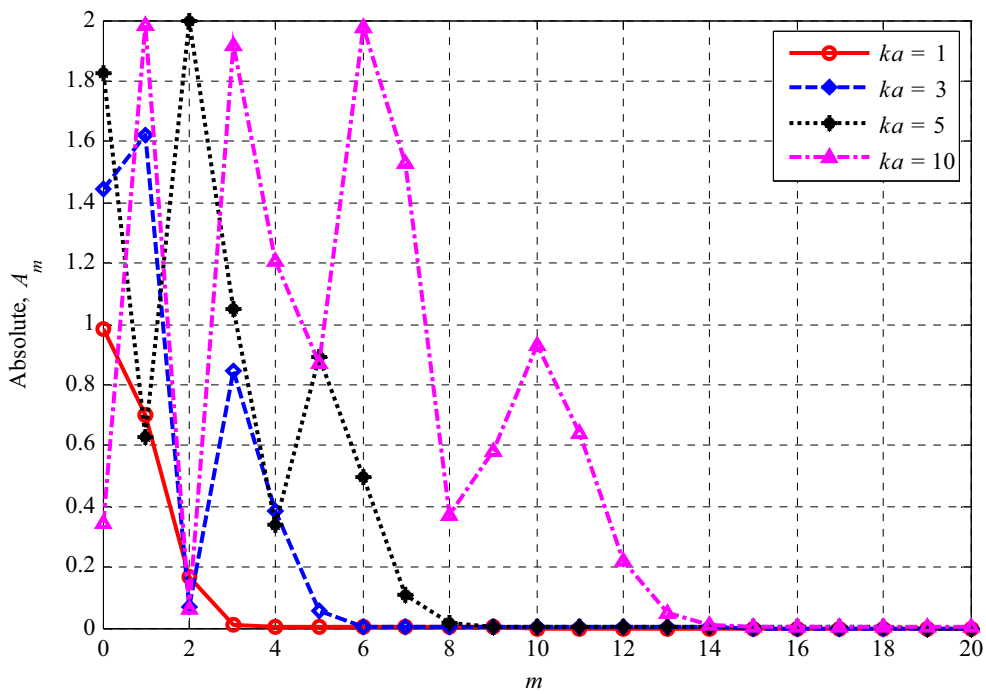


Figure 3.18(a): Characteristic behavior of A_m as a function of m , for values of $ka = 1, 3, 5$ and 10 respectively.

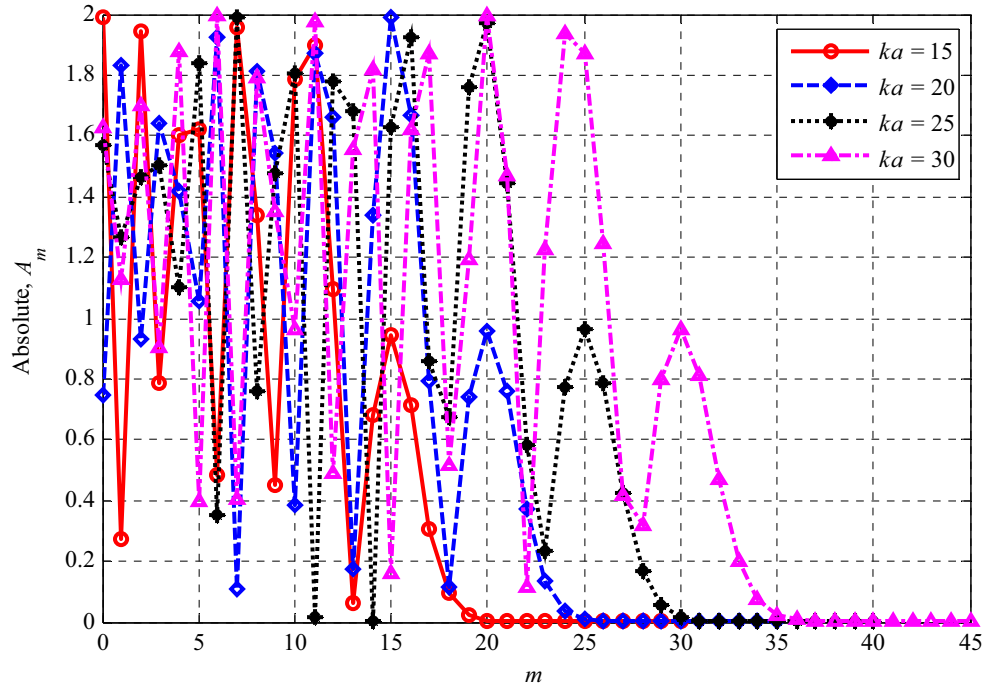


Figure 3.18(b): Characteristic behaviour of A_m as a function of m , for values of $ka = 15, 20, 25$ and 30 respectively.

ka	Total number of terms, M , needed to achieve a relative error $< 1e^{-7}$
1	7
3	11
5	12
10	18
15	28
20	34
25	40
30	44

Table 3.1: Total number of terms required in equation (3.18) for various values of ka .

3.3.4 Discussion

In the derivations presented in this chapter to determine the incident, scattered and total sound pressure at the surface of a cylinder, no limits such as large or small values of the argument ka have been used. It has been observed that using these derivations, calculations are able to converge for any argument ka . For example, the total sound pressure at the surface of a cylinder derived in equation (3.18) is suitable for any input argument of ka , and converges fully at the surface of the cylinder. Hence this equation will be used in the remainder of this thesis. However, it should be noted that there are other analyses available that are given by Morse (1936), Morse & Ingard (1986), Junger & Feit (1993) and Nye (2003). These will be discussed and compared with the current analysis in the next section.

3.4 Other Theoretical Approaches and Comparison with the Current Approach

Since the analyses of both Junger & Feit (1993) and Nye (2003) are similar, the derivations given by Junger & Feit (1993) have been chosen for comparison with the current analysis. The purpose of this comparison is to check the validity of the current analysis before applying it to an actual launch case. First of all, the equations for the incident, scattered and resultant pressures of a cylinder are given by (Junger & Feit, 1993, Ch. 10, pp-322)

$$p_i = P^o \sum_{m=0} \varepsilon_m i^m J_m(kr) \cos(m\phi_i), \quad (3.19)$$

$$p_{s\infty}(r, \phi_i) = -P^o \sum_{m=0} \varepsilon_m i^m \frac{J'_m(ka) H_m(kr)}{H'_m(ka)} \cos(m\phi_i), \quad (3.20)$$

$$p(a, \phi_i) = p_i + p_{s\infty} = P^o \sum_{m=0} \varepsilon_m i^m \left[J_m(ka) - \frac{J'_m(ka)H_m(ka)}{H'_m(ka)} \right] \cos(m\phi_i); \quad r = a, \quad (3.21)$$

where J'_m and H'_m are the derivatives of the *Bessel functions of the first and third kind* respectively (see equations 3.13 and 3.15). A comparison between the results obtained using equations (3.11) and (3.20) for the scattered sound pressure at the surface (use ' $r = a$ ' in equation 3.20) of a cylinder is shown in Figure 3.19 for $ka = 5$. The comparison reveals that equation (3.20) is able to determine the scattered sound pressure at the surface of a cylinder and it agrees well with the current analysis. Similarly, equation (3.21) also converges to the same result as equation (3.18) at the surface of a cylinder as shown in Figure 3.20. Both comparisons show that the results of the current analysis agree well with the derivation presented by Junger & Feit (1993). Although there is no significant difference

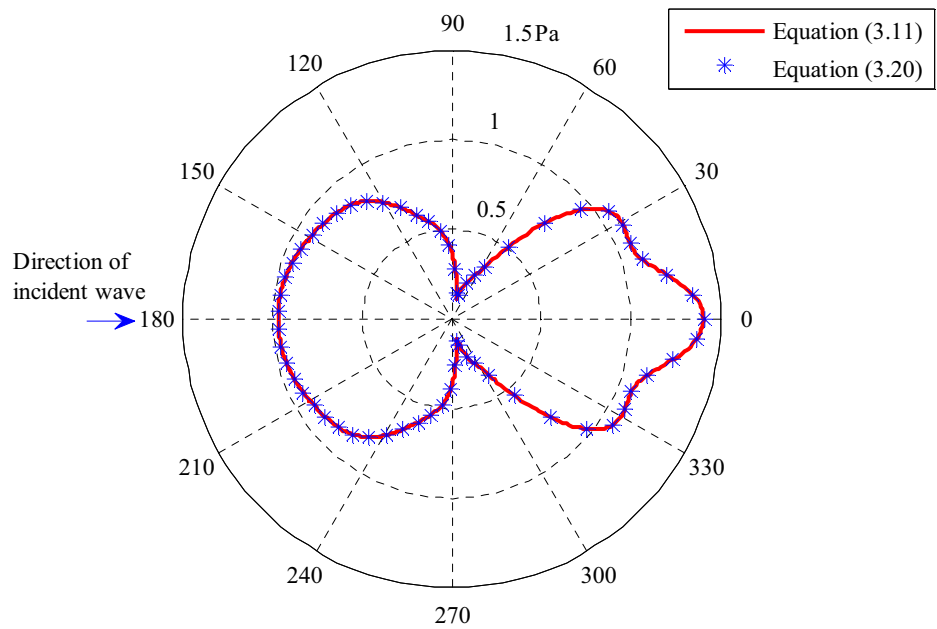


Figure 3.19: Scattered sound pressure comparison between results obtained at the surface of a cylinder of radius a using equations (3.11) and (3.20), for $ka = 5$. To calculate scattered sound pressure at the surface of the cylinder use ' $r = a$ ' in equation (3.20). [Incident pressure magnitude $P^o = 1$ Pa]

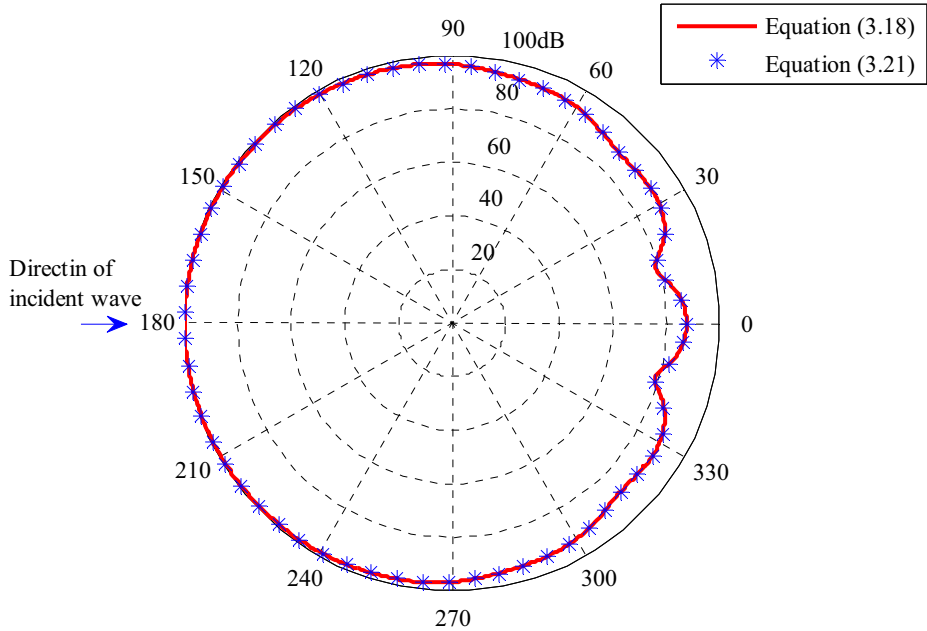


Figure 3.20: Total sound pressure comparison between results obtained at the surface of a cylinder of radius a using equations (3.18) and (3.21), for $ka = 5$. [Reference pressure $20\mu\text{Pa}$, incident pressure magnitude $P^o = 1\text{ Pa}$]

between the results, the principle difference between the current derivation and the

derivation presented by Junger & Feit (1993) is that the term $\frac{J'_m(ka)}{H'_m(ka)}$ used by Junger &

Feit (1993) is replaced by $ie^{-i\gamma_m} \sin \gamma_m$. This replacement has been done so the analysis

remains compatible with the derivations presented by Morse (1936), Morse & Feshbech

(1953b) and Morse & Ingard (1986). However, it can be shown that $\frac{J'_m(ka)}{H'_m(ka)}$ is

numerically equivalent to $ie^{-i\gamma_m} \sin \gamma_m$. According to Morse & Feshbech (1953b) and

Morse & Ingard (1986) derivatives of the Bessel functions can be written as follows:

$$\frac{J'_m(ka)}{H'_m(ka)} = \frac{-E_m^i \sin \gamma_m}{iE_m^o e^{i\gamma_m}}, \quad (3.22)$$

where E_m^i and E_m^o represent the amplitudes of the incident and outgoing waves respectively. Since the wall is hard, in this case $E_m^i = E_m^o$, on the cylinder surface to fit the coefficients, A_m , for a hard wall. The coefficients can be determined as described in equation (3.16), but if the boundary is not hard then the amplitudes need to be determined separately. Equation (3.22) reduces to

$$\frac{J'_m(ka)}{H'_m(ka)} = -i^{-1} e^{-i\gamma_m} \sin \gamma_m = i e^{-i\gamma_m} \sin \gamma_m. \quad (3.23)$$

Now substituting equation (3.23) into equation (3.21), one can obtain equation (3.18) for the total sound pressure at the surface of a cylinder.

However, Junger & Feit (1993) have used instead the Wronskian relation to simplify the equation (3.21). The simplified equation presented by Junger & Feit (1993) is

$$p(a, \phi_i) = \frac{2P^o}{\pi ka} \sum_{m=0} \frac{\varepsilon_m i^{m+1}}{H'_m(ka)} \cos(m\phi_i), \quad (3.24)$$

where according to *Wronskian* (see *Appendix C* for explanation)

$$J_m(ka)H'_m(ka) - J'_m(ka)H_m(ka) = \frac{2i}{\pi ka}. \quad (3.25)$$

Equation (3.24) gives good agreement with the current analysis as shown in Figure 3.21, but the limitation of equation (3.24) is that it is unable to determine the sound pressure at locations in the sound field away from the cylinder surface, because there is no scope in that equation to consider the radial distance in the sound field from the cylinder. This limitation does not apply to the analyses derived as part of this thesis. From the above discussions, it can be said that both Junger & Feit (1993) and the current analysis agree

well for the scattered and total sound pressure at the surface of a cylinder. However, both analyses cannot consider a source at a finite distance from the cylinder, and also cannot consider the source as a point source or a line source. Therefore, the analysis will be further extended in Chapter 5 to consider a point source and a line source placed at a defined position with respect to the cylinder.

In recent work, Friot & Bordier (2004) used similar derivations to Junger & Feit (1993). However, there are some mistakes in their work, which are discussed in *Appendix D*.

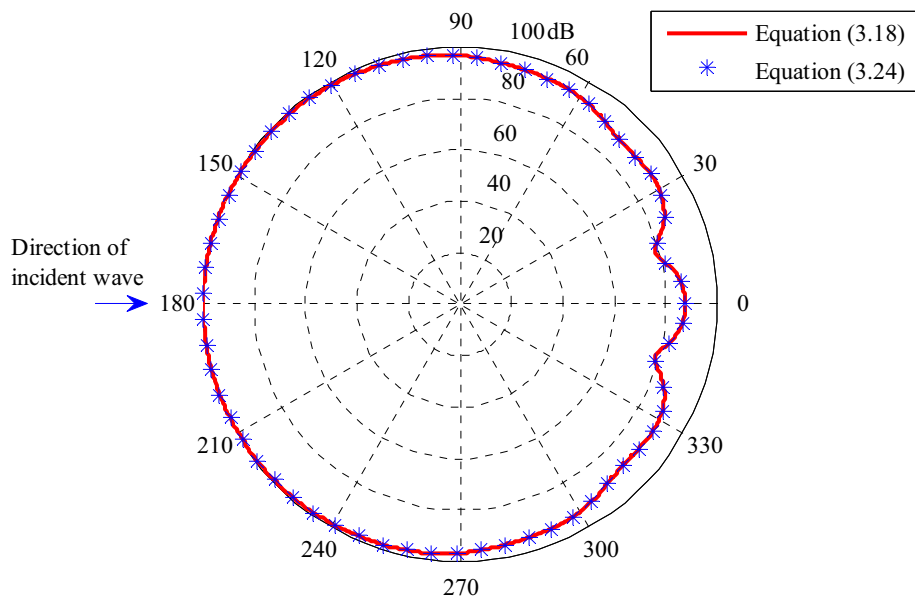


Figure 3.21: Total sound pressure comparison between results obtained at the surface of a cylinder of radius a using equations (3.18) and (3.24), for $ka = 5$. [Reference pressure $20\mu\text{Pa}$ and incident pressure magnitude $P^o = 1\text{ Pa}$]

Morse (1936, Ch.7, pp-266) and Morse & Ingard (1986, Ch. 8, pp-405), have also derived another mathematical form to calculate the total sound pressure due to both the undisturbed incident waves and the scattered waves as follows:

$$p_a = \left(\frac{4P^o}{\pi ka} \right) e^{-2\pi ift} \sum_{m=0}^{\infty} \frac{\cos(m\phi_i)}{E_m^o} e^{i(\gamma_m + \pi m/2)}, \quad (3.26)$$

where

$$E_m^o = \frac{1}{2} \sqrt{J_m'^2(ka) + N_m'^2(ka)}. \quad (3.27)$$

Equation (3.26) may be suitable for the case of radiation from a cylinder but not for the hard wall scattering case, since only the scattered waves with amplitudes E_m^o and not the incident waves have been considered. The comparison between results obtained using equations (3.26) and (3.18) is shown in Figure 3.22 for $ka = 5$, which shows clearly the difference between them. The difference between the pressure patterns indicates that equation (3.26) is not appropriate for the case of scattering by a hard wall cylinder, since the sound pressure field calculated using equation (3.26) is not similar to that obtained using equation (3.18).

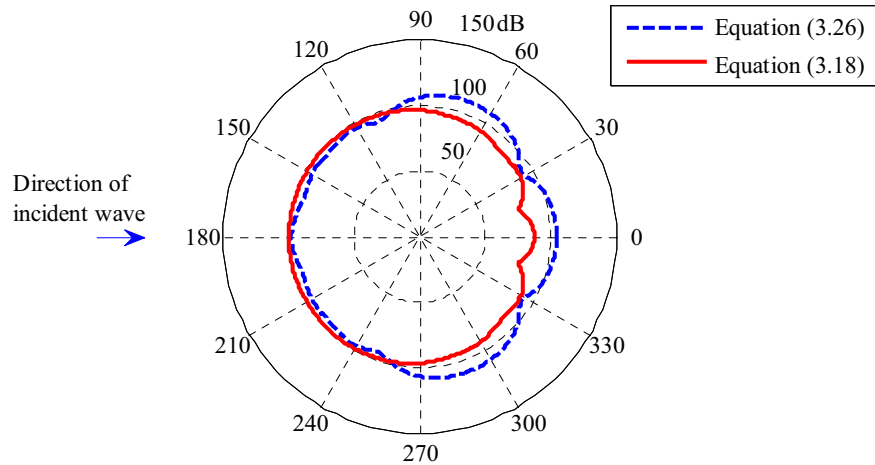


Figure 3.22: Total sound pressure comparison between results obtained at the surface of a cylinder of radius a using equations (3.26) and (3.18), for $ka = 5$. [Reference pressure $20\mu\text{Pa}$ and incident pressure magnitude $P^o = 1\text{ Pa}$]

3.5 Conclusions

The theories to calculate the incident, scattered and total sound pressure at the surface of a cylinder due to incident plane waves that strike normal to the circumference of the cylinder have been described in detail. For the theoretical analyses, it has been assumed that the cylinder is infinite in length. For the total sound pressure calculations, a suitable mathematical expression has been derived using mathematical descriptions for the incident and scattered sound pressure fields. A large number of calculated results for various values of ka have been presented. These results show that in contrast to previous work (Morse, 1936; Morse & Ingard, 1986), the derivations presented here are suitable for any argument of ka and there is no need to consider any type of limitations or restrictions, such as short or long wavelengths; or large distance.

The present work has also been compared with previous work. The comparison reveals that for the pressure field at the surface of the cylinder, the results agree well between the current analysis of this thesis and the derivation presented by Junger & Feit (1993, Ch. 10, pp-322), but not with the derivation for total sound pressure field presented by Morse (1936, Ch. 7, pp-266) and Morse & Ingard (1986, Ch. 8, pp-405).

It has been found that the simplified mathematical derivation using the *Wronskian* asymptotic relation of the Bessel functions and their derivatives as used in Junger & Feit's (1993) analysis can determine the sound pressure field at the surface of the cylinder, but it is not able to determine the sound pressure at locations in the sound field away from the cylinder surface.

The work presented here will be used in the next chapter to drive a suitable analytical form to

calculate at any location the scattered and total sound pressure fields from a cylinder. However, the theoretical framework used in this chapter is only able to consider incident plane waves from a source located at an infinite distance and thus is not able to consider the source position at a finite distance from the cylinder. Therefore, the analysis will be further extended in Chapter 5 to consider a point source and a line source placed at a defined position with respect to the cylinder

Chapter 4

Pressure at Any Location from a Cylinder in the Sound Field Due to Normal Incident Plane Waves

4.1 Introduction

The prediction of the sound pressure field in the acoustic domain caused by a diffracting object is of interest in many fields of acoustics. Applications in acoustics include detecting, locating and classifying objects that generate a scattered sound field excited by the incident sound waves.

Prediction of the sound pressure field at locations not on the surface of a cylinder can be done analytically. However, the analytical derivations of the governing equations are restricted either by a low and high frequency limit, or the argument kr (k is wave number and r is the radial distance from the origin of a cylinder) or the use of asymptotic analysis. Therefore, in the work reported in this thesis an effort has been taken to construct a suitable analytical form to overcome those shortcomings.

This chapter is concerned with the sound pressure field at locations not on the surface of a cylinder due to incident plane waves that strike normal to the circumference of the cylinder. Though it is not the primary focus of this thesis, it will help to explain the limitations of the previous analytical derivations. In the current work a suitable analytical technique has been developed, which is useful for any frequency and at any distance in the sound field. For the current development, the analytical derivations given in the previous

chapter have been used. The developed analytical technique has also been compared with Morse (1936), Morse & Ingard (1986) and Junger & Feit (1993).

4.2 Pressure at Any Location in the Sound Field

Expressions for the sound pressure on the cylindrical surface have been presented in the previous chapter; hence the interest here is to construct suitable expressions to determine the sound pressure at any location from a cylinder in the sound field. Again the cylinder has been considered as an infinite cylinder so that the effects from both edges of the cylinder can be omitted. To determine the sound pressure at any location from a cylinder it is at first important to evaluate the incident sound pressure at that location, which will interfere with the scattered sound pressure from the cylinder surface to provide the total pressure.

4.2.1 Incident Sound Pressure Field

Consider plane waves travelling in the positive x direction and impinging normal to a cylinder of radius a as shown in Figure 4.1. In the figure, r is the radial distance from the origin of the cylinder, which can be any distance of interest from the cylinder. Recalling equation (3.10) for the incident sound pressure at the surface of the cylinder, the incident sound pressure at any distance r from the cylinder can similarly be expressed by the following equation

$$P^i(r, k, \phi_i) = P^o \sum_{m=0}^{M-1} \varepsilon_m i^m \cos(m\phi_i) J_m(kr), \quad (4.1)$$

where the incident sound pressure, P^i , is a function of the radial distance r , wave number

k and azimuthal angle ϕ_i . Note the only difference between equations (3.10) and (4.1) is the use of radial distance from the origin of the cylinder instead of the radius of the cylinder. Since equation (4.1) is dependent on the distance, it is necessary to consider the impact of distance on the incident sound pressure. Although equation (4.1) considers the undisturbed incident waves in the absence of the cylinder at any location in the sound field, the complex incident sound pressure will vary with distance from the cylinder origin. The

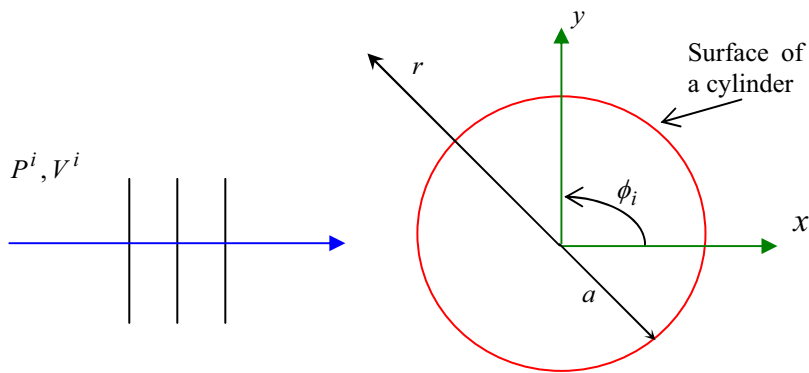


Figure 4.1: Incident plane waves travelling normal to the cylinder axis z (z axis is out of page).

differences in the complex incident sound pressure with various circumferential angles at the surface of a cylinder (in this case the Boeing cylinder radius has been used, which is $a = 1.23\text{m}$) and at some distances from the cylinder for the case $ka = 5$ are shown in Table 4.1. The values show differences in the complex incident sound pressure for various distances even though the incident sound pressure magnitude is unity. When adding this series summation with the series summation of the scattered sound pressure, there is a great effect due to the variation of distance on the total sound pressure around the cylinder. More clearly, it can be seen that in equation (4.1), the expansion of J_m is dependent on the

argument kr . Similarly, the expansion of N_m and H_m used in the equations for scattered sound pressure shown in the previous chapter will depend on the argument kr . Any small variation in distance will result in patterns for the total sound pressure in the sound field different to that on the surface of the cylinder. In the next section, the exact analytical form to calculate the scattered sound pressure at any location from a cylinder in the sound field is derived.

ϕ_i (rad)	Incident sound pressure, P^i (Pa)		
	$r = a = 1.23\text{m}$	$r = 2\text{m}$	$r = 4\text{m}$
0.0	$0.2837 + 0.9589i$	$-0.2726 - 0.9621i$	$-0.8514 + 0.5246i$
0.1	$0.2596 + 0.9657i$	$-0.2333 - 0.9724i$	$-0.8911 + 0.4537i$
0.2	$0.1868 + 0.9824i$	$-0.1138 - 0.9935i$	$-0.9741 + 0.2261i$
0.3	$0.0642 + 0.9979i$	$0.0869 - 0.9962i$	$-0.9849 - 0.1732i$
0.4	$-0.1069 + 0.9943i$	$0.3576 - 0.9339i$	$-0.7443 - 0.6679i$
0.5	$-0.3188 + 0.9478i$	$0.6588 - 0.7524i$	$-0.1321 - 0.9912i$
0.6	$-0.5528 + 0.8333i$	$0.9103 - 0.4140i$	$0.6572 - 0.7537i$
0.7	$-0.7759 + 0.6308i$	$0.9979 + 0.0649i$	$0.9916 + 0.1295i$
0.8	$-0.9421 + 0.3353i$	$0.8145 + 0.5801i$	$0.3269 + 0.9451i$
0.9	$-0.9994 - 0.0335i$	$0.3348 + 0.9423i$	$-0.7759 + 0.6309i$
1.0	$-0.9047 - 0.4260i$	$-0.3143 + 0.9493i$	$-0.8025 - 0.5967i$
1.1	$-0.6421 - 0.7667i$	$-0.8545 + 0.5194i$	$0.4604 - 0.8877i$
1.2	$-0.2387 - 0.9711i$	$-0.9809 - 0.1943i$	$0.9245 + 0.3813i$
1.3	$0.2312 - 0.9729i$	$-0.5679 - 0.8231i$	$-0.3549 + 0.9349i$
1.4	$0.6601 - 0.7512i$	$0.1878 - 0.9822i$	$-0.9294 - 0.3690i$
1.5	$0.9381 - 0.3464i$	$0.8391 - 0.5439i$	$0.4083 - 0.9128i$
1.6	$0.9894 + 0.1455i$	$0.9720 + 0.2352i$	$0.8894 + 0.4571i$
1.7	$0.7996 + 0.6006i$	$0.4997 + 0.8662i$	$-0.5006 + 0.8657i$
1.8	$0.4212 + 0.9070i$	$-0.2729 + 0.9621i$	$-0.8511 - 0.5250i$
1.9	$-0.0456 + 0.9990i$	$-0.8712 + 0.4910i$	$0.5179 - 0.8555i$
2.0	$-0.4881 + 0.8728i$	$-0.9709 - 0.2394i$	$0.8854 + 0.4648i$
2.1	$-0.8154 + 0.5789i$	$-0.5712 - 0.8208i$	$-0.3475 + 0.9377i$
2.2	$-0.9802 + 0.1978i$	$0.0721 - 0.9974i$	$-0.9896 - 0.1438i$
2.3	$-0.9820 - 0.1887i$	$0.6476 - 0.7619i$	$-0.1611 - 0.9869i$
2.4	$-0.8549 - 0.5187i$	$0.9588 - 0.2841i$	$0.8385 - 0.5449i$
2.5	$-0.6493 - 0.7605i$	$0.9736 + 0.2282i$	$0.8959 + 0.4443i$
2.6	$-0.4150 - 0.9098i$	$0.7754 + 0.6314i$	$0.2026 + 0.9793i$
2.7	$-0.1909 - 0.9816i$	$0.4828 + 0.8758i$	$-0.5339 + 0.8455i$
2.8	$-0.0013 - 1.0000i$	$0.1924 + 0.9813i$	$-0.9259 + 0.3777i$
2.9	$0.1419 - 0.9899i$	$-0.0400 + 0.9992i$	$-0.9968 - 0.0799i$
3.0	$0.2353 - 0.9719i$	$-0.1935 + 0.9811i$	$-0.9251 - 0.3797i$
3.1	$0.2795 - 0.9601i$	$-0.2658 + 0.9640i$	$-0.8587 - 0.5125i$

Table 4.1: Complex incident sound pressure at various distances for $ka = 5$.

4.2.2 Scattered Sound Pressure Field

To calculate the scattered sound pressure at any position in the sound field due to incident plane waves that strike normal to a cylinder, the phase angles and directions of the scattered waves from the surface of the cylinder need to be taken into account, assuming that the cylinder is infinite in length. For the scattered sound pressure, the scattered velocity potential ψ_m^s as a function of cylinder radius a , wave number k and circumferential angle ϕ_i can be used. The scattered velocity potential and the pressure corresponding to that velocity potential at any distance r from the cylinder origin can be derived by using equations (3.16) and (3.11) as follows:

$$\psi_m^s(a, k, \phi_i) = \varepsilon_m i^{m+1} e^{-i\gamma_m} \sin \gamma_m \cos(m\phi_i), \quad (4.2)$$

$$P^s(r, k, \phi_i) = -P^o \sum_{m=0}^{M-1} \psi_m^s H_m(kr) . \quad (4.3)$$

The scattered intensity corresponding to the far-field scattered sound pressure can be written as

$$I^s(r, k, \phi_i) = \frac{\langle P^s \rangle^2}{\rho_o c} . \quad (4.4)$$

The phase angles γ_m have already been defined in equation (3.17). Using equation (4.3), the scattered sound pressure patterns at various distances from the origin of a cylinder of radius a are shown in Figure 4.2, for $ka = 5$. The figure shows the scattered pressure pattern at the surface of the cylinder, $r = a$ (also shown in Figure 3.7c in Chapter 3), and it can be seen in the figure that pressure magnitudes decrease as the distance from the origin of the cylinder increases. This indicates that at a certain distance the scattered sound

pressure will become zero and only the undisturbed incident sound pressure will remain.

It is clear from the results that essentially there are no changes to the scattered sound pressure patterns around a cylinder in the sound field for $ka = 5$ due to the variation of distance, except for $r = a$. The scattered sound pressure magnitudes vary with distance, but the scattered sound pressure patterns will be different for different wavelengths. The variation of the scattered sound pressure patterns in the sound field at a distance of $5a$ (five times the cylinder radius) from the origin of a cylinder for various values of ka is shown in Figure 4.3. This figure shows that there is more spatial variation in the sound pressure amplitudes when the wavelength is smaller than the circumference of the cylinder, as shown for the cases when $ka = 3$ and $ka = 5$. For both these cases, the scattered sound pressure is not uniformly distributed at the front ($\phi = 180^\circ$) of the cylinder, and a predominantly higher scattered sound pressure is occurring at the back ($\phi = 0^\circ$) of the cylinder because of reinforcement of the two diffracted waves travelling around two sides of the cylinder. The smaller the wavelength relative to the circumference of the cylinder, the higher the amplitude of scattered sound pressure that will occur at the back of the cylinder. For the case when $ka = 1$, the wavelength is equal to the circumference of the cylinder, the scattered sound pressure is uniformly distributed at the front of the cylinder and there is very little scattering at the back of the cylinder. Figure 4.4 shows the scattered sound pressure variation with the circumferential angle for the three cases of ka discussed above.

From the results presented in Figure 4.3, it is interesting to see that when $ka = 1, 3$ and 5 ,

there is relatively little variation in the scattered sound pressure patterns at a distance of $5a$ compared with those at the surface of the cylinder shown in Figures 3.7(a-c), 3.8 and 3.9, in Chapter 3. Hence, the far-field approximation may be suitable to determine the sound pressure pattern at the cylinder surface only when $ka \leq 5$. If the value of ka increases or the wavelength decreases compared to the value of $ka \leq 5$, the distortion of the scattered sound field increases and the far-field approximation is no longer suitable. Therefore, the scattered sound pressure pattern will be different than that at the cylinder surface. Figures 4.5(a-e) and 4.6(a-e) respectively, show the directivity patterns and variation with the circumferential angle of the scattered sound pressure for other large values of ka , at a distance of $5a$ from the origin of a cylinder of radius a . The results show the differences of the scattered sound pressure patterns and variation (when $ka \leq 5$) with those for the cylinder surface presented in the previous chapter in Figures 3.7(d-h) and 3.9 to 3.11.

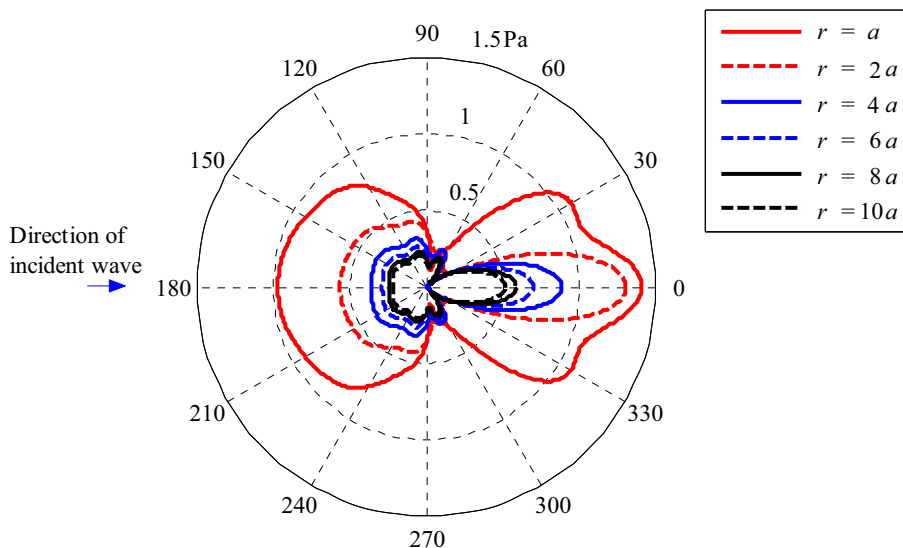


Figure 4.2: Directivity patterns of the scattered sound pressure at various distances from the origin of a cylinder of radius a , for $ka = 5$. [Incident pressure magnitude $P^o = 1 \text{ Pa}$]

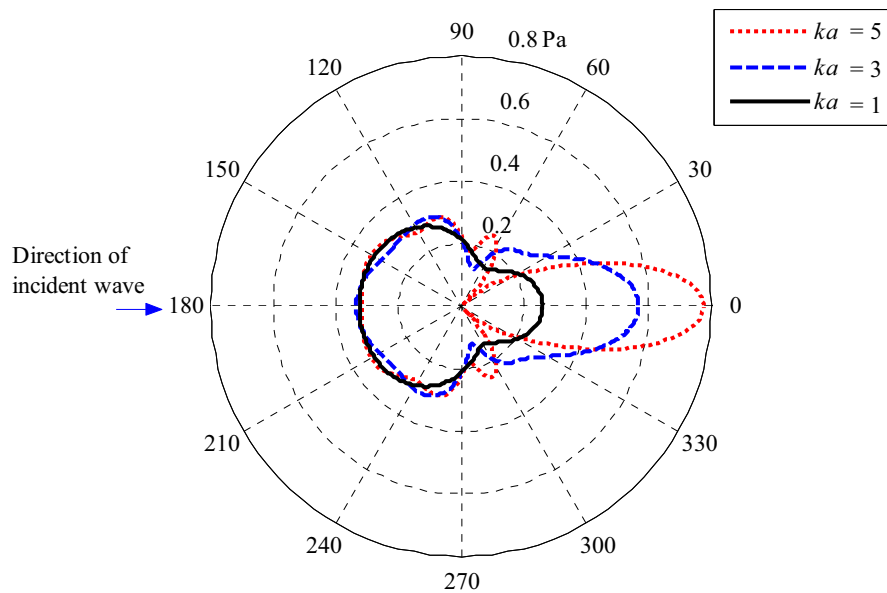


Figure 4.3: Directivity patterns of the scattered sound pressure at a distance of $r = 5a$ from the origin of a cylinder of radius a , for values of $ka = 1, 3$ and 5 respectively. [Incident pressure magnitude $P^o = 1 \text{ Pa}$]

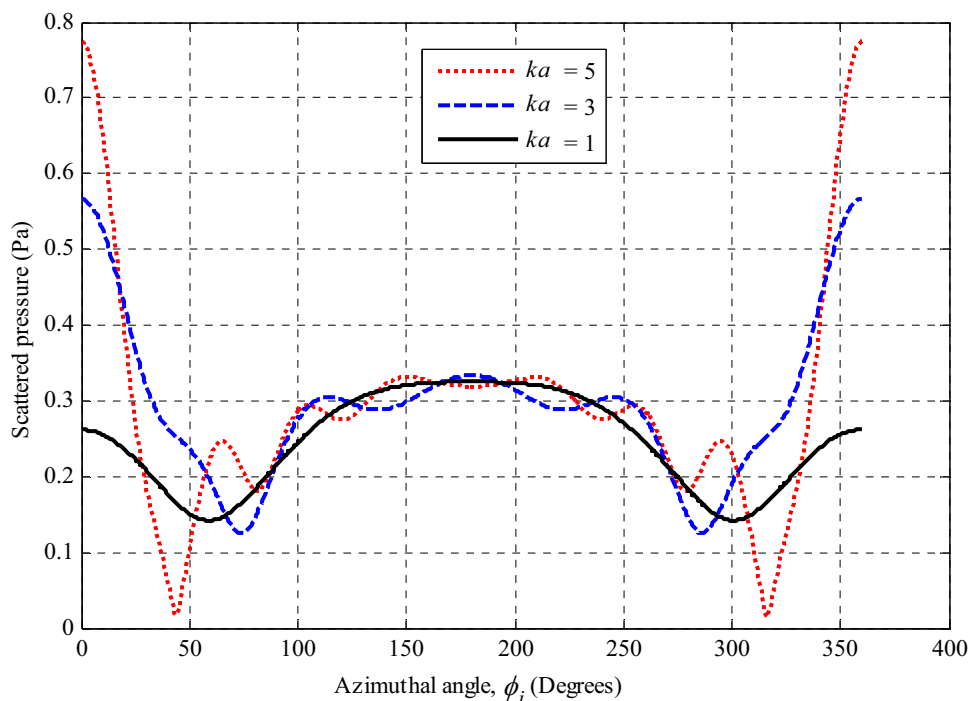


Figure 4.4: Scattered sound pressure variation as a function of azimuthal angle, ϕ_i , at a distance of $r = 5a$ from the origin of a cylinder of radius a , for values of $ka = 1, 3$ and 5 respectively. [Incident pressure magnitude $P^o = 1 \text{ Pa}$]

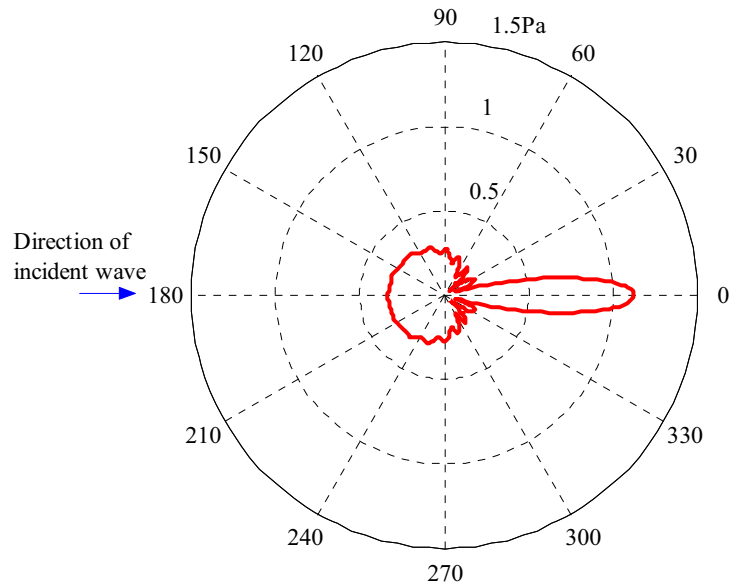


Figure 4.5(a): Directivity pattern of the scattered sound pressure at a distance of $r = 5a$ (five times the cylinder radius) from the origin of a cylinder of radius a , for $ka = 10$. [Incident pressure magnitude $P^o = 1\text{Pa}$]

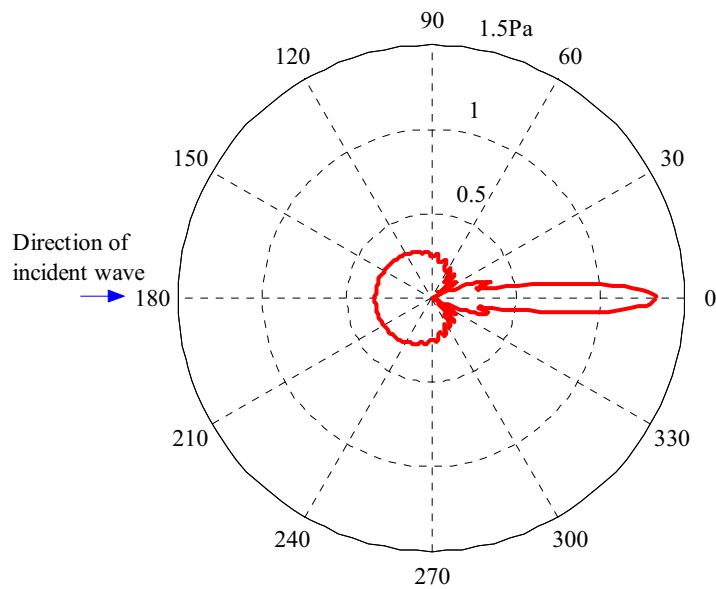


Figure 4.5(b): Directivity pattern of the scattered sound pressure at a distance of $r = 5a$ (five times the cylinder radius) from the origin of a cylinder of radius a , for $ka = 15$. [Incident pressure magnitude $P^o = 1\text{Pa}$]

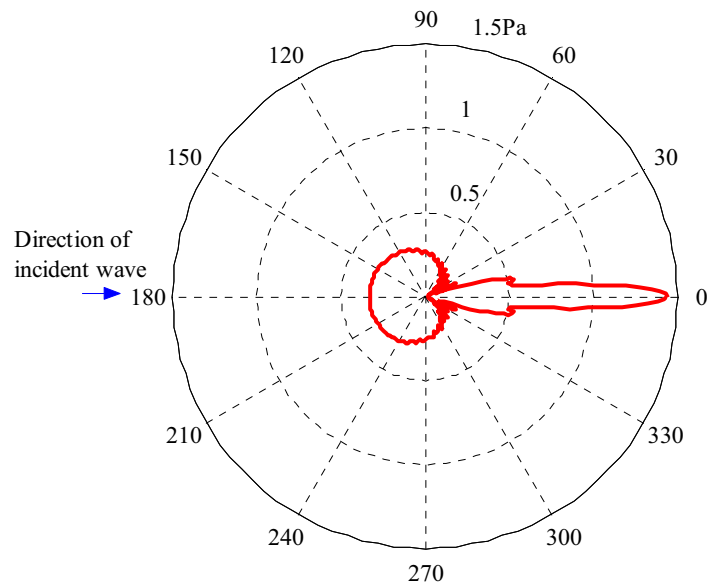


Figure 4.5(c): Directivity pattern of the scattered sound pressure at a distance of $r = 5a$ (five times the cylinder radius) from the origin of a cylinder of radius a , for $ka = 20$. [Incident pressure magnitude $P^o = 1\text{Pa}$]

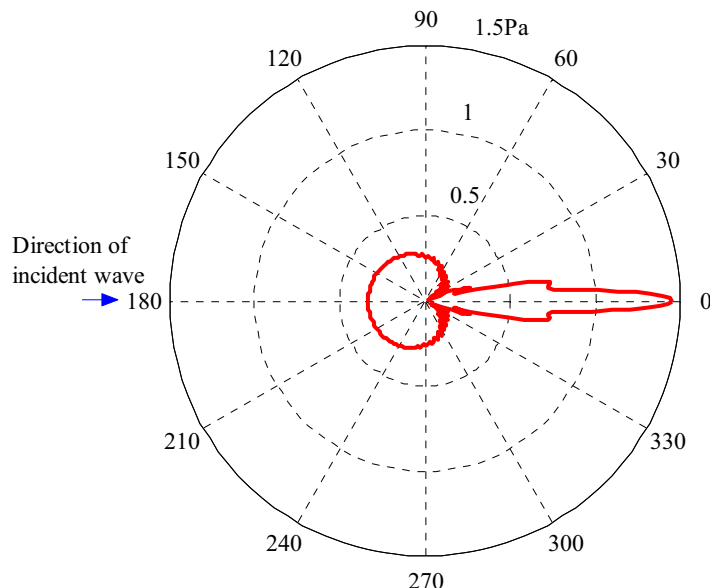


Figure 4.5(d): Directivity pattern of the scattered sound pressure at a distance of $r = 5a$ (five times the cylinder radius) from the origin of a cylinder of radius a , for $ka = 25$. [Incident pressure magnitude $P^o = 1\text{Pa}$]

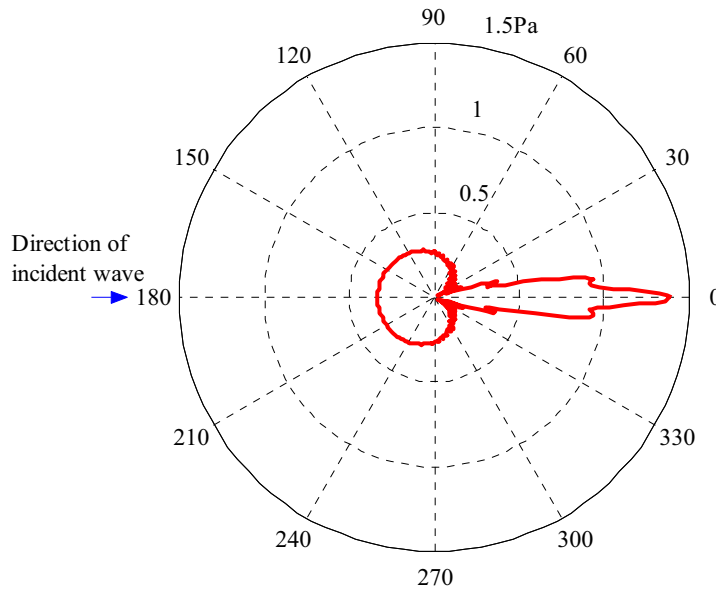


Figure 4.5(e): Directivity pattern of the scattered sound pressure at a distance of $r = 5a$ (five times the cylinder radius) from the origin of a cylinder of radius a , for $ka = 30$. [Incident pressure magnitude $P^o = 1\text{ Pa}$]

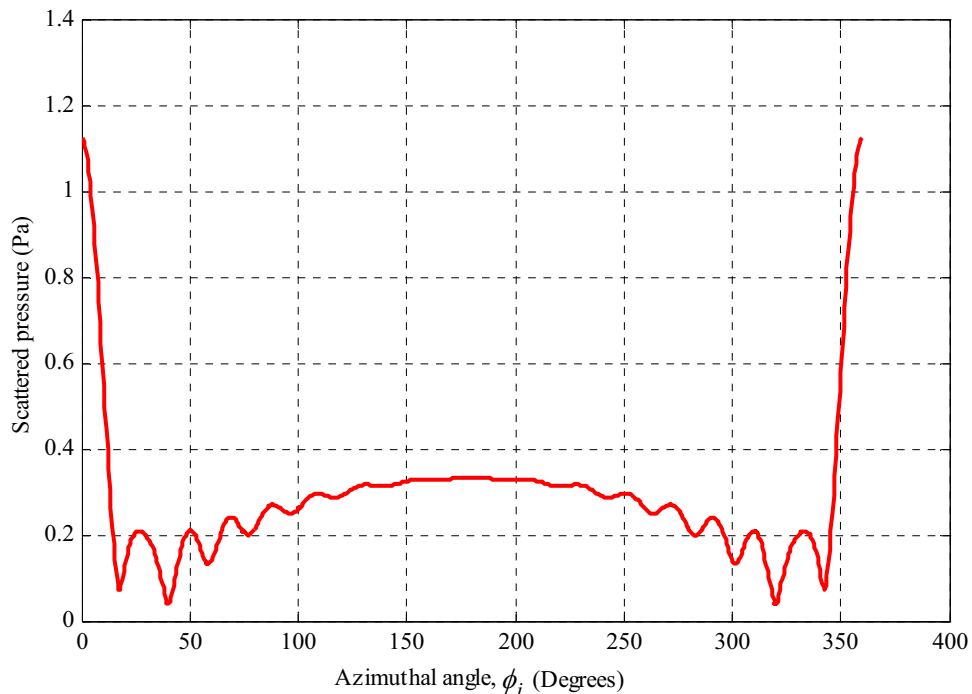


Figure 4.6(a): Scattered sound pressure variation as a function of azimuthal angle, ϕ_i , at a distance of $r = 5a$ (five times the cylinder radius) from the origin of a cylinder of radius a , for $ka = 10$. [Incident pressure magnitude $P^o = 1\text{ Pa}$]

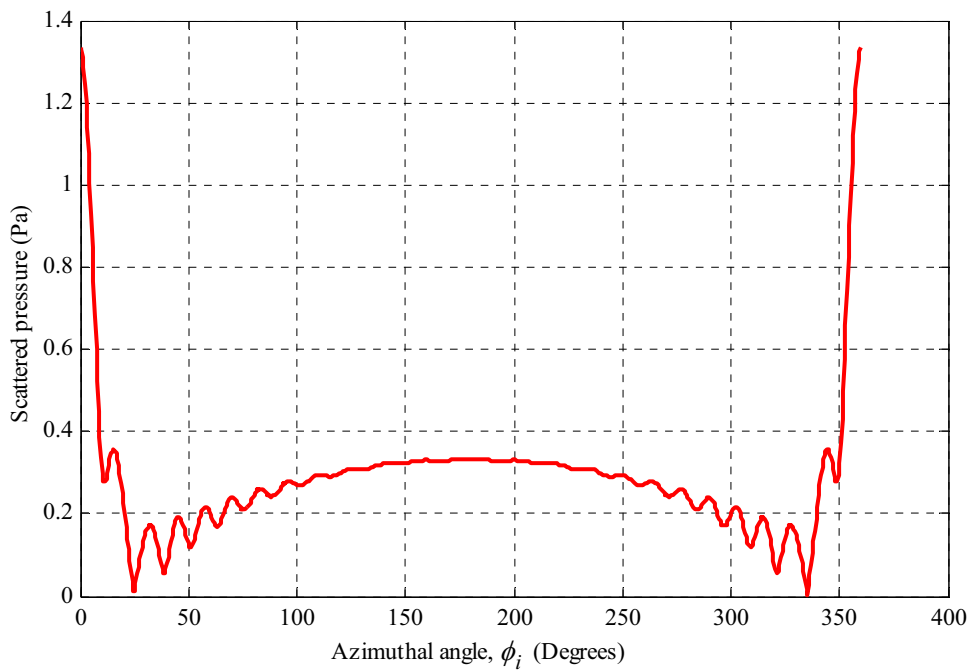


Figure 4.6(b): Scattered sound pressure variation as a function of azimuthal angle, ϕ_i , at a distance of $r = 5a$ (five times the cylinder radius) from the origin of a cylinder of radius a , for $ka = 15$. [Incident pressure magnitude $P^0 = 1 \text{ Pa}$]

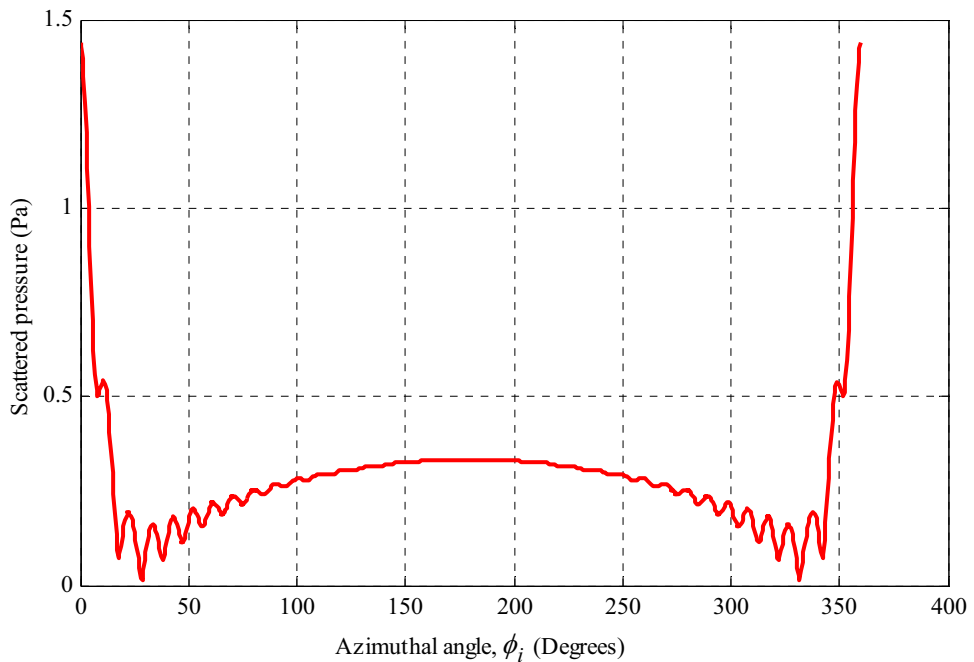


Figure 4.6(c): Scattered sound pressure variation as a function of azimuthal angle, ϕ_i , at a distance of $r = 5a$ (five times the cylinder radius) from the origin of a cylinder of radius a , for $ka = 20$. [Incident pressure magnitude $P^0 = 1 \text{ Pa}$]

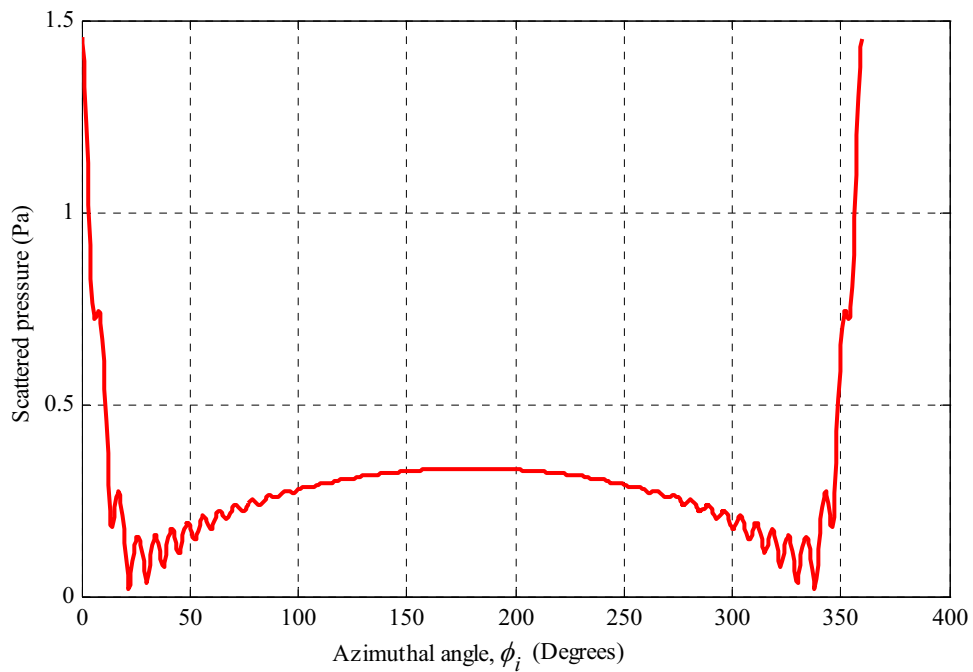


Figure 4.6(d): Scattered sound pressure variation as a function of azimuthal angle, ϕ_i , at a distance of $r = 5a$ (five times the cylinder radius) from the origin of a cylinder of radius a , for $ka = 25$. [Incident pressure magnitude $P^o = 1\text{Pa}$]

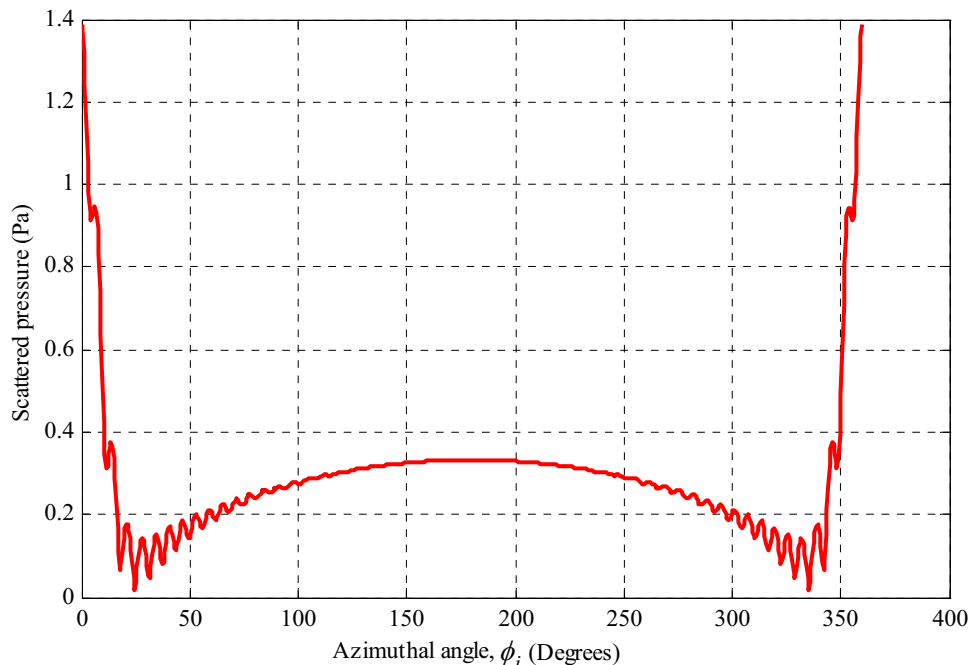


Figure 4.6(e): Scattered sound pressure variation as a function of azimuthal angle, ϕ_i , at a distance of $r = 5a$ (five times the cylinder radius) from the origin of a cylinder of radius a , for $ka = 30$. [Incident pressure magnitude $P^o = 1\text{Pa}$]

4.2.3 Total Sound Pressure Field

The total sound pressure at any position in the sound field from a cylinder due to both the incident and scattered waves can be expressed by summing equations (4.1) and (4.3) in the following form

$$P_r^t(r, k, \phi_i) = P^i(r, k, \phi_i) + P^s(r, k, \phi_i) \\ = P^o \sum_{m=0}^{M-1} \varepsilon_m i^m \cos(m\phi_i) \left[J_m(kr) - i e^{-i\gamma_m} \sin \gamma_m H_m(kr) \right] \quad (4.5)$$

Using equation (4.5), the directivity patterns of the total sound pressure for various values of ka at various distances from the origin of a cylinder are shown in Figures 4.7(a-c). In the figures, the red line (solid line) shows the total sound pressure pattern at the surface of the cylinder. The blue (dash line) and black (dash-dot line) lines show the total sound pressure patterns at a distance of $5a$ (five times the cylinder radius) and $10a$ (10 times the cylinder radius), respectively, from the origin of the cylinder of radius a . From the results, it is noticeable that the total sound pressure pattern varies significantly with distance from the cylinder. Also, when $ka = 3$ and $ka = 5$, there is a greater pressure at the back ($\phi = 0^\circ$) of the cylinder at those distances compared with the pressure for $ka = 1$ at the surface of the cylinder, as shown in Figures 4.7(a-c). This is because when the wavelength is smaller than the circumference of the cylinder, the high scattering will occur mostly in the back region of the cylinder because of reinforcement of the two diffracted waves travelling around the two sides of the cylinder, as already discussed in the previous section.

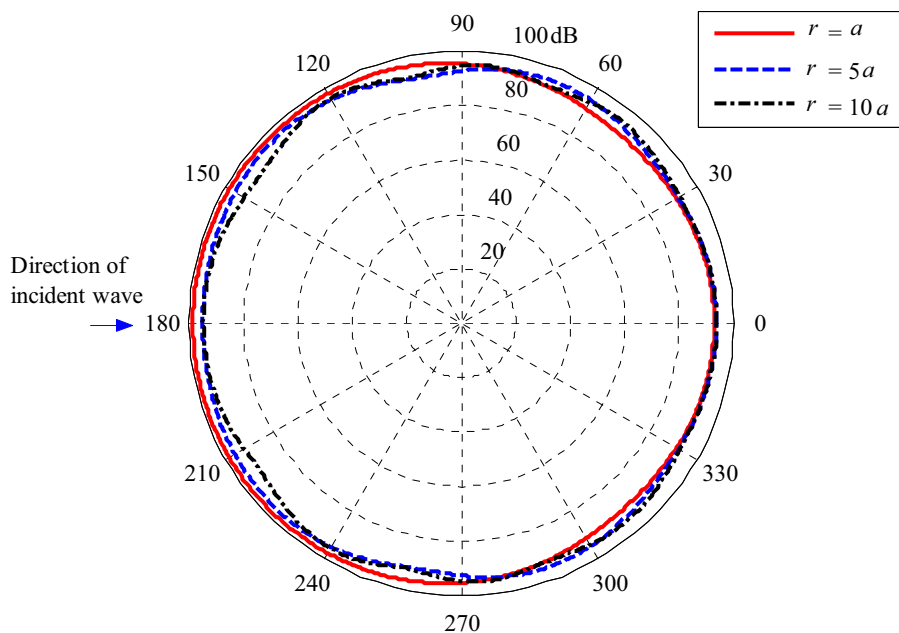


Figure 4.7(a): Directivity pattern of the total sound pressure of a cylinder of radius a at various distances, for $ka = 1$. [Reference pressure $20\mu\text{Pa}$ and incident pressure magnitude $P^o = 1\text{ Pa}$]

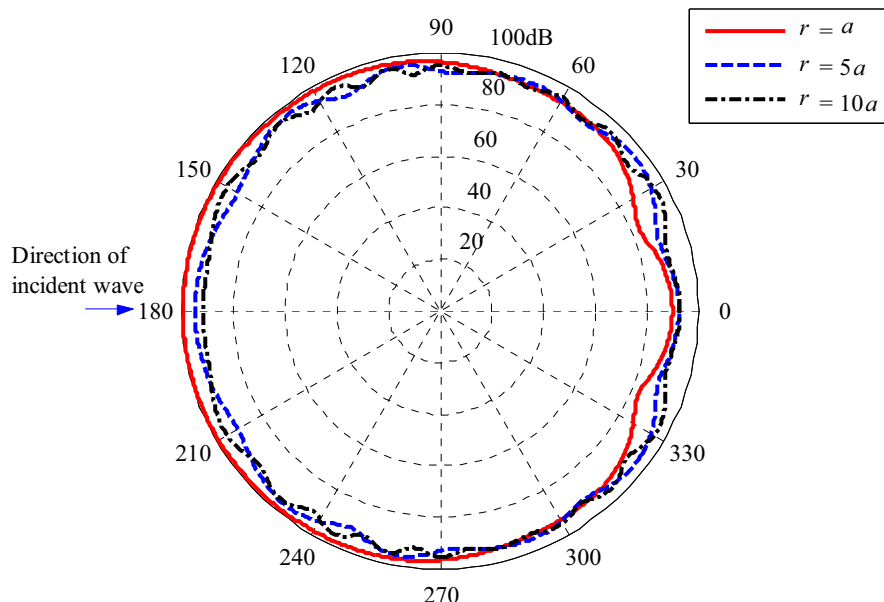


Figure 4.7(b): Directivity pattern of the total sound pressure of a cylinder of radius a at various distances, for $ka = 3$. [Reference pressure $20\mu\text{Pa}$ and incident pressure magnitude $P^o = 1\text{ Pa}$]

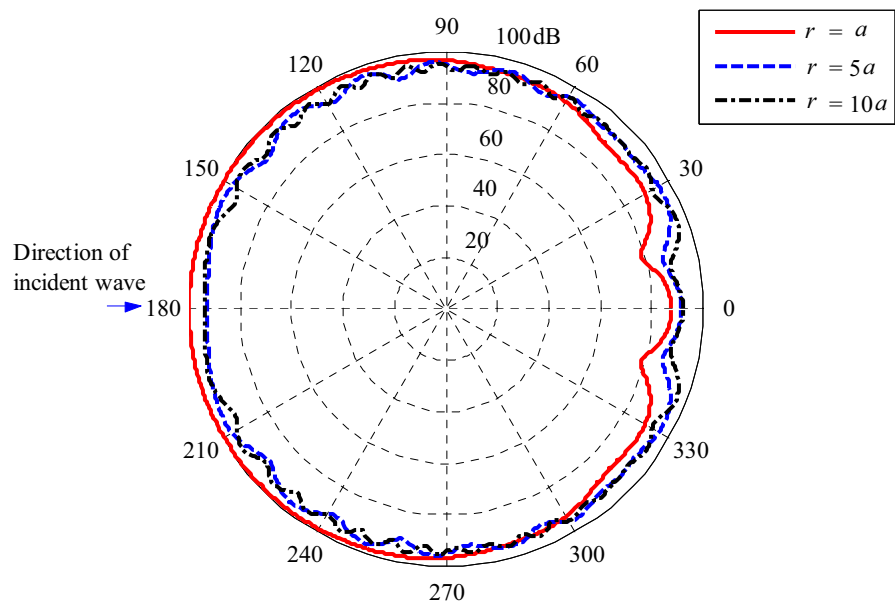


Figure 4.7(c): Directivity pattern of the total sound pressure of a cylinder of radius a at various distances, for $ka = 5$. [Reference pressure $20\mu\text{Pa}$ and incident pressure magnitude $P^o = 1 \text{ Pa}$]

4.3 Comparison with Previous Work

Firstly, the equations (3.19) to (3.21) given in Chapter 3 from Junger & Feit (1993), can be used for comparison with the current technique. Note that to calculate the incident, scattered and total sound pressure away from the surface of the cylinder using equations (3.19), (3.20) and (3.21), it is necessary to use the radial distance r instead of radius a of the cylinder in those equations. The comparisons between the results obtained using the equations of the current technique and Junger & Feit (1993) for the scattered and total sound pressure in the sound field at some distance of $5a$ (five times the cylinder radius) from the origin of a cylinder of radius a are shown in Figures 4.8(a-b), for $ka = 5$. The comparisons show that there are no significant differences between the results obtained using the current derivations and those using Junger & Feit (1993).

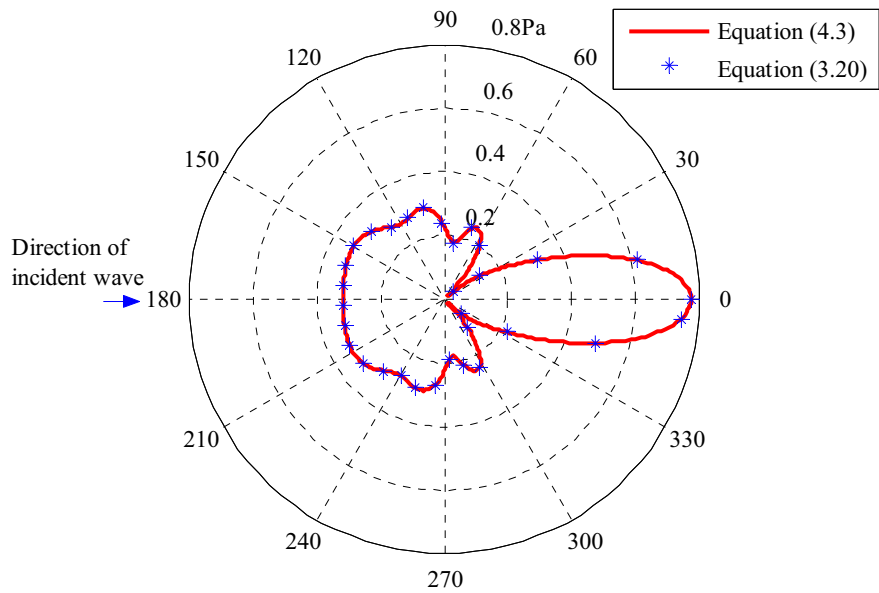


Figure 4.8(a): Scattered sound pressure comparison between results obtained at a distance of $5a$ (five times the cylinder radius) in the sound field from the origin of a cylinder of radius a , using equations (4.3) and (3.20), for $ka = 5$. [Incident pressure magnitude $P^o = 1 \text{ Pa}$]

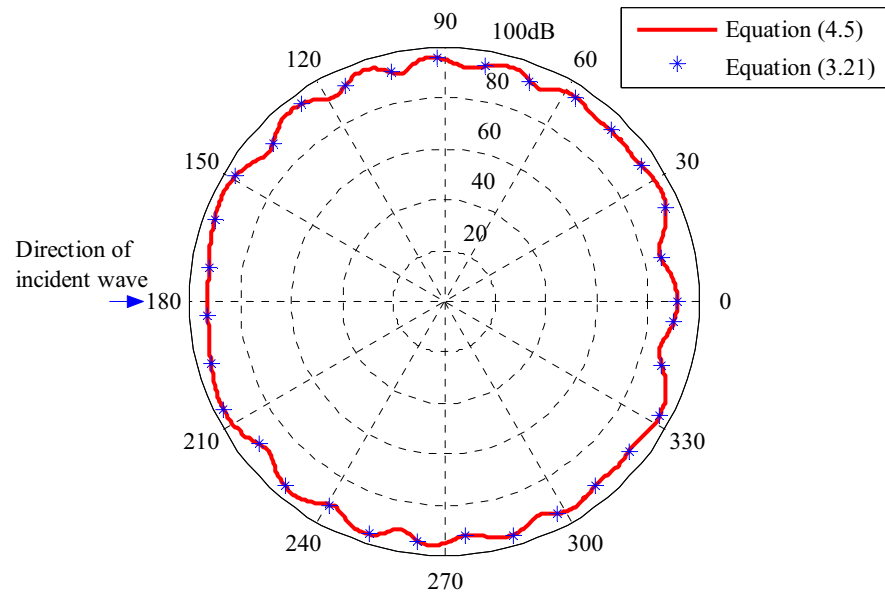


Figure 4.8(b): Total sound pressure comparison between results obtained at a distance $5a$ (five times the cylinder radius) in the sound field from the origin of a cylinder of radius a , using equations (4.5) and (3.21), for $ka = 5$. [Reference pressure $20 \mu\text{Pa}$ and incident pressure magnitude $P^o = 1 \text{ Pa}$]

Secondly, it has been observed that for the far-field scattered sound pressure from a cylinder, there are significant differences between the results obtained using the current derivations and those using the previous derivations (Morse, 1936; Morse & Ingard, 1986). It has also been observed that the previous derivations are not suitable to calculate the exact scattered sound pressure and intensity at the region close to a cylinder. The reason for this is that the former equations do not converge fully at the region close to the cylinder. However, the current technique converges fully for any position relative to the cylinder and is able to determine the exact scattered sound pressure and intensity, not only in the region close to the cylinder, but also in the far-field region. For reader convenience, the previous derivations for the scattered sound pressure, velocity potential and intensity at a very large distance from a cylinder ($kr \gg 1$) are given by (Morse & Ingard, 1986)

$$p_s \cong -\sqrt{\frac{2\rho_o c I^o a}{\pi r}} \psi_s(\phi_i) e^{ik(r-ct)}, \quad (4.6)$$

where $I^o = \frac{P^o}{\rho_o c}$. Equation (4.6) can be expressed as

$$p_s = -P^o \sqrt{\frac{2a}{\pi r}} \psi_s(\phi_i) e^{ik(r-ct)}, \quad (4.7)$$

and velocity potential

$$\psi_s(\phi_i) = \frac{1}{\sqrt{ka}} \sum_{m=0}^{\infty} \varepsilon_m \sin(\gamma_m) e^{-i\gamma_m} \cos(m\phi_i). \quad (4.8)$$

The scattered intensity is

$$I_s \cong \left(\frac{2 I^o a}{\pi r} \right) |\psi_s|^2, \quad (4.9)$$

where

$$|\psi_s|^2 = \frac{1}{ka} \sum_{m,n=0}^{\infty} \varepsilon_m \varepsilon_n \sin \gamma_m \sin \gamma_n \cos(\gamma_m - \gamma_n) \cos(m\phi_i) \cos(n\phi_i). \quad (4.10)$$

4.3.1 Sound Pressure Field

In this section, equation (4.3) developed in this thesis, has been used to calculate the scattered sound pressure field. One can easily see the difference between equations (4.3) and (4.7), presented by Morse & Ingard (1986). One major difference is that previous derivations have used the asymptotic form of the *Hankel function*. It has been found that the asymptotic form cannot give the exact results, because there are significant differences between the asymptotic values and the exact computational values of the *Hankel function* for finite values of kr . Substituting equation (4.8) in equation (4.7) one can find that the asymptotic form of the *Hankel function* used by Morse & Ingard (1986) in equation (4.7) is

$$H_m(kr) = J_m(kr) + i N_m(kr) \xrightarrow{kr \rightarrow \infty} i^{-(m+1)} \sqrt{\frac{2}{\pi kr}} e^{ikr}. \quad (4.11)$$

In the equation (4.11), the time dependent part e^{-ict} has been omitted for simplicity. The comparison between the values of this asymptotic form and the exact computational values using MATLAB of the *Hankel function* are given in Table 4.2. The table shows that the asymptotic form has no scope to vary the amplitude with the values of m for a particular value of kr , but the computational values are significantly varying and errors made by the asymptotic form with the computational values for various values of m are also reported in Table 4.2. In general, for large values of kr the asymptotic form gives relatively small error compared with the exact computational values. It is also noticeable that the

asymptotic form gives the value that is approximately equal to the 0th order of the computational *Hankel function*. This means in the previous derivations, only $m=0$ for the outgoing *Hankel function* has been considered. Hence, previous derivations may give almost exact results compared with the computational results for the case when the distance from a cylinder is very large ($kr \gg 1$), but the distance considered needs to be extremely large to converge the previous derivations (see for example the work presented by Friot & Bordier (2004), which uses $kr = 1000a$; to obtain convergence). For example, consider the case when the wavelength is very small, that is $ka = 5$. For this case, the pressure comparison between the results using the current exact equation and the asymptotic equation is shown in Figure 4.9(a). The figure shows that the previous mathematical derivation agrees well with the current result when the distance is $r=57a$ from the origin of a cylinder of radius a . If the distance decreases, the error increases compared with the computational results shown in Figures 4.9(b-d) respectively, for the distances of $5a$, $2a$ and $1.2a$ from the cylinder respectively. Therefore, the previous derivations only converge for the *Fraunhofer diffraction* region, where to calculate the scattered sound pressure or intensity (the intensity is discussed in section 4.3.2), the distance considered needs to be so large compared with the cylinder circumferential length that the diffraction angle subtended by the cylinder is negligible. However, the previous derivations do not converge in the *Fresnel diffraction* region or the near-field region. This problem can be overcome by using the current derivation. To converge the mathematical expression at any location from a cylinder, here the full expansion of the *Hankel function* has been used with the series as shown in equation (4.3). From the above discussions, it is clear that full expansion of the *Hankel function* is necessary for each particular value of

kr , as the value of *Hankel function* will vary for each value of m . This will be discussed more clearly in the next section dealing with comparison of intensity values.

kr	m	Asymptotic Values		Computational Values		Error	Error (%)
		Complex	Absolute	Complex	Absolute		
1	0	$0.6714 + 0.4311i$	0.7979	$0.7652 - 0.0883i$	0.7703	-0.0276	3.58
	1	$-0.4311 + 0.6714i$	0.7979	$0.4401 + 0.7812i$	0.8966	0.0987	11.00
	2	$-0.6714 - 0.4311i$	0.7979	$0.1149 + 1.6507i$	1.6547	0.8568	51.78
3	0	$0.0650 - 0.4560i$	0.4607	$-0.2601 - 0.3769i$	0.4579	-0.0028	0.61
	1	$0.4560 + 0.0650i$	0.4607	$0.3391 - 0.3247i$	0.4694	0.0088	1.87
	2	$-0.0650 + 0.4560i$	0.4607	$0.4861 + 0.1604i$	0.5119	0.0512	10.00
5	0	$-0.3422 + 0.1012i$	0.3568	$-0.1776 + 0.3085i$	0.3560	-0.0008	0.22
	1	$-0.1012 - 0.3422i$	0.3568	$-0.3276 - 0.1479i$	0.3594	0.0026	0.72
	2	$0.3422 - 0.1012i$	0.3568	$0.0466 - 0.3677i$	0.3706	0.0138	3.72
10	0	$-0.1373 - 0.2117i$	0.2523	$-0.2459 - 0.0557i$	0.2522	-0.0002	0.08
	1	$0.2117 - 0.1373i$	0.2523	$0.0435 - 0.2490i$	0.2528	0.0005	0.20
	2	$0.1373 + 0.2117i$	0.2523	$0.2546 + 0.0059i$	0.2547	0.0024	0.94
15	0	$0.1340 - 0.1565i$	0.2060	$-0.0142 - 0.2055i$	0.2060	0.00	0.00
	1	$0.1565 + 0.1340i$	0.2060	$0.2051 - 0.0211i$	0.2062	0.0002	0.09
	2	$-0.1340 + 0.1565i$	0.2060	$0.0416 + 0.2027i$	0.2069	0.0009	0.43

Table 4.2: Comparison between the asymptotic values using equation (4.11) and the exact computational values using MATLAB of the outgoing *Hankel function*, $H_m(kr)$.

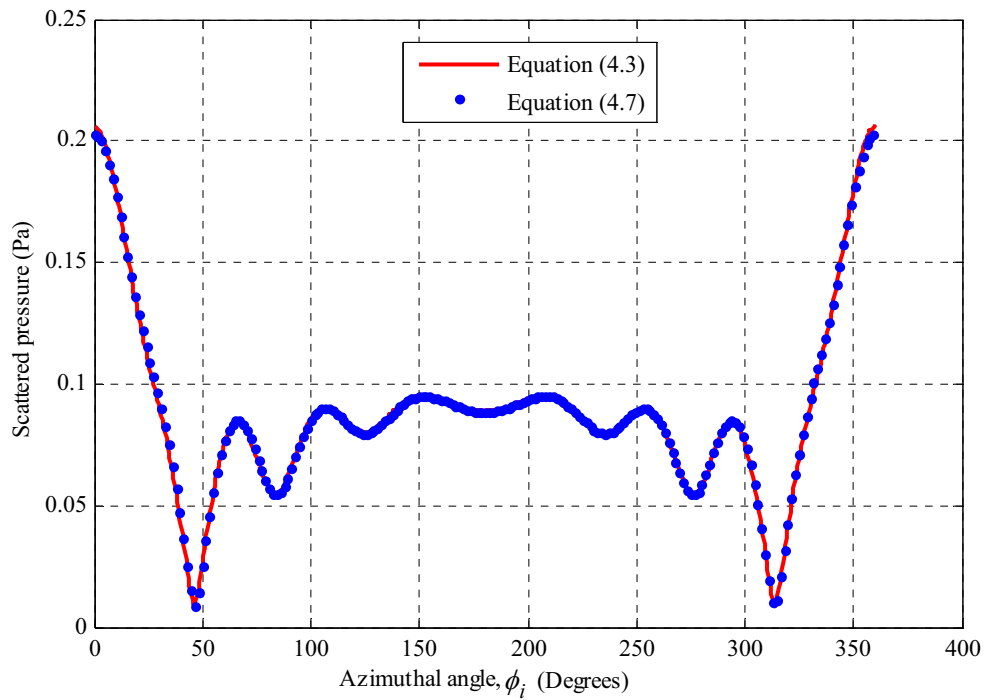


Figure 4.9(a): Scattered sound pressure comparison between results obtained using equations (4.3) and (4.7), for $ka = 5$ and $r = 57a$. [Incident pressure magnitude $P^o = 1 \text{ Pa}$]

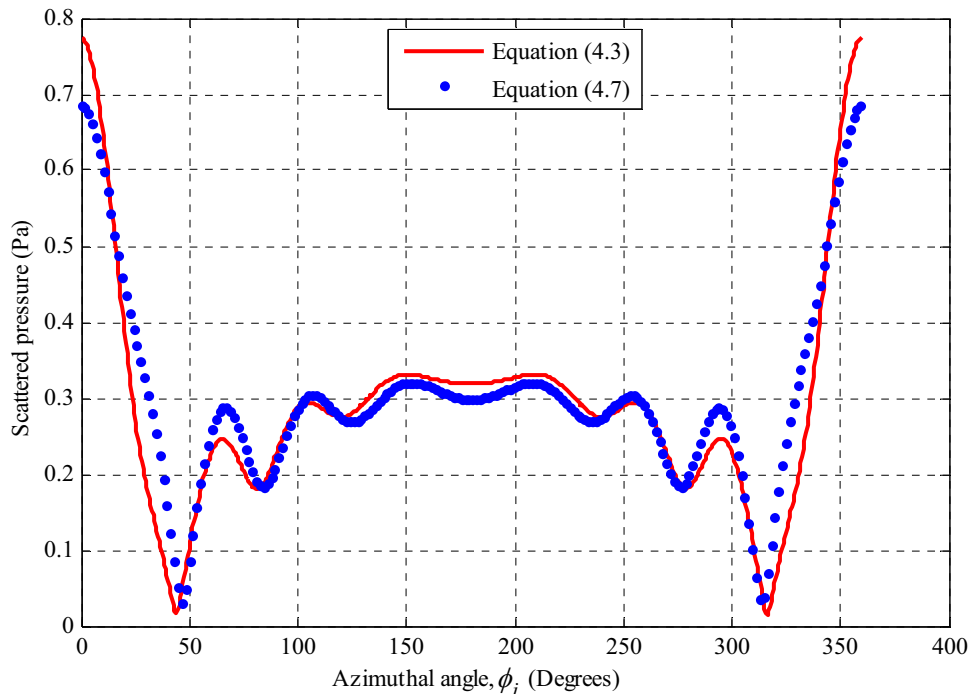


Figure 4.9 (b): Scattered sound pressure comparison between results obtained using equations (4.3) and (4.7), for $ka = 5$ and $r = 5a$. [Incident pressure magnitude $P^o = 1 \text{ Pa}$]

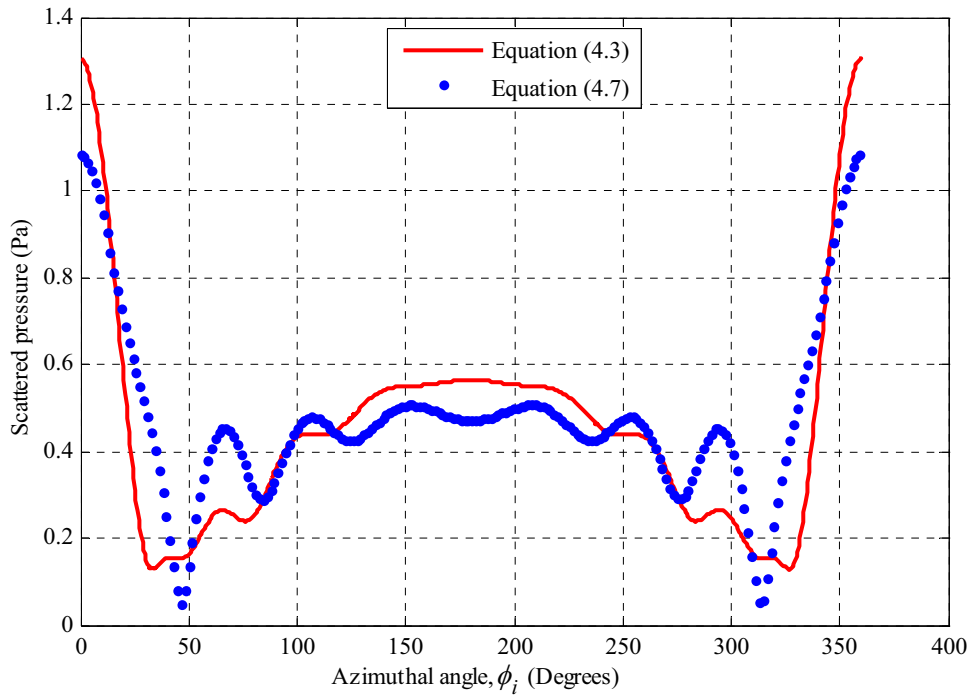


Figure 4.9(c): Scattered sound pressure comparison between results obtained using equations (4.3) and (4.7), for $ka = 5$ and $r = 2a$. [Incident pressure magnitude $P^o = 1 \text{ Pa}$]

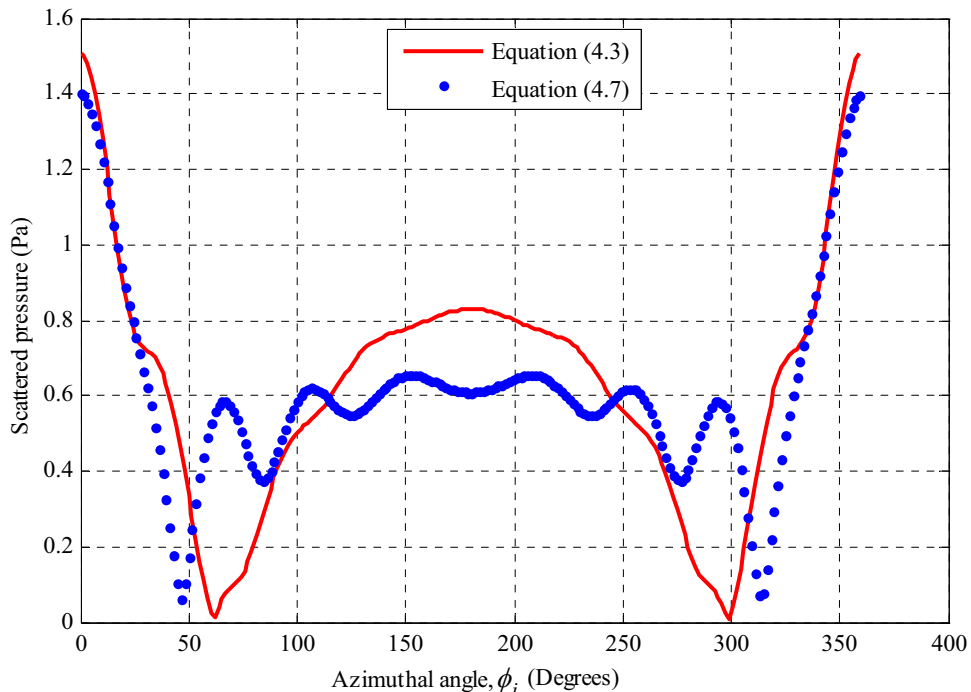


Figure 4.9(d): Scattered sound pressure comparison between results obtained using equations (4.3) and (4.7), for $ka = 5$ and $r = 1.2a$. [Incident pressure magnitude $P^o = 1 \text{ Pa}$]

4.3.2 Sound Intensity Field

In this section, comparisons have been made between the current results obtained using the theory developed here and results from the previous theory (Morse, 1936; Morse & Ingard, 1986) for three particular wavelengths, $\lambda = 2\pi a/5$, $\lambda = 2\pi a/3$ and $\lambda = 2\pi a$, respectively. It has been shown in the preceding section that one of the major limitations of the previous derivations is the use of asymptotic forms of the *Hankel function*, which give different results to the computational results obtained using an appropriate expansion of the *Hankel function*, as in the current technique. For comparisons of the intensity values, equation (4.4) has been used for the current calculations, and the distance $r = 57a$ from the origin of a cylinder of radius a has been chosen because, as has been shown earlier, at that distance the former equations can converge so that a comparison of far-field intensity can be made with the previous results at that distance. The parameters for the three cases examined are given in the Table 4.3.

Case	Wavelength, λ (m)	ka
I	$2\pi a/5$	5
II	$2\pi a/3$	3
III	$2\pi a$	1

Table 4.3: Values of λ and ka for the three cases examined.

4.3.2.1 Case I (Short Wavelength)

Consider the case where the wavelength is very small compared with the circumference of the cylinder, that is when $\lambda = 2\pi a/5$. The comparison of scattered intensity with the previous result presented by Morse (1936) and Morse & Ingard (1986) for this particular wavelength is shown in Figure 4.10. In the figure, the result has been scanned from Morse

& Ingard (1986) and the current result overlaid. Since equation (4.4) is a finite series summation, it has been observed from trial and error that, in this particular case, using only the first five scattered waves gives good agreement with the previous result at a distance of $57a$ from the origin of a cylinder of radius a . That is, the pattern of the scattered sound intensity is almost similar to the previous result presented by Morse (1936) and Morse & Ingard (1986) only when $M = 5$. However this series has not converged for m th order and consideration needs to be given to more scattered waves in the series that depend on the argument ka in the *Bessel function of first* (J_m), *second* (N_m) and *third* (H_m) *kinds* respectively. The values of J_m , N_m and H_m for different values of ka are given in Tables A1 to A8 respectively, in *Appendix A*. It has been found that for this case, using the trial and error calculations between the results for successive values of m , the series calculation required 12 terms before the phase angles, γ_m , and the velocity potential, ψ_m^s , become infinitesimally small. For the trial and error calculations the tolerance used was $1e^{-7}$. The characteristic behaviours of γ_m and ψ_m^s (similar to A_m) have already been shown in Figures 3.17 (a-b) and 3.18 (a-b) respectively for various values of ka . When γ_m and ψ_m^s become infinitesimally small, there will be no additional contribution if more terms are added into the series in equation (4.4). Finally, the intensity result using 11 terms is shown in Figure 4.11. The figure shows that the intensity distribution is almost flat in the front of the cylinder, which shows significant difference to the result shown by Morse (1936) and Morse & Ingard (1986) presented in Figure 4.10. This is due to the influence of the additional terms that have been added in the series. However, if the tolerance is decreased to $1e^{-12}$, the series calculation requires 17 terms, but there is no effect on the intensity pattern, as shown in Figure 4.12. The result using 17 terms satisfies the characteristic

behaviours of γ_m and ψ_m^s , discussed in Section 3.3.3 in Chapter 3, and indicates that the tolerance $1e^{-7}$ is enough for the series calculation for every particular frequency. The scattered sound intensity fluctuation with various azimuthal angles for the aforementioned case is also shown in Cartesian figure 4.13. From the results presented in Figures 4.11 to 4.13, it can be seen that very high scattered peak appears in the backward direction of the cylinder. The reason for this is reinforcement that occurs at the back of the cylinder due to diffracted waves around each side of the cylinder. The scattered wave is spread more or less uniformly over all other forward directions of the cylinder.

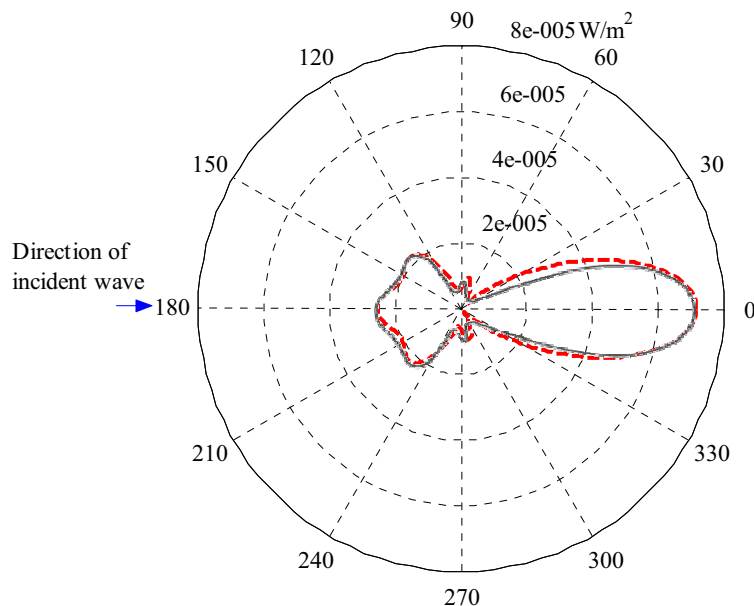


Figure 4.10: Directivity patterns of the scattered sound intensity at a distance of $r = 57a$ from the origin of a cylinder of radius a , for $ka = 5$ and $M = 5$. The red (dash line) and black (solid line) lines show the current and the previous (Morse, 1936; Morse & Ingard, 1986) results respectively. [Incident pressure magnitude $P^o = 1\text{Pa}$]

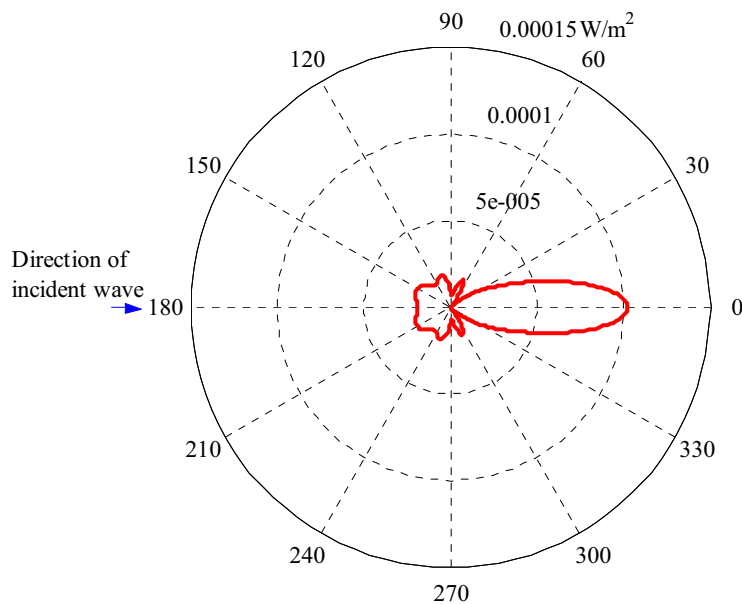


Figure 4.11: Directivity pattern of the scattered sound intensity at a distance of $r = 57a$ from the origin of a cylinder of radius a , for $ka = 5$ and $M = 12$. [Incident pressure magnitude $P^o = 1 \text{ Pa}$]

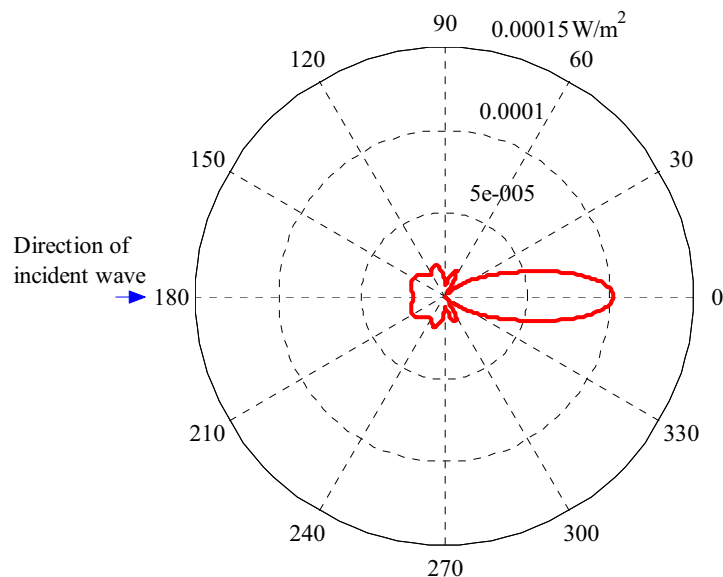


Figure 4.12: Directivity pattern of the scattered sound intensity at a distance of $r = 57a$ from the origin of a cylinder of radius a , for $ka = 5$ and $M = 17$. [Incident pressure magnitude $P^o = 1 \text{ Pa}$]

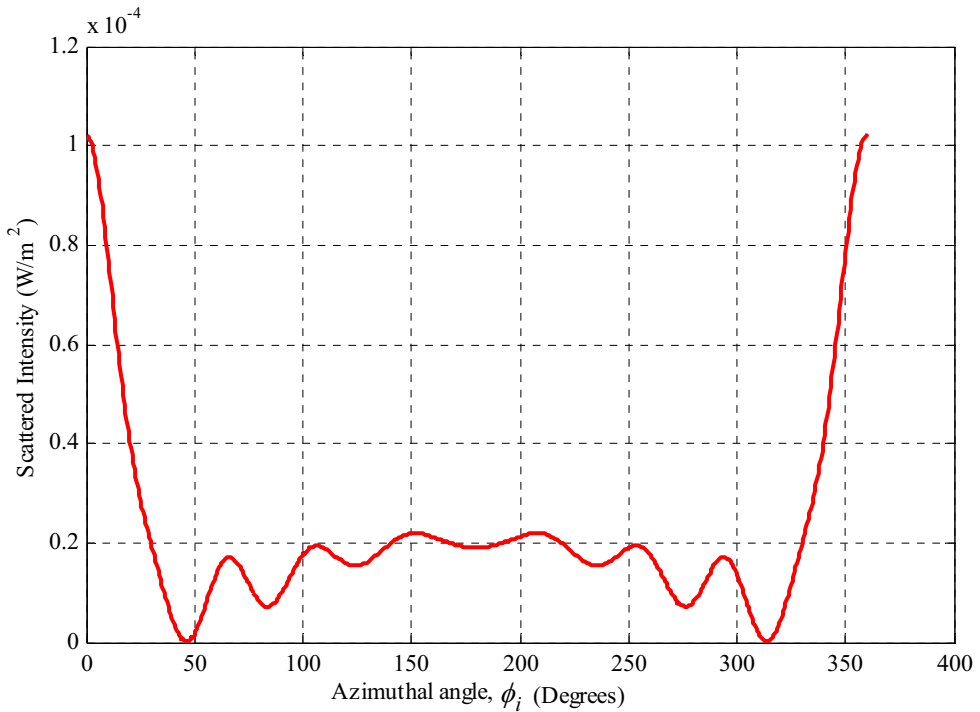


Figure 4.13: Scattered sound intensity fluctuations with various azimuthal angle at a distance of $r = 57a$ from the origin of a cylinder of radius a , for $ka = 5$ and $M = 12$. [Incident pressure magnitude $P^o = 1 \text{ Pa}$]

4.3.2.2 Case II and Case III (Medium and Large Wavelength)

For the cases when $\lambda=2\pi a/3$ and $\lambda=2\pi a$, the same technique was applied for the comparison of intensity with the previous results presented by Morse (1936) and Morse & Ingard (1986) at a distance of $57a$ from the origin of a cylinder of radius a . The comparisons are shown in Figures 4.14 and 4.15, where the results have been scanned from Morse & Ingard (1986) and the current results overlaid. For each case, using the trial and error calculations between the results for successive values of m , the series required 8 and 6 terms respectively, until γ_m and ψ_m^s become infinitesimally small. For the trial and error calculations the tolerance used was $1e^{-7}$. Again the terms required for each case satisfy the characteristic behaviours of γ_m and ψ_m^s presented in Figures 3.17(a-b) and 3.18(a-b), in Chapter 3. For case II, the current result shows quite a different pattern than the previous

result (Morse, 1936; Morse & Ingard, 1986). In the current result, the scattered waves are not creating a sharp peak in the backward direction of the cylinder, in contrast with the previous result. For case III, there is good agreement between the results. The intensity is uniformly distributed in the forward direction of the cylinder and there is very little scattering in the backward direction of the cylinder. This result indicates that the former derivations may be useful for small values of ka , since few terms are required for small ka in the calculations. The variations in intensity with various azimuthal angles for both cases are also shown in Figure 4.16. The total terms required for each case examined are summarised in Table 4.4. It should be take into account that for accurate results the number of terms should not be less than that required for γ_m and A_m to become infinitesimally small as shown in Figures 3.17(a-b) and 3.18(a-b), in Chapter 3.

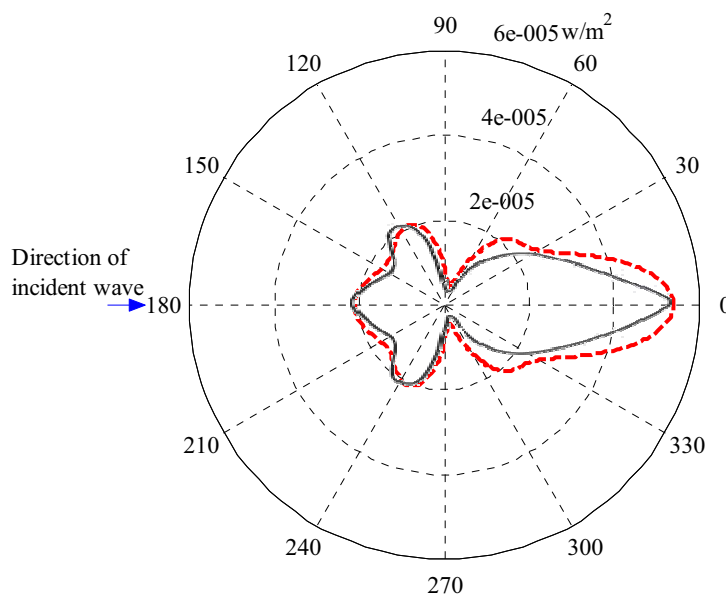


Figure 4.14: Directivity patterns of the scattered sound intensity at a distance of $r = 57a$ from the origin of a cylinder of radius a , for $ka = 3$ and $M = 8$. The red (dash line) and black (solid line) lines show the current and the previous (Morse, 1936; Morse & Ingard, 1986) results respectively. [Incident pressure magnitude $P^o = 1\text{ Pa}$]

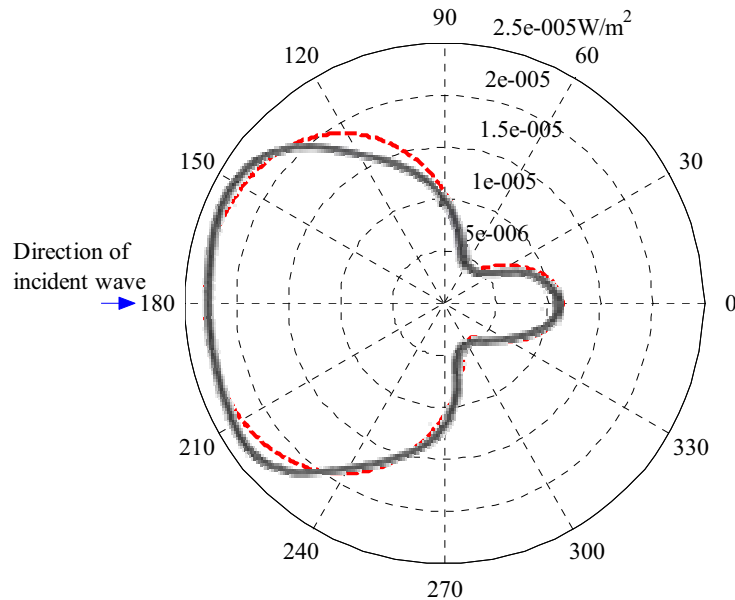


Figure 4.15: Directivity patterns of the scattered sound intensity at a distance of $r = 57a$ from the origin of a cylinder of radius a , for $ka = 1$ and $M = 6$. The red (dash line) and black (solid line) lines show the current and the previous (Morse, 1936; Morse & Ingard, 1986) results respectively. [Incident pressure magnitude $P^o = 1 \text{ Pa}$]

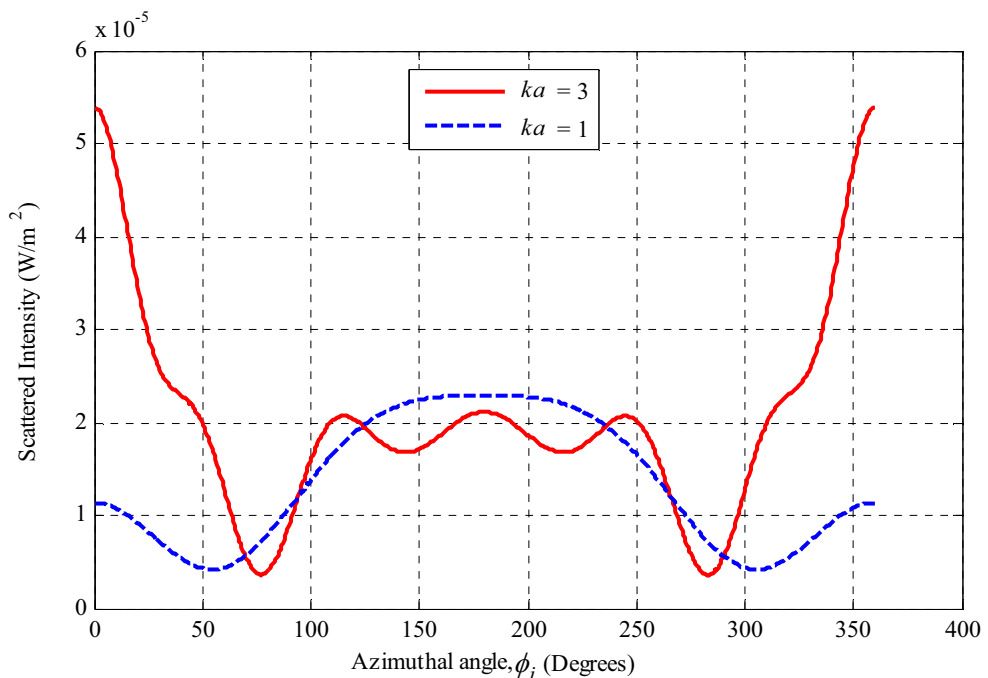


Figure 4.16: Scattered sound intensity with various azimuthal angles at a distance of $r = 57a$ from a cylinder of radius a , for $ka = 3$ and $ka = 1$. [Incident pressure magnitude $P^o = 1 \text{ Pa}$]

Case	Wavelength, λ (m)	ka	Total number of terms, M , needed to achieve a relative error $< 1e^{-7}$
I	$2\pi a/5$	5	12
II	$2\pi a/3$	3	8
III	$2\pi a$	1	6

Table 4.4: Total number of terms required in the series calculation in equation (4.4), for scattered sound intensity.

4.4 Conclusions

In section 4.2, a suitable mathematical model has been presented which predicts the scattered and total sound pressure fields at locations away from the surface of the cylinder due to incident plane waves that strike normal to the circumference of the cylinder. This model is suitable for both near-field and far-field calculations of the sound pressure field.

In section 4.3, the current model has been compared with Junger & Feit (1993). The comparisons show that there are no significant differences between the results obtained using the current derivations and those using Junger & Feit (1993).

The current model has also been compared with Morse (1936) and Morse & Ingard (1986). Both scattered sound pressure and intensity fields have been compared, and it was shown that the previous mathematical derivations were not suitable for near-field calculations. It was also shown that the previous intensity results were not correct. The use of the asymptotic form of the *Hankel function* is the main reason for the limitations of the previous work.

The near-field and far-field sound pressures of a cylinder will be used in Chapter 8 to verify the Boundary Element Method (BEM) technique.

Chapter 5

Sound Pressure at the Surface of a Cylinder Due to a Point Source and Line Source

5.1 Introduction

For the launch environment of a launch vehicle, the identification of source position and strength are necessary to determine the external sound pressure excitations on the vehicle. Thus it is important to consider these in the theoretical modelling. Unfortunately, the theories described so far are not able to do that. Previously the source had been assumed to be at an infinite distance from the cylinder; also there is no scope in these theories to consider the decay of source strength due to wave propagation. Therefore, effort has been spent here to modify the existing theories to make them applicable for finite distance of source position and decay of source strength due to wave propagation.

In this chapter, the modification of the theory to predict the sound pressure at the surface of a cylinder due to a point source positioned at a finite distance has been undertaken. The sound pressure due to a point source positioned inclined with respect to a cylinder coordinates has also been discussed. Finally, further modification of the theory has been derived to predict the sound pressure at the surface of a cylinder due to a line source. All these modifications have been done using the *Green's function* and will be discussed accordingly.

5.2 Green's Function

The *Green's function* gives the solution of the inhomogeneous *Helmholtz equation*. The inhomogeneous *Helmholtz equation* given in equation (3.6) in Chapter 3, can be derived using *Green's function* as follows (Pierce, 1981; Fahy & Walker, 1998):

$$(\nabla^2 + k^2)G(\mathbf{a}|\mathbf{r}') = -4\pi\delta(\mathbf{a} - \mathbf{r}'), \quad (5.1)$$

where $G(\mathbf{a}|\mathbf{r}')$ represents the *Green's function* and gives the sound pressure field at a point due to a monopole source; \mathbf{a} is the observation point and \mathbf{r}' is the source distance.

5.3 Monopole or Point Source

For the following development, the use of a monopole or point source is essential. A point source occurs when the size of the source is small compared with the wavelength, that is $ka \ll 1$. The sound pressure at a point due to a monopole or point source in an unbound medium can be given using the free space *Green's function* and equation (5.1) reduces to (Filippi *et al.*, 1999)

$$G(R) = \frac{e^{ikR}}{4\pi R}, \quad (5.2)$$

where $R = |\mathbf{a} - \mathbf{r}'|$ is the distance between the point source and observation point.

5.4 Sound Pressure Due to a Point Source

Consider a point source placed at a distance \mathbf{r}' from the origin of the cylinder as shown in Figure 5.1, where $\phi_i = 0^\circ$ and $\phi_i = 180^\circ$ from the positive x axis are the back and front of the

cylinder respectively. The first task is to find the distance between the point source and the observation point at the surface of the cylinder. Each observation point at the surface of the cylinder will have an azimuthal angle ϕ_i . The distances between the point source and the i th observation point at the surface of the cylinder can be calculated by using trigonometric formula considering a polar coordinate system as follows:

$$R_i = \sqrt{a^2 + r'^2 - 2ar'\cos\phi_i} . \quad (5.3)$$

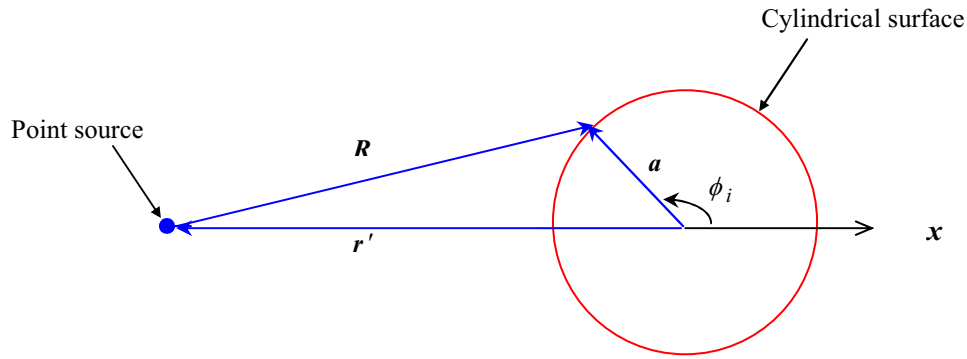


Figure 5.1: Geometry of the sound pressure field due to a point source for two-dimensional coordinate axes.

Now a spatially dependent factor can be considered, which can give the solution for the sound pressure produced by a point source, as a function of distance between the point source and observation points at the surface of the cylinder. This spatially dependent factor can be written as (Morse, 1936; Fahy, 1987)

$$P'(R_i) = -i\omega\rho_o \frac{Q_s}{4\pi R_i} e^{ikR_i} , \quad (5.4)$$

where ω is the angular frequency, ρ_o is the density of air and Q_s is the source strength. The source strength Q_s is defined as a complex volume velocity amplitude. In general, it is a known or estimated parameter but the unknown is the resultant sound pressure at the

surface of the cylinder due to a point source. Hence, the total resultant sound pressure at the surface of the cylinder due to a point source can be expressed using equations (5.4) and (3.18) as follows:

$$P_a^t(R_i, a, k, \phi_i, Q_s) = P'(R_i) \sum_{m=0}^{M-1} \varepsilon_m i^m \cos(m\phi_i) [J_m(ka) - i e^{-i\gamma_m} \sin \gamma_m H_m(ka)], \quad (5.5)$$

where the incident pressure amplitude P^O in equation (3.18) has been replaced by equation (5.4). Equation (5.5) is similar in form to equation (3.18). The difference is that equation (5.5) can consider a source at a finite distance from the cylinder. Suppose a point source of complex strength, $Q_s = 1 + i \text{ m}^3/\text{s}$, is placed at a distance of $r' = -3a$ (three times the cylinder radius) from the origin of a cylinder of radius $a = 1.23\text{m}$ (Boeing cylinder radius) in the $\phi_i = \pi$ direction, as shown in Figure 5.1. The total resultant sound pressure calculated using equation (5.5) at the surface of the cylinder due to this point source is shown in Figure 5.2, where the result using equation (3.18) is also shown for comparison. The comparison of these results shows that there is a difference in sound pressure amplitudes between the two results. This difference is due to the consideration of the spatially dependent factor $P'(R_i)$ in equation (5.5), which is more realistic for a source at a finite distance from the cylinder than the former equation. In the real case, the total sound pressure magnitude at the surface of a cylinder will depend on the source distance and strength. The total sound pressure magnitude will reduce as the distance of the source from the origin of the cylinder increases. Figure 5.3 shows the differences in the total sound pressure magnitudes per doubling of the distance of the source from the origin of the cylinder. The pressure magnitudes at the surface of the cylinder vary by approximately 5dB to 8dB over the cylinder circumference due to the increase of source distance. Without

the cylinder present, the sound pressure at the centre of the cylinder would reduce by 6dB per doubling of source distance. Note that with the cylinder present, the sound pressure magnitudes at the surface of the cylinder varying by approximately 5dB to 8dB per doubling of source distance because there is a scattered sound pressure in addition with the incident sound pressure. Also, at the back of the cylinder, reinforcement occurs between the diffracted waves around each side of the cylinder, which added with the sound pressure magnitudes. This is why the difference in the sound pressure magnitudes for each case is approximately 5dB at the back of the cylinder per doubling of source distance. The directivity patterns of the total sound pressure at the surface of the cylinder of radius a due to a point source positioned at distances of $-3a$, $-6a$ and $-12a$, respectively, are also shown in Figure 5.4. The figure shows clearly that the sound pressure directivity pattern at the surface of a cylinder for a particular value of ka will not change due to the variation of source distance, but the sound pressure magnitude will vary depending on the source distance and strength.

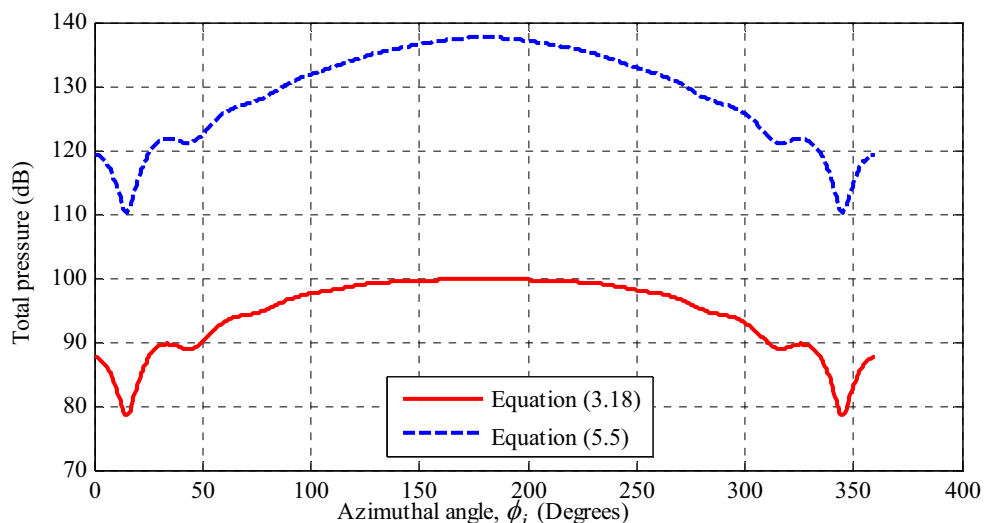


Figure 5.2: Total sound pressure at the surface of a cylinder of radius $a = 1.23\text{m}$ (Boeing cylinder radius), calculated using equations (3.18) and (5.5), for $ka = 5$ and $r' = -3a$. [Source strength, $Q_s = 1 + i \text{ m}^3/\text{s}$ and reference pressure $20\mu\text{Pa}$]

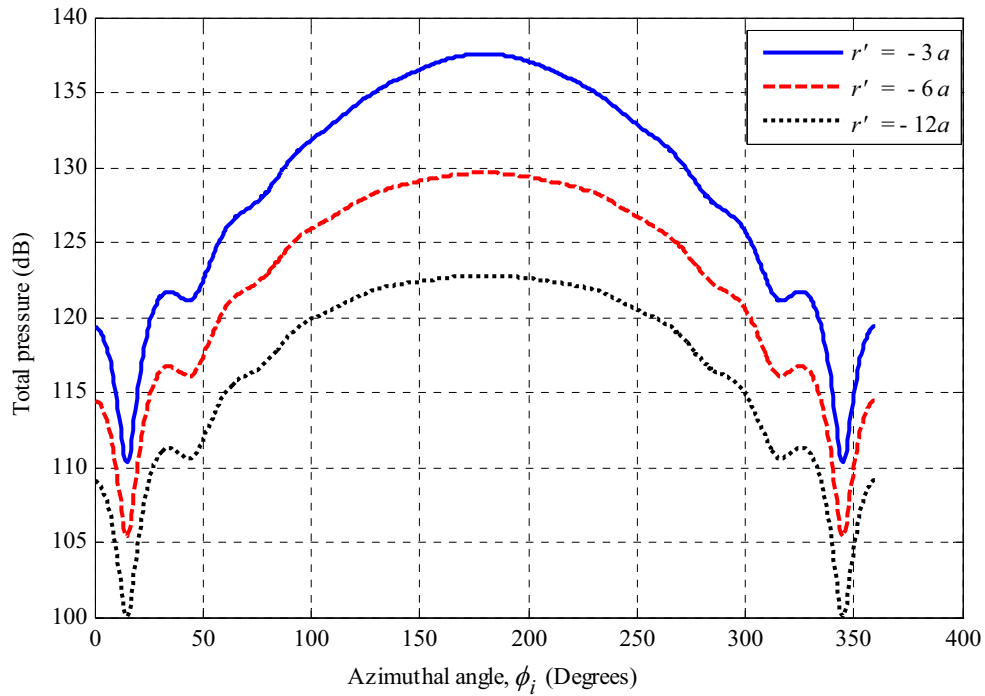


Figure 5.3: Total sound pressure at the surface of a cylinder of radius $a = 1.23\text{m}$ (Boeing cylinder radius), due to a point source positioned at various distances from the origin of the cylinder, for $ka = 5$. [Source strength, $Q_s = 1+i \text{ m}^3/\text{s}$ and reference pressure $20\mu\text{Pa}$]

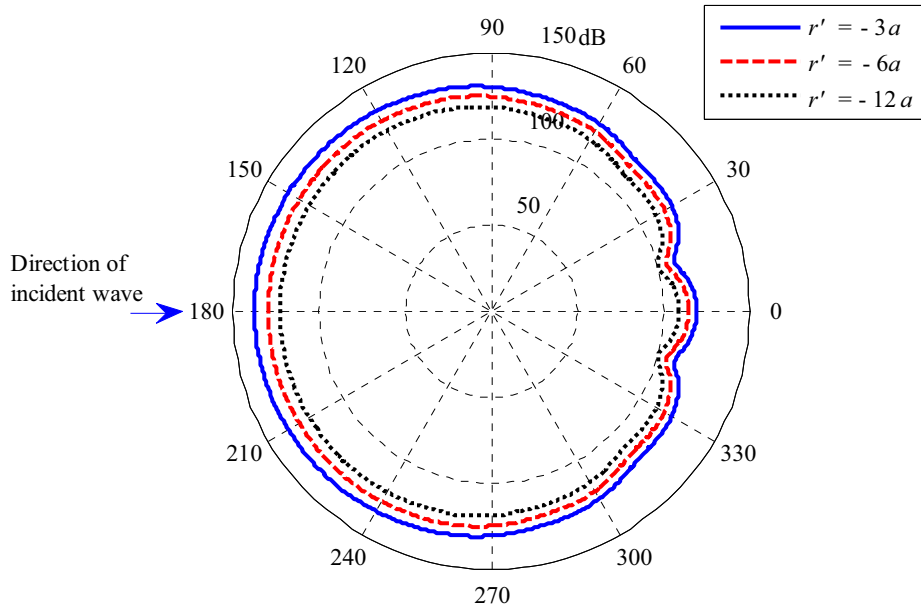


Figure 5.4: Directivity patterns of the total sound pressure at the surface of a cylinder of radius $a = 1.23\text{m}$ (Boeing cylinder radius), due to a point source placed at various distances from the origin of the cylinder, for $ka = 5$. [Source strength, $Q_s = 1+i \text{ m}^3/\text{s}$ and reference pressure $20\mu\text{Pa}$]

5.5 Sound Pressure Due to a Point Source Location Inclined with Respect to the Cylinder Coordinates

In this section, the sound pressure due to a point source of unit complex strength, $Q_s = 1 + i \text{ m}^3/\text{s}$, which is positioned such that its location is inclined with respect to the coordinate axes of a cylinder of radius $a = 1.23\text{m}$ (Boeing cylinder radius) has been investigated. The interest was to see the effects on the sound pressure pattern for such a point source location, and that the resulting sound pressure pattern is rotated about the cylinder origin accordingly. Figure 5.5 shows the source position from which the incident waves are propagating towards the cylinder. Let the source be placed at a distance of $r' = -3a$ (three times the cylinder radius) from the origin of the cylinder and at an angle $\beta = \pi/3$ from the x axis. So the incident waves are impinging on the surface of the cylinder from an inclined angle of $\beta = \pi/3$ with respect to the cylinder origin. The total sound pressure at the surface of the cylinder due to this inclined source can be determined by using the same spatially dependent equation (5.5). Figures 5.6(a-h) show the directivity patterns of the total sound pressure at the surface of the cylinder due to the inclined incident waves for various values of ka . It is possible to show the scattered sound pressure

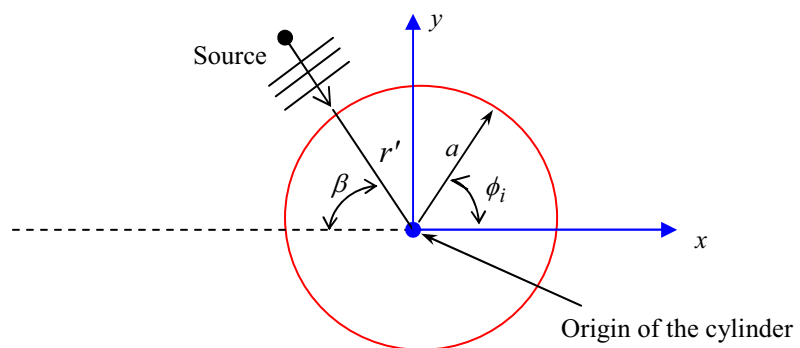
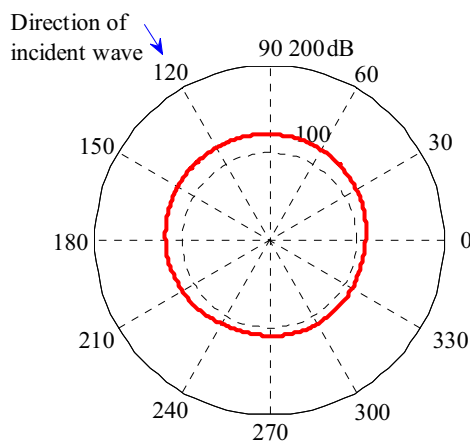
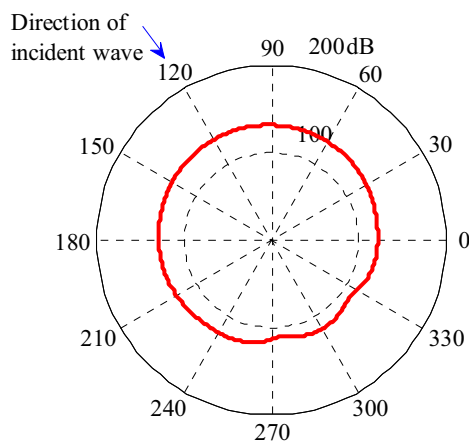
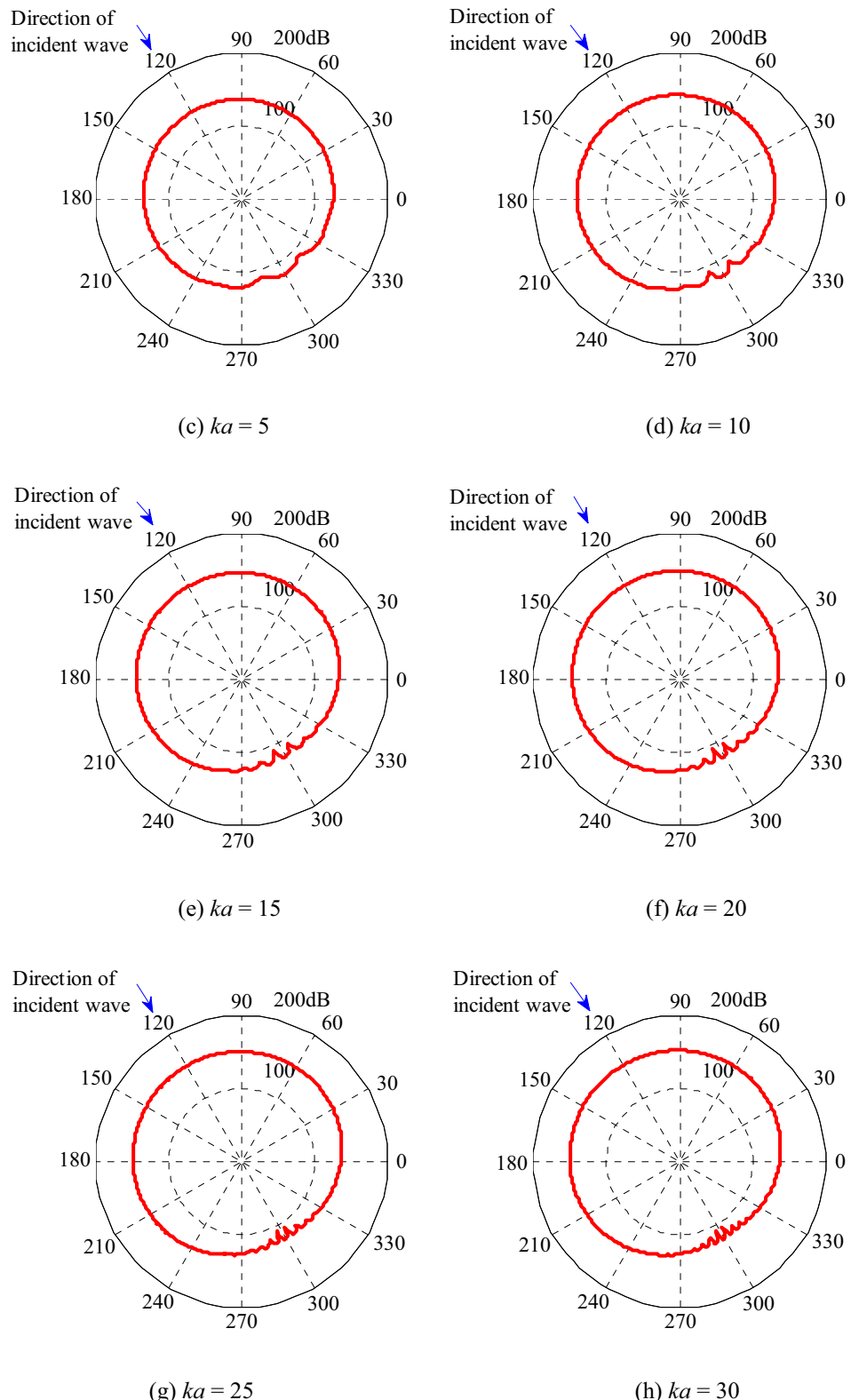


Figure 5.5: Geometry of the inclined point source for two-dimensional cylinder coordinate axes.

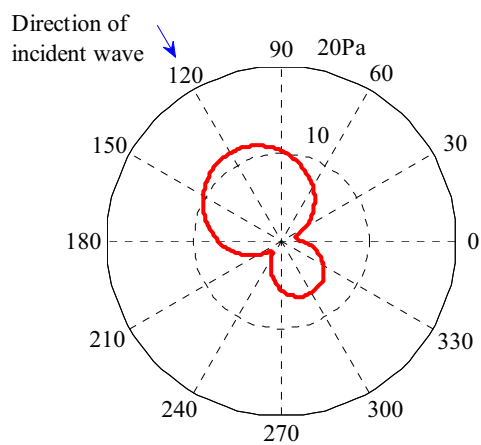
pattern separately due to the inclined incident waves using equations (3.11) and (5.4) for $\beta = \pi/3$. Figures 5.7(a-h) show the directivity patterns of the scattered sound pressure at the surface of the cylinder due to the inclined incident waves for various values of ka . For both scattered and total sound pressure calculations, the spatially dependent factor $P'(R_i)$ in equation (5.5) has been used. This is why the sound pressure magnitudes are greater for these results in contrast to the results that have been presented in Figures 3.12(a-h) and 3.7(a-h) in Chapter 3, where unit pressure amplitude was arbitrarily considered to determine the sound pressure on the cylinder. However, the sound pressure amplitude will vary depending on the value of source strength, Q_s .

Comparison between the results obtained for a point source located on the cylinder coordinate axes and for a point source location inclined with respect to the cylinder coordinate axes, such as those shown in Figures 5.4 and 5.6(c) for $r' = -3a$, reveals that the sound pressure patterns and magnitudes are the same, but rotated about the cylinder origin by the angle of inclination, β .

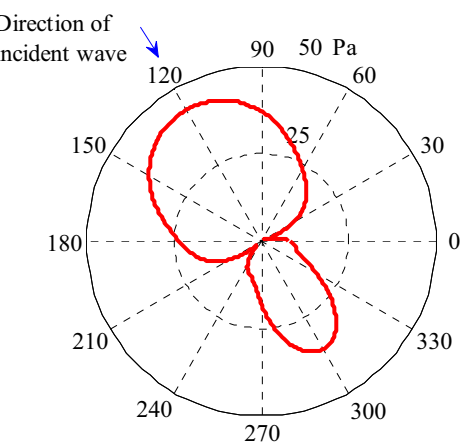
(a) $ka = 1$ (b) $ka = 3$



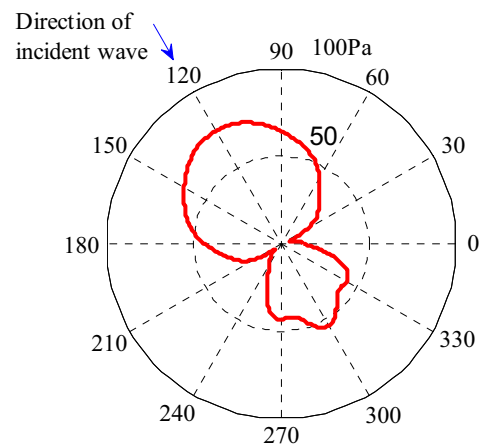
Figures 5.6(a-h): Directivity patterns of the total sound pressure due to inclined incident waves for various values of ka at the surface of a cylinder of radius $a = 1.23\text{m}$ (Boeing cylinder radius). The source of strength $Q_s = 1+i \text{ m}^3/\text{s}$ is placed at an angle $\beta = \pi/3$ from the x axis (see Figure 5.5) and at a distance of $r' = -3a$ from the origin of the cylinder. [Reference pressure $20\mu\text{Pa}$]



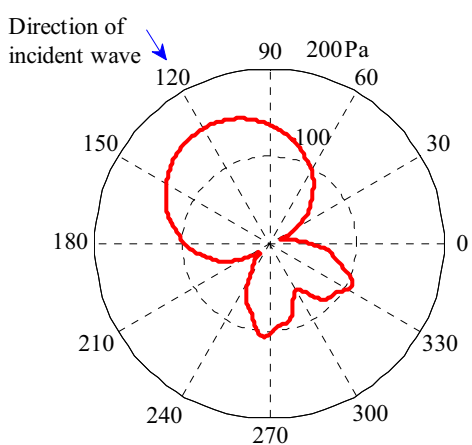
(a) $ka = 1$



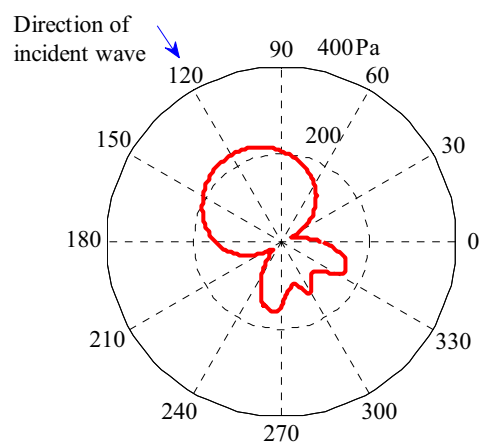
(b) $ka = 3$



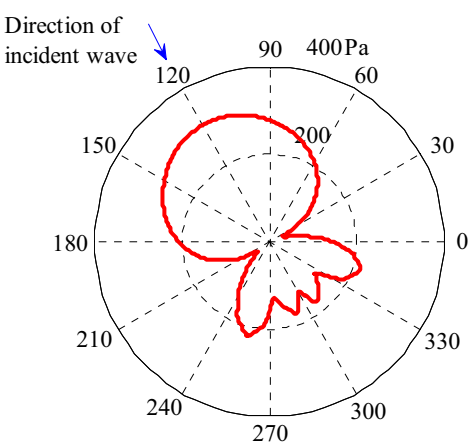
(c) $ka = 5$



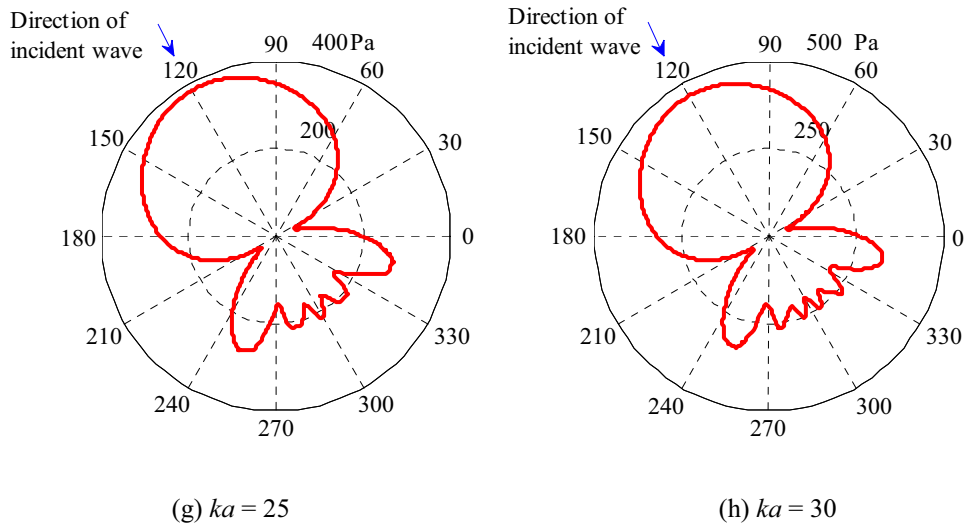
(d) $ka = 10$



(e) $ka = 15$



(f) $ka = 20$



Figures 5.7(a-h): Directivity patterns of the scattered sound pressure due to inclined incident waves for various values of ka at the surface of a cylinder of radius $a = 1.23\text{m}$ (Boeing cylinder radius). The source of strength $Q_s = 1+i \text{ m}^3/\text{s}$ is placed at an angle $\beta = \pi/3$ from the x axis (see Figure 5.5) and at a distance of $r' = -3a$ from the origin of the cylinder.

5.6 Sound Pressure Due to a Line Source

The total sound pressure at the surface of a cylinder due to a linear array of point sources acting as a line source has been investigated in this section. In the actual launch case, the sources along the exhaust flow are normally considered as a line source. The concept for a line source has been adapted from Bies & Hansen (2003), where both a finite and infinite line source have been described. Figure 5.8 shows an arrangement of point sources lying on the negative x axis along a line normal to the cylinder; where b is the distance between each of the sources and d is the distance between the nearest source and the cylinder surface.

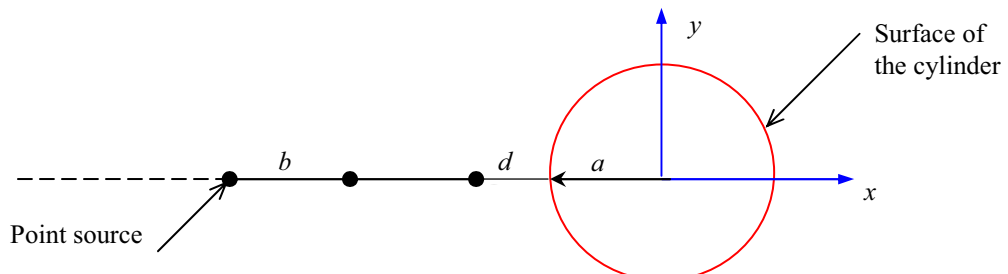


Figure 5.8: Geometry of the line source for two-dimensional cylinder coordinate axes.

Let there be in total N point sources. The distance from the centre of the cylinder to each source can be calculated as

$$r_n = (nb + d + a), \quad (5.6)$$

where a is the radius of the cylinder and n is the source number. Using equation (5.6), the spatially dependent factor can be determined for each of the sources as discussed previously in section 5.4. So the equation (5.5) finally becomes for N sources

$$P'_a(R_i, k, a, \phi_i, Q_s) = \sum_{n=0}^{N-1} P'(R_i) \sum_{m=0}^{M-1} \varepsilon_m i^m \cos(m\phi_i) [J_m(ka) - i e^{-i\gamma_m} \sin \gamma_m H_m(ka)]. \quad (5.7)$$

Equation (5.7) considers the source nearest to the cylinder surface as $n = 0$. If d also becomes zero, the equation would assume that the first source is on the surface of the cylinder.

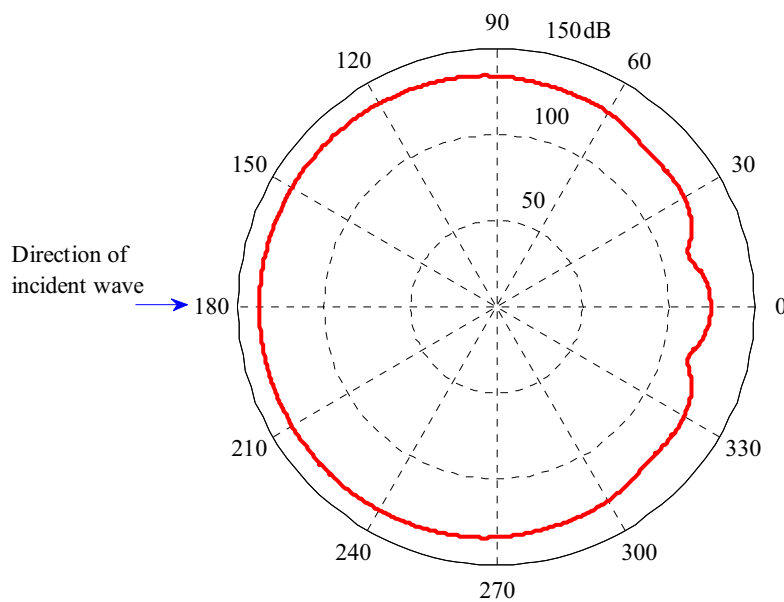
Let us consider 15 point sources placed along the negative x axis. The distance between each of them is 1.5m. The distance of the nearest source from the surface of the cylinder (radius, $a = 1.23\text{m}$) is 1m. Each source is generating the same frequency. Different arbitrary complex strengths have been chosen for each source as shown in Table 5.1. In general, for the actual launch case, all the sources along the exhaust line will be of different strengths and relative phases, which is the reason that different arbitrary complex strengths are chosen for each source. The resultant sound pressure due to the 15 point sources of arbitrary strengths acting as a line source is shown in Figure 5.9 for the case $ka = 5$. The figure shows that a line source with arbitrary amplitudes and phases does not change the total sound pressure pattern at the surface of a cylinder compared with Figure

5.4, which shows the result for a single point source for $ka = 5$. Only the total sound pressure magnitudes are affected depending on the distance of each source, source strengths and number of sources. This is because the individual sources of the line source can be considered to combine to one equivalent source for excitation at a single frequency.

However, the situation described above does not fit with the actual launch situations, where it can be expected that each of the sources is generating a different frequency. Consider the same fifteen sources and their arrangement described in the preceding paragraph, having the same source strengths as given in Table 5.1, but with frequencies distributed from 50Hz to 400Hz, where the closest source generates 50Hz, with the frequency of excitation increasing of 25Hz for each source until at the farthest source it is 400Hz. The resulting sound pressure due to the line source consisting of 15 point sources of different arbitrary amplitudes and frequencies is shown in Figure 5.10. The result shows that the pressure pattern and pressure amplitude are different compared with the result presented in Figure 5.9, for the line source of same frequency. The reason is the use of different frequencies and as the frequency increases the interference of the diffracted waves around two sides of the cylinder increases at the back of the cylinder; resulting more pressure fluctuation at the back of the cylinder.

A detailed examination of the characteristics of the noise sources for an exhaust plume at launch is beyond the scope of the current examination; however, the work presented here allows the total sound pressure at the surface of the cylindrical launch vehicle to be determined given the strengths and locations at the source distribution.

Source Number	Source Strength, Q_s
1	-10.354 - 8.788i
2	-3.2172 - 3.1019i
3	7.5915 - 1.8143i
4	7.982 - 5.8757i
5	-3.2182 - 18.933i
6	7.398 + 4.3279i
7	4.9357 + 8.1667i
8	3.9313 - 7.6881i
9	16.047 + 1.5075i
10	-0.28561 - 8.4273i
11	4.245 + 13.448i
12	1.2148 - 8.0121i
13	8.354 - 5.7843i
14	-0.43143 + 9.042i
15	-11.497 + 5.4793i

Table 5.1: Arbitrary strengths for fifteen point sources.**Figure 5.9:** Directivity pattern of the total sound pressure at the surface of a cylinder of radius $a = 1.23\text{m}$ (Boeing cylinder radius) due to a line source of different arbitrary amplitudes and phases (see table 5.1), for $ka = 5$. [Reference pressure $20\mu\text{Pa}$]

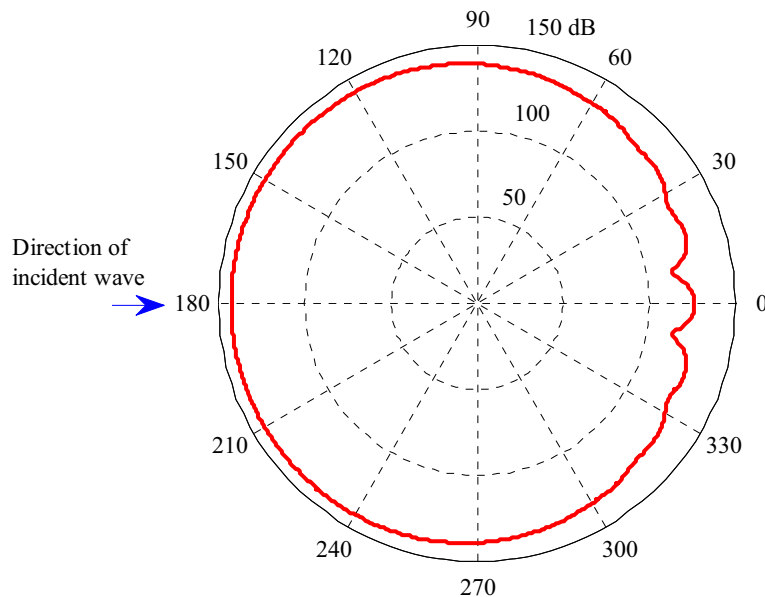


Figure 5.10: Directivity pattern of the total sound pressure at the surface of a cylinder of radius $a = 1.23\text{m}$ (Boeing cylinder radius) due to a line source of different arbitrary amplitudes and phases (see Table 5.1) with distributed frequencies from 50 Hz to 400Hz. [Reference pressure $20\mu\text{Pa}$]

5.7 Conclusions

In section 5.4, a method to calculate the sound pressure at the surface of a cylinder due to a point source positioned at a finite distance from the cylinder has been described. This method is similar to the method described in section 3.3.3 in Chapter 3, but differs in that the current method can consider the source at a finite distance rather than at an infinite distance from the cylinder. The current method can also consider the decay of source strength due to wave propagation. Comparing the results using a point source at various finite distances from the cylinder, it has been shown that for a particular frequency the sound pressure magnitudes at the surface of a cylinder will vary due to the source position and strength, but the sound pressure pattern will not change.

Using the same method, the sound pressure at the surface of the cylinder due to a point source positioned at an angle with respect to the cylinder coordinate axes has been investigated. For this case, both the scattered and total sound pressure patterns at the surface of the cylinder have been presented for various values of ka . It has been shown that for a particular frequency, there is no difference between the sound pressure patterns obtained for a point source located on the cylinder coordinate axes and for a point source location inclined with respect to the cylinder coordinate axes, but the sound pressure pattern rotated about the cylinder origin by the angle of inclination, β .

The method has been further modified for a line source. The sound pressure patterns at the surface of the cylinder due to a line source which has 15 point sources of different arbitrary strengths have been investigated analytically for two cases: all of the point sources having the same frequency ($ka = 5$); and different frequencies from 50Hz to 400Hz. The results revealed that for both cases the sound pressure patterns are different.

The method described in this chapter will be compared with the experimental results in the next chapter. It will be further modified to investigate the sound pressure field at the surface of a cylinder due to oblique incident waves in Chapter 7. The method will also be used in Chapter 8 to investigate the Boundary Element Method (BEM) technique.

Chapter 6

Experimental Work

6.1 Introduction

In the previous chapter, theory was derived to predict the sound pressure pattern at the surface of a cylinder for a source positioned at a finite distance from the cylinder. To verify this equation an experiment was conducted in the anechoic chamber at the University of Adelaide to measure the surface sound pressure patterns of an experimental cylinder for various frequencies due to a point source positioned at a finite distance. The purpose of this experiment was to obtain the sound pressure pattern on the cylinder surface only for comparison with the analytical results. Hence the source strength was not taken into account. The scope of this experiment was to determine whether it is possible to analytically predict the sound pressure patterns at the surface of a cylinder due to a source positioned at a finite distance from the cylinder.

6.2 Experimental Arrangement

The experimental arrangement inside the 4.79m x 3.90m x 3.94m anechoic chamber is shown in Figure 6.1. A hard cylindrical PVC tube was used and mounted on a turntable which was used to rotate the cylinder 360° about its longitudinal axis. A B&K 4133 half-inch microphone was placed half way along the cylinder length and inside the experimental cylinder such that the microphone face was flat with the outer surface of the cylinder, as shown in Figure 6.1(b). A loudspeaker was placed approximately 4.1m away

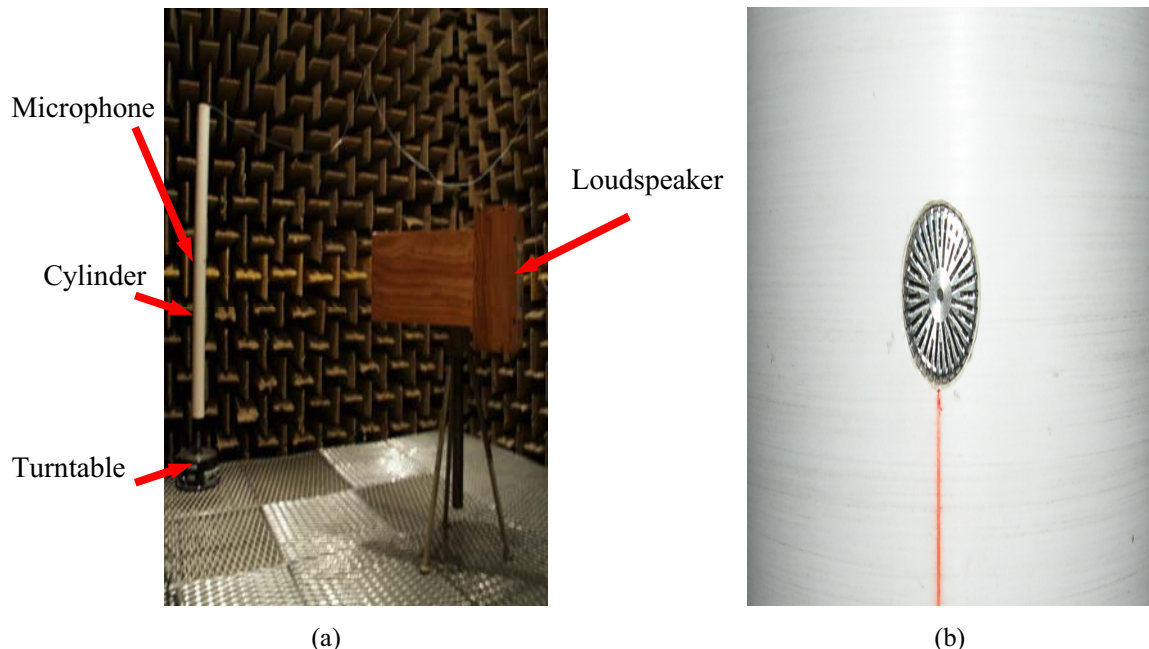


Figure 6.1: (a) Picture of the experimental setup inside the anechoic chamber, (b) picture showing the placement of the microphone inside the experimental cylinder.

Object	Parameter	Value
Experimental cylinder	Overall length	1.446 m
	Outside diameter	0.114 m
	Wall thickness	0.0035 m
Microphone	Height (position from the floor)	≈ 1.13 m
Speaker	Height (speaker centre from the floor)	≈ 1.13 m
	Distance from front face of the cylinder	≈ 4.1 m

Table 6.1: Physical parameters of the experimental setup.

from the cylinder front face and the speaker centre was approximately at the same height as the microphone position. In the experiment the orientation of the microphone directly towards the speaker was chosen to be $180^\circ/-180^\circ$ or the front side of the cylinder where the sound waves impinge directly from the speaker. The specifications of this experimental rig are reported in Table 6.1. The input signal for the loudspeaker was generated by using a Function Generator (Hewlett Packard 3325B) and provided to the loudspeaker through a Power Amplifier (Playmaster Proseries Three). The sound pressure on the surface of the cylinder due to the sound waves produced from the loudspeaker was measured by the B&K 4133 half-inch microphone. The output signal of the microphone was calibrated using a Frequency Analyser (B&K 2120) and measured using Data Acquisition Software known as TracerDAQ for 360° rotation of the cylinder and the embedded microphone.

6.3 Experimental Results and Discussion

The sound pressure at the surface of the experimental cylinder (the length to diameter ratio is 12.7) was measured for excitation frequencies of 700 Hz, 1.5 kHz, 3 kHz and 5 kHz, respectively. The descriptions of each applied frequency in the experiment are given in Table 6.2. The measurements were taken using TracerDAQ (Data Acquisition Software) for each 0.01s interval of the total time of one rotation of the cylinder and the embedded microphone. The sample rate was 100Hz and a total of 8,100 samples were counted for each applied frequency and the results for the various frequencies are shown in Figures 6.2 to 6.5 respectively. The results shown are normalised relative to the measured sound pressure level at 180° . From these results it is interesting to see that the sound pressure amplitude is relatively smoothly varying at the front face ($\phi_i = 180^\circ/-180^\circ$) of the cylinder

and varies more aggressively at the back face ($\phi_i = 0^\circ$) of the cylinder. The reason for this was discussed in Section 3.3.2 in Chapter 3, and is a result of positive and/or negative interference of the two diffracted waves travelling around the two sides of the cylinder. For small values of ka , that is when the wavelength is bigger than the circumferential length of the cylinder, the sound pressure amplitudes vary less at the back of the cylinder due to a lesser amount of interference of the two diffracted waves travelling around the two sides of the cylinder, as shown in Figure 6.2 for $ka = 0.73$ ($f = 700\text{Hz}$). On the other hand, when the value of ka is large, that is when the wavelength is smaller than the circumferential length of the cylinder, the sound pressure amplitudes vary aggressively at the back of the cylinder because the amount of interference of the diffracted waves increases as the value of ka increases, as shown in Figures 6.3 to 6.5 for excitation frequencies of 1.5kHz ($ka = 1.57$), 3kHz ($ka = 3.13$) and 5kHz ($ka = 5.22$) respectively. The minimum frequency of 700 Hz and higher frequencies of 1.5 kHz, 3 kHz and 5 kHz were chosen in the experiment so that differences in the sound pressure variations at the surface of the experimental cylinder could be observed for a range of wavelengths relative to the cylinder circumference, and the theoretical modelling accuracy verified.

Circumferential length of the cylinder (m)	Applied frequency, f (kHz)	Wavelength, λ (m)	ka
0.3581	0.7	0.49	0.73
	1.5	0.2286	1.57
	3	0.1143	3.13
	5	0.0686	5.22

Table 6.2: Descriptions of the applied parameters in the experiment.

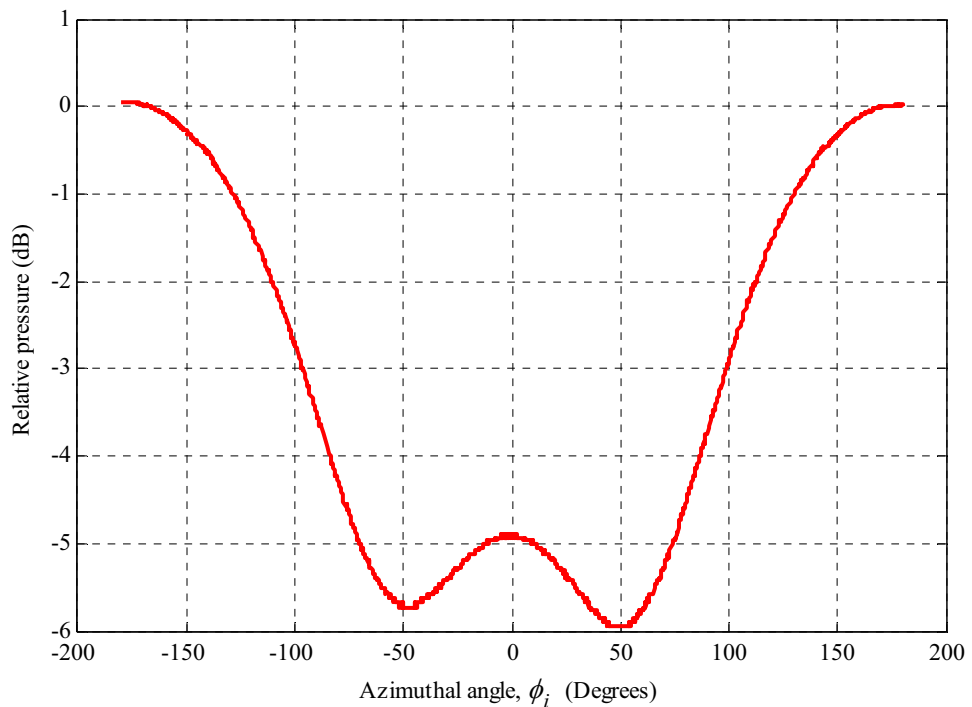


Figure 6.2: Relative sound pressure at the surface of the experimental cylinder, for $f = 700$ Hz and $ka = 0.73$.

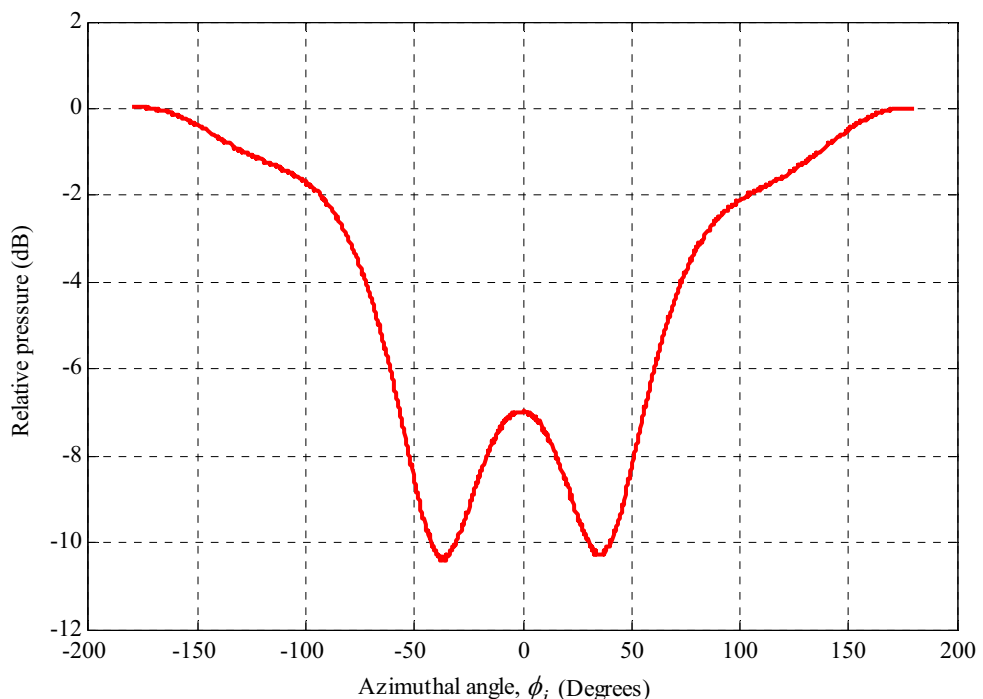


Figure 6.3: Relative sound pressure at the surface of the experimental cylinder, for $f = 1.5$ kHz and $ka = 1.57$.

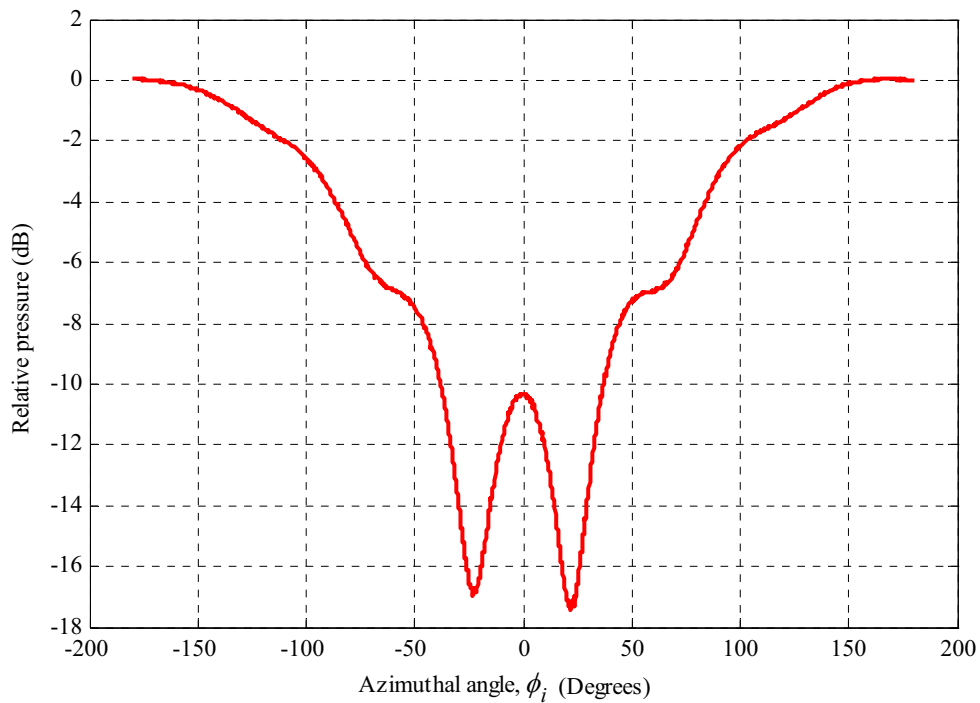


Figure 6.4: Relative sound pressure at the surface of the experimental cylinder, for $f = 3$ kHz and $ka = 3.13$.

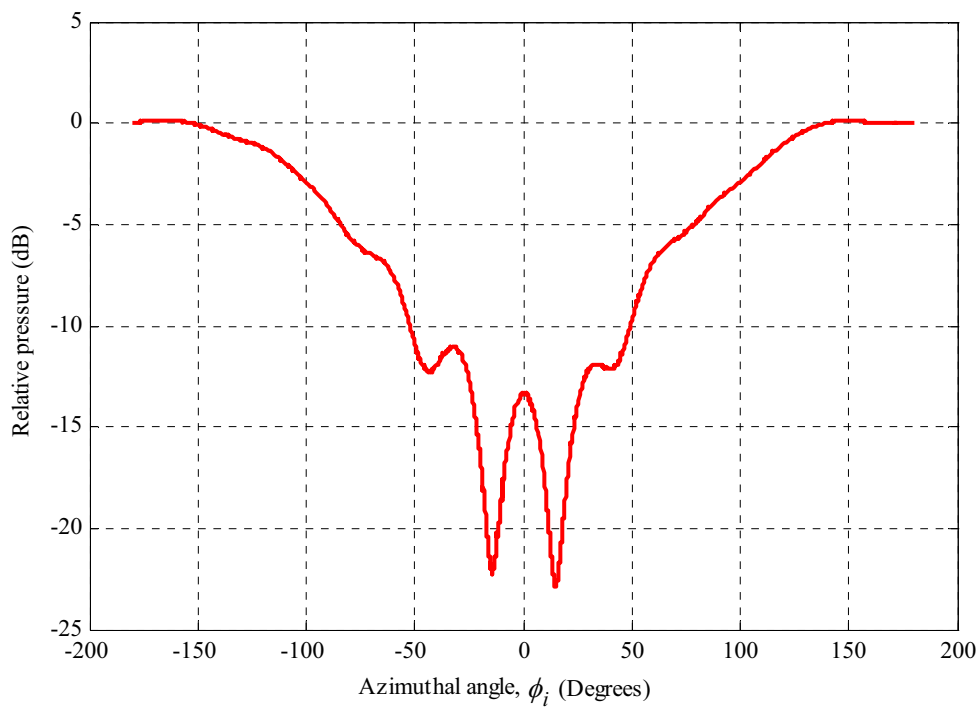


Figure 6.5: Relative sound pressure at the surface of the experimental cylinder, for $f = 5$ kHz and $ka = 5.22$.

6.4 Comparison between Analytical and Experimental Results

The analytical results are compared with the experimental results in this section. Equation (5.5), which was derived in the previous chapter for a point source, has been used here to calculate the analytical results for a point source positioned at a distance of 4.1m from the cylinder as in the experimental arrangement, and compared with the experimental results. Figures 6.6, 6.7, 6.8 and 6.9 show the comparisons between the normalised analytical results and experimental results for various frequencies. Note that the source strength was not measured in the experiment, since the aim of this experiment was to obtain the surface sound pressure patterns for each applied frequency and normalised analytical results are presented here for comparison with the experimental results. The sound pressure at $180^\circ/-180^\circ$ obtained from the experimental result at each frequency was used to normalise the analytical result. The normalised analytical sound pressure directivity patterns are also shown and compared with the experimental results for various frequencies in polar Figures 6.10 to 6.13. To plot the directivity patterns in the polar figures, a reference pressure of 30dB at $\phi_i=180^\circ$ has been used for each applied frequency to normalise the analytical and experimental relative sound pressure distributions presented in Figures 6.6 to 6.9. From these results it can be seen that the analytical results show very good agreement with the experimental results. For each frequency there is no significant difference between the analytical and experimental sound pressure patterns. The only difference between them is in the sound pressure magnitudes in some regions at the lower frequencies, especially at the back region of the cylinder. This is because at the lower frequencies a small amount of sound energy is reflected from the walls of the anechoic chamber and hit the surface of the cylinder, which added with the total amount of

reinforcement and cancellation that occurs between the two diffracted waves passing around each side of the cylinder, results in increased sound pressure amplitudes compared with the analytical results. For higher frequencies almost no sound energy is reflected by the walls and the experimental results show very good agreement with the analytical results. The fibreglass wedges that line the anechoic chamber become more absorptive at higher frequencies compared with the lower frequencies, and the effect of the reflection of sound energy from the walls is not observable in the experimental results at higher frequencies, where the agreement between the experimental results and the analytical results is excellent. In the experimental arrangement the cylinder was placed at one corner of the anechoic chamber, relatively close to the walls, whereas the speaker was placed at the diagonally opposite corner (see Figure 6.1a), to provide the maximum distance between the cylinder and speaker. This type of arrangement was chosen so that the sound waves produced by the speaker become plane waves over the distance from the speaker to the cylinder surface, especially at the lower frequencies where the wavefront is large compared with the higher frequencies. Also, the asymmetry of the experimental results about 0° , such as in Figure 6.6 at $+50^\circ$ and -50° , is a result of the difference in the distances from the anechoic chamber walls to the cylinder centre line, and the contribution of reflections of sound energy from the chamber walls, which affected the total amount of reinforcement and cancellation that occurs between the two diffracted waves passing around each side of the cylinder.

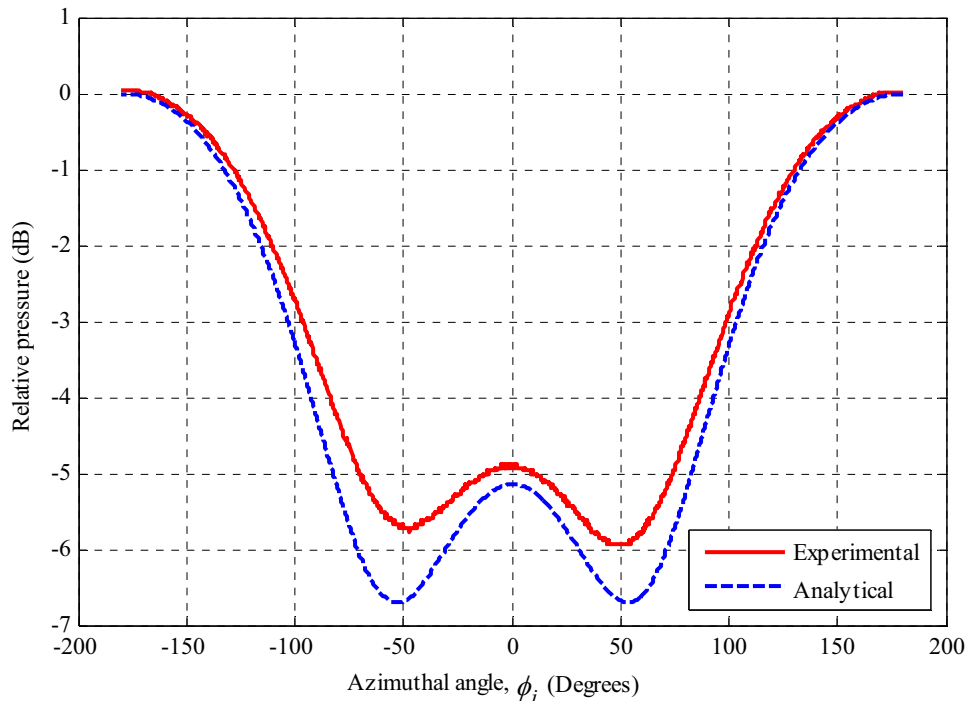


Figure 6.6: Comparison between the experimental and normalised analytical results for relative sound pressure at the surface of the experimental cylinder, for $f = 700$ Hz and $ka = 0.73$.

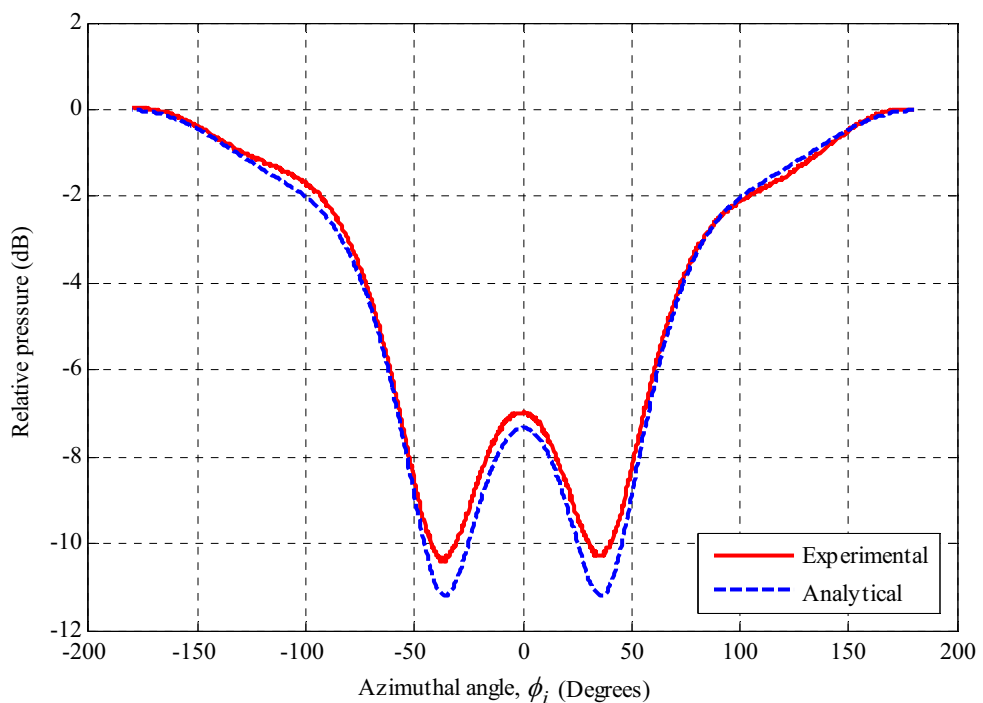


Figure 6.7: Comparison between the experimental and normalised analytical results for relative sound pressure at the surface of the experimental cylinder, for $f = 1.5$ kHz and $ka = 1.57$.

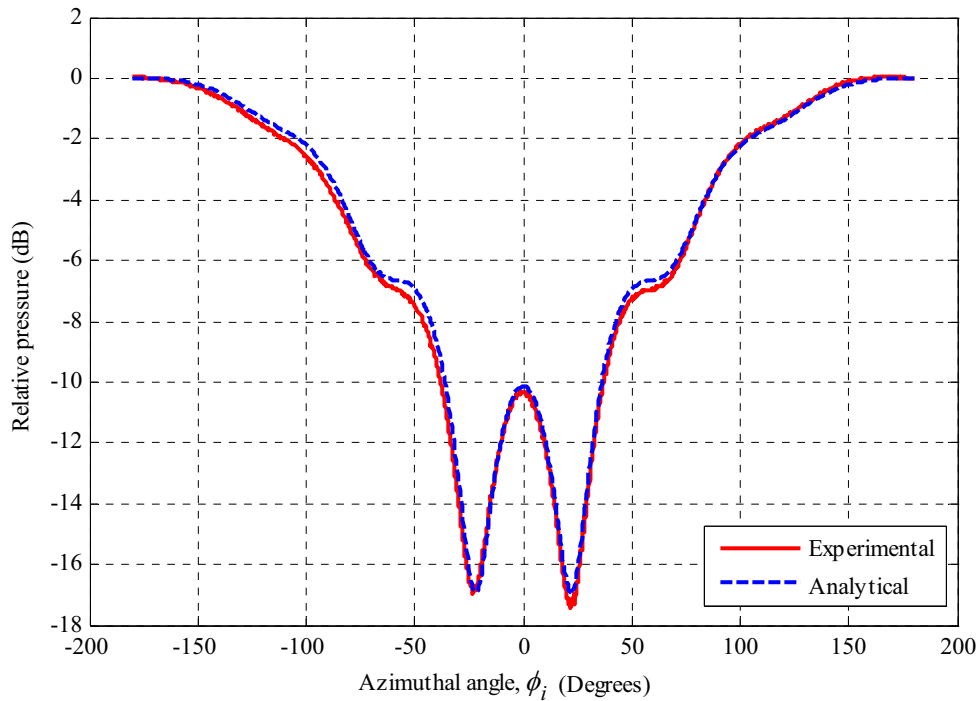


Figure 6.8: Comparison between the experimental and normalised analytical results for relative sound pressure at the surface of the experimental cylinder, for $f = 3$ kHz and $ka = 3.13$.

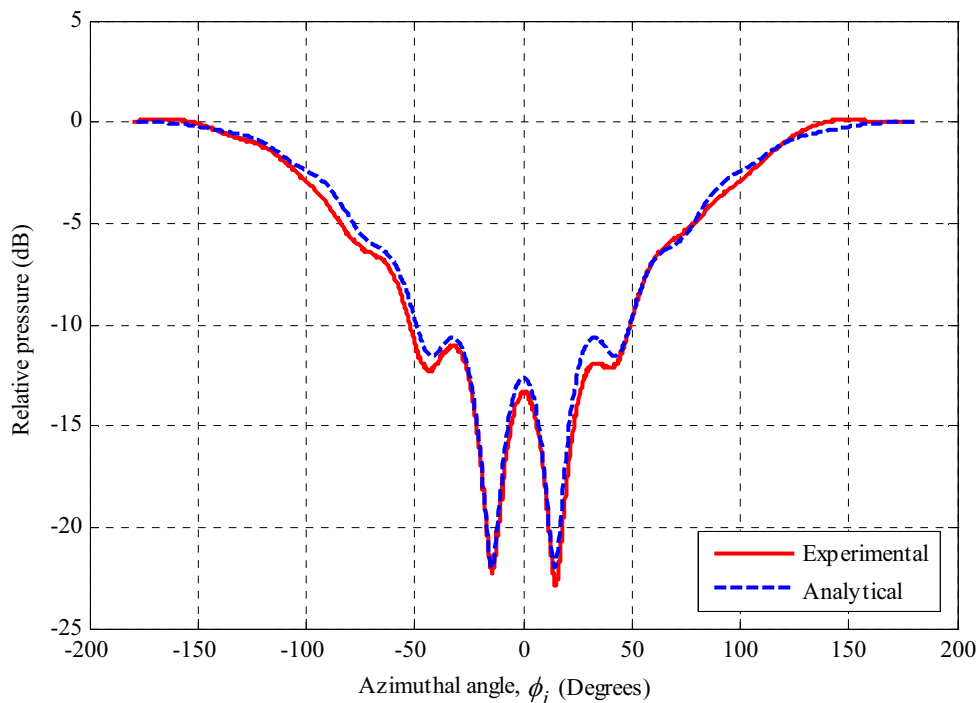


Figure 6.9: Comparison between the experimental and normalised analytical results for relative sound pressure at the surface of the experimental cylinder, for $f = 5$ kHz and $ka = 5.22$.

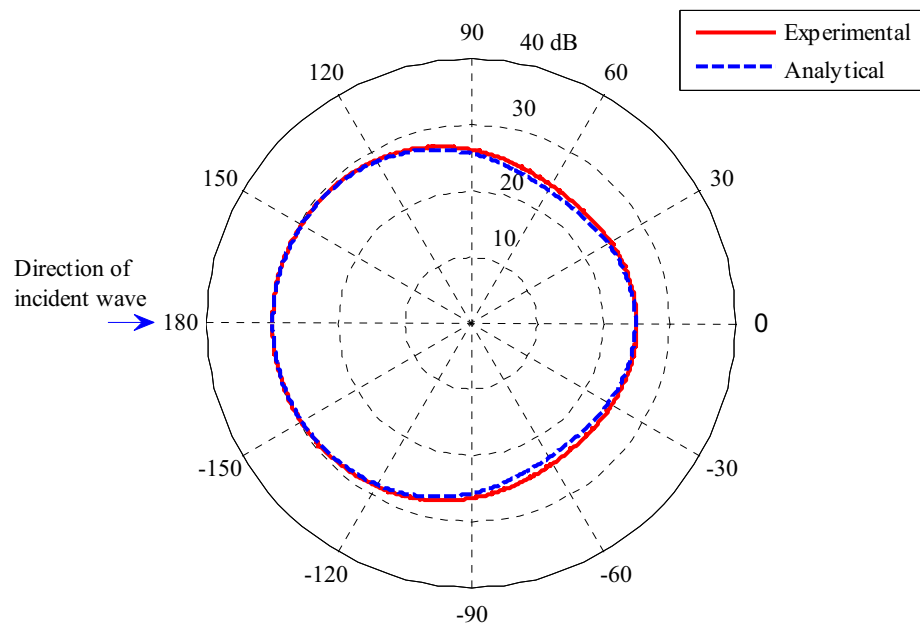


Figure 6.10: Sound pressure directivity comparison between the experimental and normalised analytical results at the surface of the experimental cylinder, for $f = 700$ Hz and $ka = 0.73$.

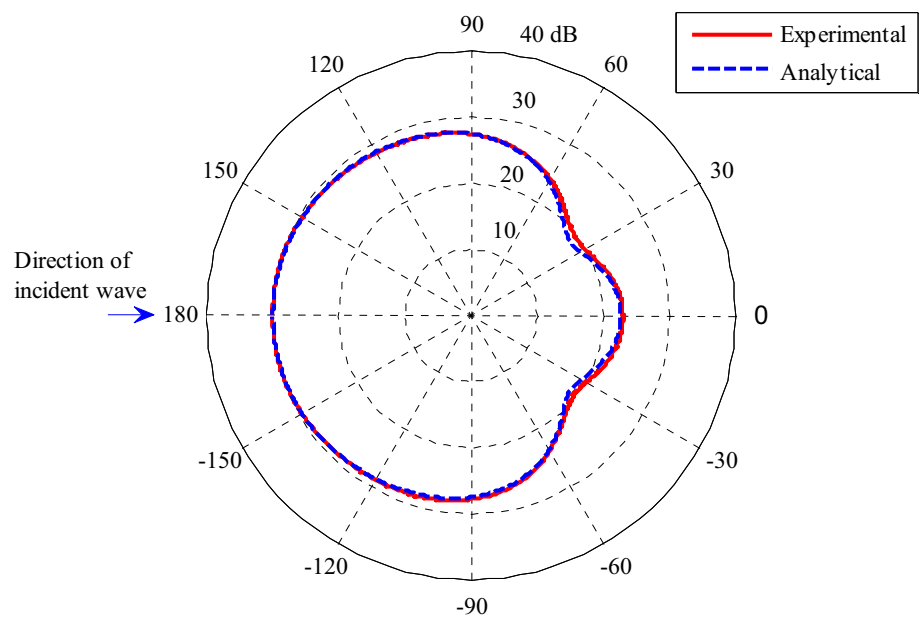


Figure 6.11: Sound pressure directivity comparison between the experimental and normalised analytical results at the surface of the experimental cylinder, for $f = 1.5$ kHz and $ka = 1.57$.

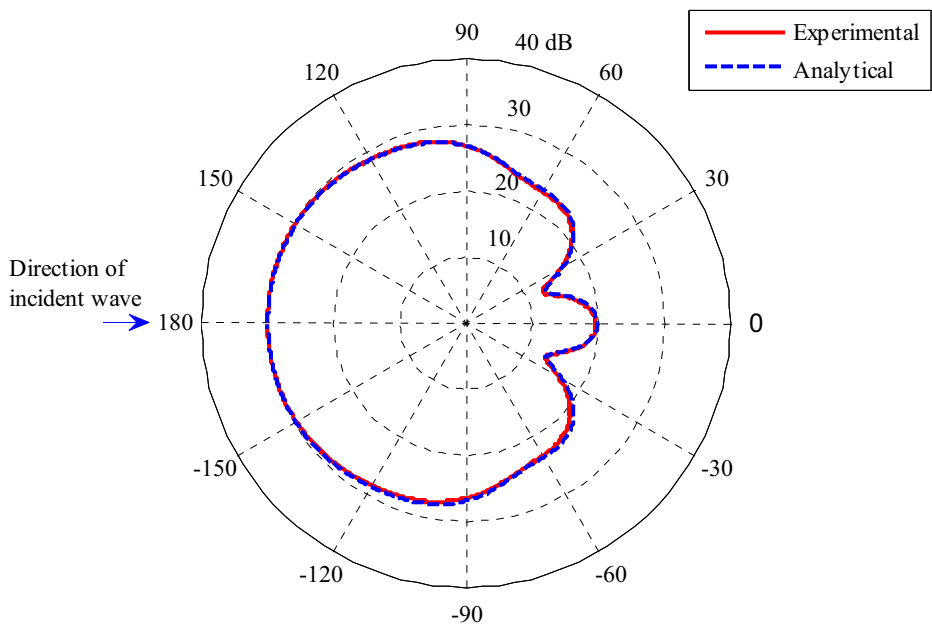


Figure 6.12: Sound pressure directivity comparison between the experimental and normalised analytical results at the surface of the experimental cylinder, for $f = 3$ kHz and $ka = 3.13$.

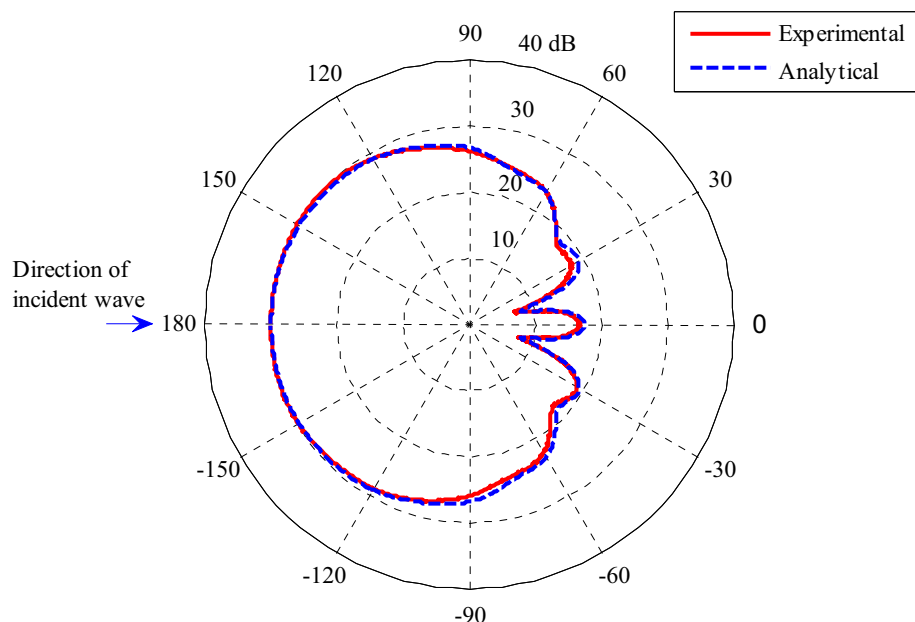


Figure 6.13: Sound pressure directivity comparison between the experimental and normalised analytical results at the surface of the experimental cylinder, for $f = 5$ kHz and $ka = 5.22$.

6.5 Conclusions

The comparisons between the analytical and experimental results presented in this chapter show that the theoretical model used to predict the sound pressure at the surface of a cylinder when the source is positioned at a finite distance from the cylinder is valid. The theoretical analysis can be further extended for the actual launch vehicle lift-off conditions and can also be compared with the Boundary Element Method (BEM) technique, as is done in Chapter 8, to investigate whether BEM can produce equivalent results. To extend the theoretical model to represent the actual launch conditions, modifications can be done considering oblique incident waves from a point source and line source. These are discussed in the next chapter.

Chapter 7

Sound Pressure Field Due to Obliquely Incident Waves on a Boeing Cylinder and an RSLVF

7.1 Introduction

To obtain the actual acoustic loading of a launch vehicle fairing structure, it is necessary to determine the incident sound field in three-dimensional space. The traditional approach commonly used to analyse three-dimensional sound fields is to consider the propagation wave vector and resolve it into its component axes. Morse & Feshbach (1953b) and Morse & Ingard (1986) used the propagation wave vector approach where the propagation wave vector was defined as the wave number for a wave travelling in a particular direction. This approach has been used recently to determine the acoustic loading due to a source located at an arbitrary angle to the cylinder axis (Gardonio *et al.*, 2001; Johnson *et al.*, 2001; Esteve & Johnson, 2002a, 2002b). They separated the incident wave into two components; one propagating perpendicular to the cylinder axis and the other propagating along the cylinder axis to evaluate the oblique wave in the air.

In the early stages of research into the acoustic loading on launch vehicles, equations for the acoustic loading on a cylinder due to oblique incident plane waves were derived and used on the Saturn V vehicle to determine the correlation patterns of the external acoustic pressure excitations due to the engine exhaust noise (Potter, 1966). In this work, one component of the sound wave was considered as propagating perpendicular to the cylinder

axis and another component as propagating along the cylinder axis. The form of the equation was given as (Potter, 1966)

$$p^i = P^o e^{ik(r \cos \phi \cos \beta - ct)} e^{ik z \sin \beta}, \quad (7.1)$$

where the first exponential is for the component normal to the cylinder and the second exponential is for the component along the cylinder. Both include the elevation angle β . This technique cannot consider the oblique distance from the source to a point of interest on the cylinder on which the waves are travelling, as the assumption is that plane waves are incident obliquely on the cylinder. However, the effect of source location has been taken into account in the analysis undertaken in this thesis.

In this chapter, a method has been developed to determine the sound pressure field due to oblique incident waves on the cylinder incorporating a spatially dependent factor. This method has been extended further to investigate a Boeing cylinder and a Representative Small Launch Vehicle Fairing (RSLVF). The investigations have been done in the frequency range from 50Hz to 400 Hz. For both the Boeing cylinder and the RSLVF, a large number of calculations have been done at various frequencies to determine the external sound pressure field acting on the Boeing cylinder and the RSLVF, and the results are presented here.

7.2 Method to Determine the Sound Pressure Due to Obliquely Incident Waves on a Cylinder

To determine the sound pressure at the surface of a cylinder due to oblique incident waves, it is assumed that there will be very little effect on the external sound pressure field due to the diffraction of sound waves from the ends of the cylinder. The diffraction of sound

waves from both ends of the cylinder are thus neglected in the following analysis. Figure 7.1 shows the geometry of obliquely incident waves impinging on a cylinder from a source located on the x axis. The cylinder axis is aligned with the z axis and the y axis is then perpendicular to these two axes. The angle ϕ defines the position of the observation point at the surface of the cylinder. First, consider the pressure field due to incident waves propagating from a point source in a direction normal to the x axis. This follows the approach derived in Chapter 5. Since in the present case the incident waves are oblique to the cylinder, the resultant circumferential sound pressure at a point on the cylinder will depend not only on its location in the x - y plane but also along the z axis.

The approach used here considers a finite portion of the cylinder of length L , and z is the elevation within the region of the cylinder where the resultant pressure is to be evaluated due to a point source positioned on the x axis as shown in the Figure 7.1. Let the projection point of the point of interest p on the x - y plane be p' . Then, recalling equation (5.3), the projected distance, R' , can be calculated as follows:

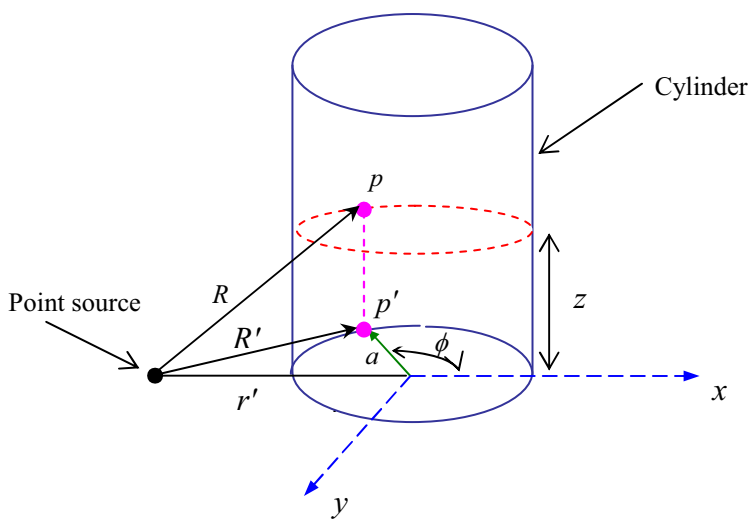


Figure 7.1: Geometry of obliquely incident waves for three-dimensional cylinder coordinate axes.

$$R' = \sqrt{a^2 + r'^2 - 2ar' \cos \phi} . \quad (7.2)$$

The resultant oblique distance can then be calculated as

$$R = \sqrt{R'^2 + z^2} . \quad (7.3)$$

Then the distances from the source to the i th number of observation points on the cylinder become

$$R_i = \sqrt{R_i'^2 + z^2} . \quad (7.4)$$

Substituting equation (7.4) into equation (5.4), the spatially dependent factor P' can be determined as

$$P'(R_i, z) = -i \omega \rho_o \frac{Q_s}{4\pi R_i} e^{ikR_i} , \quad (7.5)$$

where Q_s is the source strength. Finally, using this spatially dependent factor, the total resultant pressure at the surface of the cylinder as a function of z can be derived as

$$P_a^t(R_i, k, a, z, \phi_i, Q_s) = \sum_{n=0}^{N-1} P'(R_i, z) \sum_{m=0}^{M-1} \varepsilon_m i^m \cos(m\phi_i) [J_m(ka) - i e^{-i\gamma_m} \sin \gamma_m H_m(ka)] , \quad (7.6)$$

where the first summation on the right hand side is for N point sources and the second summation is in the same form as described in equations (5.5).

Using the preceding method, the total sound pressure has been calculated at various vertical positions along the cylinder of radius $a = 1.23\text{m}$ (Boeing cylinder radius) and the results are shown in Figure 7.2 for $ka = 5$ for a single point source of complex strength $Q_s = 1 + i \text{ m}^3/\text{s}$, placed on the negative x axis at a distance of $r' = -5a$ (five times the cylinder radius) from the cylinder axis and at $z = 0$ from the base of the cylinder. The figure

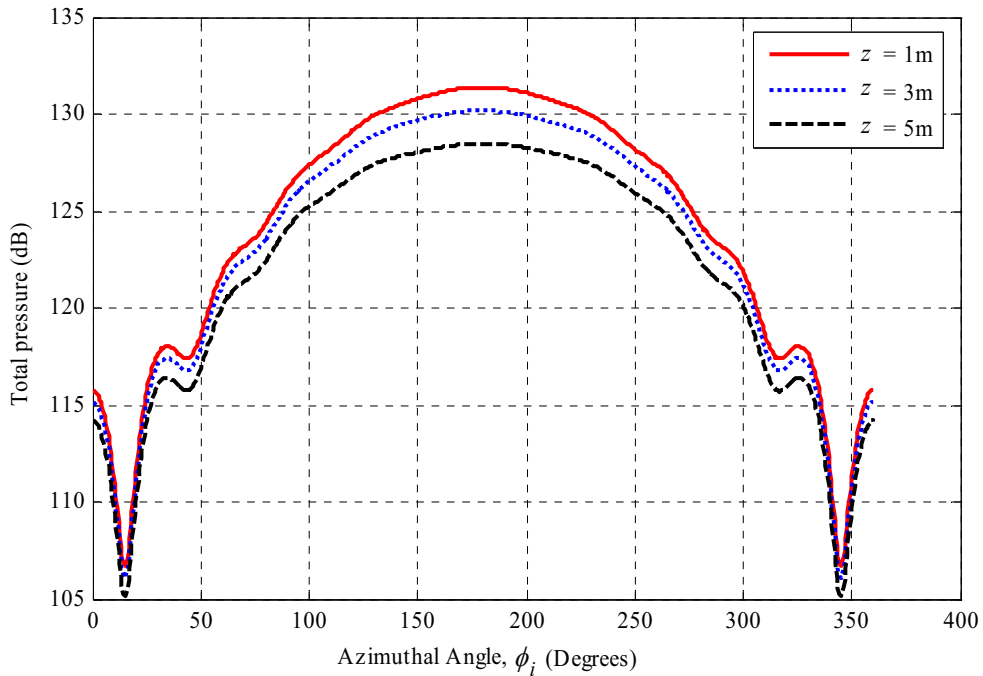


Figure 7.2: Total sound pressure at the surface of a cylinder of radius $a = 1.23\text{m}$, for various heights, z , along the cylinder for $ka = 5$. The point source of complex strength of $Q_s = 1 + i \text{ m}^3/\text{s}$, is placed at a distance of $r' = -5a$ (five times the cylinder radius) from the cylinder axis at $z = 0$. [Reference pressure $20\mu\text{Pa}$]

shows that the total sound pressure pattern is similar at different heights but the total sound pressure magnitude reduces as the height increases. This is because the decay of source strength due to wave propagation increases as the distance from the source to the observation point on the cylinder increases. The results also show that the sound pressure magnitude is relatively smoothly varying and is a maximum in the region from approximately 100° to 260° , at the front face of the cylinder. The sound pressure mostly fluctuates in the regions from approximately 0° to 100° and 260° to 360° of the cylinder. The reason for the above is shown in Figures 3.7(c) and 3.9 in Chapter 3 for $ka = 5$, where it can be seen that the scattered wave amplitude is relatively smoothly varying in the region from approximately 100° to 260° and mostly fluctuates in the regions from approximately 0° to 100° and 260° to 360° of the cylinder. This fluctuation is a result of the positive and/or

negative interference of the two diffracted waves travelling around the two sides of the cylinder. It is noticeable that behind the cylinder at $0^\circ/360^\circ$, the total sound pressure increases because a high scattered pressure peak occurs due to reinforcement of the two diffracted waves travelling around each side of the cylinder (See Figures 3.7(c) and 3.9 in Chapter 3).

7.3 Application of the Method to a Boeing Cylinder

The method derived in the previous section has been used to calculate the external sound pressure exciting the surface of a Boeing cylinder. The overall dimensions of the cylinder are given in Table 7.1. The aspect ratio (length to diameter ratio) of the cylinder is 1.13, which is close to unity. A full investigation has been done in the frequency range of interest from 50Hz to 400 Hz.

A single point source of complex strength of $Q_s = 1 + i \text{ m}^3/\text{s}$ has been considered to exist on the negative x axis at a distance of $r' = -5a$ from the axis of the cylinder at the base, $z = 0$ (see Figure 7.1). The total circumferential sound pressure on the surface of the Boeing cylinder due to the point source has been estimated using equation (7.6). Figures 7.3 and 7.4 show the total circumferential sound pressure distribution in the middle of the Boeing cylinder at various frequencies from 50Hz to 400 Hz. The results show that the sound pressure magnitude is relatively smoothly varying and is a maximum in the region from approximately 100° to 260° at the front face of the cylinder and varies more aggressively in the regions from approximately 0° to 100° and 260° to 360° of the cylinder. The reason has been discussed in the preceding paragraph and is a result of

positive and/or negative interference of the two diffracted waves travelling around the two sides of the cylinder. It is noticeable that behind the cylinder at $0^\circ/360^\circ$, the sound pressure increases because of reinforcement of the two diffracted waves travelling around each side of the cylinder. The results also show that the sound pressure fluctuation increases as the frequency increases. The reason, discussed previously in Section 6.3 in Chapter 6, is there will be an increase in the variation of pressure around the cylinder since the wavelength becomes smaller than the cylinder circumference, resulting in an increase in the amount of interference of the two diffracted waves travelling around the two sides of the cylinder.

NOTE:

This table is included on page 120 of the print copy of the thesis held in the University of Adelaide Library.

Table 7.1: Boeing cylinder physical properties (Hansen *et al.*, 2001a).

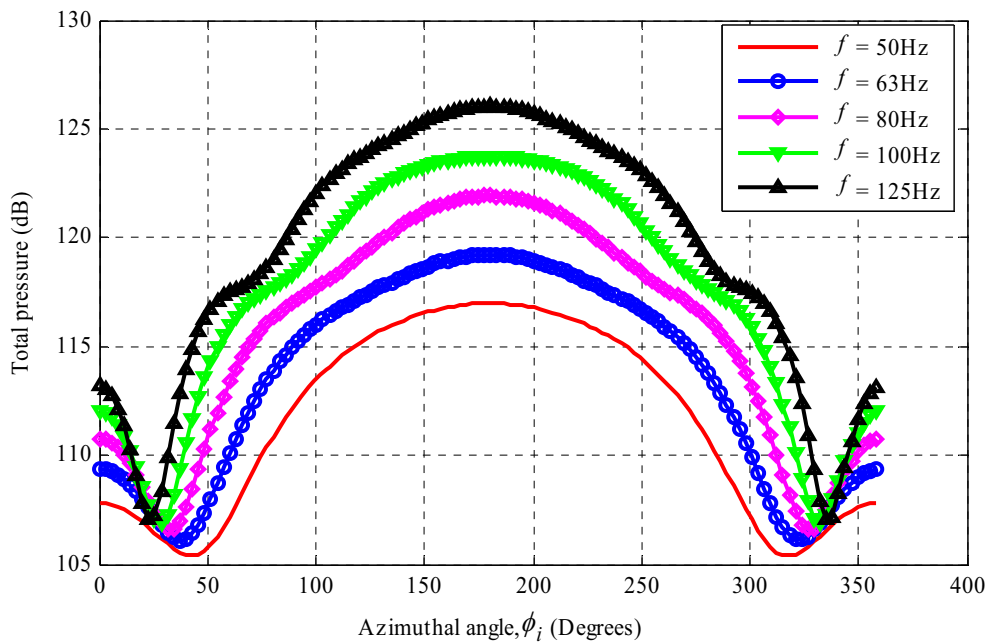


Figure 7.3: Total sound pressure distributions as a function of circumferential angles at various frequencies from 50Hz to 125Hz in the middle ($z = 1.395\text{m}$) of the Boeing cylinder. The point source of complex strength of $Q_s = 1 + i \text{ m}^3/\text{s}$, is placed at a distance of $r' = -5a$ from the cylinder axis at $z = 0$. [Reference pressure $20\mu\text{Pa}$]

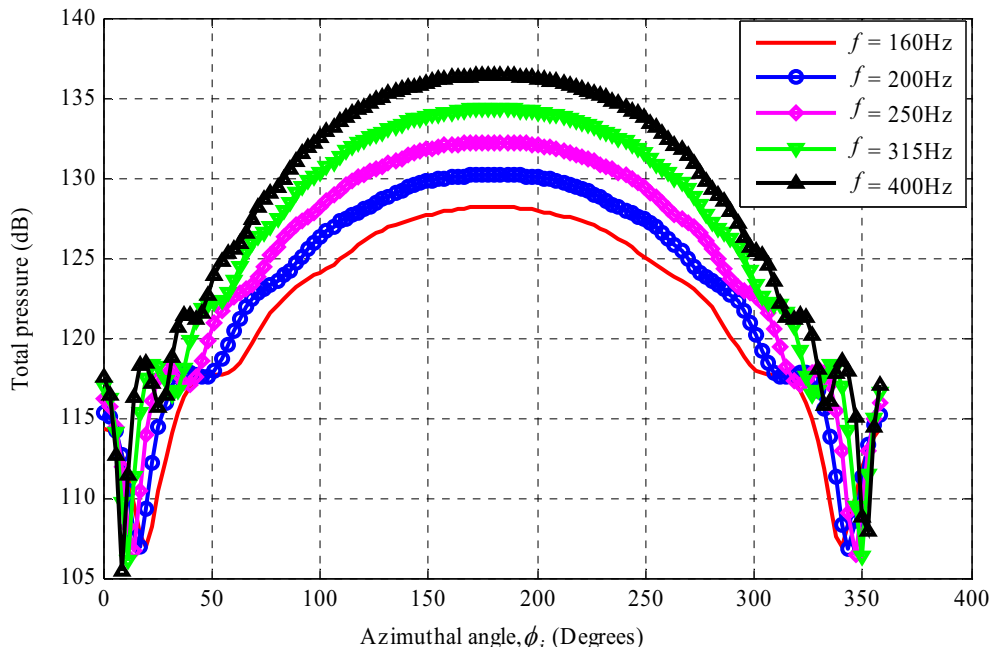


Figure 7.4: Total sound pressure distributions as a function of circumferential angles at various frequencies from 160Hz to 400Hz in the middle ($z = 1.395\text{m}$) of the Boeing cylinder. The point source of complex strength of $Q_s = 1 + i \text{ m}^3/\text{s}$, is placed at a distance of $r' = -5a$ from the cylinder axis at $z = 0$. [Reference pressure $20\mu\text{Pa}$]

7.4 Application of the Method to a Launch Vehicle Fairing

In this section the prediction methodology for oblique incident waves is extended to investigate the external sound pressure incident on a Representative Small Launch Vehicle Fairing (RSLVF), which has been used in previous work (Hansen *et al.*, 2001a, 2001b). The overall dimensions of the RSLVF are given in Table 7.2. In the current analysis, the RSLVF has been divided into four sections as shown in Figure 7.5. To determine the circumferential sound pressure a circular thin slice has been assumed at the middle of each section. The approximate radius and vertical position of each slice are given in Table 7.3. The methodology has been used for each slice separately to predict the external sound pressure in the frequency range of interest from 50Hz to 400 Hz.

Property	Value
Maximum Diameter	1.552 m
Overall Length	5.33 m

Table 7.2: RSLVF physical dimensions.

Slice	Vertical position, z (m)	Radius, a (m)
One	0.560	0.704
Two	2.065	0.776
Three	3.660	0.649
Four	4.744	0.410

Table 7.3: Approximate parameters of four slices.

A point source of complex strength of $Q_s = 1 + i \text{ m}^3/\text{s}$ has been placed at the bottom of the RSLVF at $z = 0$ on the negative x axis at a distance of $r' = -5\text{m}$ from the axis of the RSLVF. The external sound pressure at each vertical position along the RSLVF due to the

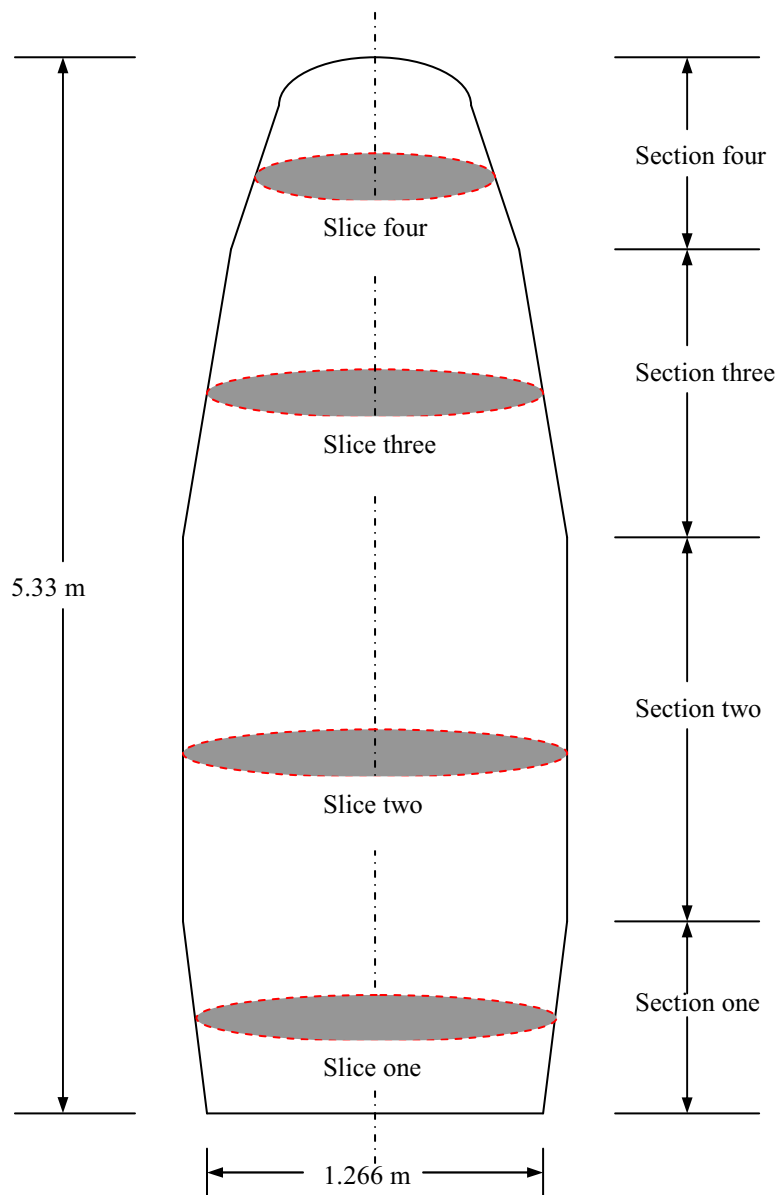


Figure 7.5: RSLVF cross-section and modelled different sections.

point source has been estimated using equation (7.6). The total circumferential sound pressure distribution at the surface of each slice of the RSLVF at various frequencies from 50Hz to 400Hz is shown in Figures 7.6(a-b), 7.7(a-b), 7.8(a-b) and 7.9(a-b) respectively. The results show that at a particular frequency the total sound pressure pattern on each slice is similar since the frequency is unchanged but the sound pressure amplitude decreases as the height increases. This is a result of the decay of sound pressure amplitude as the distance from the source (at $z = 0$) increases. The results also show that the total sound pressure magnitude is relatively smoothly varying and is a maximum in the region from approximately 100° to 260° at the front face of the RSLVF. The total sound pressure varies more aggressively in the regions from approximately 0° to 100° and 260° to 360° of the RSLVF due to the positive and/or negative interference of the two diffracted waves travelling around the two sides of the RSLVF. It is noticeable that behind the RSLVF at $0^\circ/360^\circ$ the sound pressure increases because of reinforcement of the two diffracted waves travelling around each side. It is interesting to note that the sound pressure fluctuation increases as the frequency increases because the wavelength becomes smaller than the RSLVF circumference, resulting in an increase in the amount of interference of the two diffracted waves travelling around each side of the RSLVF.

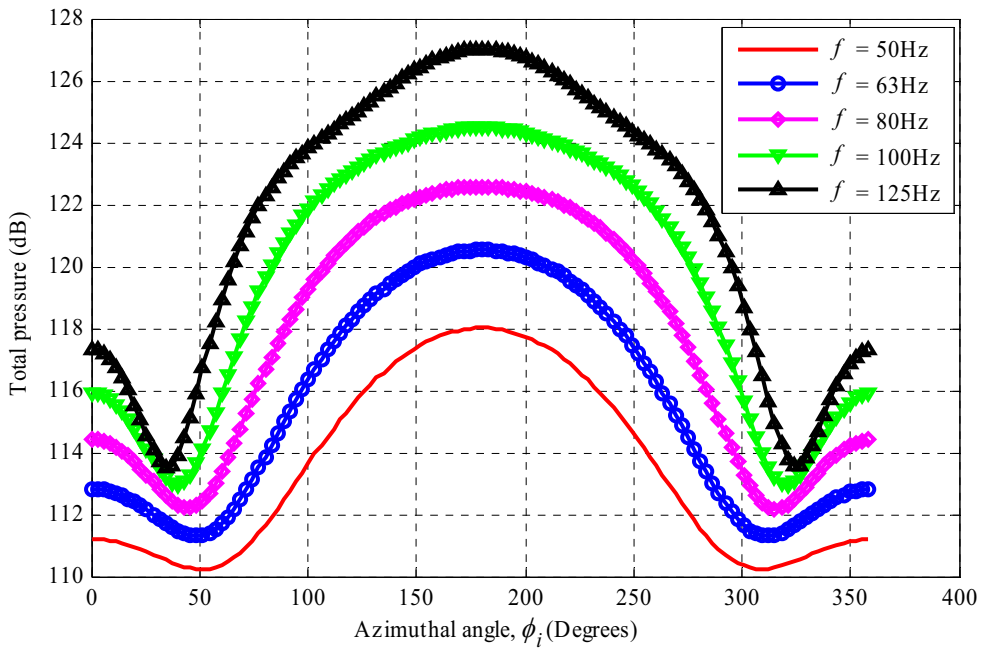


Figure 7.6(a): Total circumferential sound pressure at various frequencies from 50Hz to 125 Hz at the surface of slice one of the RSLVF. The point source of complex strength of $Q_s = 1 + i \text{ m}^3/\text{s}$, is placed at a distance of $r' = -5\text{m}$ from the RSLVF axis at $z = 0$. [Reference pressure $20\mu\text{Pa}$]

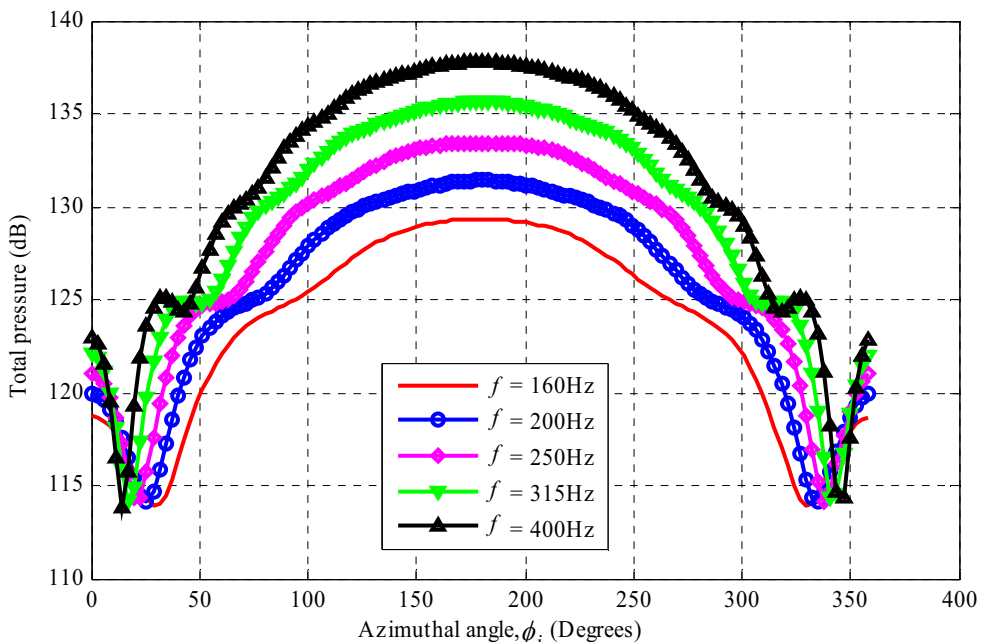


Figure 7.6(b): Total circumferential sound pressure at various frequencies from 160Hz to 400 Hz at the surface of slice one of the RSLVF. The point source of complex strength of $Q_s = 1 + i \text{ m}^3/\text{s}$, is placed at a distance of $r' = -5\text{m}$ from the RSLVF axis at $z = 0$. [Reference pressure $20\mu\text{Pa}$]

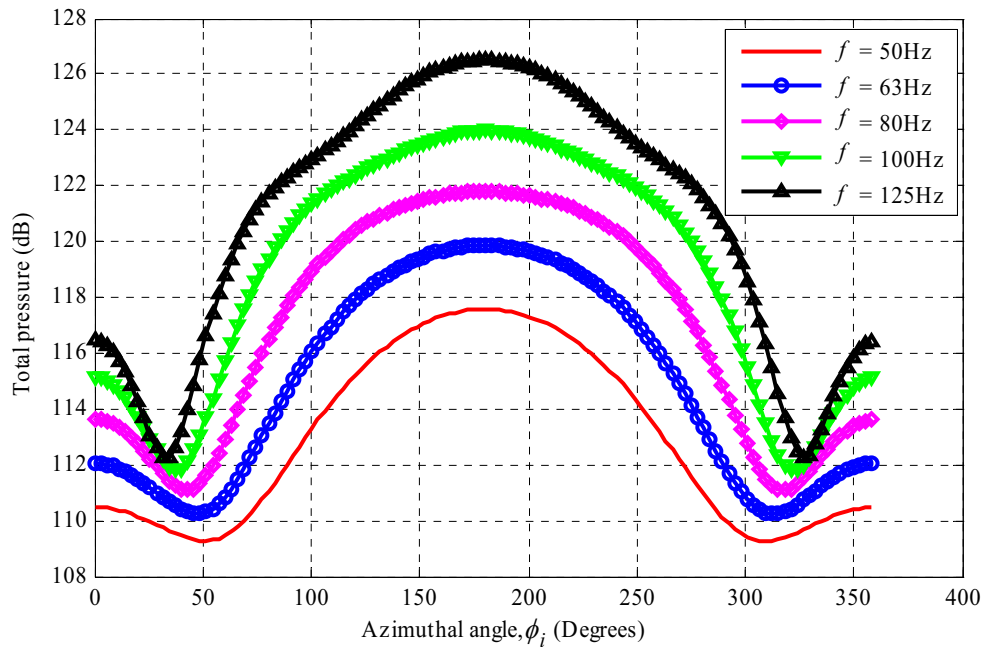


Figure 7.7(a): Total circumferential sound pressure at various frequencies from 50Hz to 125 Hz at the surface of slice two of the RSLVF. The point source of complex strength of $Q_s = 1 + i \text{ m}^3/\text{s}$, is placed at a distance of $r' = -5\text{m}$ from the RSLVF axis at $z = 0$. [Reference pressure $20\mu\text{Pa}$]

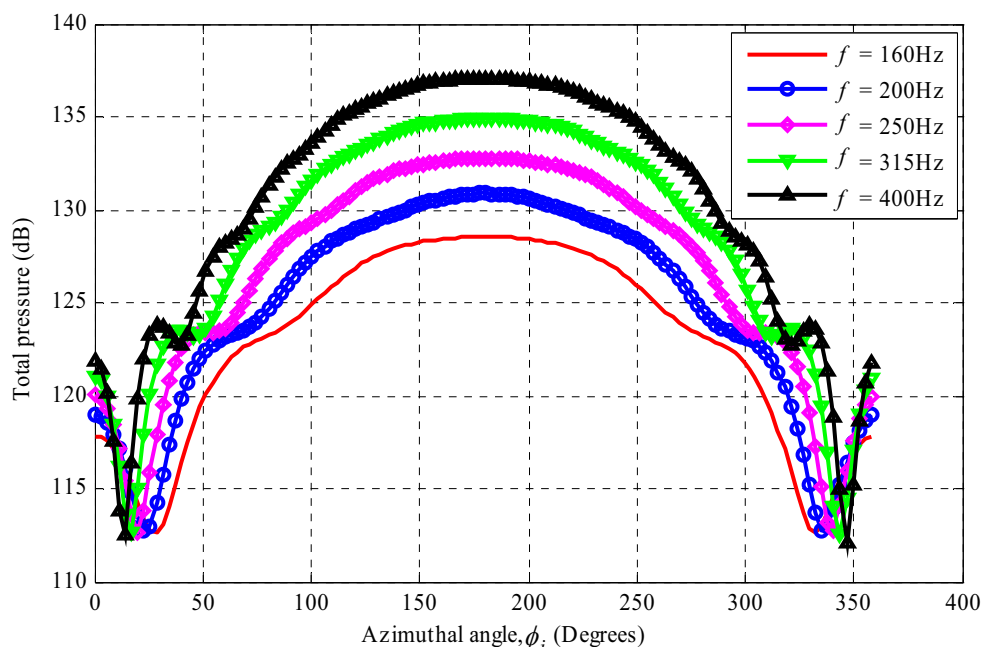


Figure 7.7(b): Total circumferential sound pressure at various frequencies from 160Hz to 400 Hz at the surface of slice two of the RSLVF. The point source of complex strength of $Q_s = 1 + i \text{ m}^3/\text{s}$, is placed at a distance of $r' = -5\text{m}$ from the RSLVF axis at $z = 0$. [Reference pressure $20\mu\text{Pa}$]

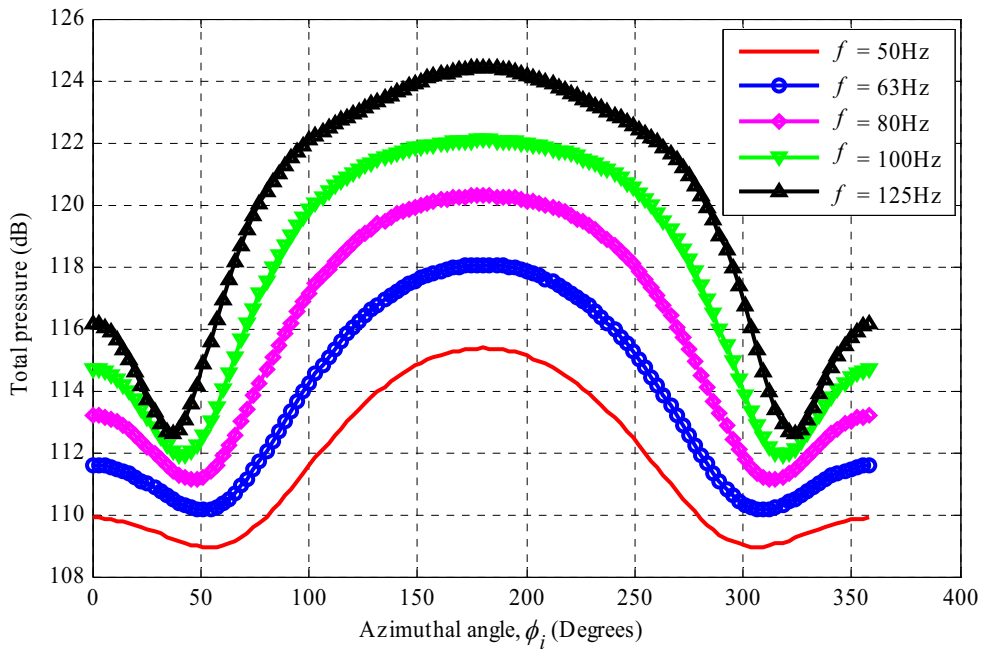


Figure 7.8(a): Total circumferential sound pressure at various frequencies from 50Hz to 125 Hz at the surface of slice three of the RSLVF. The point source of complex strength of $Q_s = 1 + i \text{ m}^3/\text{s}$, is placed at a distance of $r' = -5\text{m}$ from the RSLVF axis at $z = 0$. [Reference pressure $20\mu\text{Pa}$]

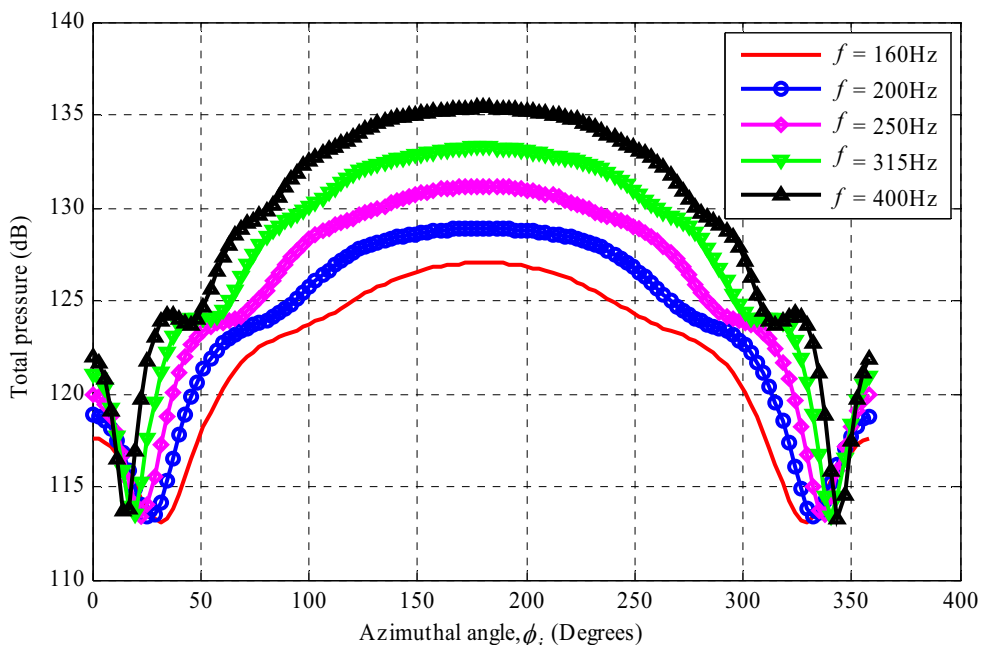


Figure 7.8(b): Total circumferential sound pressure at various frequencies from 160Hz to 400 Hz at the surface of slice three of the RSLVF. The point source of complex strength of $Q_s = 1 + i \text{ m}^3/\text{s}$, is placed at a distance of $r' = -5\text{m}$ from the RSLVF axis at $z = 0$. [Reference pressure $20\mu\text{Pa}$]

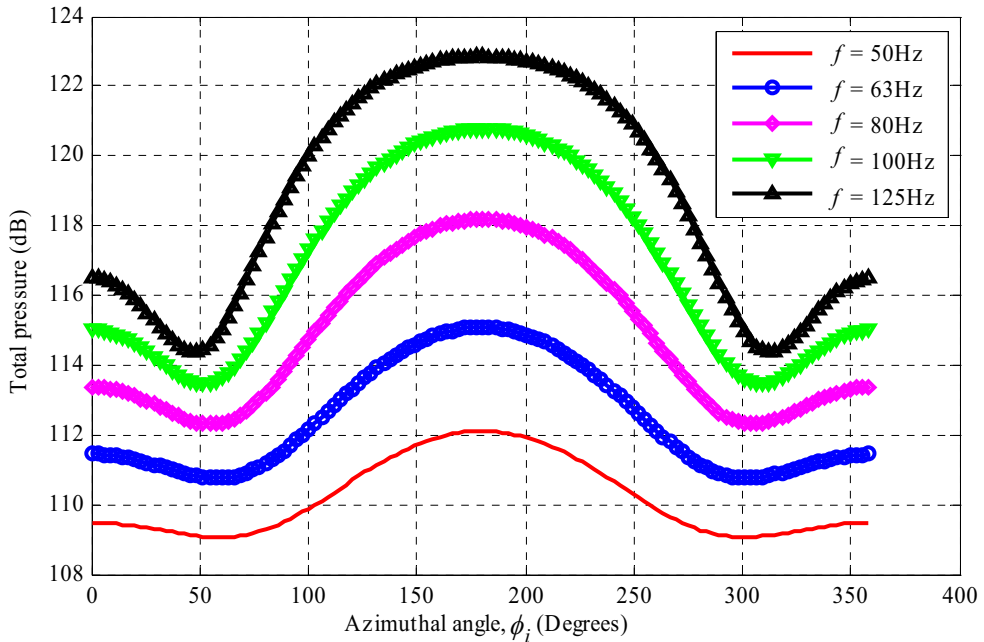


Figure 7.9(a): Total circumferential sound pressure at various frequencies from 50Hz to 125 Hz at the surface of slice four of the RSLVF. The point source of complex strength of $Q_s = 1 + i \text{ m}^3/\text{s}$, is placed at a distance of $r' = -5\text{m}$ from the RSLVF axis at $z = 0$. [Reference pressure $20\mu\text{Pa}$]

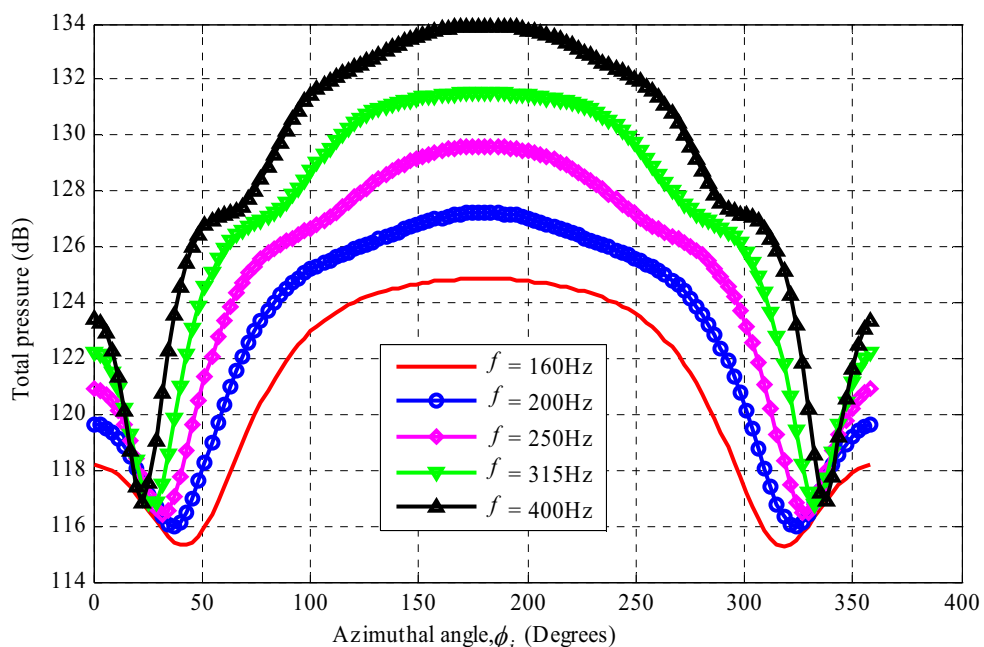


Figure 7.9(b): Total circumferential sound pressure at various frequencies from 160Hz to 400 Hz at the surface of slice four of the RSLVF. The point source of complex strength of $Q_s = 1 + i \text{ m}^3/\text{s}$, is placed at a distance of $r' = -5\text{m}$ from the RSLVF axis at $z = 0$. [Reference pressure $20\mu\text{Pa}$]

7.5 Conclusions

In section 7.2, a method has been described that predicts the sound pressure field at the surface of a cylinder due to oblique incident waves. The methodology has been applied to a Boeing cylinder to investigate the surface sound pressure field due to a point source placed on the negative x axis at a distance of 5 times the cylinder radius from the cylinder axis and at a height equal to that of the base of the cylinder. The total circumferential sound pressure distributions in the middle of the cylinder at various frequencies from 50Hz to 400Hz have been presented.

Similar methodology has been applied to an RSLVF where the RSLVF has been divided into four sections. For each section an individual thin slice has been assumed to estimate the circumferential sound pressure field at the surface of the slice. The results have been presented for each of the four slices. The results indicate that the sound pressure pattern at a particular frequency on each slice is similar, but the sound pressure amplitude decreases as the height increases because the decay of source strength due to wave propagation increases as the distance increases with respect to the increase of height.

From the analytical results of both the Boeing cylinder and the RSLVF, it can be concluded that the maximum sound pressure occurs at the position 180° at the front face of the Boeing cylinder and the RSLVF where the sound wave impinges. The sound pressure amplitude is relatively smoothly varies in the region from approximately 100° to 260° at the front face of the Boeing cylinder and the RSLVF. The sound pressure mostly fluctuates in the regions from approximately 0° to 100° and 260° to 360° at the rear face of the Boeing cylinder and the RSLVF due to positive and/or negative interference of the

diffracted waves travelling around the two sides towards the back of the Boeing cylinder and the RSLVF. The sound pressure fluctuation increases as the frequency increases because interference of the two diffracted waves increases at the back of the Boeing cylinder and the RSLVF. The sound pressure increases at the position $0^\circ/360^\circ$ behind the Boeing cylinder and the RSLVF due to reinforcement of the two diffracted waves travelling around each side.

The methodology described in this chapter is not able to consider sound diffractions from the ends of the Boeing cylinder and the RSLVF. This could be investigated in future work, where the effects due to the ends could be taken into account to develop the full theoretical model. However, for the current development this shortcoming of the theoretical approach can be overcome using the Boundary Element Method (BEM), which will be discussed in the next chapter. Using an analytical model that excludes diffraction around the ends is sufficiently accurate to act as a check the validity of the BEM model. Therefore, the methodology will be used in the next chapter to check the validity of the BEM model for oblique incident waves from a point source and a line source.

Chapter 8

Numerical Calculations of the Sound Pressure Field

8.1 Introduction

The acoustic loads induced on the payload fairing during launch of a space vehicle are complicated in nature, particularly when the vehicle rocket-propulsion system is operated at full power at the instant of take-off. The prediction of these acoustic loads is difficult due to the complex geometry of the payload fairing and the complex acoustic field generated by the rocket motors. The complex fairing geometry results in complicated wave reflection and diffraction. The theoretical methods described in the previous chapters of this thesis have been developed extensively for a point source, line source and oblique wave, and are capable of predicting the circumferential acoustic pressure field, including the effect of the scattered acoustic pressure from the cylinder surface. However, they are not suitable for complex geometry because they do not account for diffraction from the ends of the cylinder and the Representative Small Launch Vehicle Fairing (RSLVF, as already mentioned in the previous chapter. The problem of complex geometry can be overcome by using computational numerical analysis, and this approach is the subject of this chapter.

The Boundary Element Method (BEM) technique relies on the solution of the *Helmholtz Integral Equations* on the discretized boundary rather than the entire problem domain. For the problem of scattering, the integration on the boundary directly satisfies *Sommerfeld's*

radiation condition. Therefore, the 3D (three-dimensional) scattering problem is reduced to the discretization of a 2D (two-dimensional) boundary surface. Hence few nodes are required for surface meshing, resulting in less computational time than if Finite Element Analysis (FEA) is used.

This chapter uses the BEM technique to predict the acoustic loads on the Boeing cylinder and the RSLVF. The BEM software used here is written in MATLAB and is publicly available software known as Open BEM, which has been mainly developed by the Acoustic Laboratory, Technical University of Denmark. The Open BEM codes are able to treat 2D, 3D and axisymmetric problems. In the current work, both 2D and 3D techniques have been used to solve the 2D and 3D problem geometries. The numerical results using 2D BEM for the experimental cylinder are compared with the analytical and experimental results described in Chapter 6 to ensure the validity of the 2D numerical results. Also, the numerical results using 3D BEM for a simple, long cylinder are compared with the analytical results using the method described in the previous chapter to ensure the validity of the 3D numerical results.

8.2 Boundary Integral Formulation of *Helmholtz Equation*

Consider an arbitrary shaped structure of volume V_i surrounded by surface S and placed in an acoustic domain of volume V_e , as shown in Figure 8.1, where p and q are two points at some distance r_p and r_q respectively, from the centre of the body. In other words, one is the integration point on the boundary and the other is the field point or source point which may be placed in V_e , V_i or on S . The free field *Green's function* for

the *Helmholtz equation* used in Chapter five can be used as the solution for this particular case and can be written as

$$(\nabla^2 + k^2) G(r_p, r_q) = -4\pi\delta(r_p - r_q), \quad (8.1)$$

where k is the wave number and G represents *Green's function*. To solve equation (8.1) an appropriate boundary condition is required. An evaluation of the unknown pressure gradients from the known velocity distribution of the sources along the surface S , can be used to define the boundary condition. The relation of the velocity at the interface S to the gradient of pressure is as follows (Juhl, 1993; Wu, 2000):

$$\frac{\partial P(r_p)}{\partial n} = -i\omega\rho_o u_n(r_p), \quad (8.2)$$

where P and u_n are the acoustic pressure and outward normal particle velocity at point p , respectively, and ρ_o is the medium density. The radiated and scattered acoustic field within an infinite acoustic domain, V_e , exterior to a finite body of surface S , satisfies *Sommerfeld's radiation condition* which is (Pierce, 1981):

$$\lim_{r \rightarrow \infty} [r(P - \rho_o c u_r)] = 0, \quad (8.3)$$

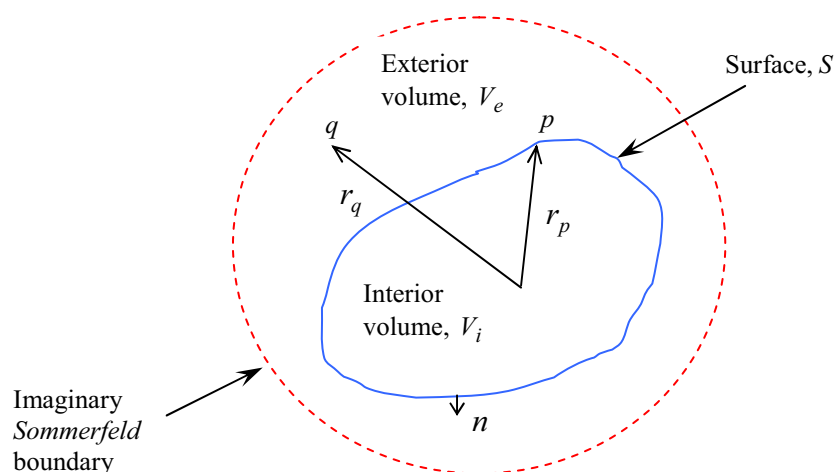


Figure 8.1: Geometry of the exterior boundary problem.

where u_r is the particle velocity at infinite radial distance r from the radiator. Therefore, the value of the integral over the far field surface goes to zero for $r \rightarrow \infty$ in *Green's second identity* of the *Helmholtz equation*, which is (Juhl, 1993; Wu, 2000)

$$\begin{aligned} & - \int_V \left(G(r_p, r_q) \frac{\partial^2 P(r_p)}{\partial^2 n} - P(r_p) \frac{\partial^2 G(r_p, r_q)}{\partial^2 n} \right) dV = \\ & - \int_S \left(G(r_p, r_q) \frac{\partial P(r_p)}{\partial n} - P(r_p) \frac{\partial G(r_p, r_q)}{\partial n} \right) dS. \end{aligned} \quad (8.4)$$

Substituting equations (8.1) and (8.2) into equation (8.4) yields

$$4\pi \int_V P(r_p) \delta(r_p - r_q) dV = \int_S \left(i\omega \rho_o u_n(r_p) G(r_p, r_q) + P(r_p) \frac{\partial G(r_p, r_q)}{\partial n} \right) dS, \quad (8.5)$$

which is the required *Helmholtz integral equation* for the Boundary Element Method (BEM). The integral on the left side of equation (8.5) depends on the position of point q either inside, on the surface or outside the surface. Hence equation (8.5) can be rewritten in the form (Seybert *et al.*, 1985, 1986, 1990; Seybert & Casey, 1988; Juhl, 1993; Wu, 2000)

$$C(q)P(q) = \int_S \left(i\omega \rho_o u_n(p) G(R) + P(p) \frac{\partial G(R)}{\partial n} \right) dS, \quad (8.6)$$

where $R = |r_p - r_q|$ and the coefficient $C(q)$ is the solid angle measured from V :

$$\begin{aligned} C(q) &= 0; & q \in V_i \\ &= 4\pi + \int_S \frac{\partial}{\partial n} \left(\frac{1}{R(p, q)} \right) dS; & q \in S \\ &= 4\pi. & q \in V_e \end{aligned} \quad (8.7)$$

8.3 Reduced Integral Formulation for Scattering Problem

Equation (8.6) can be used for various types of analysis such as sound radiation from a structure. In this case, the wave superposition technique is often used, where a continuous series of monopoles or dipoles or a combination of the two with known strengths can be distributed over the discrete surface to calculate the sound pressure at a field point. The use of this technique has been discussed in detail in the literature, such as Koopmann *et al.* (1989), Fahline & Koopmann (1991), Song *et al.* (1991a, 1991b), Jeans & Mathews (1992), and Morgan *et al.* (2004). However, since the aim of the current work is to investigate the scattering problem from a hard wall, only the second term of the integration in equation (8.6) is important, because the first term, which represents the velocity normal on the surface of the body, can be omitted for a rigid surface. Hence, for scattering from a rigid body, equation (8.6) reduces to

$$C(q)P(q) = \int_S P(p) \frac{\partial}{\partial n} \left(\frac{e^{-ikR(p,q)}}{R(p,q)} \right) dS, \quad (8.8)$$

where $G(R) = \frac{e^{-ikR(p,q)}}{R(p,q)}$; is the free field *Green's function*.

Finally, introducing an incident term, the total sound pressure can be written as

$$C(q)P(q) = \int_S P(p) \frac{\partial}{\partial n} \left(\frac{e^{-ikR(p,q)}}{R(p,q)} \right) dS + 4\pi P^I(q), \quad (8.9)$$

where P^I represents the incident sound pressure.

8.4 Numerical Implementation

Equation (8.9) can be evaluated numerically by discretizing the boundary surface into N surface elements. The discretization of the integral equation (8.9) can be approximated by the sum of integrals over the elements as follows:

$$C(q)P(q) = \sum_{i=1}^N \left(\int_{S_i} P_i(p) \frac{\partial}{\partial n} \left(\frac{e^{-ikR(p,q)}}{R(p,q)} \right) dS \right) + 4\pi P^I(q), \quad (8.10)$$

where $P_i(p)$ are the constant nodal pressures for each element. The elementary solution can be given more precisely by introducing element shape functions as

$$C(q)P(q) = \sum_{i=1}^N \left(P_i(p) N_i(\xi) \frac{\partial}{\partial n} \left(\frac{e^{-ikR(p,q)}}{R(p,q)} \right) dS \right) + 4\pi P^I(q), \quad (8.11)$$

where $N_i(\xi)$ are the element shape functions. For a surface formulation where $q = p$, solving N calculations for all the elements on the surface, equation (8.11) can be written in the following matrix form

$$[\mathbf{C}]\{\mathbf{P}\} = \{\mathbf{P}\}[\mathbf{H}] + 4\pi \mathbf{P}^I, \quad (8.12)$$

where $[\mathbf{C}]$ is the $\mathbf{C} \times \mathbf{C}$ diagonal matrix which indicates the solid angles from the surface and is equal to $2\pi C_N$ for the surface formulation, and $[\mathbf{H}]$ is an $\mathbf{H} \times \mathbf{H}$ coefficient matrix of the j th calculation points on the i th elements. Here both $[\mathbf{C}]$ and $[\mathbf{H}]$ are known but $\{\mathbf{P}\}$ is unknown. Therefore to find $\{\mathbf{P}\}$, equation (8.12) reduces to

$$[\mathbf{A}]\{\mathbf{P}\} = -4\pi \mathbf{P}^I, \quad (8.13)$$

where $[\mathbf{A}] = [\mathbf{H} - \mathbf{C}]$.

8.5 Verifications of Open BEM (Boundary Element Method)

The Open BEM code written in MATLAB is available for 2D and 3D analysis (Juhl, 1993). In this section, the verifications of the 2D and 3D BEM are presented, where two-dimensional and three-dimensional problem geometries were analysed respectively, so that the BEM technique could be extended further for the Boeing cylinder and the RSLVF, in order to determine the external acoustic pressure loading.

8.5.1 Verifications of 2D BEM

First, plane waves that strike normal to a cylinder of radius a were considered for comparison between the analytical and 2D BEM results. It is assumed that the sound waves are travelling from left to right. The plane wave theory derived in Chapter 3, particularly equation (3.18) for the total circumferential sound pressure at the cylinder surface, was used to determine the analytical results and compared with the numerical results at various frequencies. For the numerical calculations the cylinder surface was divided into 40 elements. Each element had two end nodes and one mid node, and there were in total 80 nodes on the surface, as shown in Figure 8.2. On each node the incident sound pressure P^I of equation (8.13) could be calculated for plane waves as follows:

$$P^I = P^o e^{ikxy}, \quad (8.14)$$

where x and y represent the node position along the X and Y coordinates respectively. The total sound pressure comparisons between the analytical and numerical results at various frequencies are shown in Figures 8.3 (a-d). It is interesting to see that there is good agreement between the analytical and 2D BEM results at different

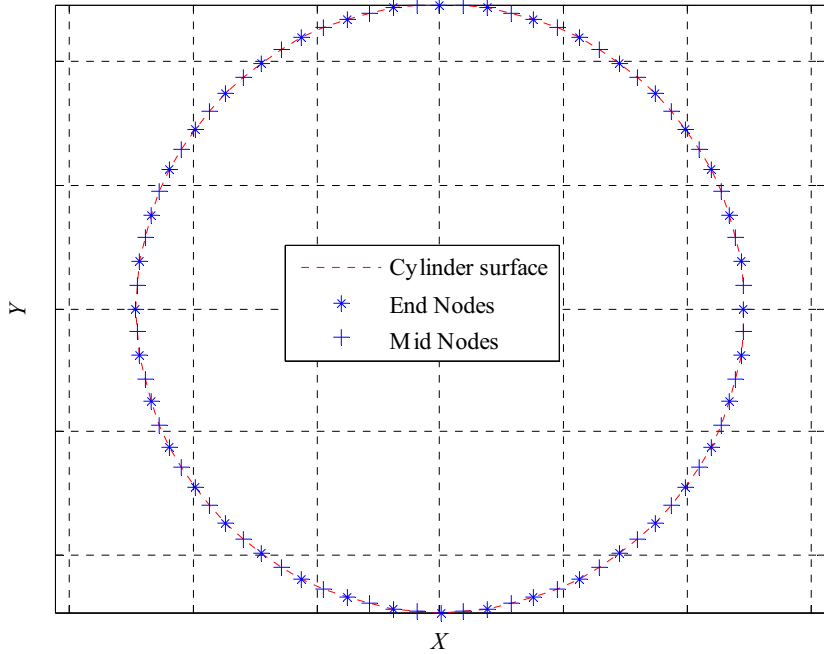


Figure 8.2: 2D BEM surface discretization of a cylinder of radius a , contains 40 elements and 80 nodes on the surface. X and Y represents the coordinates of the cylinder respectively.

frequencies. This indicates that the 2D BEM can predict the sound pressure on the surface accurately and it also provides further verification of the validity of the analytical results.

However, it was found that the 2D BEM technique is only applicable when $ka \leq 15$ (the reason is discussed in the following paragraph). In Figures 8.3 (a-d), it can be seen that the analytical and 2D BEM results give exactly the same values for the argument, ka , up to 15. If $ka > 15$, the 2D BEM technique fails to produce a reliable result at the surface compared with the analytical result, as shown in Figure 8.4 for the case $ka = 16$. The dissimilarity between the analytical and 2D BEM results increases when $ka > 16$, as shown in Figure 8.5 for $ka = 20$.

The problem described above is a well-known problem for the BEM technique. For the

exterior BEM case, the integration of *Helmholtz equation* does not behave uniquely at certain characteristic frequencies (also known as an Eigenfrequencies) (Wu, 2000). Seybert & Rengarajan (1987) reported that the nonuniqueness problem is fully mathematical and the characteristic frequencies have no physical meaning for the exterior boundary problem. In general, it is understood that as the excitation frequency increases, the eigenfrequencies and the nodal surfaces become more closely spaced (Ciskowski & Brebbia, 1991). As the distance tends to zero, the surface integration breaks down as the coefficient matrix becomes singular. The problem is sometimes called “thin-shape breakdown” (Martinez, 1991; Cutanda, 1999). This non-uniqueness problem can be solved using CHIEF (Combined Helmholtz Integral Equation Formulation) points as a constraint to the surface integration. This was well reported by Jhul (1993) and is also available in the Open BEM software package. The nonuniqueness problem could be investigated in future work. For the current work, further investigations on 2D BEM analysis were confined to the range $ka \leq 15$ because, in that range of the argument ka , the surface integration does not break down as the coefficient matrix remains non-singular resulting in no nonuniqueness problem and also the analytical and 2D BEM results agree well.

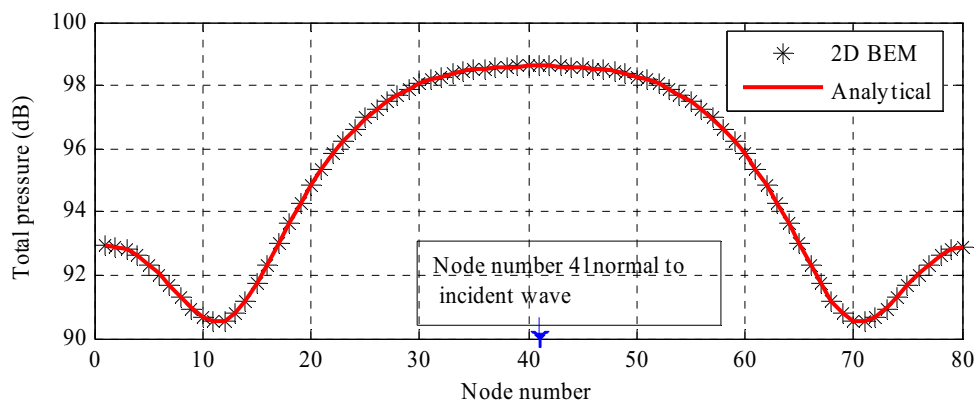


Figure 8.3(a): Total sound pressure comparison between the analytical and 2D BEM results at the surface of a cylinder of radius a , for incident plane waves travelling from left to right, for $ka = 1$. [Reference pressure $20\mu\text{Pa}$ and incident pressure magnitude $P^o = 1\text{ Pa}$]

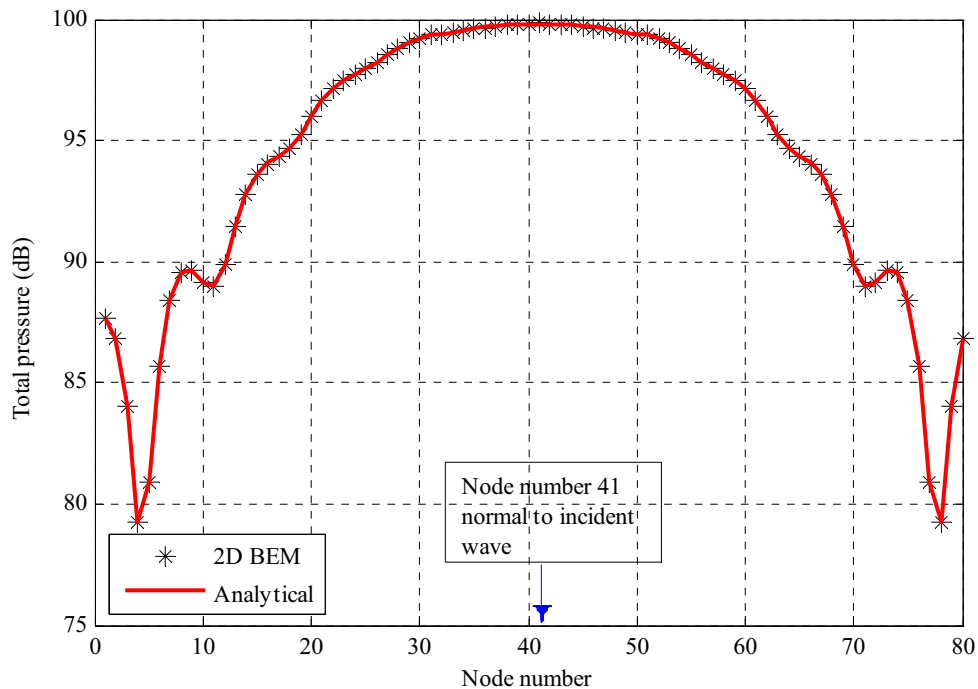


Figure 8.3(b): Total sound pressure comparison between the analytical and 2D BEM results at the surface of a cylinder of radius a , for incident plane waves travelling from left to right, for $ka = 5$. [Reference pressure $20\mu\text{Pa}$ and incident pressure magnitude $P^o = 1\text{ Pa}$]

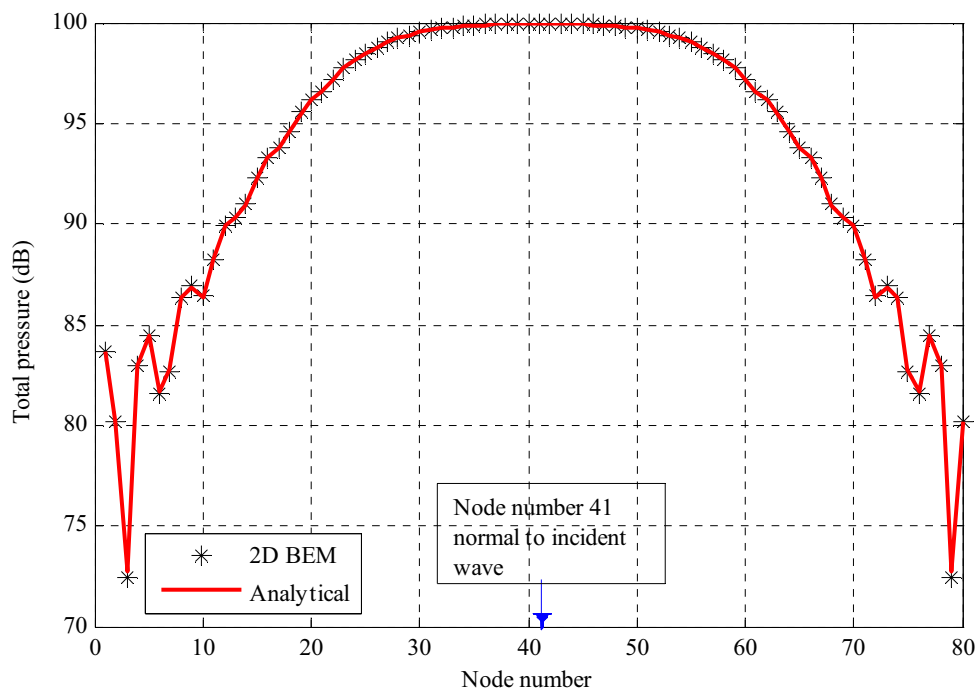


Figure 8.3(c): Total sound pressure comparison between the analytical and 2D BEM results at the surface of a cylinder of radius a , for incident plane waves travelling from left to right, for $ka = 10$. [Reference pressure $20\mu\text{Pa}$ and incident pressure magnitude $P^o = 1\text{ Pa}$]

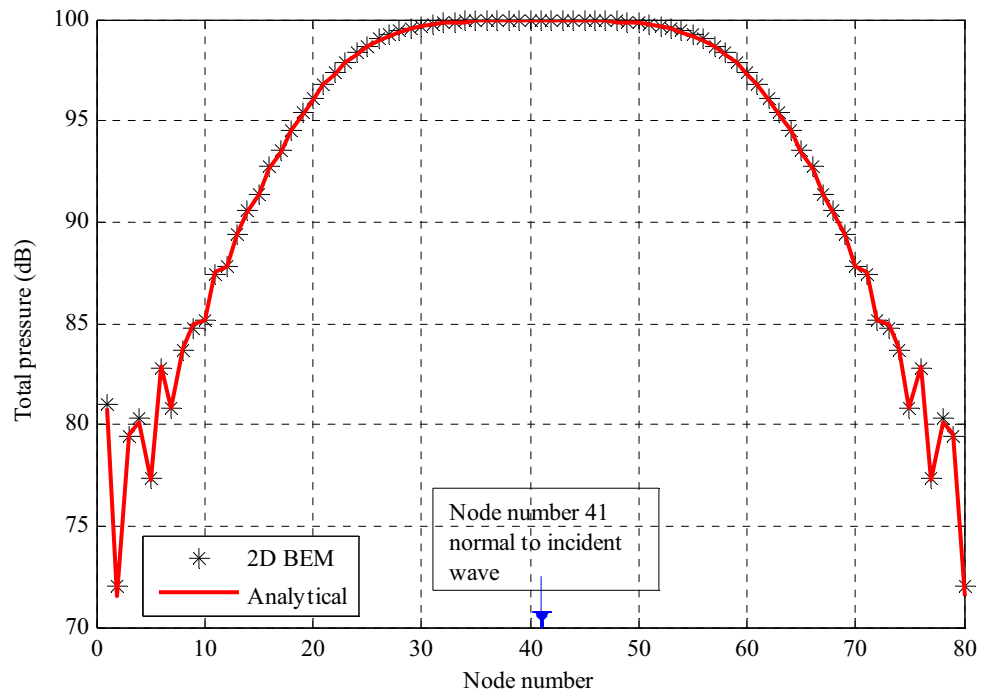


Figure 8.3(d): Total sound pressure comparison between the analytical and 2D BEM results at the surface of a cylinder of radius a , for incident plane waves travelling from left to right, for $ka = 15$. [Reference pressure $20\mu\text{Pa}$ and incident pressure magnitude $P^o = 1\text{ Pa}$]

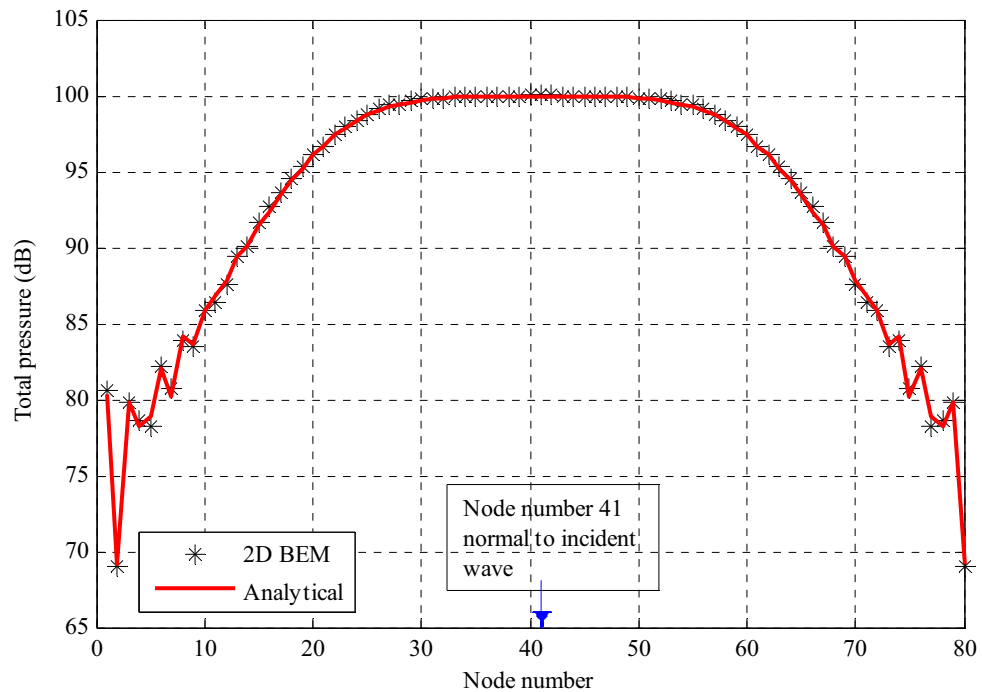


Figure 8.4: Total sound pressure comparison between the analytical and 2D BEM results at the surface of a cylinder of radius a , for incident plane waves travelling from left to right, for $ka = 16$. [Reference pressure $20\mu\text{Pa}$ and incident pressure magnitude $P^o = 1\text{ Pa}$]

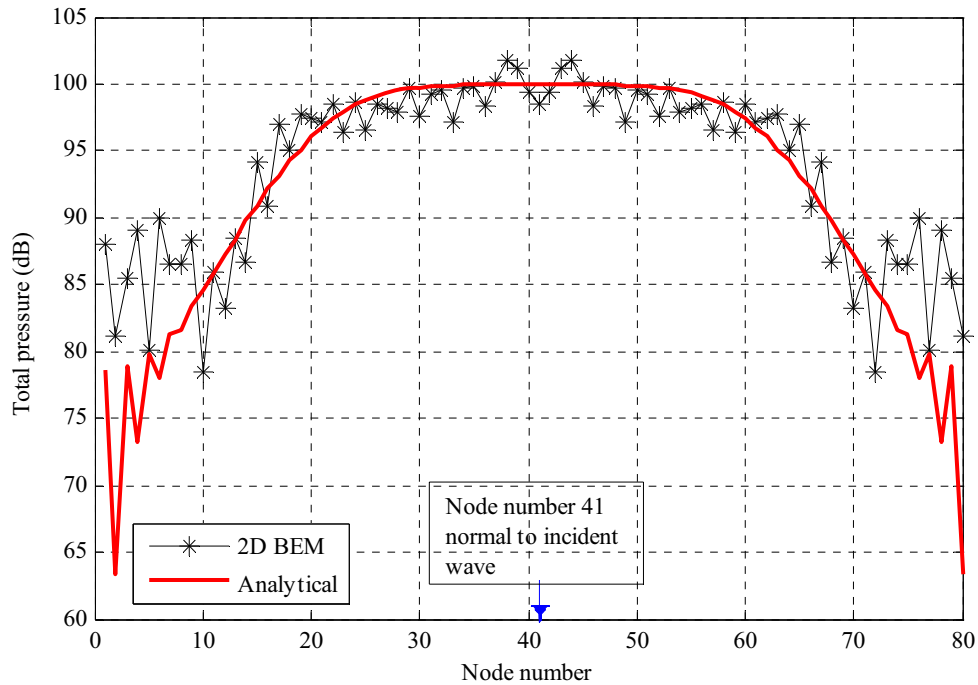


Figure 8.5: Total sound pressure comparison between the analytical and 2D BEM results at the surface of a cylinder of radius a , for incident plane waves travelling from left to right, for $ka = 20$. [Reference pressure $20\mu\text{Pa}$ and incident pressure magnitude $P^o = 1\text{ Pa}$]

A point source at a distance of $X = -4.1\text{m}$ and $Y = 0\text{m}$ from the centre of a cylinder of radius 0.057m (the radius of the experimental cylinder was 0.057m), was considered in order to compare the numerical results with the analytical and experimental results presented in Chapter 6 (Figures 6.6 to 6.9). For the numerical calculations, the cylinder surface was divided in to 40 elements. Each element had two end nodes and one mid node, and there were in total 80 nodes, as shown in Figure 8.2. The incident sound pressure P^I of the equation (8.13) on each node due to a point source can be calculated numerically as follows:

$$P^I = -i\omega\rho_o \frac{Q_s}{4\pi R} e^{ikR}, \quad (8.15)$$

where $R = \sqrt{q^2(X, Y) - p^2(x, y)}$, is the distance between the integration point $p(x, y)$

and the source point $q(X, Y)$, and Q_s is the source amplitude. Figures 8.6, 8.7, 8.8 and 8.9 show the experimental and normalised analytical and numerical results for various frequencies. Note that in the experimental findings the source strength was not measured. Hence the source amplitude $1 + i \text{ m}^3/\text{s}$ was used for the analytical and numerical calculations, and the normalised analytical and numerical results are shown in Figures 8.6 to 8.9. The relative sound pressure at 180° or -180° , obtained from the experimental result at each frequency, has been used to normalise the analytical and numerical results, which show very good agreement with the experimental results. The difference in relative sound pressure magnitude at the back of the experimental cylinder between the experimental and analytical results has already been discussed in Chapter 6 (Section 6.4) for frequencies of 700Hz and 1.5 kHz respectively. It can be seen that the sound pressure amplitude at $\phi_i = 0^\circ$ at the back of the cylinder, using numerical calculations is very close to the analytical results. It is worth noting that only 80 surface nodes were used for the numerical calculations to keep the computational time manageable, which is very small. In spite of that, for each frequency there is no significant difference between the analytical and numerical sound pressure patterns. This indicates that the BEM technique can be used for point source calculations for more complex structures such as the Boeing cylinder and the RSLVF.

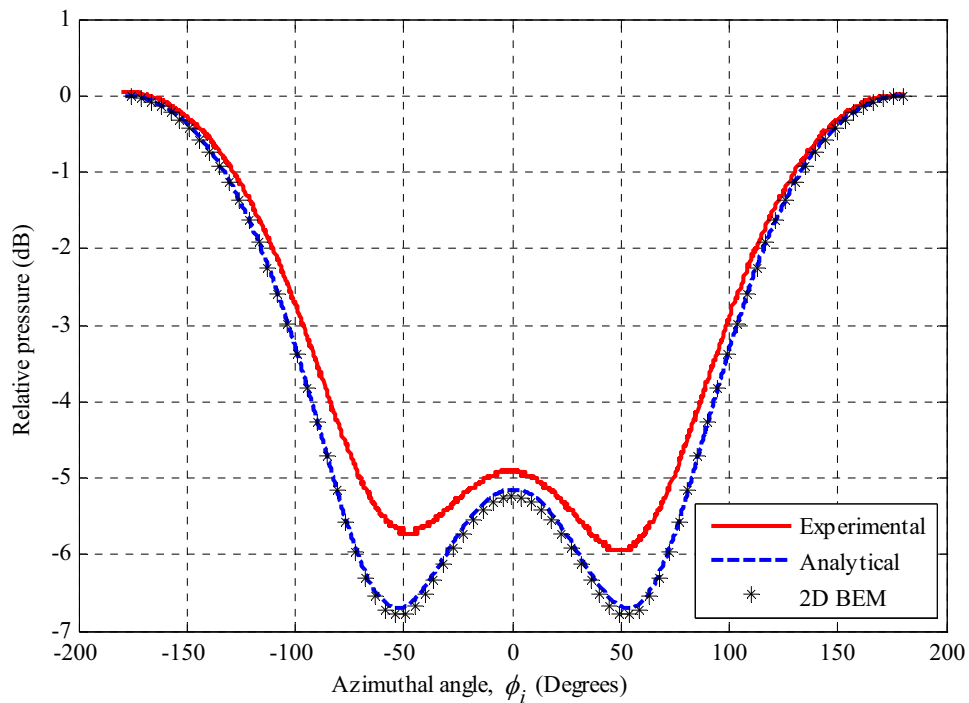


Figure 8.6: Comparisons between the experimental, analytical and 2D BEM results for pressure at the surface of the experimental cylinder of radius 0.057m, for $f = 700$ Hz and $ka = 0.73$.

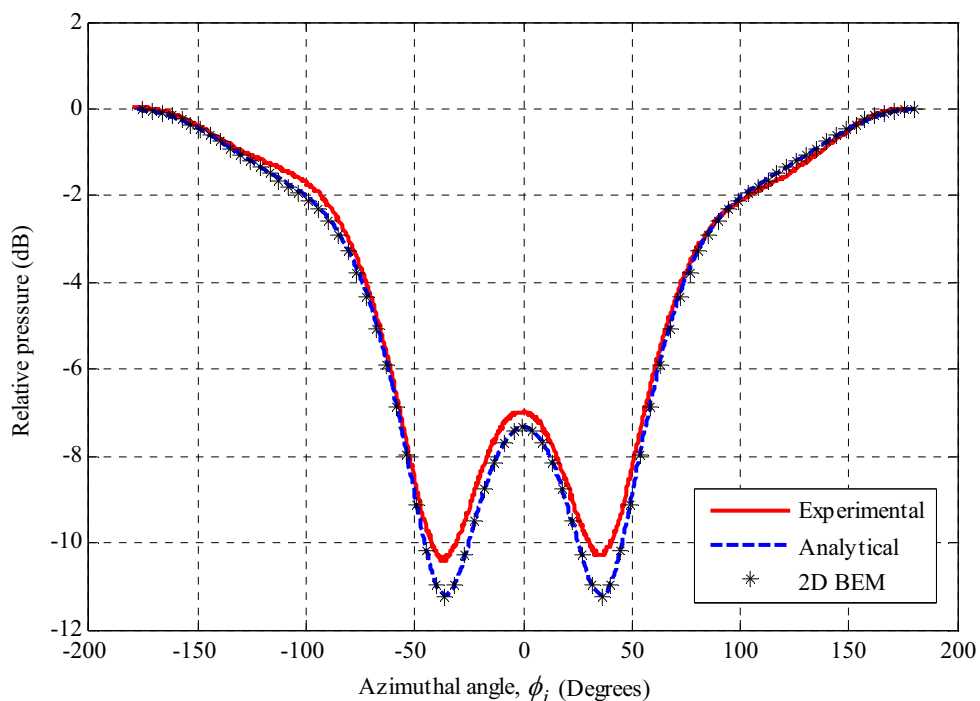


Figure 8.7: Comparisons between the experimental, analytical and 2D BEM results for pressure at the surface of the experimental cylinder of radius 0.057m, for $f = 1.5$ kHz and $ka = 1.57$.

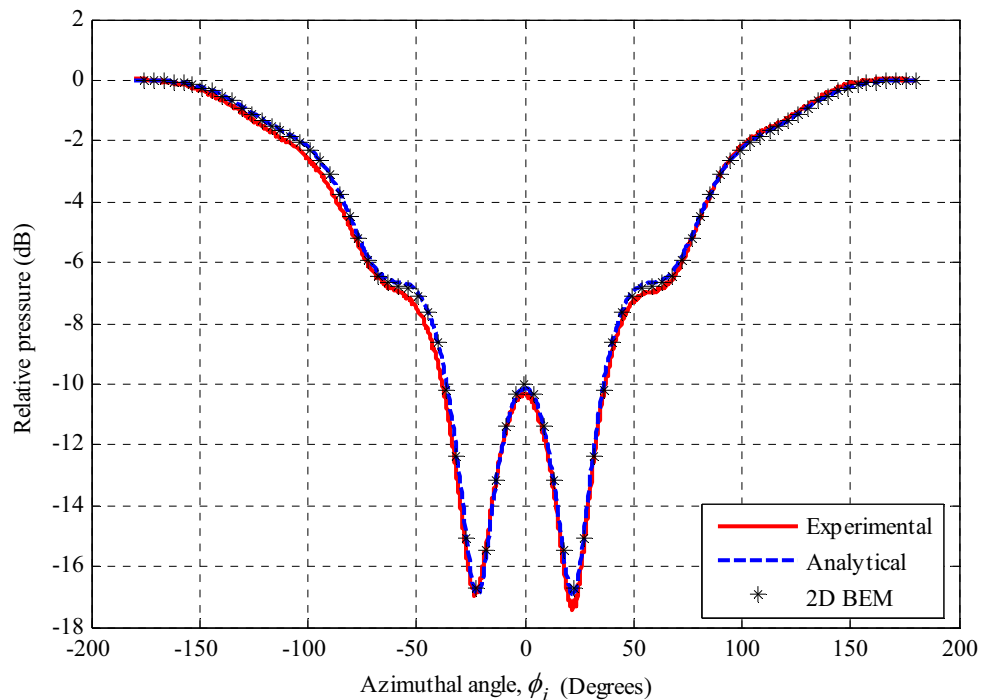


Figure 8.8: Comparisons between the experimental, analytical and 2D BEM results for pressure at the surface of the experimental cylinder of radius 0.057m, for $f = 3$ kHz and $ka = 3.13$.

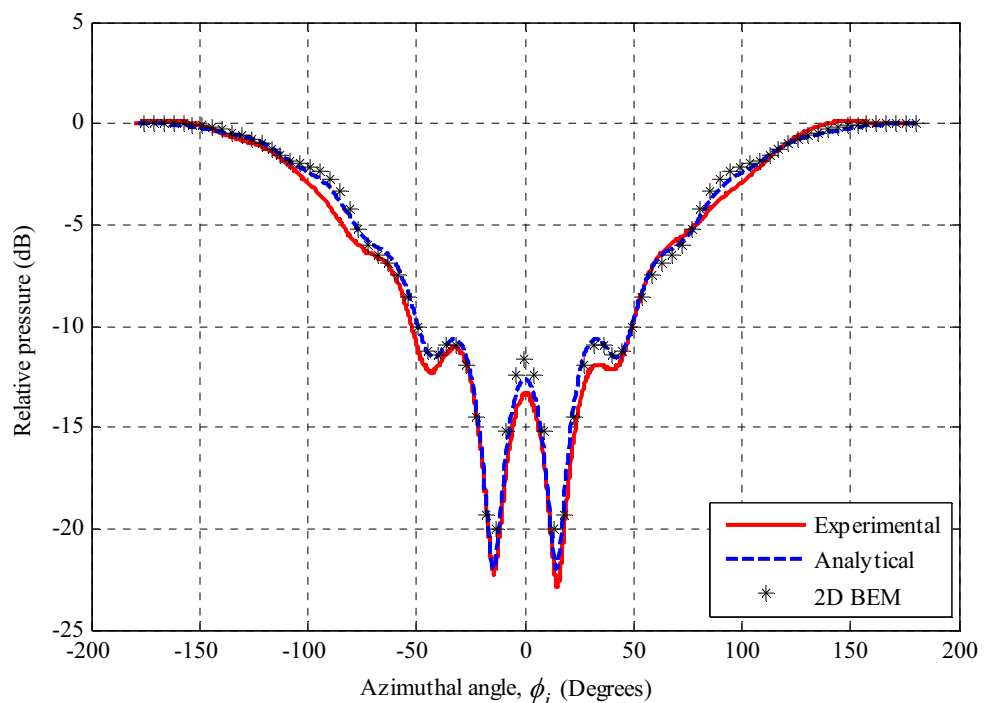


Figure 8.9: Comparisons between the experimental, analytical and 2D BEM results for pressure at the surface of the experimental cylinder of radius 0.057m, for $f = 5$ kHz and $ka = 5.22$.

A comparison was made between the use of the line source theory derived in Chapter 5 and the same problem solved here using 2D BEM. In this case, since n point sources, $q_n(X, Y)$, are located outside the solid surface, the distances between m integration points, $p_m(x, y)$, and n source points, $q_n(X, Y)$, need to be determined for the incident sound pressure resulting from each source. Hence, the right side of the equation (8.13) can be calculated as follows:

$$P^I = \sum_{n=0}^{N-1} -i\omega\rho_o \frac{Q_s}{4\pi R} e^{ikR}, \quad (8.16)$$

where $R = \sqrt{q_n^2(X, Y) - p_m^2(x, y)}$, n and N are the point source number and total number of point sources in an array acting as a line source respectively, and Q_s is the source amplitude. Consider the case of 15 point sources placed along the negative X axis outside of a cylinder of radius 0.057m (see Figure 5.8 in Chapter 5 for the line source arrangement), which is the radius of the experimental cylinder. The distance between sources is 1.5m. The distance of the nearest source from the cylinder surface is 1m. Each source generates the same frequency. The total sound pressure comparison between the analytical and 2D BEM results due to the 15 point sources of arbitrary amplitudes and random phases (Table 5.1 in Chapter 5 has been used for arbitrary amplitudes and phases) is shown in Figure 8.10 for $ka = 5$. This shows good agreement between the analytical and BEM results and indicates that the BEM technique can be used for line source calculations for more complex structures such as the Boeing cylinder and the RSLVF.

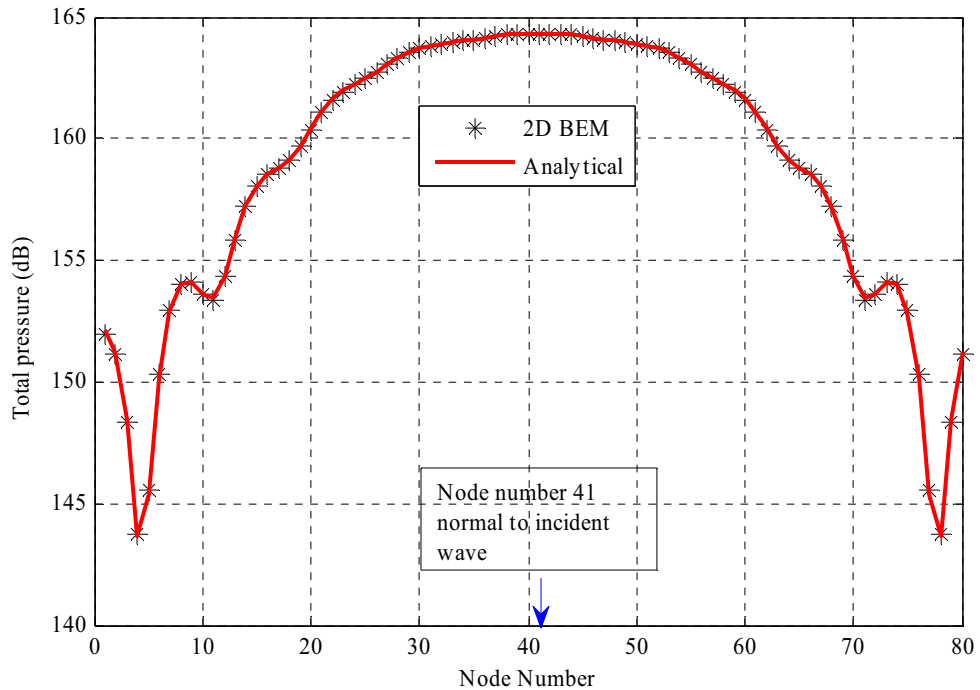


Figure 8.10: Total sound pressure comparison between the analytical and 2D BEM results for a line source of 15 point sources of arbitrary amplitudes and phases (see Table 5.1 in Chapter 5) placed on the negative X axis for $ka = 5$. The radius of the cylinder is 0.057m. [Reference pressure $20\mu\text{Pa}$]

Finally, the results from the derivation given in Chapter 4, to calculate the sound pressure field at locations outside of a cylinder were compared with results calculated using 2D BEM. In this case, from the BEM point of view, the sound pressure needs to be calculated on the field points outside the surface, and the matrix formulation for the total sound pressure on the field points becomes

$$\{\mathbf{P}_f\} = [\mathbf{A}_f] \{\mathbf{P}_i\} - \mathbf{P}_f^I, \quad (8.17)$$

where the subscripts f and i denote the field points and the integration points on the surface respectively. $[\mathbf{A}_f]$ is the coefficient matrix for the field points, \mathbf{P}_f^I is the incident sound pressure on the field points and $\{\mathbf{P}_i\}$ is the pressure associated with each node on the surface. $\{\mathbf{P}_i\}$ can be calculated in a similar way as indicated in equation (8.13) for the

total pressure on the surface. On each field node the incident sound pressure P_f^I of equation (8.17) can be calculated for plane waves as follows:

$$P_f^I = P^o e^{ikxy}, \quad (8.18)$$

where x and y represent the field node position along the X and Y coordinates respectively. To calculate only the scattered sound pressure at the field points, the incident sound pressure term given in equation (8.17) can be omitted. The comparisons are shown between the analytical and 2D BEM results (considering plane incident waves travelling from left to right) for the scattered and total sound pressure distributions on the 80 field points placed circumferentially at a distance of $5a$ (five times the cylinder radius) from the origin of a cylinder of radius a , for different values of ka in Figures 8.11(a-c) and 8.12(a-c) respectively. The results show very good agreement between the analytical and BEM techniques. From these results it can be concluded that the mathematical derivations presented in Chapter 4 are suitable for calculating the sound pressure field at any location from a cylinder, or alternatively it can be stated that the BEM technique is also suitable. However, it can be shown that the 2D BEM technique is not applicable when $ka > 15$. The discrepancies between the analytical and BEM results for the scattered and total sound pressures on the field points around a cylinder of radius a are shown for the case when $ka = 20$ in Figures 8.13 and 8.14. It is notable that the discrepancies between the analytical and BEM results are presented here for $ka = 20$ and not for $ka = 16$, because the discrepancies between the results are more clearly visible when $ka = 20$.

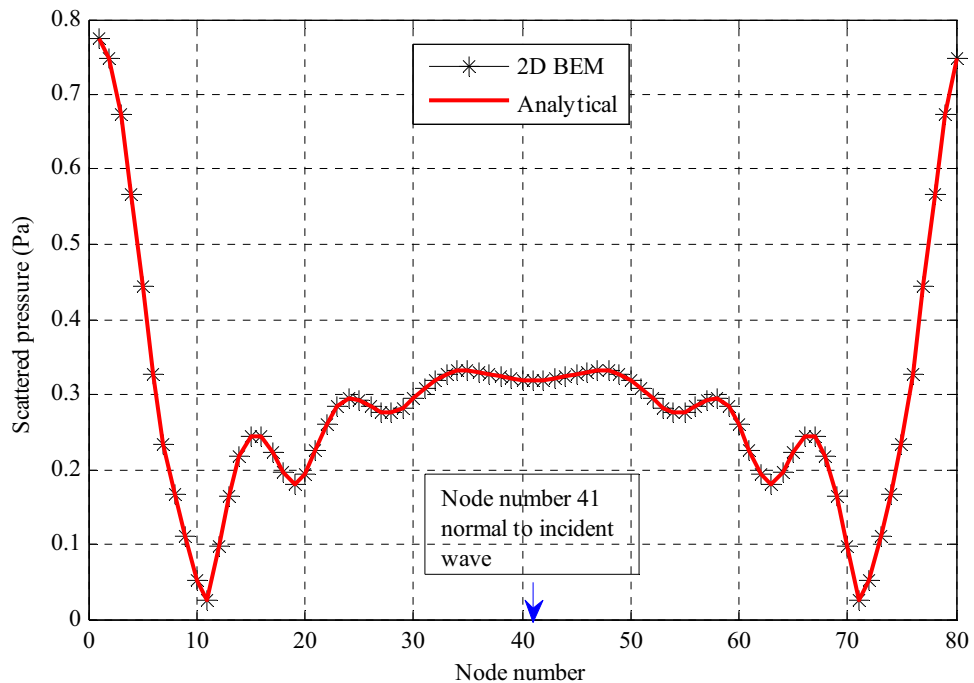


Figure 8.11(a): Scattered sound pressure comparison between the analytical and 2D BEM results at a distance of $5a$ (five times the cylinder radius) from the origin of a cylinder of radius a , for incident plane waves travelling from left to right, for $ka = 5$. [Incident pressure amplitude $P^o = 1 \text{ Pa}$]

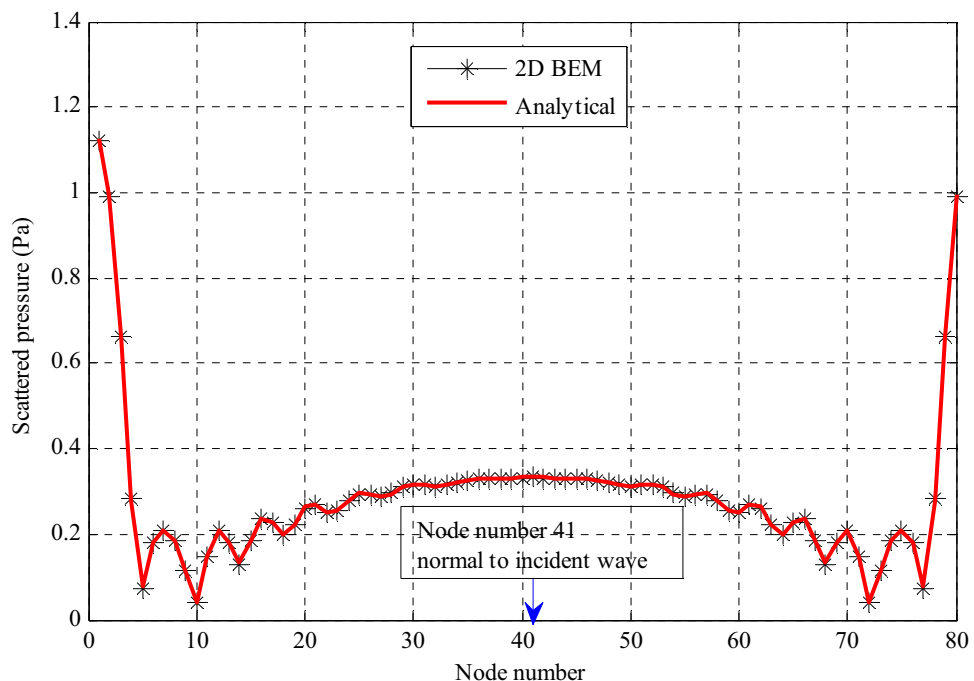


Figure 8.11(b): Scattered sound pressure comparison between the analytical and 2D BEM results at a distance of $5a$ (five times the cylinder radius) from the origin of a cylinder of radius a , for incident plane waves travelling from left to right, for $ka = 10$. [Incident pressure amplitude $P^o = 1 \text{ Pa}$]

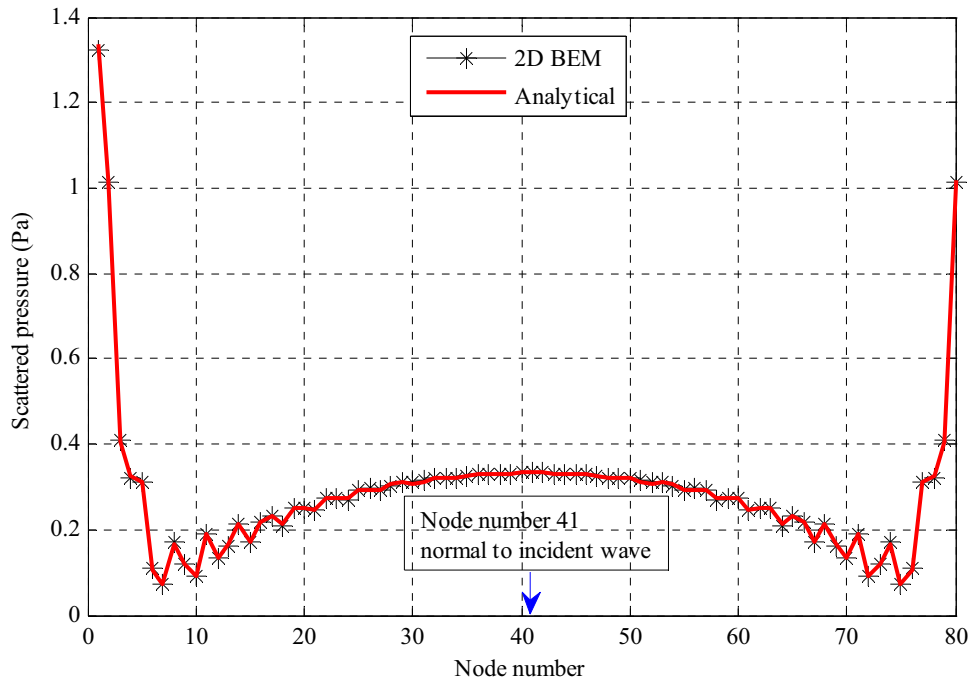


Figure 8.11(c): Scattered sound pressure comparison between the analytical and 2D BEM results at a distance of $5a$ (five times the cylinder radius) from the origin of a cylinder of radius a , for incident plane waves travelling from left to right, for $ka = 15$. [Incident pressure amplitude $P^0 = 1 \text{ Pa}$]

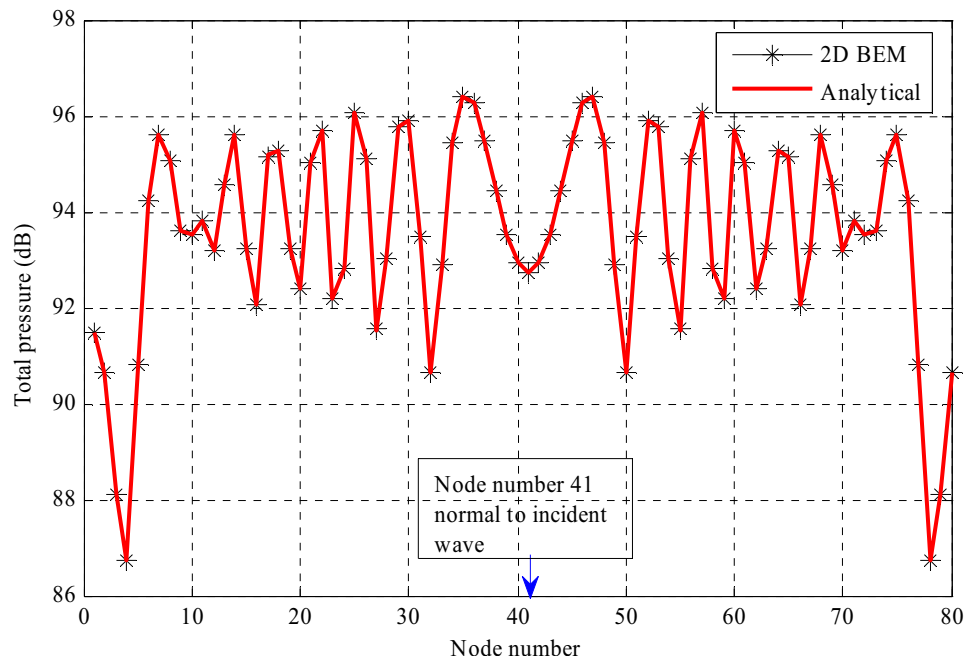


Figure 8.12(a): Total sound pressure comparison between the analytical and 2D BEM results at a distance of $5a$ (five times the cylinder radius) from the origin of a cylinder of radius a , for incident plane waves travelling from left to right, for $ka = 5$. [Reference pressure $20 \mu\text{Pa}$ and incident pressure amplitude $P^0 = 1 \text{ Pa}$]

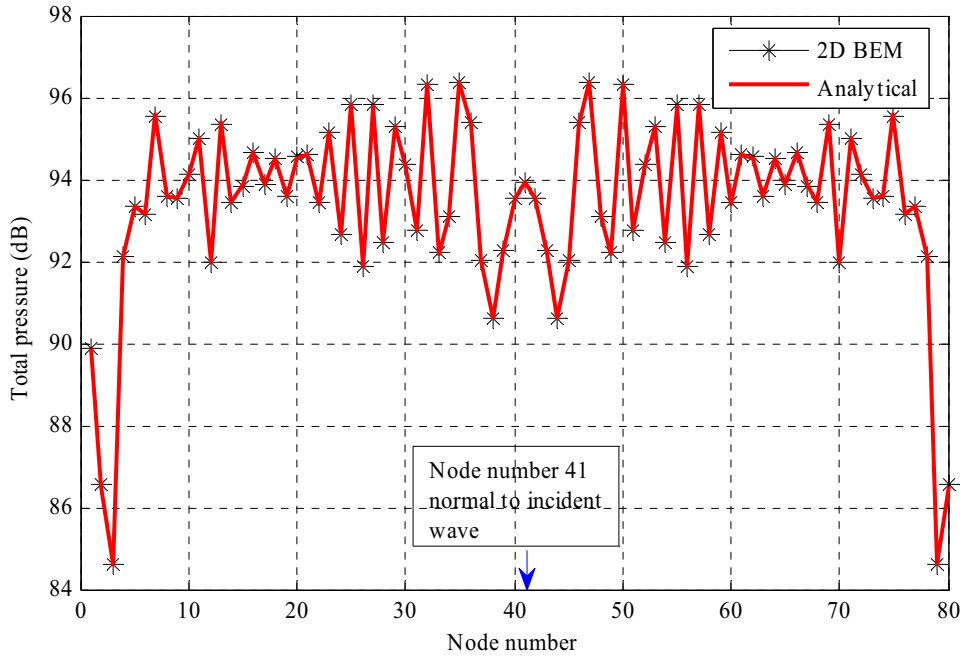


Figure 8.12(b): Total sound pressure comparison between the analytical and 2D BEM results at a distance of $5a$ (five times the cylinder radius) from the origin of a cylinder of radius a , for incident plane waves travelling from left to right, for $ka = 10$. [Reference pressure $20\mu\text{Pa}$ and incident pressure amplitude $P^o = 1\text{ Pa}$]

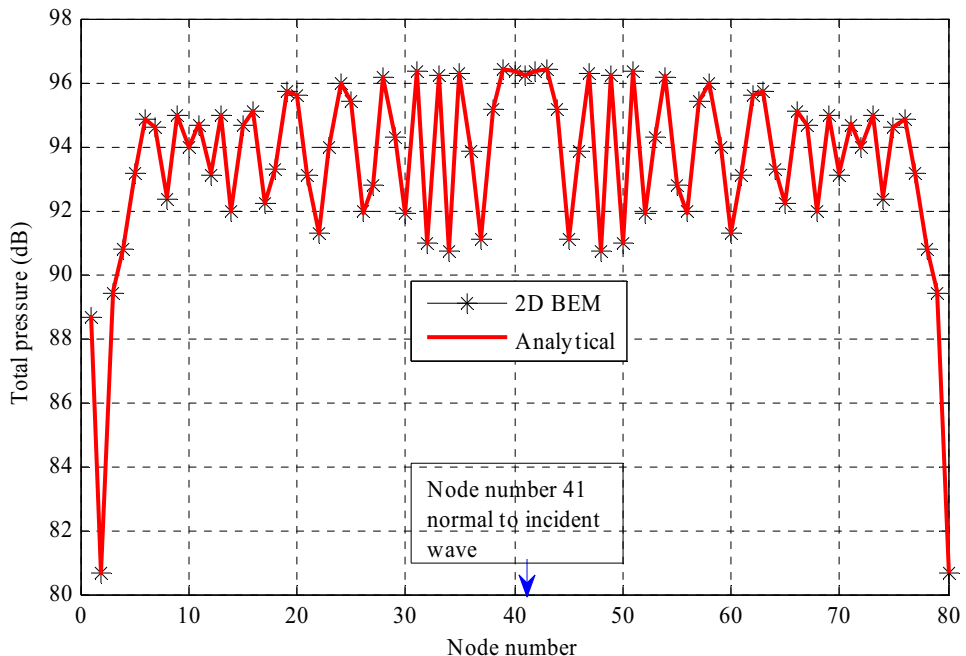


Figure 8.12(c): Total sound pressure comparison between the analytical and 2D BEM results at a distance of $5a$ (five times the cylinder radius) from the origin of a cylinder of radius a , for incident plane waves travelling from left to right, for $ka = 15$. [Reference pressure $20\mu\text{Pa}$ and incident pressure amplitude $P^o = 1\text{ Pa}$]

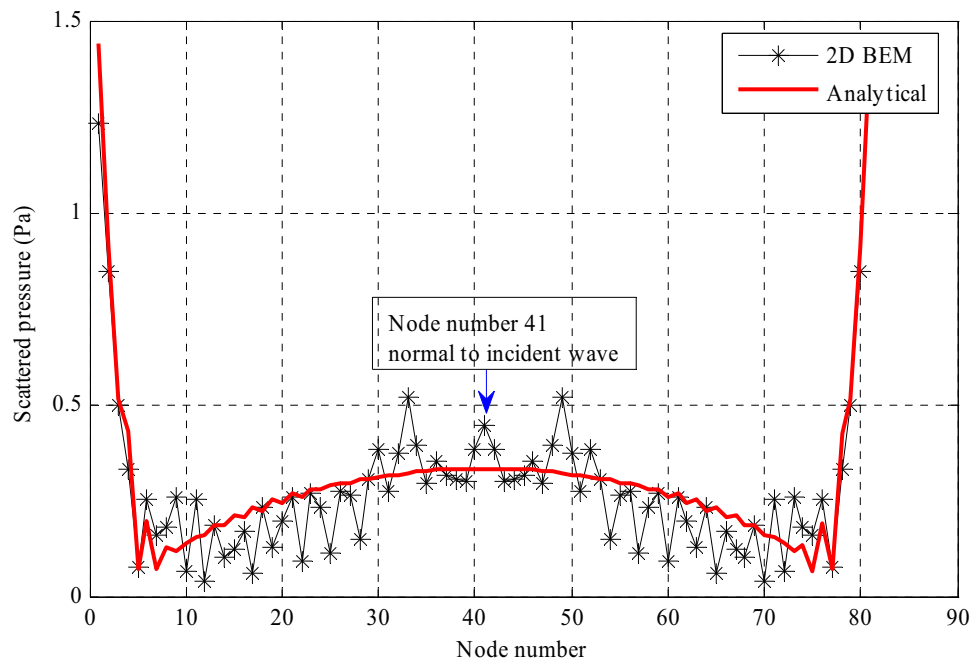


Figure 8.13: Scattered sound pressure comparison between the analytical and 2D BEM results at a distance of $5a$ (five times the cylinder radius) from the origin of a cylinder of radius a , for incident plane waves travelling from left to right, for $ka = 20$. [Incident pressure amplitude $P^o = 1 \text{ Pa}$]

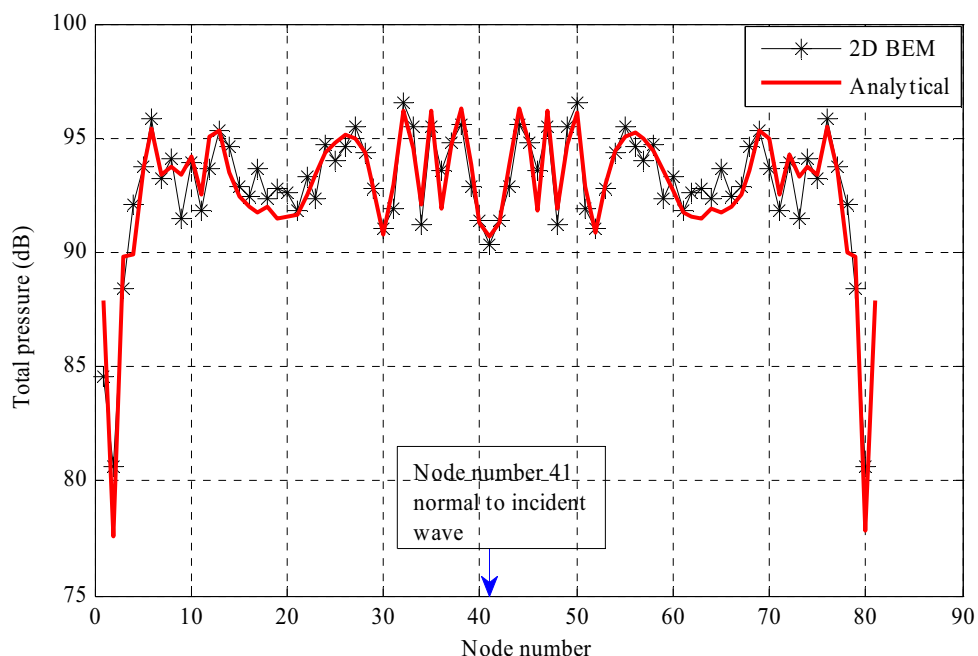


Figure 8.14: Total sound pressure comparison between the analytical and 2D BEM results at a distance of $5a$ (five times the cylinder radius) from the origin of a cylinder of radius a , for incident plane waves travelling from left to right, for $ka = 20$. [Reference pressure $20 \mu\text{Pa}$ and incident pressure amplitude $P^o = 1 \text{ Pa}$]

8.5.2 Verifications of 3D BEM

For the 3D BEM verification the experimental cylinder was used and a frequency of 1.5kHz (the same as investigated in the experiment) was applied. The purpose of this verification was to see whether the 3D BEM technique could give good results for the small diameter cylinder (diameter is 0.114m and aspect ratio is 12.7). The geometry of the cylinder was built in ANSYS using quadratic eight node elements, as shown in Figure 8.15(a). A ‘mesh-only’ element, which is MESH200, was used to generate surface elements and nodes. Figure 8.15(b) shows the FEA model of the experimental cylinder built in ANSYS. The model consists of 200 elements and 582 nodes on the surface. It was then imported into MATLAB for 3D BEM analysis. Figure 8.16 shows the imported model of the experimental cylinder and also shows the surface elements and nodes.

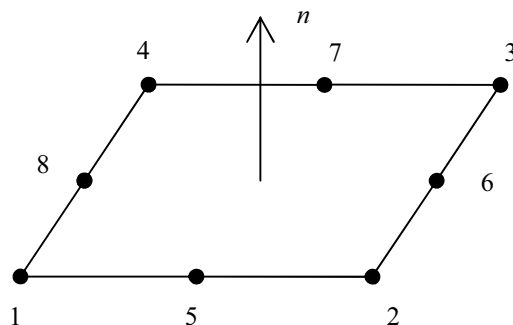


Figure 8.15(a): 8-node quadratic element.

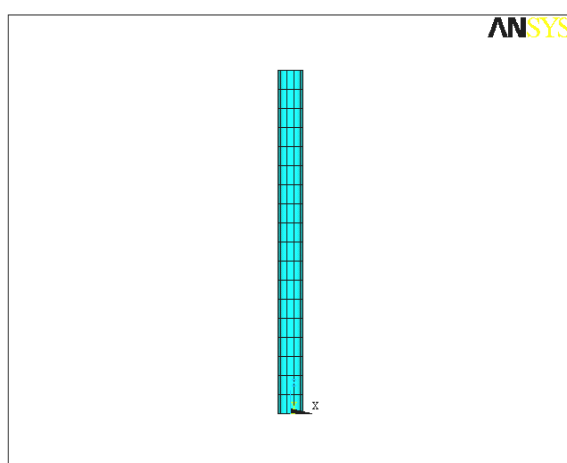


Figure 8.15(b): FEA model of the experimental cylinder.

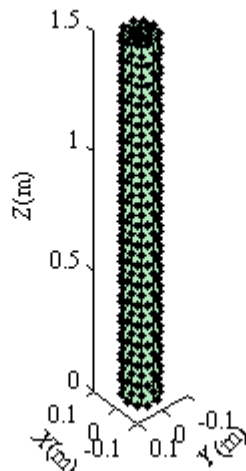


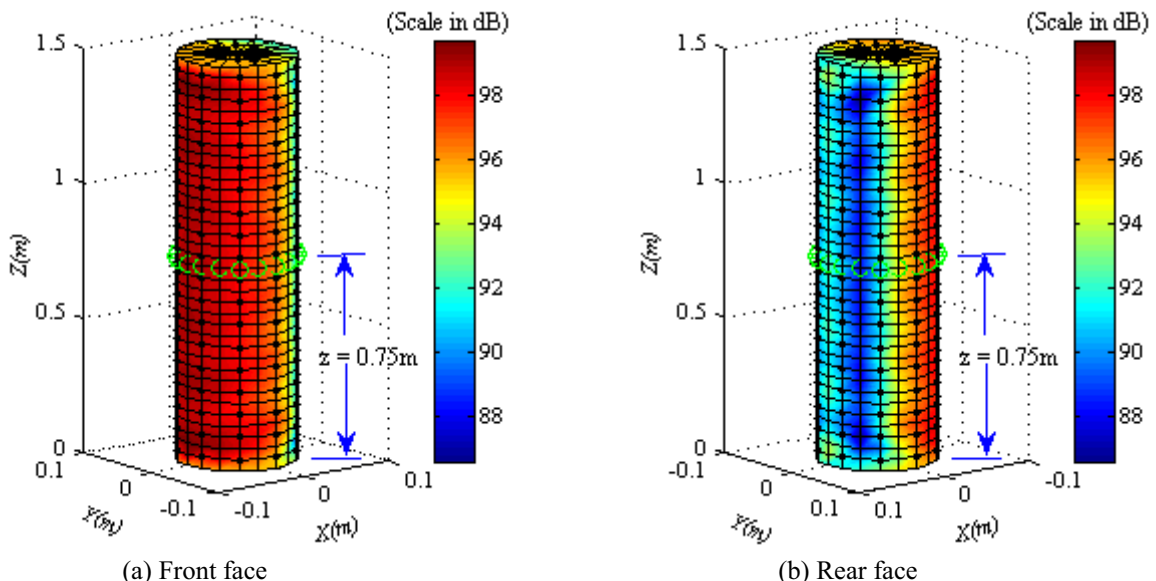
Figure 8.16: BEM model of the experimental cylinder showing the surface elements and nodes.

At first, a plane wave situation was considered where the source is assumed located at an infinite distance from the cylinder with the waves travelling in the positive X direction. For this case, the incident sound pressure P^I of equation (8.13) on each node due to plane waves could be calculated numerically as follows:

$$P^I = P^o e^{ikxyz}, \quad (8.19)$$

where x, y and z represent the node position along the X, Y and Z coordinates respectively. The total sound pressure calculated using BEM is shown in Figures 8.17 (a-b) for frequency, $f = 1.5$ kHz ($ka = 1.57$). The pressure on each circumferential node at the middle of the cylinder (nodes are shown by green circles in Figures 8.17a and 8.17b) was calculated using BEM analysis and compared with the analytical result calculated using equation (3.18). The comparison is shown in Figure 8.18, which shows good agreement between the two results. The small difference in sound pressure magnitude between the results occurs because the BEM analysis can take into account the diffraction effects due to both ends of the experimental cylinder whereas the analytical model assumes the cylinder length to be infinite with no ends. It can be seen in Figures 8.17(a-b) that the sound pressure is maximum near the ends of the cylinder due to diffraction around both ends. The BEM analysis can determine the

sound pressure near the ends of a rigid object by using a quarter-point technique ($r^{2/3}$) for particle velocity near the edge of the rigid object, where r is distance from the edge. This approach approximates the condition that the particle velocity tends to infinity as r tends to zero. This has been explained in detail by Juhl (1993). Unfortunately, it is not yet possible to consider that analytically. However, it can be shown that the analytical and BEM results match more accurately if the height of the cylinder in the BEM model is made sufficiently large so that the wave diffraction from the ends to the middle of the cylinder is reduced to an insignificant amount. Figures 8.19 (a-b) show the total sound pressure distribution on the surface of the extended cylinder of length 5m (aspect ratio is 43.86). For this case, the pressure comparison between the analytical and BEM results on the circumferential nodes at the middle of the cylinder is shown in Figure 8.20. The comparison indicates that the BEM technique can produce results that agree well with the analytical results when the aspect ratio is high. Based on the work of Juhl (1993), it can be assumed that the quarter-point technique can accurately take into account the diffraction effects from the ends for the BEM analysis.



Figures 8.17(a-b): Numerical results of the total sound pressure distribution at the surface of the experimental cylinder, for plane waves incident on the front face, for $f = 1.5$ kHz and $ka = 1.57$. The green circles show the circumferential nodes at the middle of the cylinder. [Reference pressure $20\mu\text{Pa}$ and incident pressure magnitude $P^O = 1\text{ Pa}$]

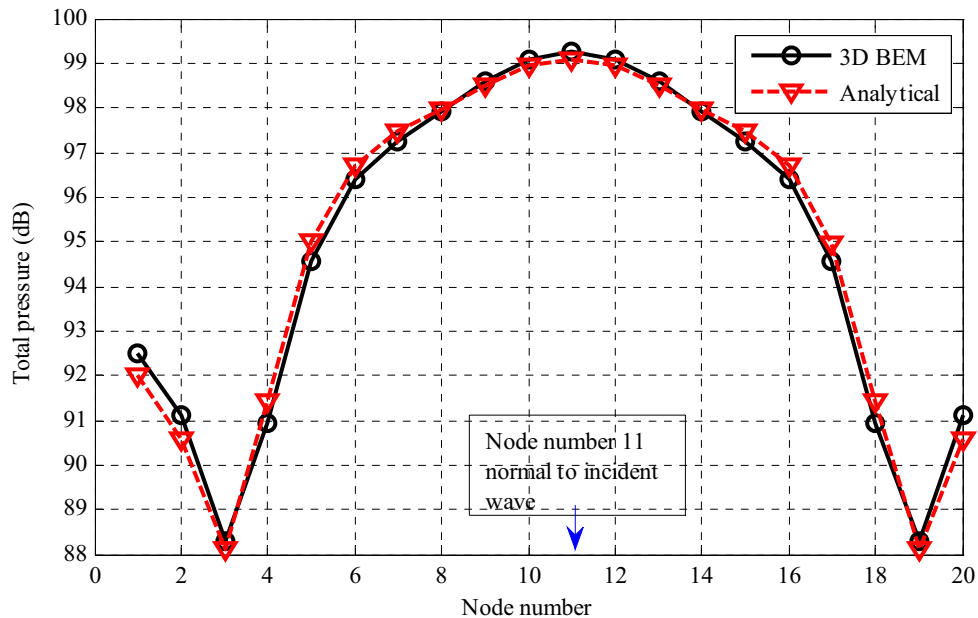
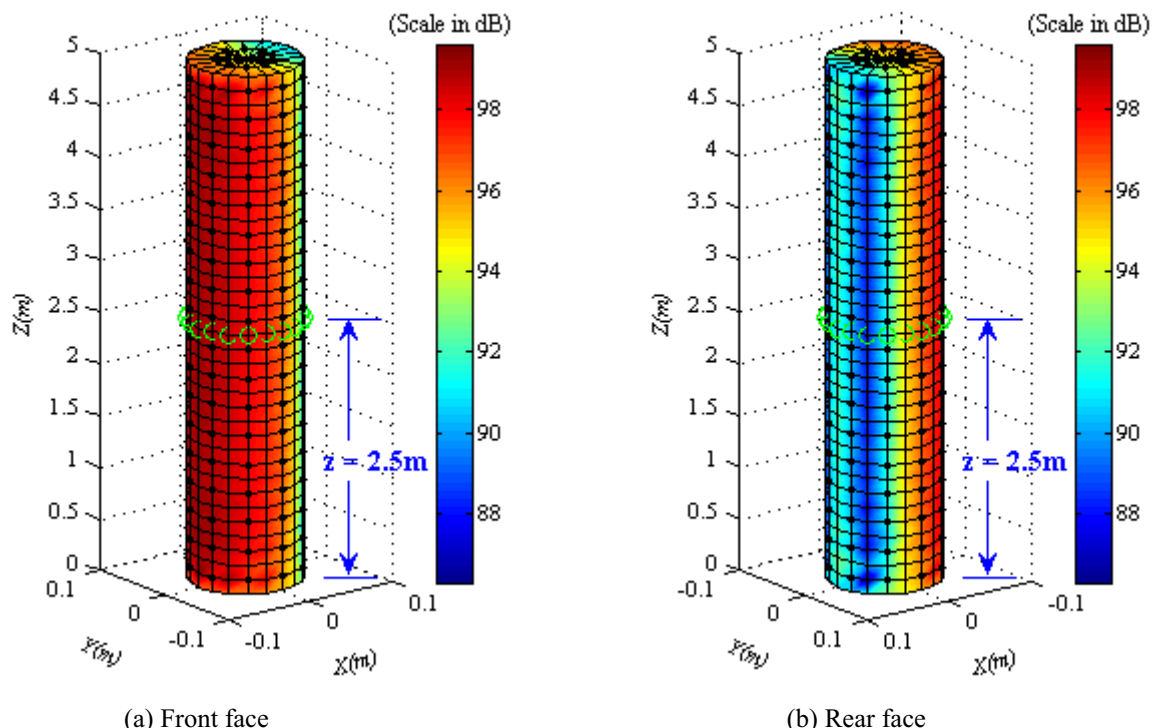


Figure 8.18: Total sound pressure comparison between the analytical and 3D BEM results calculated on the circumferential nodes at the middle ($z = 0.75\text{m}$, see Figures 8.17a and 8.17b) of the experimental cylinder, for plane waves incident on the front face, for $f = 1.5\text{kHz}$ and $ka = 1.57$. [Reference pressure $20\mu\text{Pa}$ and incident pressure magnitude $P^O = 1\text{Pa}$]



Figures 8.19(a-b): Numerical results of the total sound pressure distribution at the surface of the extended cylinder, for plane waves incident on the front face, for $f = 1.5\text{ kHz}$ and $ka = 1.57$. The green circles show the circumferential nodes at the middle of the cylinder. [Reference pressure $20\mu\text{Pa}$ and incident pressure magnitude $P^O = 1\text{Pa}$]

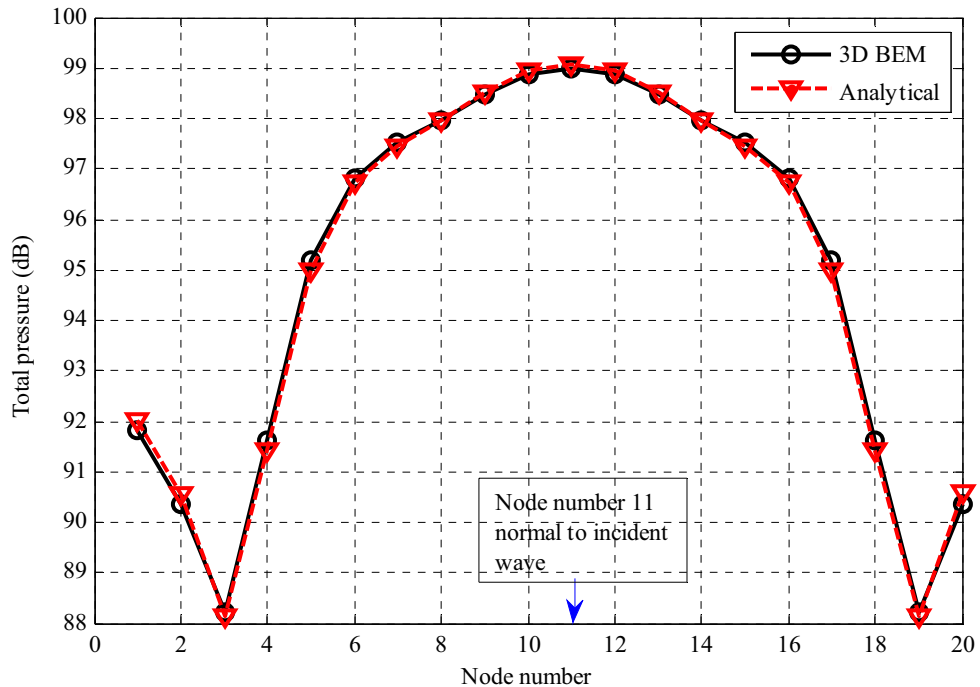
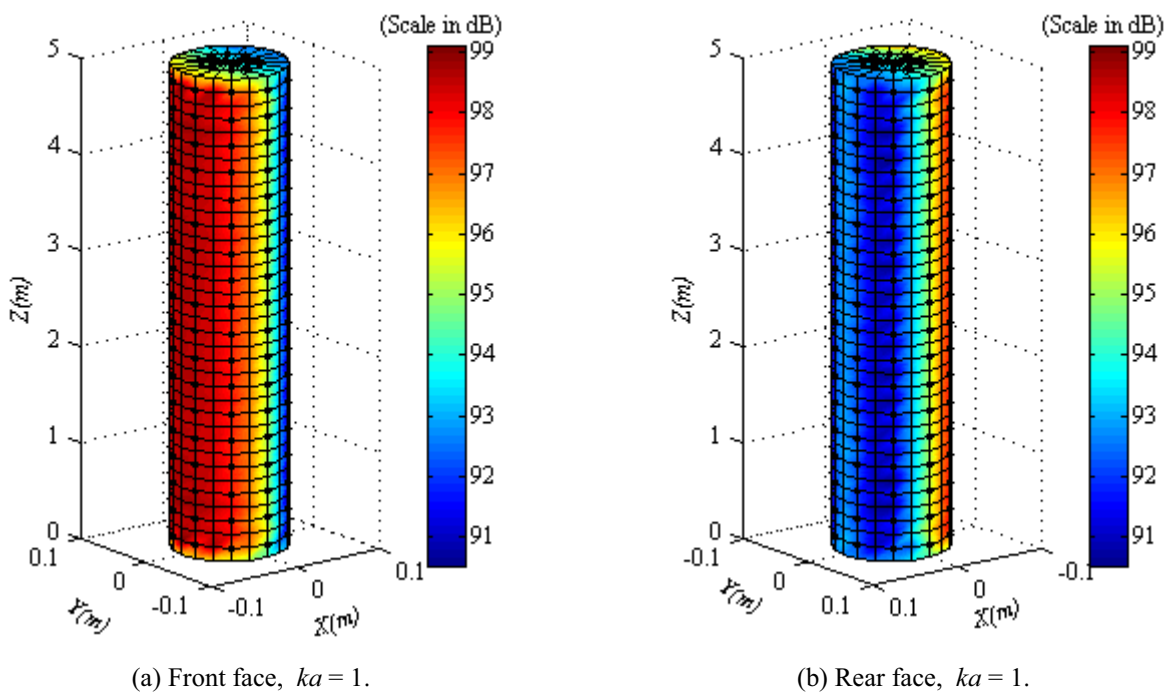
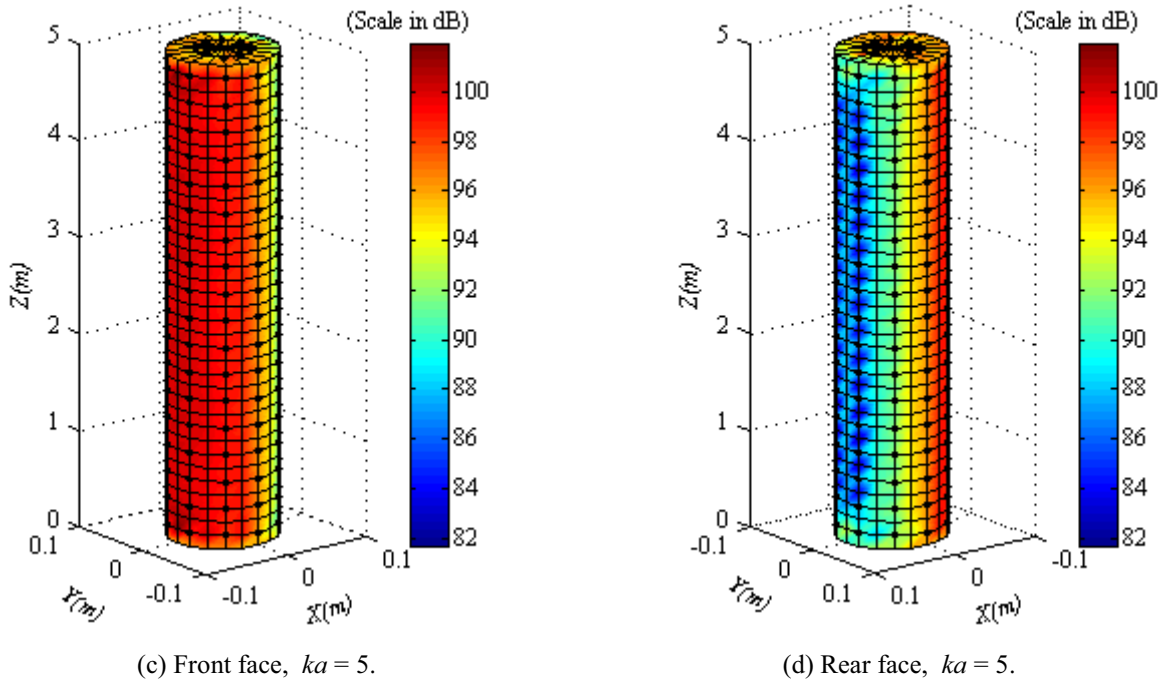


Figure 8.20: Total sound pressure comparison between the analytical and 3D BEM results calculated on the circumferential nodes at the middle ($z = 2.5\text{m}$, see Figures 8.19a and 8.19b) of the extended cylinder of length 5m, for plane waves incident on the front face, for $f = 1.5\text{kHz}$ and $ka = 1.57$. [Reference pressure $20\mu\text{Pa}$ and incident pressure magnitude $P^o = 1\text{ Pa}$]

The limiting value of ka for valid BEM analysis for the extended cylinder of length 5m and radius $a = 0.057\text{m}$ (aspect ratio is 43.86) was investigated. The extended cylinder was considered to avoid the effects of diffraction of sound from both ends to the middle of the cylinder, which could not be easily modelled analytically. The numerical results for the sound pressure distribution at the surface of the cylinder for $ka = 1$ and 5 respectively, are shown in Figures 8.21(a-d). The sound pressures on each circumferential node at the middle of the cylinder ($Z = 2.5\text{m}$, nodes are shown by green circles in Figures 8.19a and 8.19b) was calculated using BEM and compared with the analytical results calculated using equation (3.18) in Figures 8.22 and 8.23 respectively. The comparisons show good agreement with the analytical results. However, when $ka = 6$, the 3D BEM analysis breaks

down for using quadratic eight node elements. For this particular case, the numerical result is shown in Figures 8.24(a-b) and the comparison with the analytical result calculated using equation (3.18) is shown in Figure 8.25, where a discrepancy can be seen. As already discussed in the preceding section, the reason of this type of break down is that the integration of *Helmholtz equation* does not behave uniquely at a certain characteristic frequency. Thus, It can be concluded that the 3D BEM analysis using quadratic eight node elements gives reliable results for the extended cylinder of length 5m and radius 0.057m for values of ka up to $ka = 5$ ($f \leq 4.8\text{kHz}$). If the value of ka increases beyond $ka = 5$, the analysis breaks down (as already shown for the case, $ka = 6$). However, the range over which 3D BEM gives good results could be increased by increasing the density of nodes and elements on the surface, but this would result in an excessive increase in the computational time with little benefit and hence was not done for the current numerical analyses.





Figures 8.21(a-d): Numerical results of the total sound pressure distribution at the surface of the extended cylinder of length 5m, for plane waves incident on the front face, for $ka = 1$, and 5 respectively. [Reference pressure $20\mu\text{Pa}$ and incident pressure magnitude $P^o = 1\text{ Pa}$]

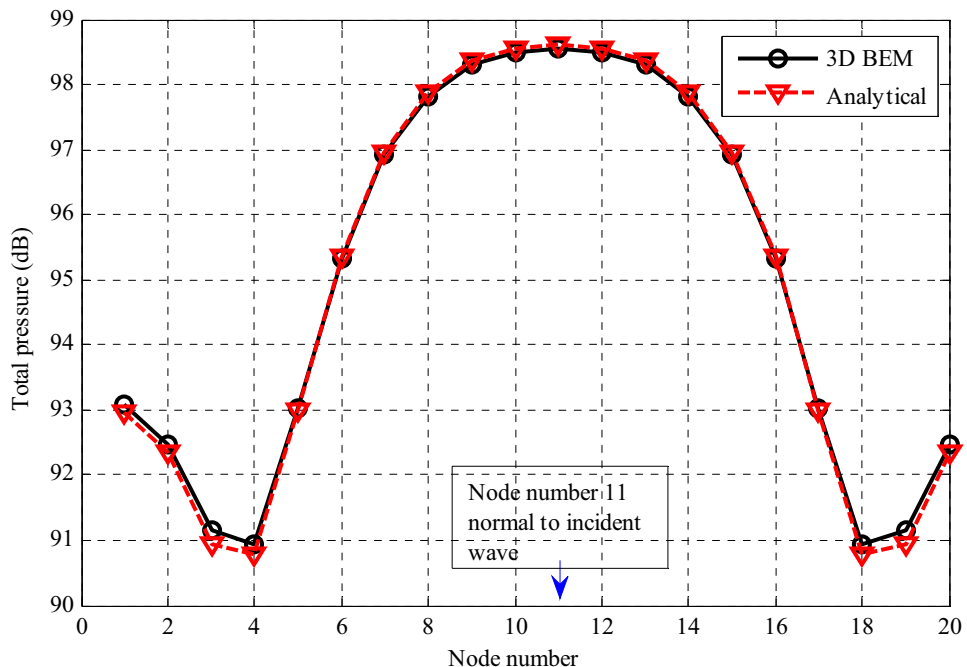


Figure 8.22: Total Sound pressure comparison between the analytical and 3D BEM results calculated on the circumferential nodes at the middle ($z = 2.5\text{m}$, see Figures 8.19a and 8.19b) of the extended cylinder of length 5m, for plane waves incident on the front face, for $ka = 1$. [Reference pressure $20\mu\text{Pa}$ and incident pressure magnitude $P^o = 1\text{ Pa}$]

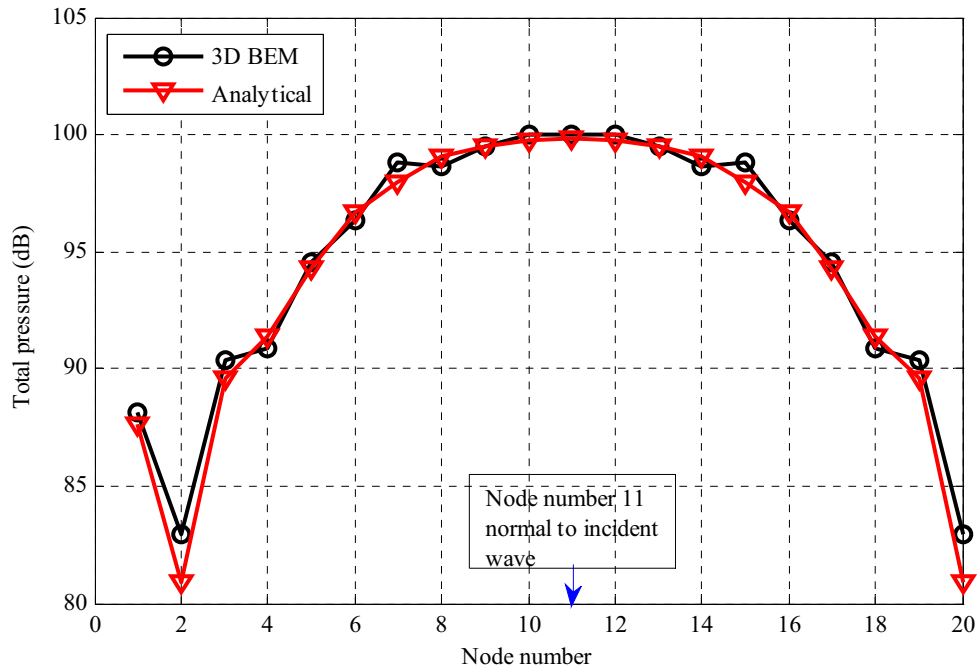
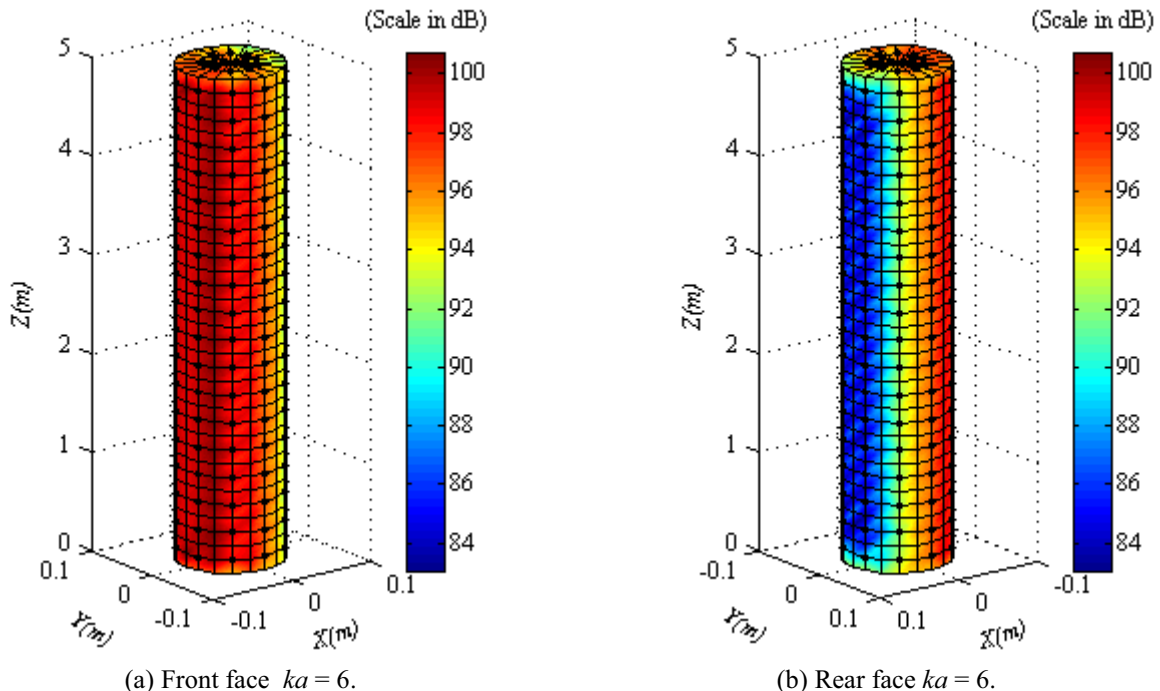


Figure 8.23: Total sound pressure comparison between the analytical and 3D BEM results calculated on the circumferential nodes at the middle ($z = 2.5\text{m}$, see Figures 8.19a and 8.19b) of the extended cylinder of length 5m, for plane waves incident on the front face, for $ka = 5$. [Reference pressure $20\mu\text{Pa}$ and incident pressure magnitude $P^O = 1\text{ Pa}$]



Figures 8.24(a-b): Numerical results of the total sound pressure distribution at the surface of the extended cylinder of length 5m, for plane waves incident on the front face, for $ka = 6$. [Reference pressure $20\mu\text{Pa}$ and incident pressure magnitude $P^O = 1\text{ Pa}$]

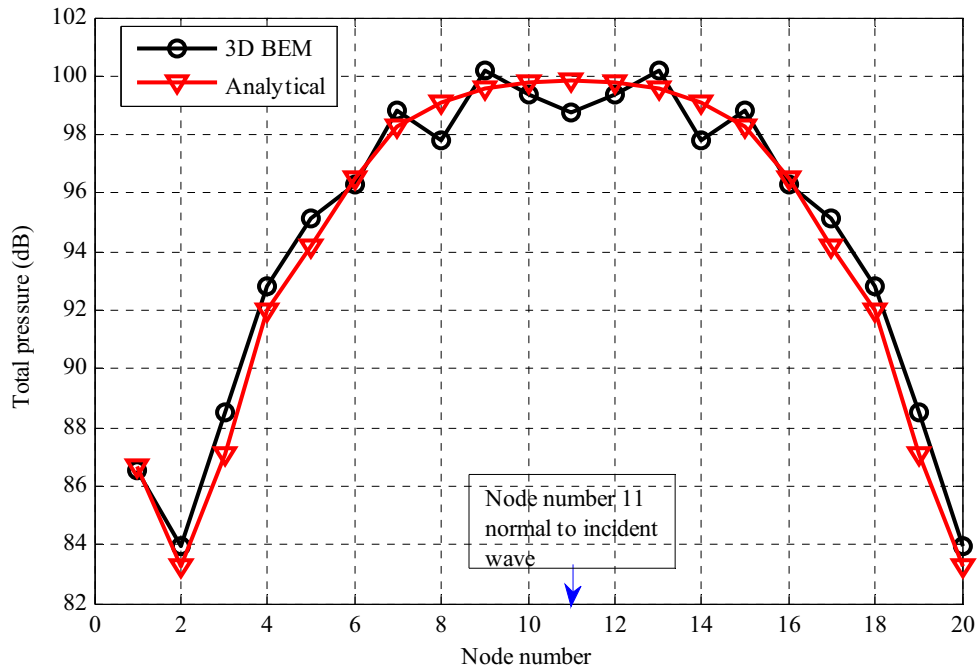


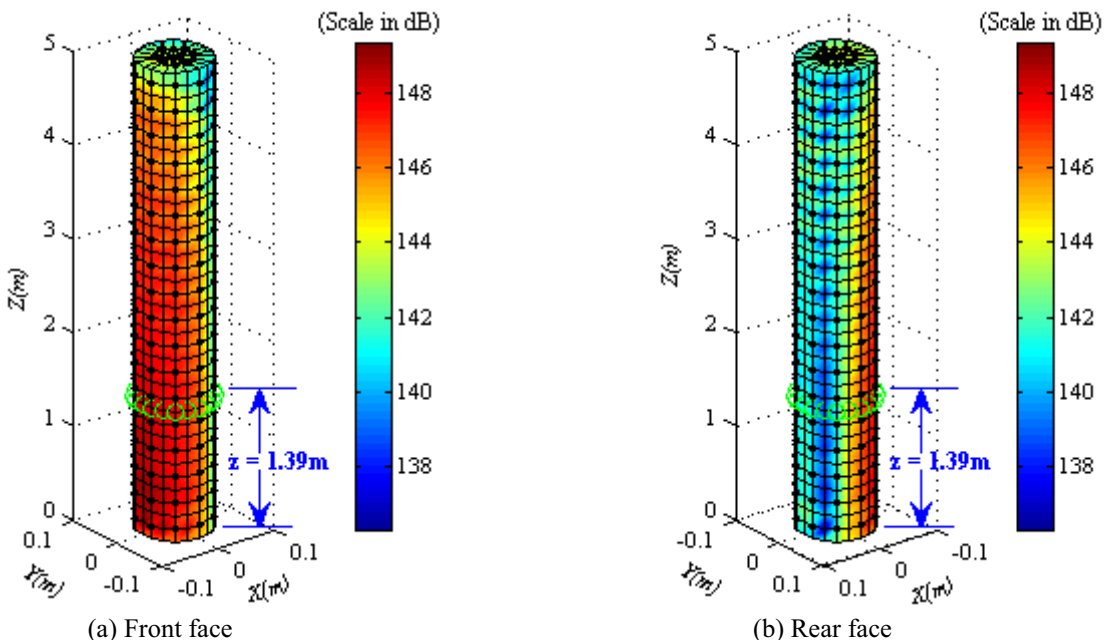
Figure 8.25: Total sound pressure comparison between the analytical and 3D BEM results calculated on the circumferential nodes at the middle ($z = 2.5\text{m}$, see Figures 8.19a and 8.19b) of the extended cylinder of length 5m, for plane waves incident on the front face, for $ka = 6$. [Reference pressure $20\mu\text{Pa}$ and incident pressure magnitude $P^O = 1\text{ Pa}$]

Another verification of the 3D BEM technique was conducted by placing a point source of amplitude $1 + i \text{ m}^3/\text{s}$ at a location $X = -4.1\text{m}$ (same as used in the experiment), $Y = 0\text{m}$ and $Z = 0\text{m}$ (consider Figure 7.1 for the source geometry), and predicting the acoustic pressure on the surface of the extended cylinder of length 5m and radius 0.057m (aspect ratio is 43.86). For this case, the incident pressure P^I of equation (8.13) on each node due to a point source may be calculated numerically as follows:

$$P^I = -i\omega\rho_o \frac{Q_s}{4\pi R} e^{ikR}, \quad (8.20)$$

where $R = \sqrt{q^2(X, Y, Z) - p^2(x, y, z)}$ is the distance between the integration point $p(x, y, z)$, and the source point $q(X, Y, Z)$ and Q_s is the source amplitude. Figures 8.26(a-

b) show the numerical results for the total sound pressure distribution at the surface of the cylinder for $f = 1.5\text{kHz}$ ($ka = 1.57$). Similarly as before, the total sound pressure on the circumferential nodes at a height of $z = 1.39\text{m}$ (see Figures 8.26a and 8.26b) of the cylinder was calculated using BEM and compared with the analytical result calculated using equation (7.6) for a point source. For this case, the sound pressures were calculated using BEM on the circumferential nodes at a height of $z = 1.39\text{m}$ of the cylinder since the maximum pressure occurs at the bottom of the cylinder for the source positioned close to the cylinder. The comparison is shown in Figure 8.27, where it can be seen that the sound pressure magnitude is less than the result shown previously in Figure 8.20. This is a result of a point source at a finite distance from the cylinder origin rather than a plane wave being used and indicates that the 3D BEM technique can be used for a point source calculation for more complex structures such as the Boeing cylinder and the RSLVF.



Figures 8.26(a-b): Numerical results of the total sound pressure distribution at the surface of the extended cylinder of length 5m and radius 0.057m, due to a point source of $f = 1.5\text{ kHz}$ and $ka = 1.57$ is placed at a location of $X = -4.1\text{m}$, $Y = 0\text{m}$ and $Z = 0\text{m}$ (consider Figure 7.1 for the source geometry). The green circles show the circumferential nodes at a height of $z = 1.39\text{m}$ of the cylinder. [Reference pressure $20\mu\text{Pa}$]

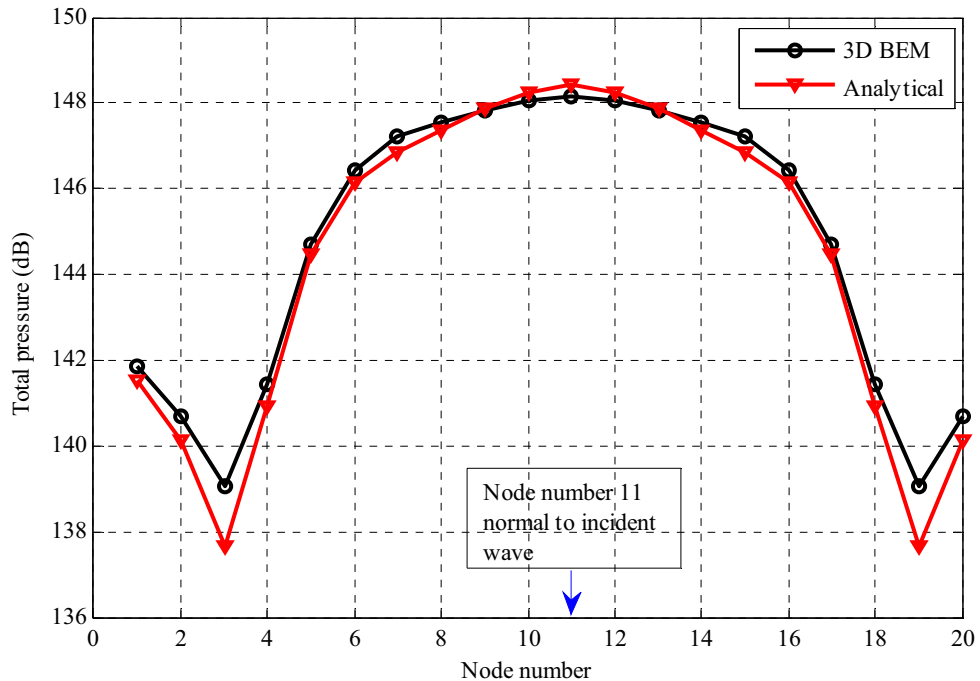


Figure 8.27: Total sound pressure comparison between the analytical and 3D BEM results calculated on the circumferential nodes at a height of $z = 1.39\text{m}$ (see Figures 8.26a and 8.26b) of the extended cylinder of length 5m and radius 0.057m, due to a point source of $f = 1.5\text{ kHz}$ and $ka = 1.57$ is placed at a location of $X = -4.1\text{m}$, $Y = 0\text{m}$ and $Z = 0\text{m}$ (consider Figure 7.1 for the source geometry). [Reference pressure $20\mu\text{Pa}$]

Finally, a comparison was conducted with the line source theory derived in Chapter 7 and the same problem solved using 3D BEM for the extended cylinder of length 5m and radius 0.057m (aspect ratio is 43.86). In this case, n point sources, $q_n(X, Y, Z)$, are located at distances outside the solid surface. Hence, the distances between m integration points $p_m(x, y, z)$, and n source points $q_n(X, Y, Z)$, need to be determined for the incident sound pressure from each source. Hence, the right side of the equation (8.13) may be calculated as follows:

$$P^I = \sum_{n=0}^{N-1} -i\omega\rho_o \frac{Q_s}{4\pi R} e^{ikR}, \quad (8.21)$$

where $R = \sqrt{q_n^2(X, Y, Z) - p_m^2(x, y, z)}$, n and N are the point source number and total

number of point sources in an array acting as a line source respectively, and Q_s is the source amplitude. Consider 15 point sources spaced 1.5m apart and placed along the negative X axis outside of the cylinder as shown in Figure 8.28, such that the distance of the nearest source from the cylinder surface is 1m. Each source generates the same frequency 1.5kHz ($ka = 1.57$). Figures 8.29(a-b) show the numerical results for the total sound pressure distribution at the surface of the cylinder due to 15 point sources of arbitrary amplitudes and random phases (Table 5.1 was used for the arbitrary amplitudes and phases). The total sound pressure comparison between the 3D BEM result and the analytical result calculated using equation (7.6) on the circumferential nodes at the middle ($z = 2.5$ m, see Figures 8.19a and 8.19b) of the cylinder is shown in Figure 8.30 for $ka = 1.57$. This shows good agreement between the analytical and 3D BEM results and indicates that the 3D BEM technique can be used for line source calculations for more complex structures such as the Boeing cylinder and the RSLVF.

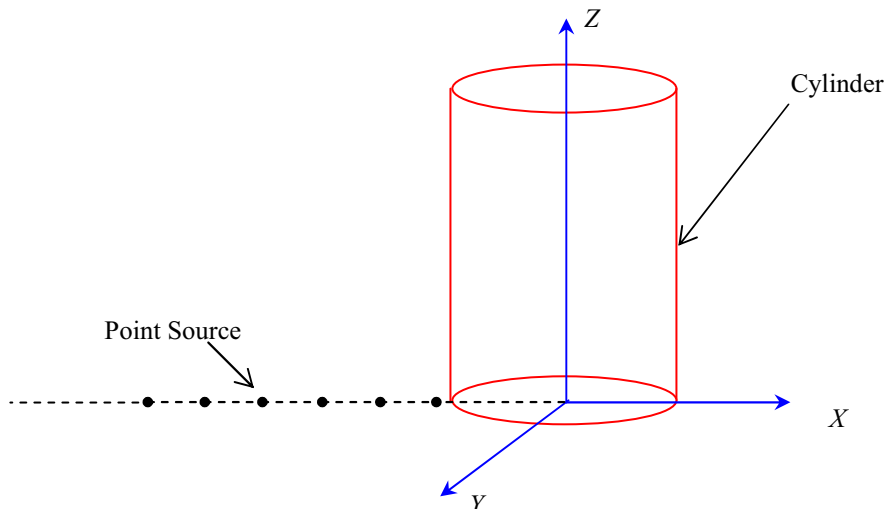
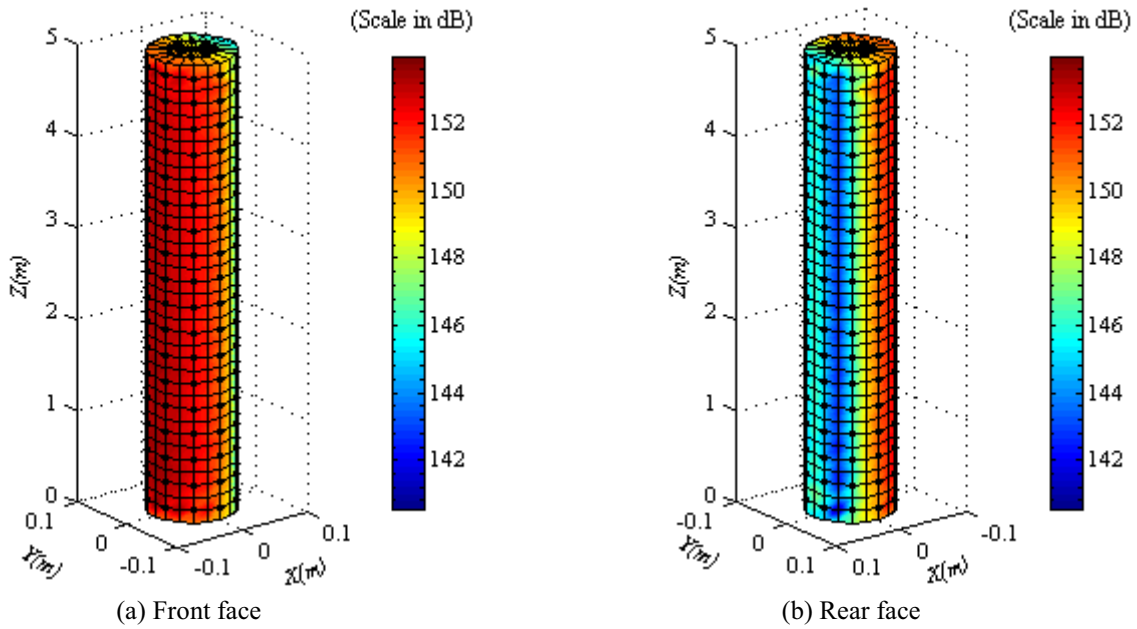


Figure 8.28: 3D arrangement of a line source.



Figures 8.29(a-b): Numerical results of the total sound pressure distribution at the surface of the extended cylinder of length 5m and radius 0.057m, due to a line source of 15 point sources of arbitrary amplitudes and phases (Table 5.1 was used) placed on the negative X axis, for $f = 1.5\text{kHz}$ and $ka = 1.57$. [Reference pressure $20\mu\text{Pa}$]

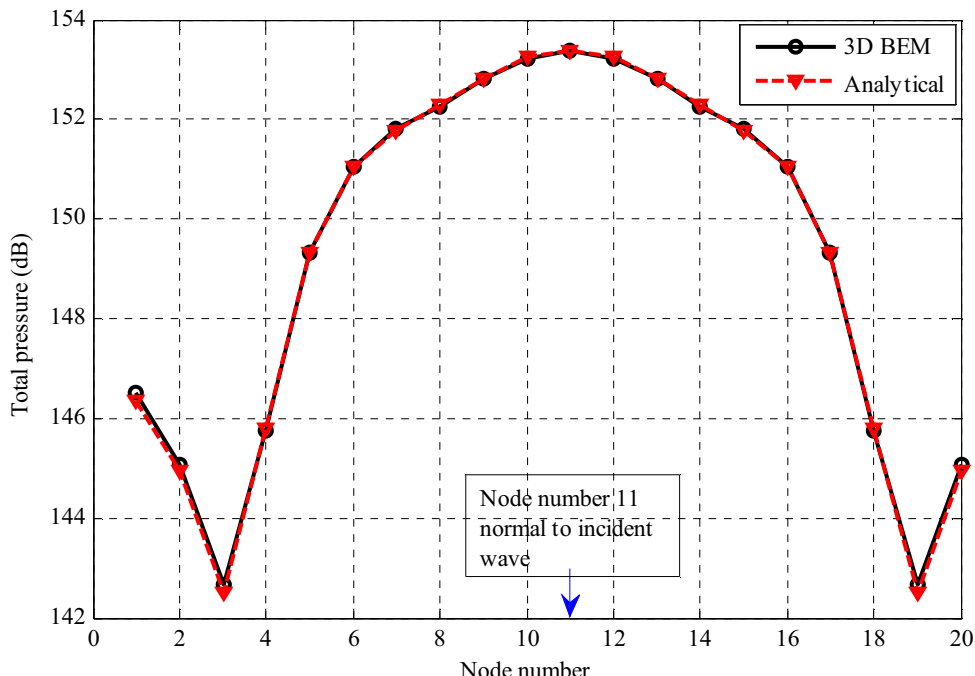


Figure 8.30: Total sound pressure comparison between the 3D BEM and analytical results calculated on the circumferential nodes at the middle ($z = 2.5\text{m}$, see Figures 8.19a and 8.19b) of the extended cylinder of length 5m and radius 0.057m, due to a line source of 15 point sources of arbitrary amplitudes and phases (Table 5.1 was used) placed on the negative X axis, for $f = 1.5\text{kHz}$ and $ka = 1.566$. [Reference pressure $20\mu\text{Pa}$]

8.5.3 Concluding Remarks

From the preceding results, it can be concluded that both 2D and 3D BEM techniques were validated. It was found that compared with the analytical results, the 2D BEM agrees well in the range $ka \leq 15$ ($f \leq 14,366$ Hz), whereas the 3D BEM agrees well in the range $ka \leq 5$ ($f \leq 4.8$ kHz), for the extended cylinder which has a small diameter of only 0.114m and aspect ratio of 43.86. The range of 3D BEM could be increased for the cylinder by increasing the density of nodes and elements on the surface over that used in the current analyses. However, the range of 3D BEM indicates that the value of ka could be increased for a large cylinder such as the Boeing cylinder (diameter, $D = 2.46$ m) but the maximum applied frequency (or value of k) could be less compared with the extended cylinder. This is verified simultaneously with the analysis of the Boeing cylinder in the next section before the 3D BEM is applied to the RSLVF. Overall, the BEM can be used in the low frequency range to analyse the external pressure excitations of complex structures such as the Boeing cylinder and the RSLVF.

8.6 Application of BEM Analysis to a Boeing Cylinder

In this section the BEM technique is extended to investigate the sound pressure external to the Boeing cylinder. The Boeing cylinder is a composite cylinder constructed by Boeing for the US Air Force to simulate a launch vehicle. The physical dimensions of the Boeing cylinder are given in Table 7.1 in Chapter 7, which has an aspect ratio of 1.13. Several analyses were conducted numerically and are discussed in the following sections. A large number of numerical results for the Boeing cylinder are also presented.

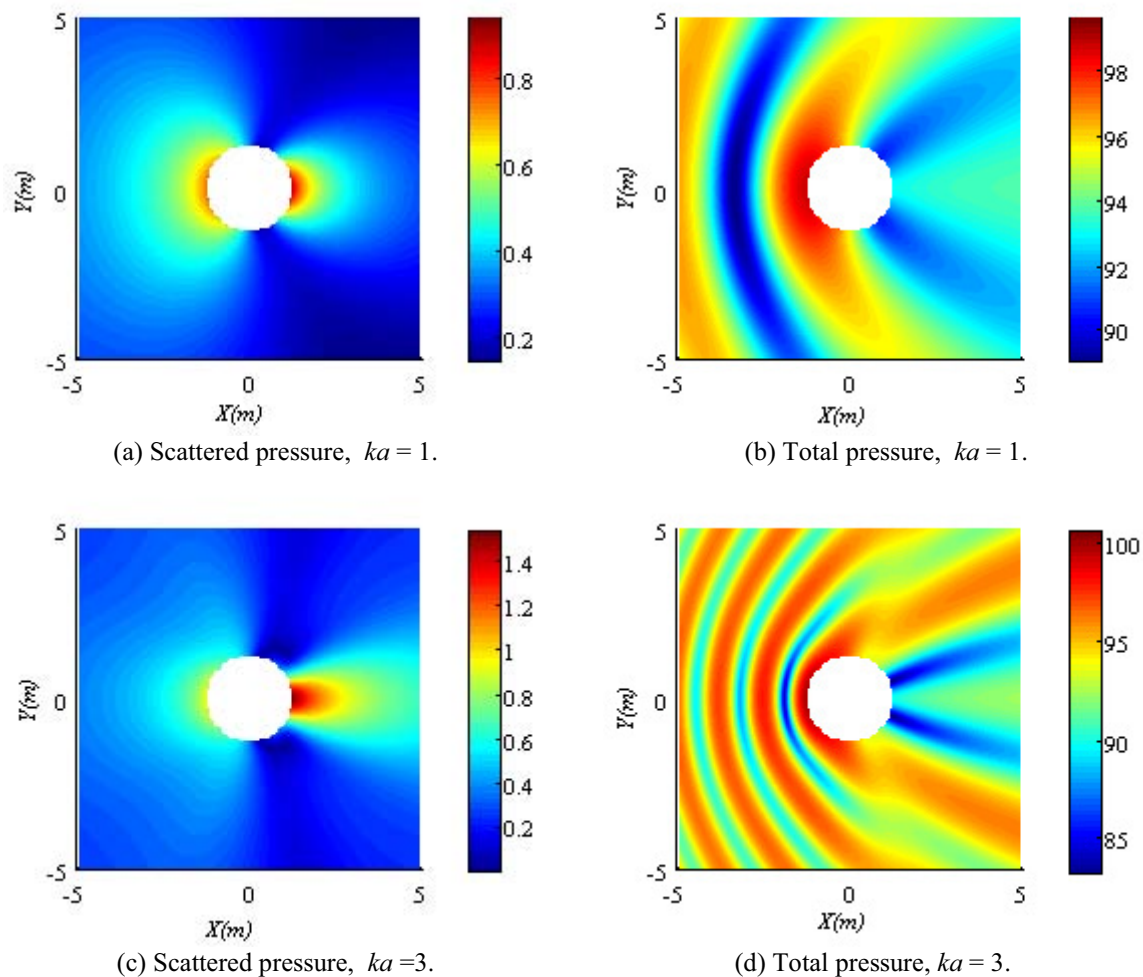
8.6.1 2D BEM Results

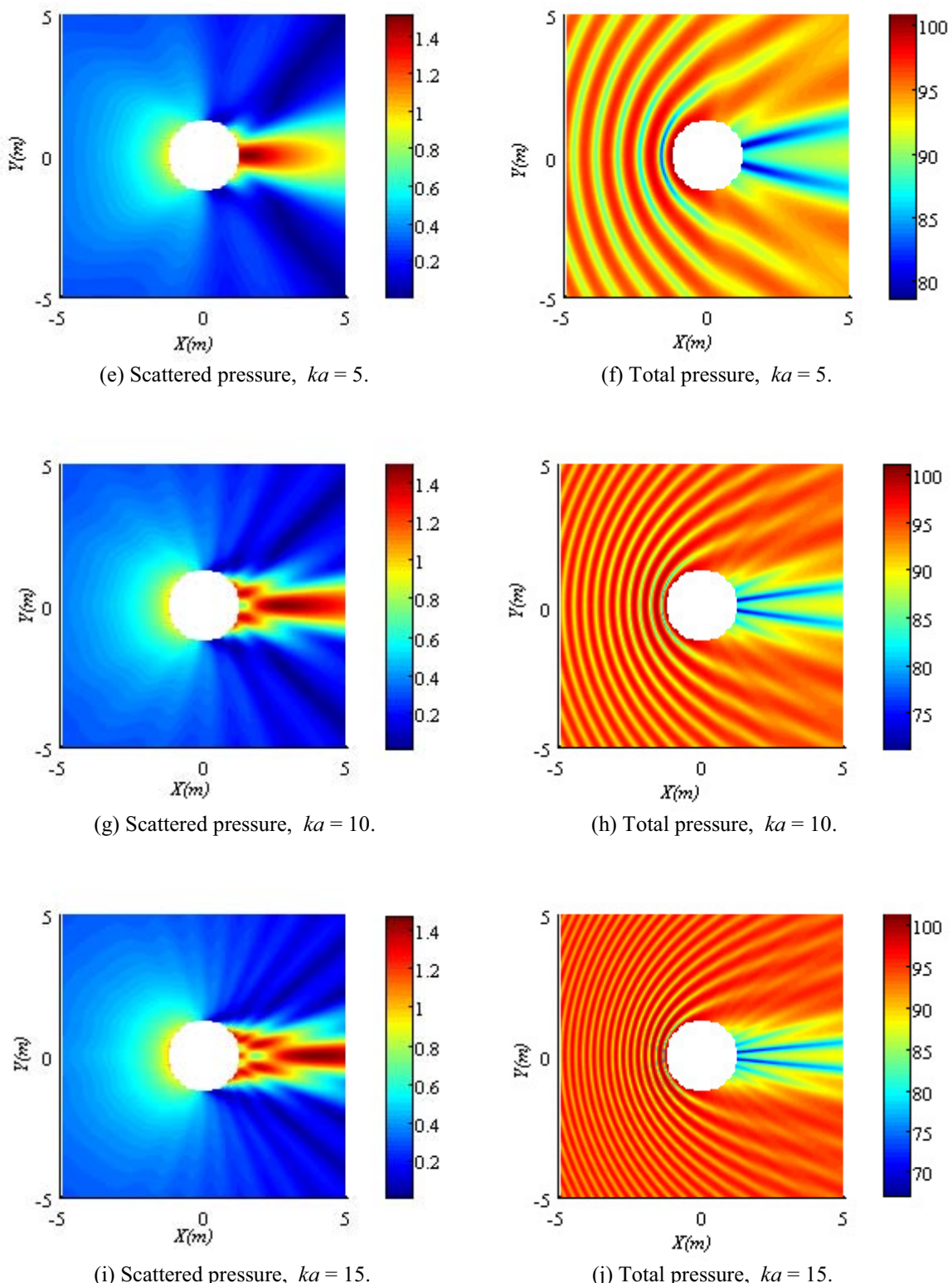
The 2D BEM analysis has been conducted in this section, which treats the 2D geometry of the Boeing cylinder to analyse the sound pressure field. Assuming plane wave propagation along the positive X axis towards the cylinder, a large number of 2D calculations were conducted numerically to determine the scattered and total sound pressure fields around the cylinder. The calculations were made on 40,401 field points outside the cylinder for various values of ka up to 15. Numerical results are given for various values of ka in Figures 8.31(a-j). The figures are a very good representation of the scattered and total pressure patterns for each value of ka around the cylinder. It can be seen that the scattered and total sound pressure are relatively smoothly varying, maximum at the front (left side of the figures) of the cylinder and varying more aggressively at the back (right side of the figures) of the cylinder. The reason is due to the positive and/or negative interference of the two diffracted waves travelling around the two sides of the cylinder. Note that the scattered and total sound pressure patterns for each value of ka are similar to those presented analytically in Chapters 3 and 4.

Figure 8.32 shows the numerical results for the total sound pressure at the surface of the Boeing cylinder for $ka = 5$, due to a point source of arbitrary amplitude $1 + i$ m³/s placed at a distance $X = -20D$ m (D = diameter of the cylinder) and $Y = 0$ m, and shows very good agreement compared with the analytical result calculated using equation (5.5). The source position $X = -20D$ m was chosen because it was reported that for a 1,650-pound-thrust solid fuel rocket engine, the source appeared approximately at a distance 20 diameters downstream of the nozzle exit, in the low frequency range (Mayes *et al.* 1959).

The total sound pressure calculated using 2D BEM at the surface of the Boeing cylinder due to a

line source, containing 15 point sources of arbitrary amplitudes and phases (see Table 5.1), is also shown in Figure 8.33 for $ka = 5$. In the numerical calculation, all the sources were placed along the negative X axis outside the Boeing cylinder as shown in Figure 5.8 in Chapter 5. The distance between each of them was 1.5m. The distance of the nearest source from the cylinder surface was 1m. Each source generated the same frequency ($ka = 5$). The total sound pressure comparison between the 2D BEM result and the result calculated using equation (5.7) is also shown in Figure 8.33 for $ka = 5$, which shows good agreement between the two methods. The small differences in pressure magnitudes are a result of diffraction around the two dimensional geometry of the cylinder which is taken into account in the BEM analysis but not in the analytical model.





Figures 8.31(a-j): 2D BEM results showing the scattered and total pressure fields around the Boeing cylinder, for plane waves incident from the left, for different values of ka . The scales for the scattered and total pressures are (Pa) and (dB) respectively. [Incident pressure magnitude $P^0 = 1 \text{ Pa}$ and reference pressure $20 \mu\text{Pa}$]

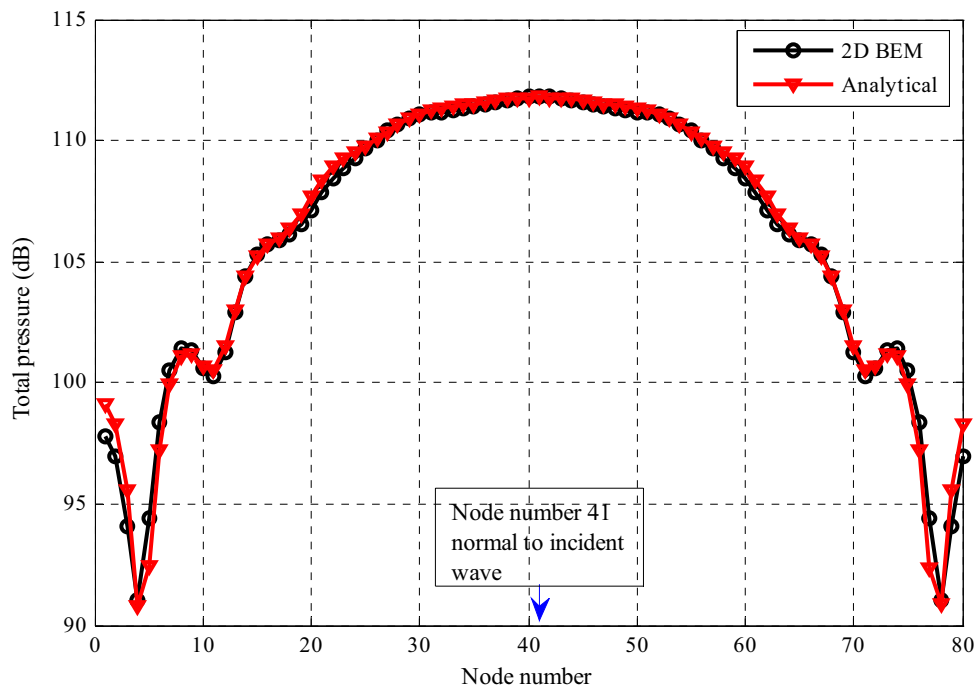


Figure 8.32: Total sound pressure comparison between the 2D BEM and analytical results at the surface of the Boeing cylinder, for a point source is placed at $X = -20D$ m and $Y = 0$ m, for $ka = 5$. [Diameter of the cylinder is $D = 2.46$ m and reference pressure $20\mu\text{Pa}$]

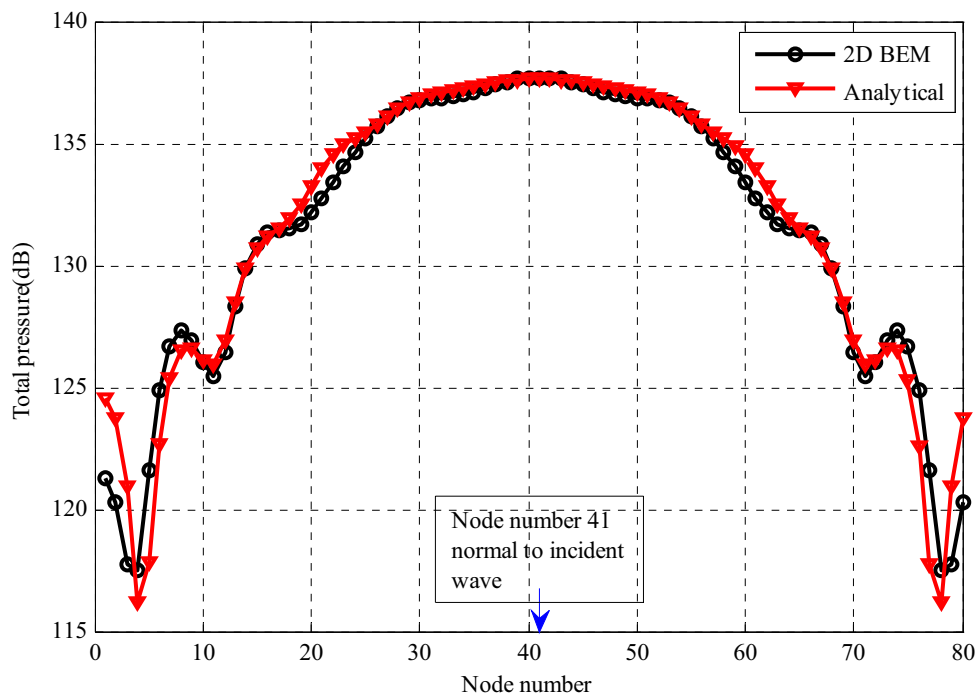


Figure 8.33: Total sound pressure comparison between the 2D BEM and analytical results at the surface of the Boeing cylinder, for a line source of 15 point sources of arbitrary amplitudes and phases (see Table 5.1) placed on the negative X axis, for $ka = 5$. [Reference pressure $20\mu\text{Pa}$]

8.6.2 3D BEM Results

The 3D BEM analysis has been conducted in this section, which treats the 3D geometry of the Boeing cylinder to analyse the sound pressure field. For 3D BEM analysis of the Boeing cylinder which has a aspect ratio of 1.13, a similar technique was applied as used for the BEM analysis of the experimental cylinder. The FEA model of the Boeing cylinder is shown in Figure 8.34. A quadratic eight node element shape was used to build the model, which had 492 elements and 1440 nodes at the surface as shown more clearly in Figure 8.35. The model was imported into MATLAB for numerical analysis.

Several numerical analyses have been conducted to investigate the external sound pressure excitations of the Boeing cylinder due to incident plane waves, point source and line source, and the results are discussed in the following sections.

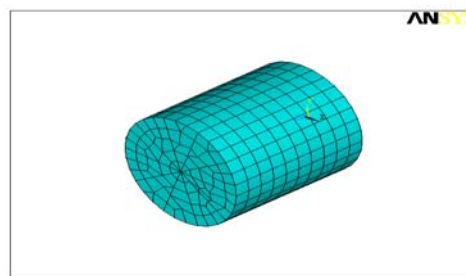


Figure 8.34: FEA model of the Boeing cylinder.

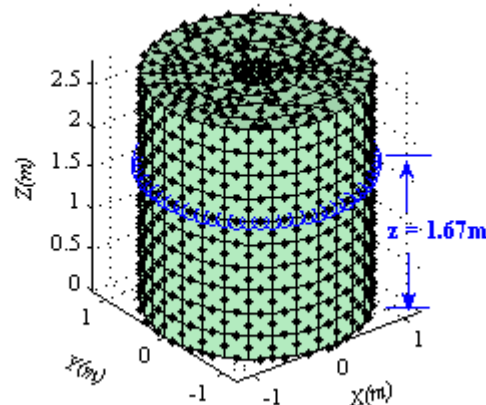
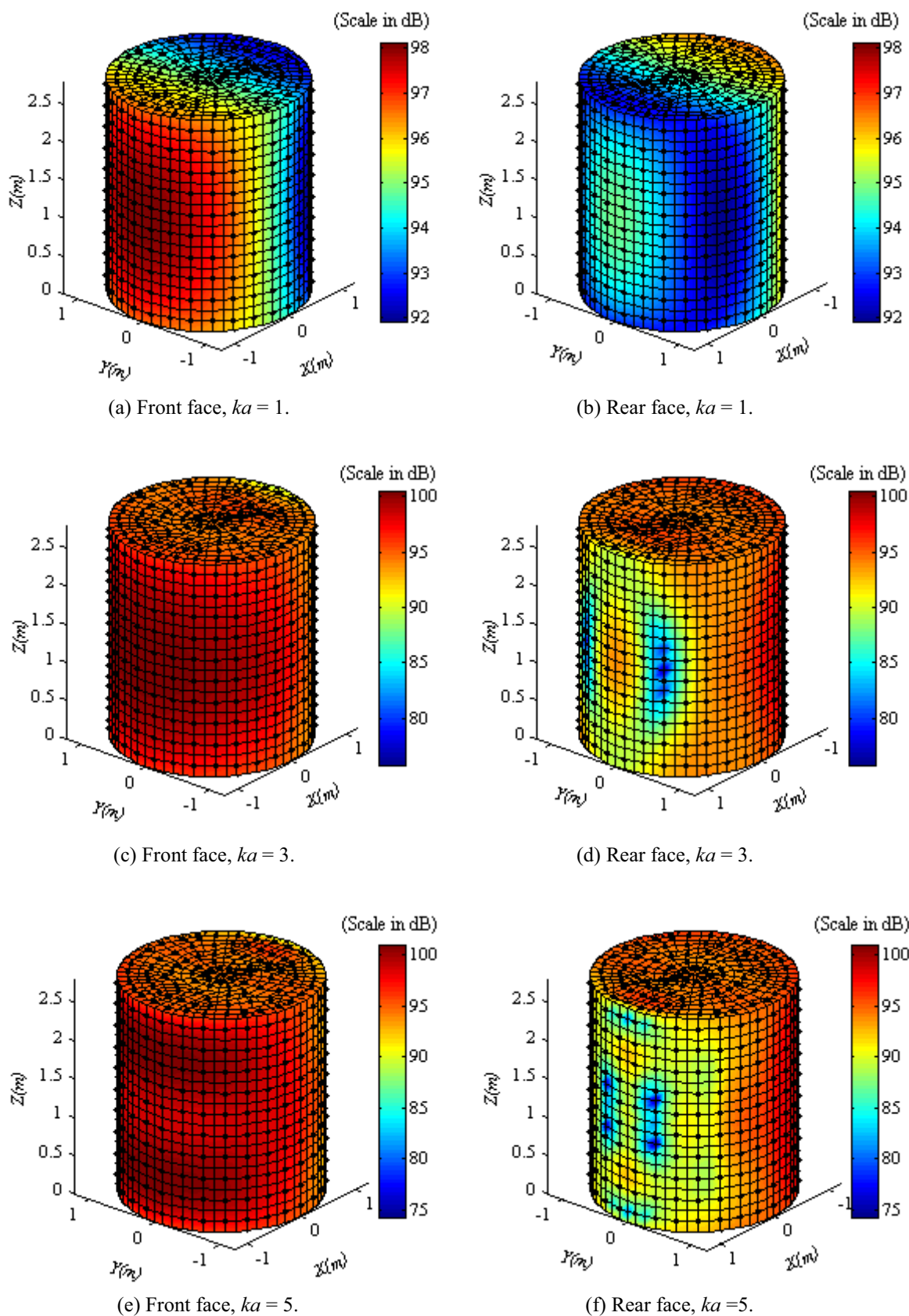
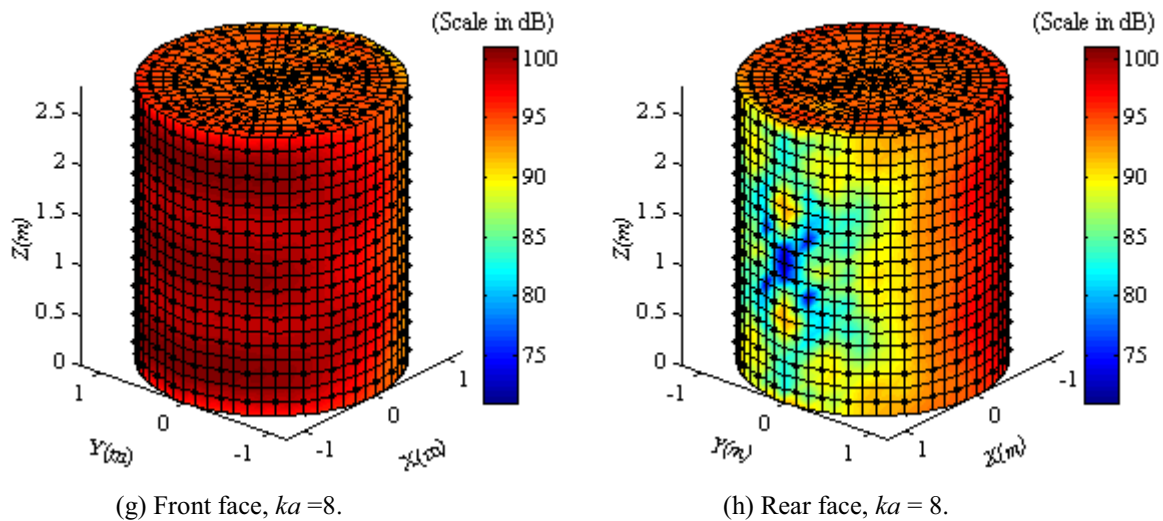


Figure 8.35: Boeing cylinder geometry showing the surface elements and nodes. The green circles are showing the positions of the circumferential nodes (60 nodes) at a height of $z = 1.67\text{m}$ of the cylinder.

8.6.2.1 Sound Pressure Due to Incident Plane Waves

Numerical analyses to calculate the sound pressure on the surface of the Boeing cylinder due to incident plane waves were undertaken for different values of ka up to 8, assuming plane waves travelling in the positive X direction, and the results are shown individually for each value of ka , respectively, in Figures 8.36(a-h). The sound pressures on the circumferential nodes (60 nodes) at a height of $z = 1.67\text{m}$ (see Figure 8.35) were calculated using BEM for each value of ka and are shown in Figure 8.37 for $ka = 1, 3$ and 5 . For the value of $ka = 8$ ($f = 355\text{Hz}$), the sound pressure distribution on the circumferential nodes at a height of $z = 1.67\text{m}$ of the cylinder was compared separately with the analytical result calculated using equation (3.18) and is shown in Figure 8.38. The comparison shows good agreement and validates the 3D BEM analysis for the Boeing cylinder up to the value of $ka = 8$. The value of ka for which the current analysis is valid has increased over that for the thin experimental cylinder because the density of nodes has increased for the Boeing cylinder compared with the experimental cylinder discussed in Section 8.5.2. However, for $ka > 8$, the analysis does not perform well, as shown in Figures 8.39(a-b) for $ka = 10$. For this case, the sound pressure on the circumferential nodes (60 nodes) at a height of $z = 1.67\text{m}$ of the cylinder (see Figures 8.35) was calculated using BEM and compared with the analytical results calculated using equation (3.18). The comparison is shown in Figure 8.40, which clearly shows that for $ka = 10$ the BEM analysis is becoming very inaccurate compared with the analytical result. The analysis can be improved by increasing the density of nodes and elements, but this will increase the computational time. Therefore, for the numerical analysis of the Boeing cylinder, using quadratic eight node elements, the maximum applied frequency for reliable results was 355Hz ($ka = 8$). Thus the results of the analyses reported in the following sections are for values of $ka \leq 8$.





Figures 8.36(a-h): Numerical results for the total sound pressure distribution at the surface of the Boeing cylinder due to incident plane waves on the front face for various values of ka . [Reference pressure $20\mu\text{Pa}$ and incident pressure magnitude $P^o = 1\text{ Pa}$]

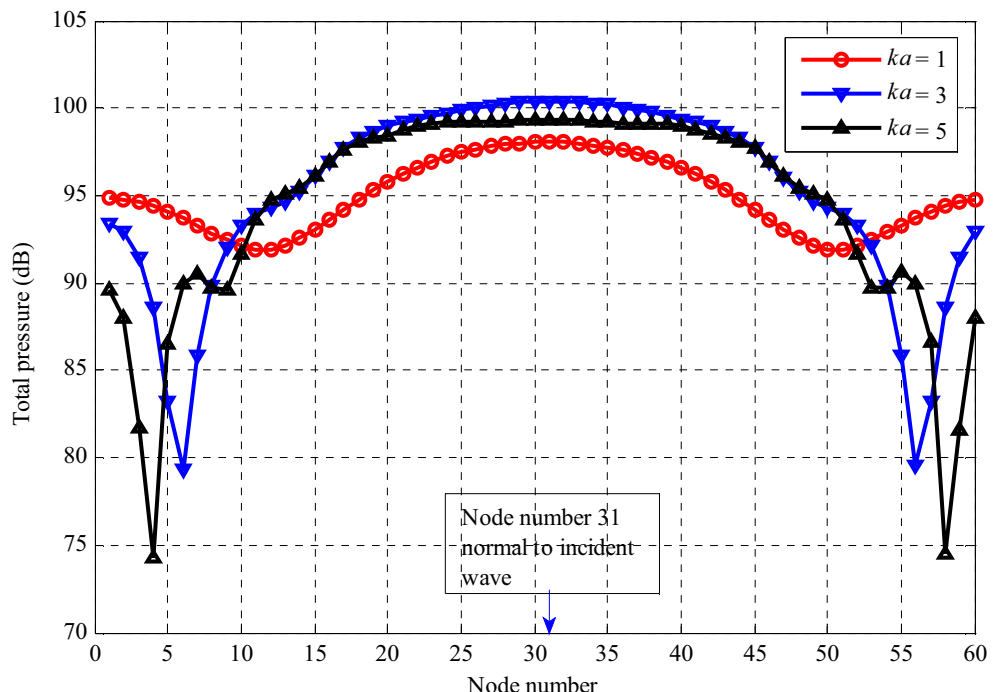


Figure 8.37: Total sound pressure calculated using BEM on the circumferential nodes (60 nodes) at a height of $z = 1.67\text{m}$ (see Figure 8.35) of the Boeing cylinder, for incident plane waves on the front face, for various values of ka . [Reference pressure $20\mu\text{Pa}$ and incident pressure magnitude $P^o = 1\text{ Pa}$]

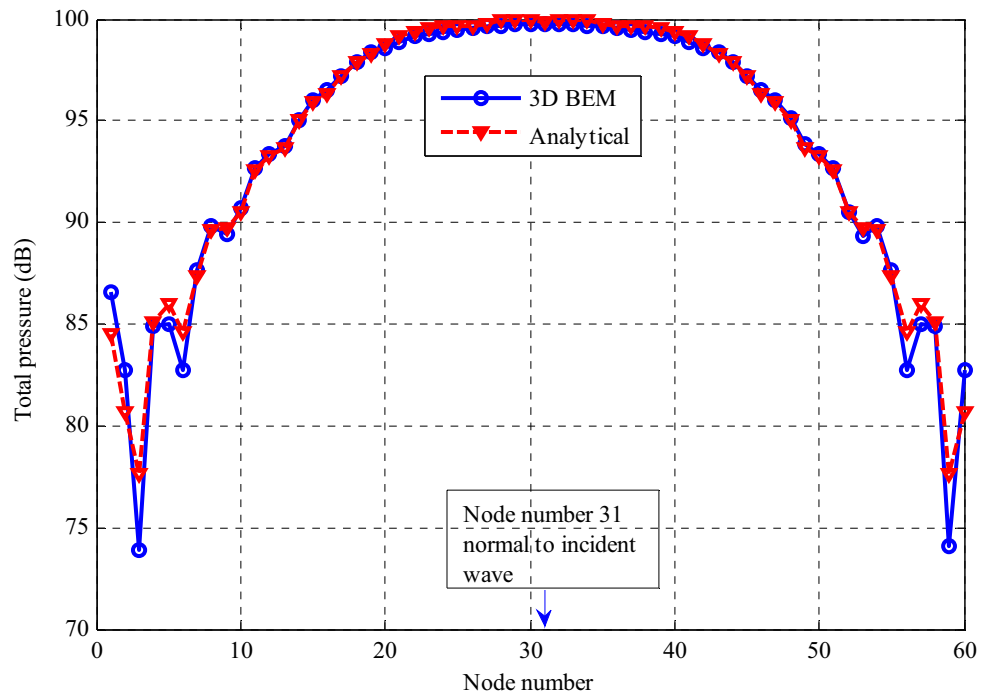
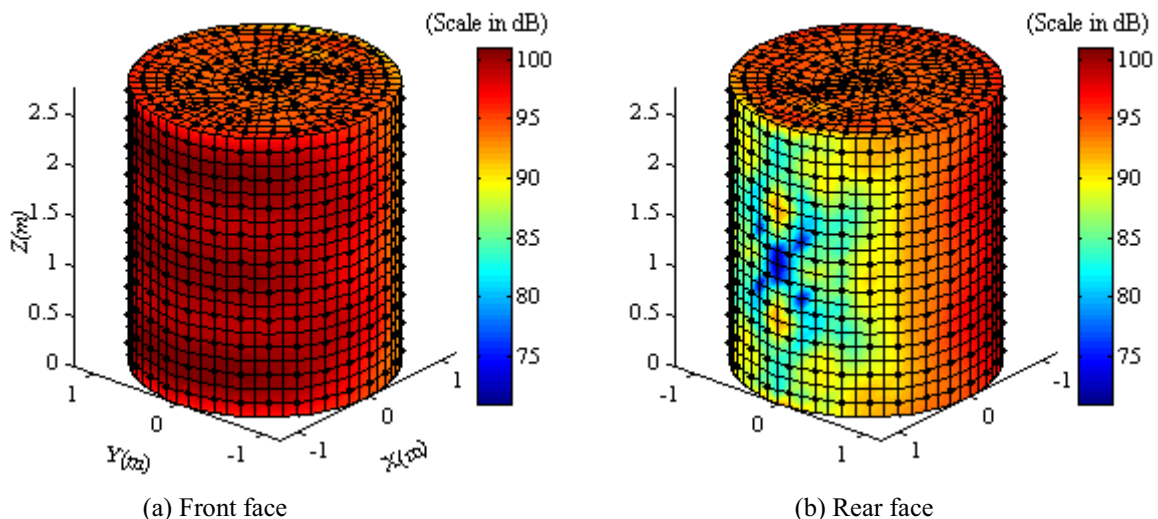


Figure 8.38: Total sound pressure comparison between the 3D BEM and analytical results calculated on the circumferential nodes at a height of $z = 1.67\text{m}$ (see Figure 8.35) of the Boeing cylinder, for plane incident waves on the front face, for $ka = 8$. [Reference pressure $20\mu\text{Pa}$ and incident pressure magnitude $P^O = 1\text{ Pa}$]



Figures 8.39(a-b): Numerical results for the sound pressure distribution at the surface of the Boeing cylinder due to incident plane waves on the front face, for $ka = 10$. [Reference pressure $20\mu\text{Pa}$ and incident pressure magnitude $P^O = 1\text{ Pa}$]

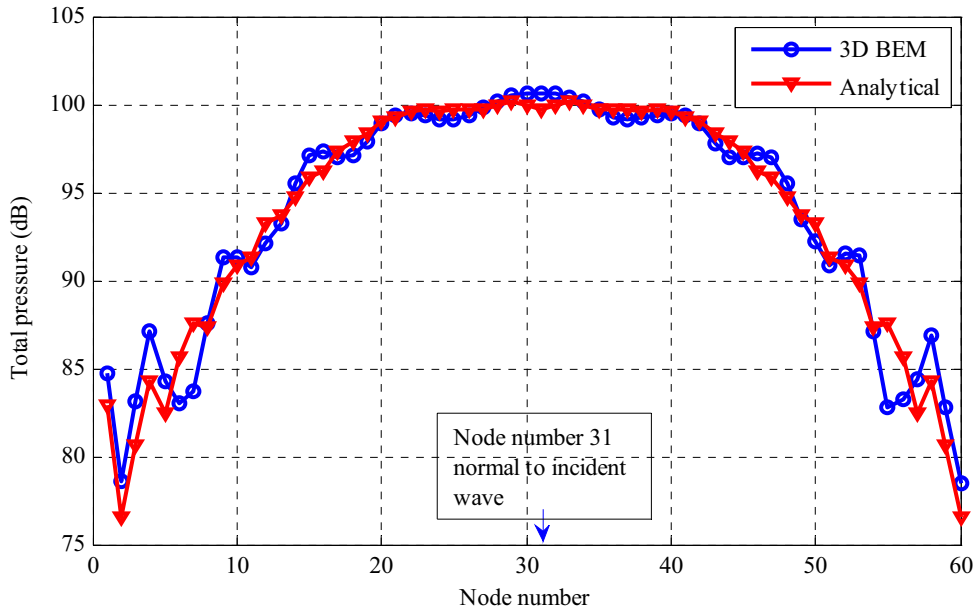
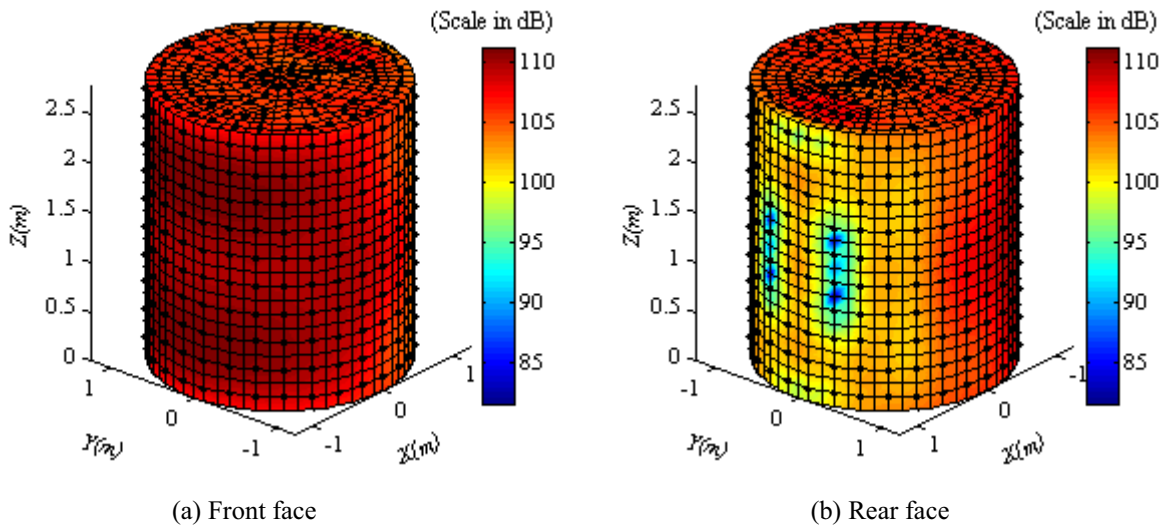


Figure 8.40: Total sound pressure comparisons between the 3D BEM and analytical results calculated on 60 circumferential nodes at a height of $z = 1.67\text{m}$ (see Figure 8.35) of the Boeing cylinder, for plane incident waves on the front face, for $ka = 10$. [Reference pressure $20\mu\text{Pa}$ and incident pressure magnitude $P^o = 1\text{ Pa}$]

8.6.2.2 Sound Pressure Due to a Point Source

A point source of arbitrary amplitude $1 + i \text{ m}^3/\text{s}$ was placed at $X = -20D \text{ m}$ ($D = \text{diameter}$ of the cylinder), $Y = 0\text{m}$ and $Z = 0\text{m}$ (see Figure 7.1 for the source geometry). Excitation at a frequency 250Hz was applied and the results are shown in Figures 8.41(a-b). It can be seen that maximum sound pressure occurs near the ends of the cylinder because there are a greater diffraction of sound waves occurring from the ends of the cylinder. The sound pressure on the circumferential nodes at a height of $z = 1.67\text{m}$ (see Figure 8.35) of the cylinder was calculated and compared with the analytical result calculated using equation (7.6) and is shown in Figure 8.42. The comparison shows good agreement with the analytical result, but there is a slight difference in pressure magnitudes between the results and is a result of diffraction around the ends of the Boeing cylinder which is taken into account in the BEM analysis but not in the analytical model.



Figures 8.41(a-b): Numerical results for the total sound pressure distribution at the surface of the Boeing cylinder due to a point source of 250Hz placed at $X = -20D$ m, $Y = 0$ m and $Z = 0$ m (see Figure 7.1 for the source geometry). [Diameter of the cylinder, $D = 2.46$ m and reference pressure $20\mu\text{Pa}$]

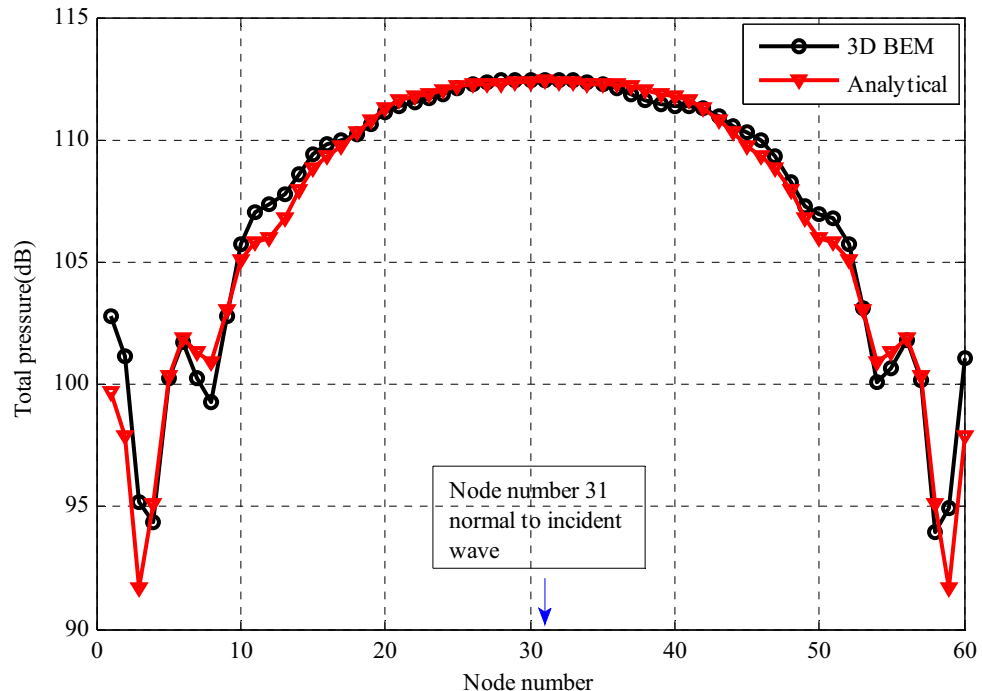


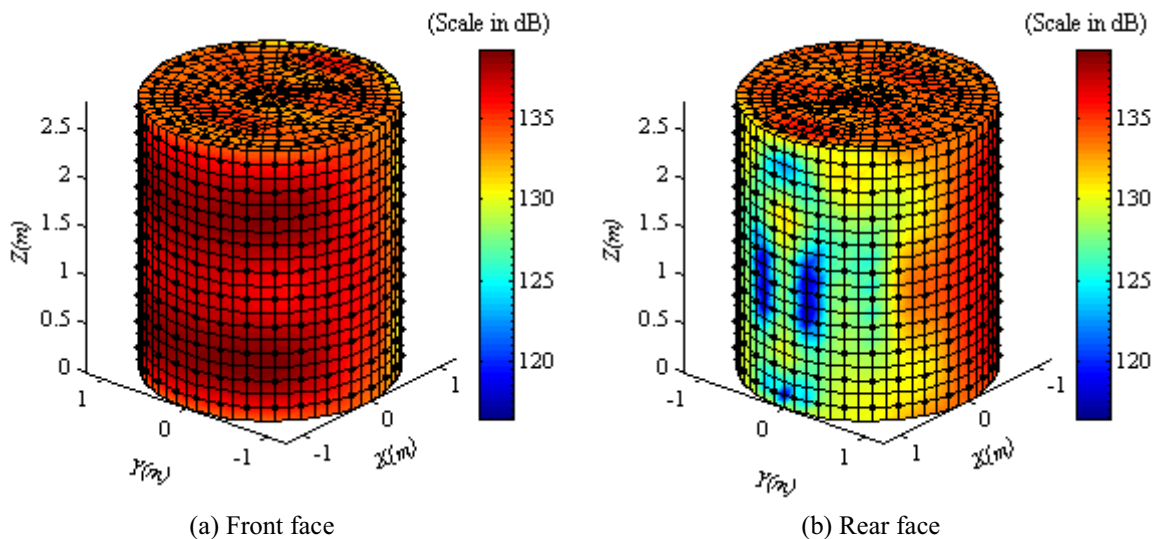
Figure 8.42: Total sound pressure comparison between the 3D BEM and analytical results calculated on the circumferential nodes (60 nodes) at a height of $z = 1.67$ m on the Boeing cylinder, due to a point source of 250Hz placed at $X = -20D$ m, $Y = 0$ m and $Z = 0$ m (see Figure 7.1 for the source geometry). [Diameter of the cylinder, $D = 2.46$ m, and reference pressure $20\mu\text{Pa}$]

8.6.2.3 Sound Pressure Due to a Line Source

The sound pressure at the surface of the Boeing cylinder due to an arbitrarily arranged horizontal line source laid on the negative X axis was investigated. The cylinder was arranged so that its axis is vertical and the line source consisting of fifteen point sources is in a horizontal line normal to the bottom edge of the cylinder (see Figure 8.28). For the line source arrangement the first source was located at a distance of 1m from the surface of the cylinder with 1.5m equal spaces between each adjacent source. The arbitrary source amplitudes presented in Table 5.1 were used for this analysis. Figures 8.43(a-b) show the numerical results for the sound pressure loading on the Boeing cylinder surface, due to a line source consisting of fifteen point sources, each generating a frequency of 250Hz. The sound pressure distribution on the circumferential nodes at a height of $z = 1.67\text{m}$ (see Figure 8.35) was calculated using BEM and compared with the analytical result calculated using equation (7.6), and is shown in Figure 8.44. For this case, the pressure distribution pattern on the circumferential nodes at the middle of the cylinder is similar to the case for a point source of 250Hz located at a distance of $20D$ m from the surface of the cylinder as shown in Figure 8.42. The only difference is that the pressure amplitude is greater because fifteen point sources of arbitrary amplitudes were used for the line source.

Another case was investigated where each point source generates a different frequency. For that case, a line source consisting of nine point sources was considered along the negative X axis at the bottom of the cylinder, similar to the arrangement discussed in the previous paragraph. For simplicity, one-third octave band centre frequencies from 50Hz to 315Hz were distributed for each source where the closest source generates 50Hz, with the frequency of excitation increasing in 1/3 octave steps until at the farthest source it is

315Hz. The sound pressure distribution calculated using 3D BEM at the surface of the Boeing cylinder is shown in Figures 8.45(a-b). The sound pressure distribution on the circumferential nodes at a height of $z = 1.67\text{m}$ (see Figure 8.35) of the cylinder calculated using BEM and is compared in Figure 8.46 with the analytical result calculated using equation (7.6). The comparison shows good agreement between the two methods. However, the pressure amplitudes calculated using BEM on the nodes situated at the back of the cylinder is high compared with the analytical result. The reason could be the effect of positive interference of the diffracted sound waves over the ends of the cylinder at that height back of the cylinder and this is not possible to take into account in the analytical model, which assumes the cylinder length to be infinite with no ends.



Figures 8.43(a-b): Numerical results for the total sound pressure distribution at the surface of the Boeing cylinder, due to a line source of fifteen point sources (see Figure 8.28 for the line source geometry) of arbitrary amplitudes (see Table 5.1), placed on the negative X axis. Each source generated a frequency of 250Hz. [Reference pressure $20\mu\text{Pa}$]

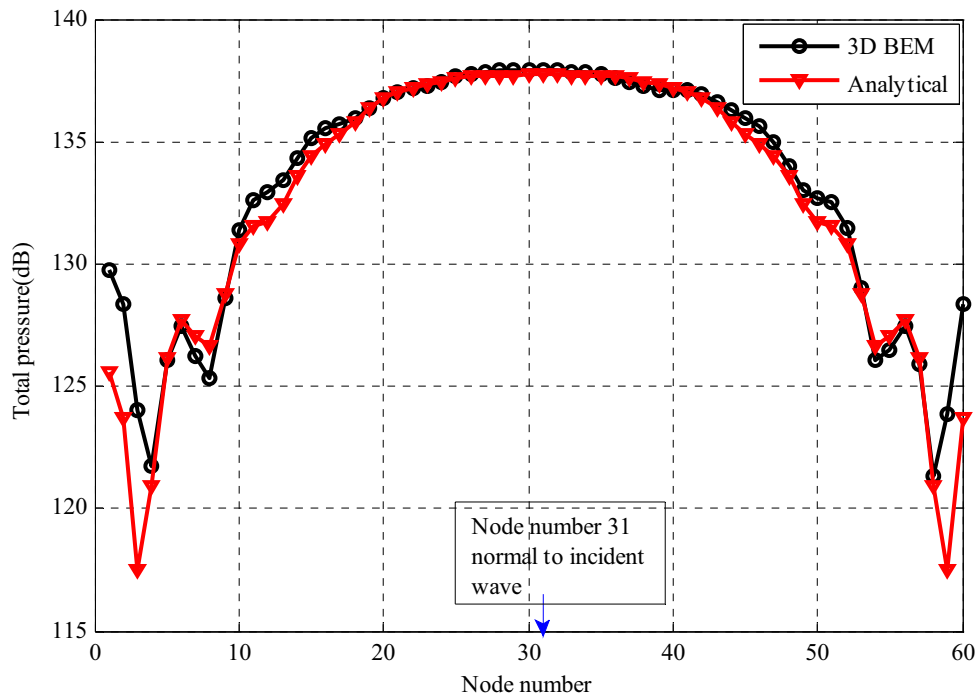
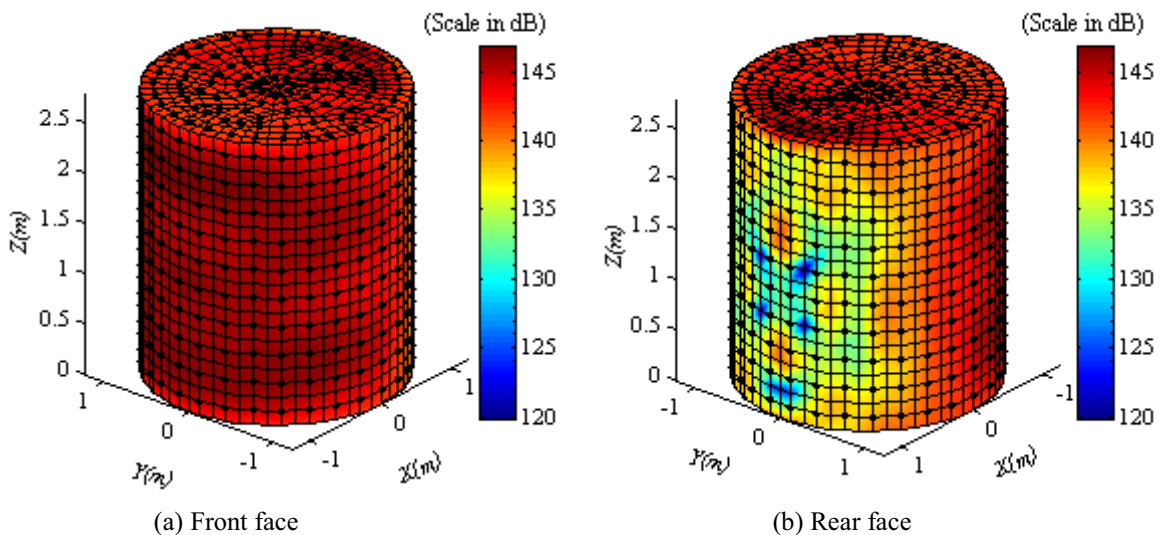


Figure 8.44: Total sound pressure comparison between the BEM and analytical results calculated on the circumferential nodes at a height of $z = 1.67\text{m}$ on the Boeing cylinder, due to a line source of fifteen point sources (see Figure 8.28 for the line source geometry) of arbitrary amplitudes (see Table 5.1), placed on the negative X axis at the bottom of the Boeing cylinder. Each source generated a frequency of 250Hz. [Reference pressure $20\mu\text{Pa}$]



Figures 8.45(a-b): Numerical results for the total sound pressure distribution at the surface of the Boeing cylinder, due to a line source of varying frequencies corresponding to one-third-octave centre frequencies from 50Hz to 315Hz. Arbitrary strengths given in Table 5.1 were used for each point source. [Reference pressure $20\mu\text{Pa}$]

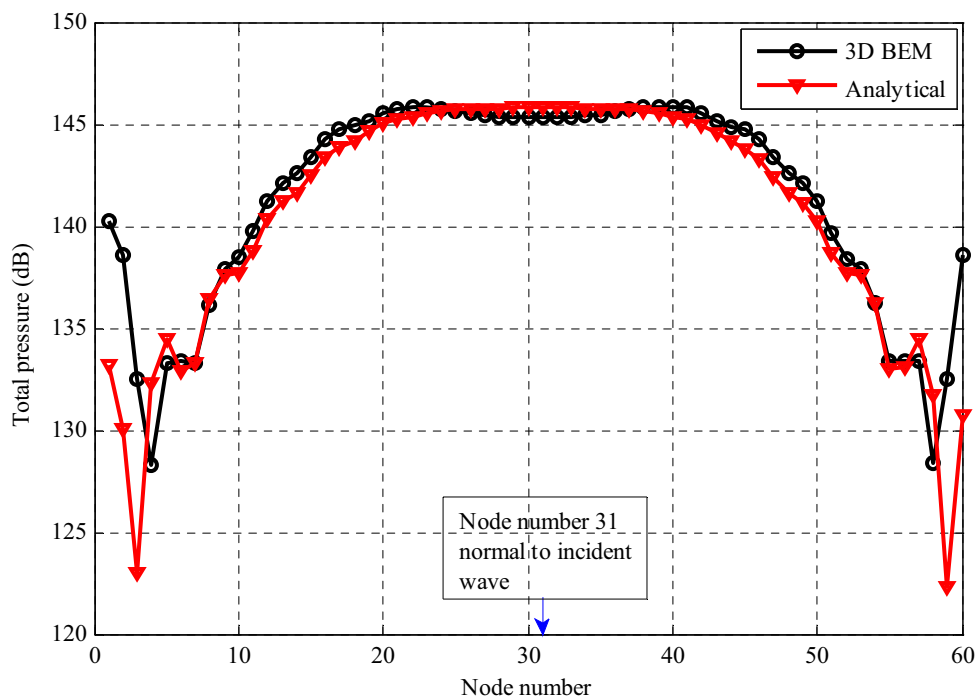


Figure 8.46: Total sound pressure comparison between the BEM and analytical results calculated on the circumferential nodes at a height of $z = 1.67\text{m}$ on the Boeing cylinder, due to a line source of nine point sources (see Figure 8.28 for the line source geometry) of varying frequencies corresponding to one-third octave centre frequencies from 50Hz to 315Hz, placed on the negative X axis at the bottom of the Boeing cylinder. Arbitrary strengths given in Table 5.1 were used for each point source. [Reference pressure $20\mu\text{Pa}$]

8.7 Application of BEM Analysis to an RSLVF

In the previous numerical analysis of a Boeing cylinder (diameter, $D = 1.23\text{m}$), it has been seen that for the nodal density chosen, the analysis is valid up to $ka = 8$. That means that a maximum excitation frequency around 355Hz was valid for the Boeing cylinder. Since the maximum diameter of the RSLVF is 1.552m (radius 0.776m, see Table 7.2 in Chapter 7) and a similar nodal density was used as for the Boeing cylinder, the maximum valid applied frequency will be around 562Hz to ensure reliable results. Therefore, the frequency range 50Hz to 400Hz was used in the current numerical analysis to determine the external sound pressure excitation on the RSLVF.

The FEA model of the RSLVF, shown in Figure 8.47, was used for the numerical analysis. The model was built using quadratic, eight node elements, which are the same as were used for the Boeing cylinder. The model consists of 726 elements and 2120 nodes at the surface shown in Figure 8.48, which was imported into MATLAB for numerical analysis.

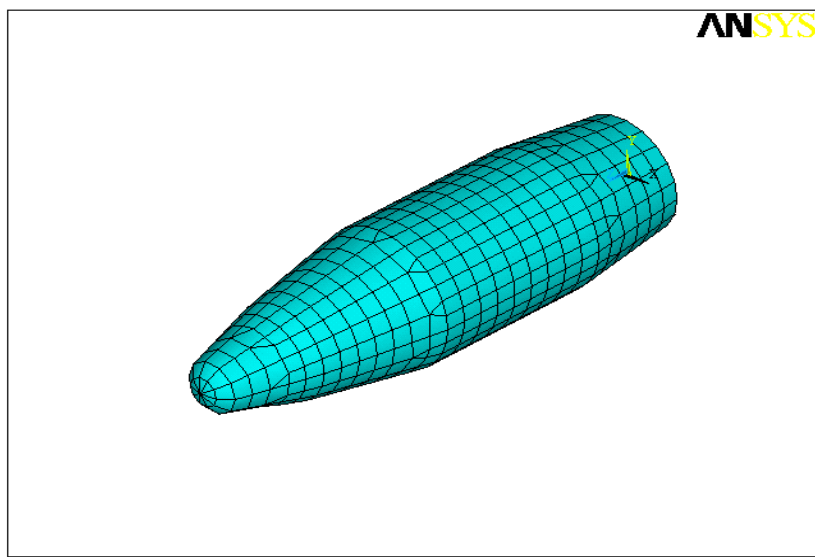


Figure 8.47: FEA model of an RSLVF

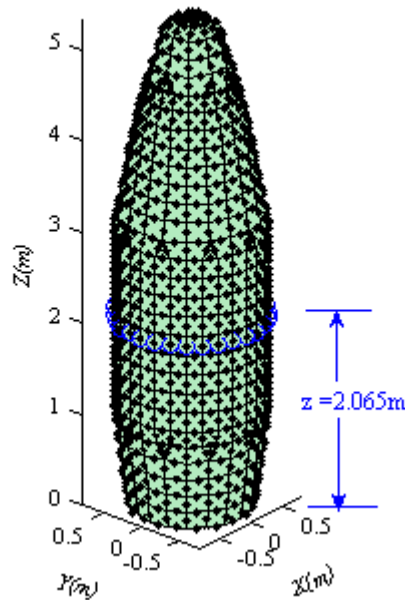
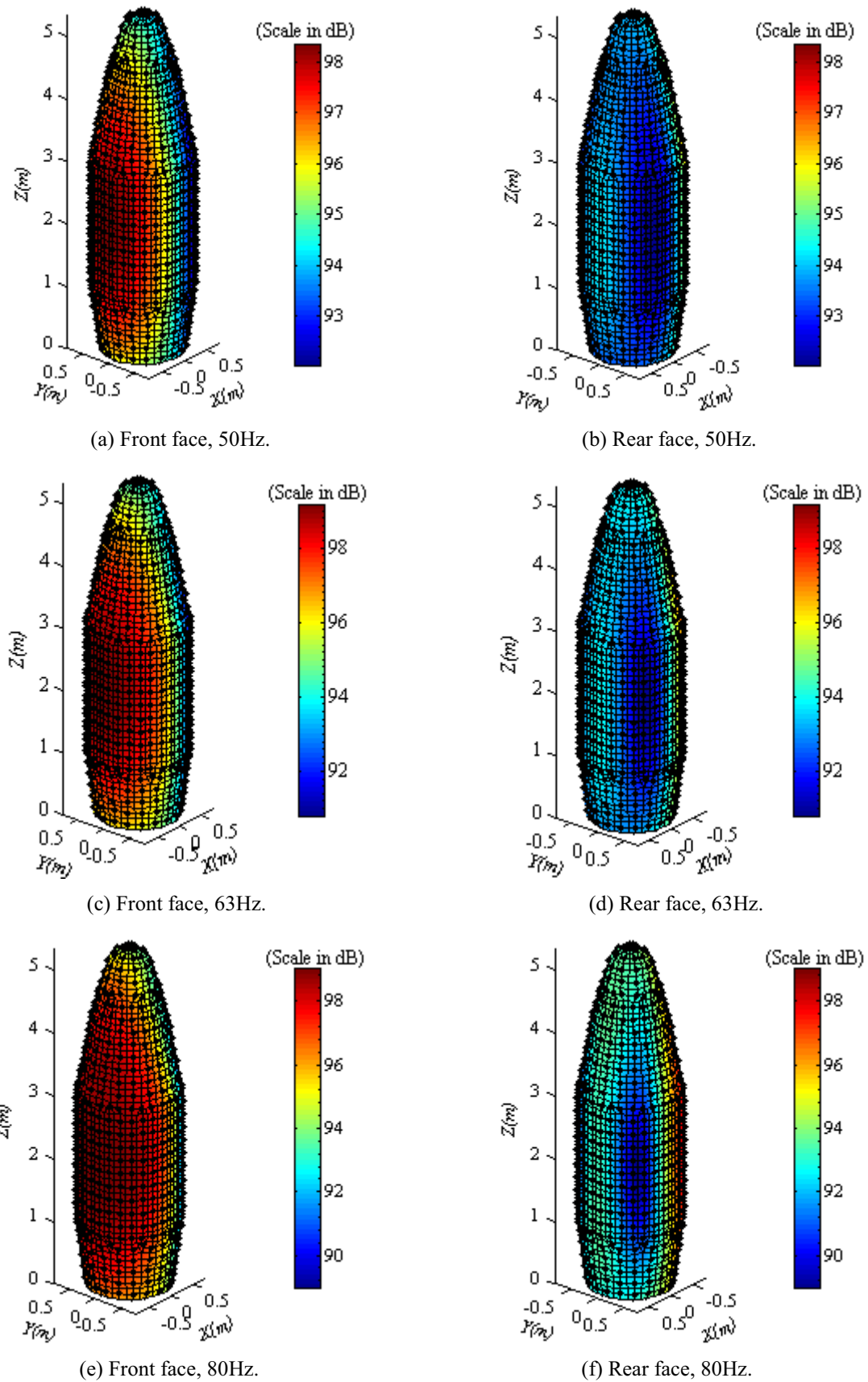
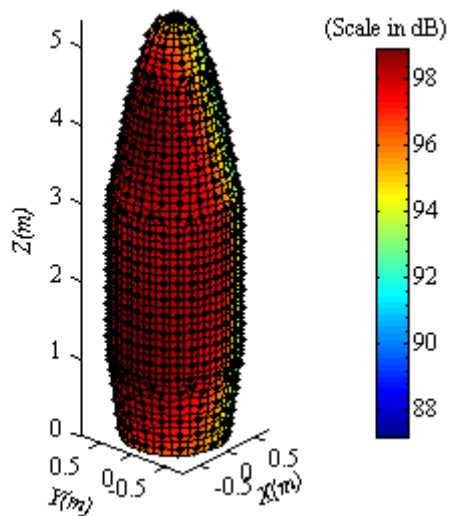


Figure 8.48: RSLVF surface elements and nodes. Geometry imported into the Open BEM. The blue circles show the circumferential nodes at a height of $z = 2.065\text{m}$ on the RSLVF.

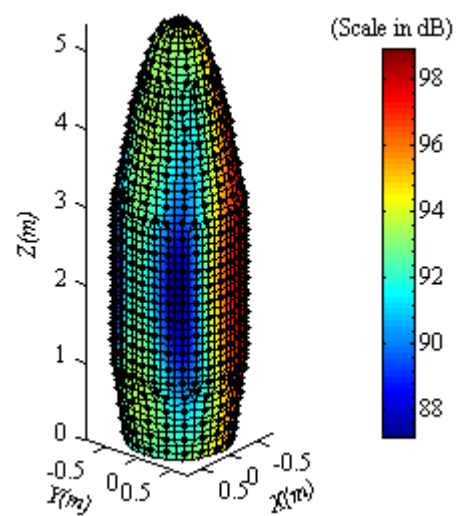
8.7.1 Sound Pressure Due to Incident Plane Waves

The sound pressure at the surface of the RSLVF due to incident plane waves travelling in the positive X direction were calculated numerically for various frequencies from 50Hz to 400Hz. Figures 8.49 (a-t) show the sound pressure excitations at the surface of the RSLVF at various 1/3-Octave band centre frequencies from 50Hz to 400Hz. The results show that at the low frequencies, the high sound pressures are distributed mostly at the second section (see Figure 7.5 in Chapter 7) of the RSLVF, where the plane wave impinges first and less is scattered on the other sections of the RSLVF. As the frequency increases the sound pressure excitations increase on the whole body of the RSLVF because the scattering of sound waves increases from the second section to the other sections of the RSLVF. The total sound pressure distribution on the circumferential nodes at a height of $z = 2.065\text{m}$ (see Figure 8.48) on the RSLVF was calculated using BEM for each applied frequency and is shown in Figures 8.50, 8.51 and 8.52. Figure 8.53 shows a comparison of the total sound pressure distribution between the BEM and analytical results calculated on the circumferential nodes at a height of $z = 2.065\text{m}$ on the RSLVF. The comparison shows very good agreement between the two methods. The small differences in sound pressure magnitudes between the two results are due to the diffraction of sounds around the ends of the RSLVF, which is taken into account in the BEM analysis but not in the analytical model.

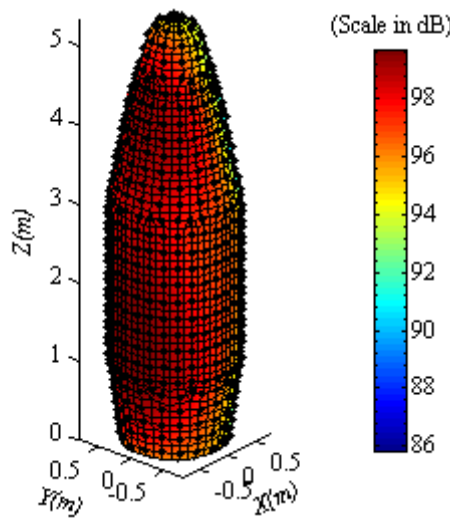




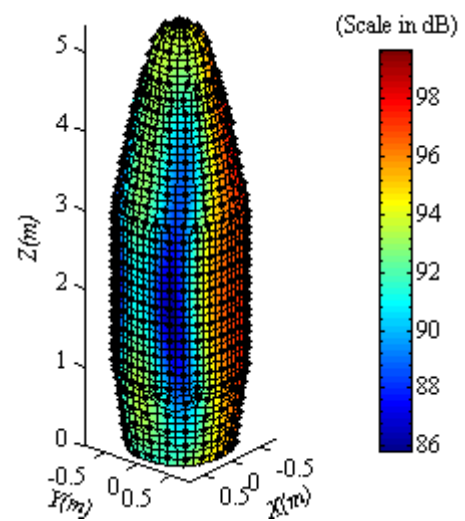
(g) Front face, 100Hz.



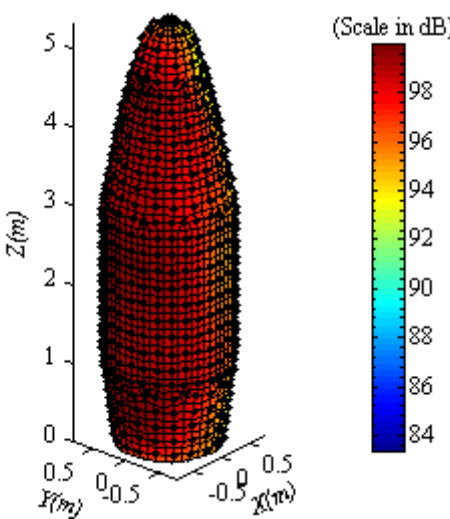
(h) Rear face, 100Hz.



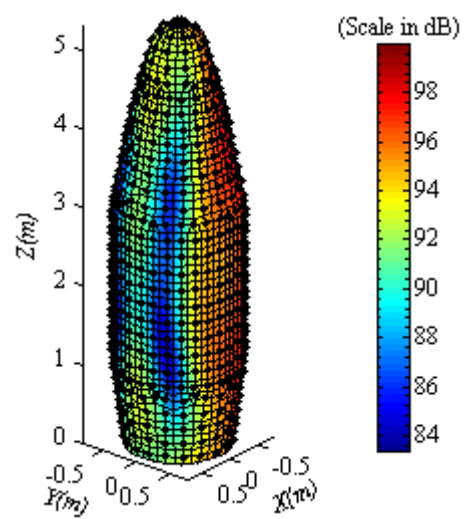
(i) Front face, 125Hz.



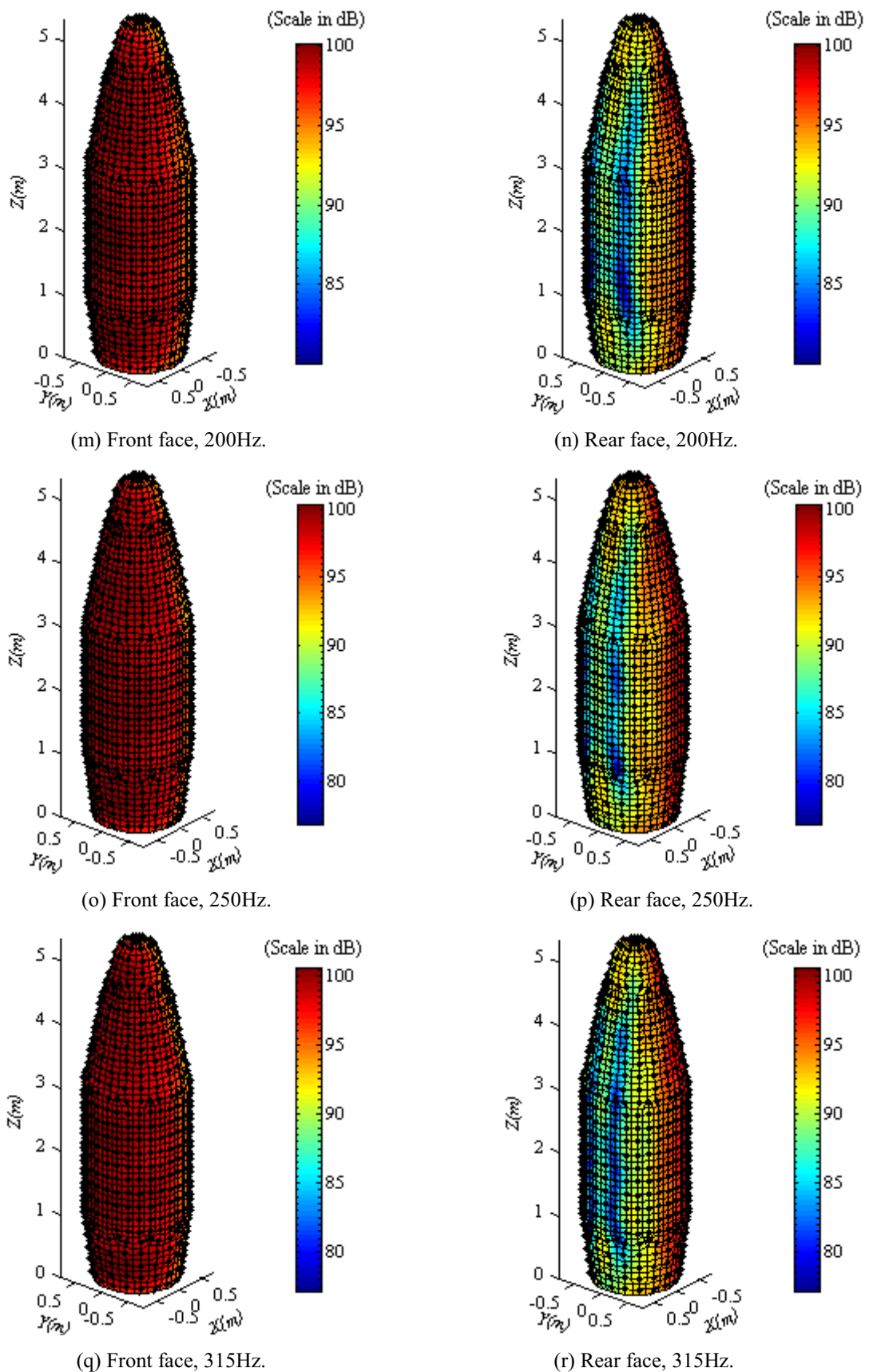
(j) Rear face, 125Hz.

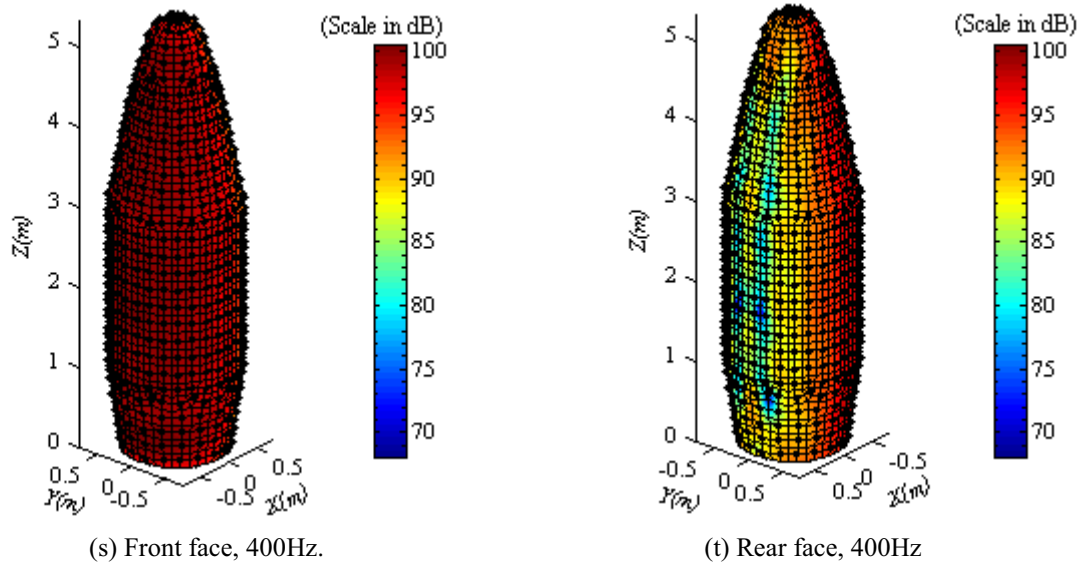


(k) Front face, 160Hz.



(l) Rear face, 160Hz.





Figures 8.49 (a-t): Numerical results for the sound pressure distribution at the surface of the RSLVF for plane waves incident on the front face at various 1/3-octave band centre frequencies from 50Hz to 400Hz. [Reference pressure $20\mu\text{Pa}$ and incident pressure magnitude $P^o = 1\text{ Pa}$]

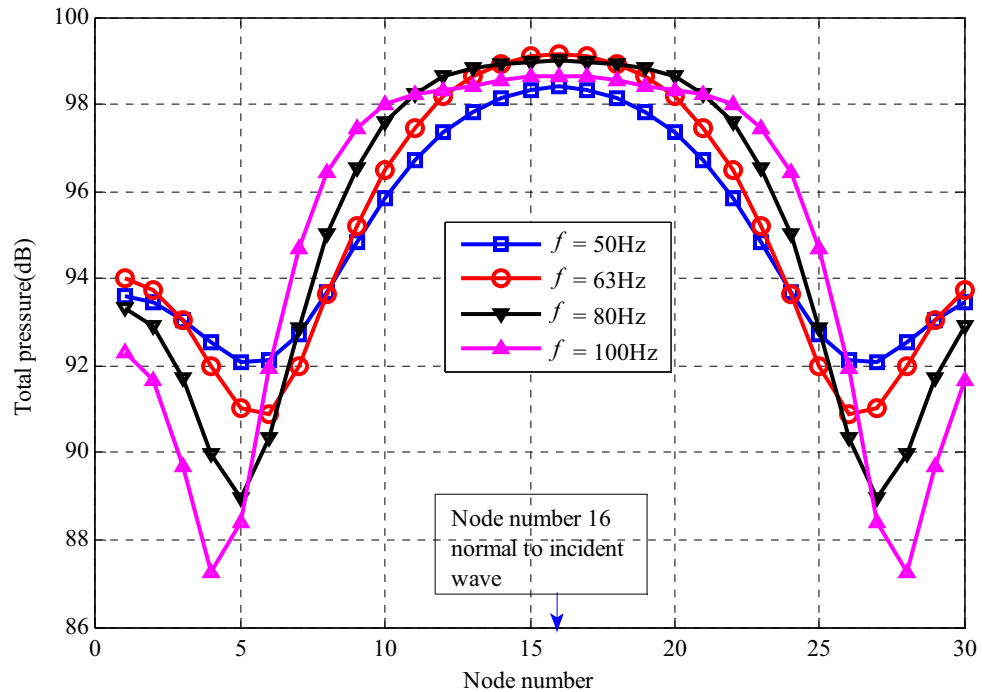


Figure 8.50: Total sound pressure calculated using BEM on the circumferential nodes at a height of $z = 2.065\text{m}$ (see Figure 8.48) on the RSLVF, for plane waves incident on the front face, for various 1/3-octave band centre frequencies from 50Hz to 100Hz. [Reference pressure $20\mu\text{Pa}$ and incident pressure magnitude $P^o = 1\text{ Pa}$]

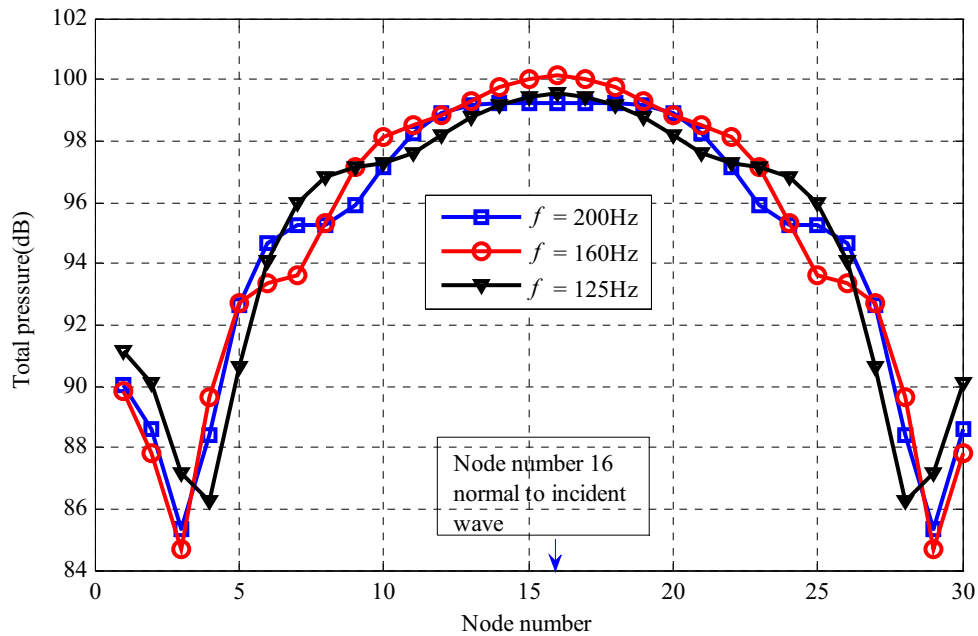


Figure 8.51: Total sound pressure calculated using BEM on the circumferential nodes at a height of $z = 2.065\text{m}$ (see Figure 8.48) on the RSLVF, for plane waves incident on the front face, for various 1/3-octave band centre frequencies from 125Hz to 200Hz. [Reference pressure $20\mu\text{Pa}$ and incident pressure magnitude $P^O = 1\text{Pa}$]

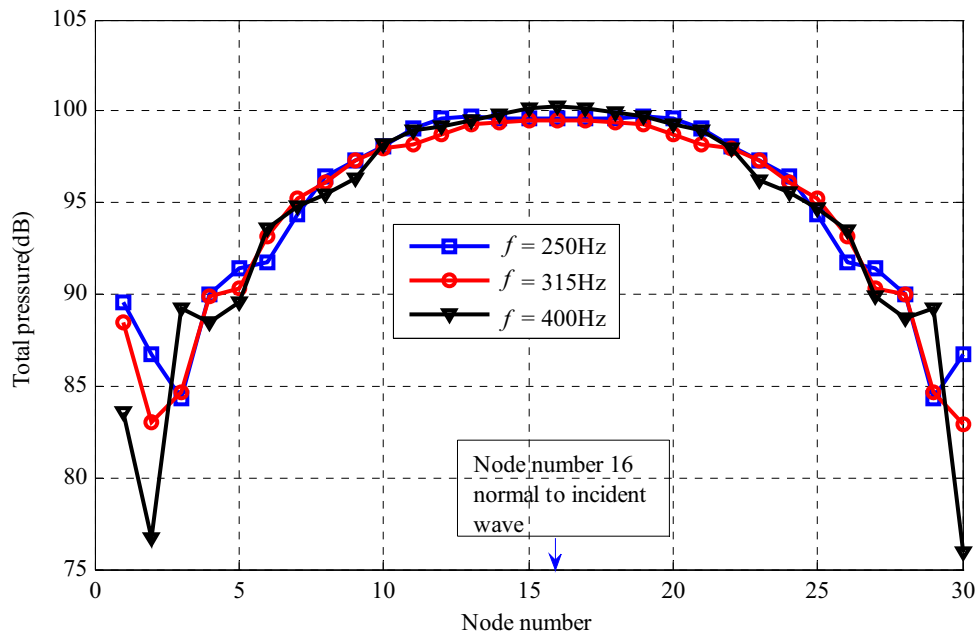


Figure 8.52: Total sound pressure calculated using BEM on the circumferential nodes at a height of $z = 2.065\text{m}$ (see Figure 8.48) on the RSLVF, for plane waves incident on the front face, for various 1/3-octave band centre frequencies from 250Hz to 400Hz. [Reference pressure $20\mu\text{Pa}$ and incident pressure magnitude $P^O = 1\text{Pa}$]

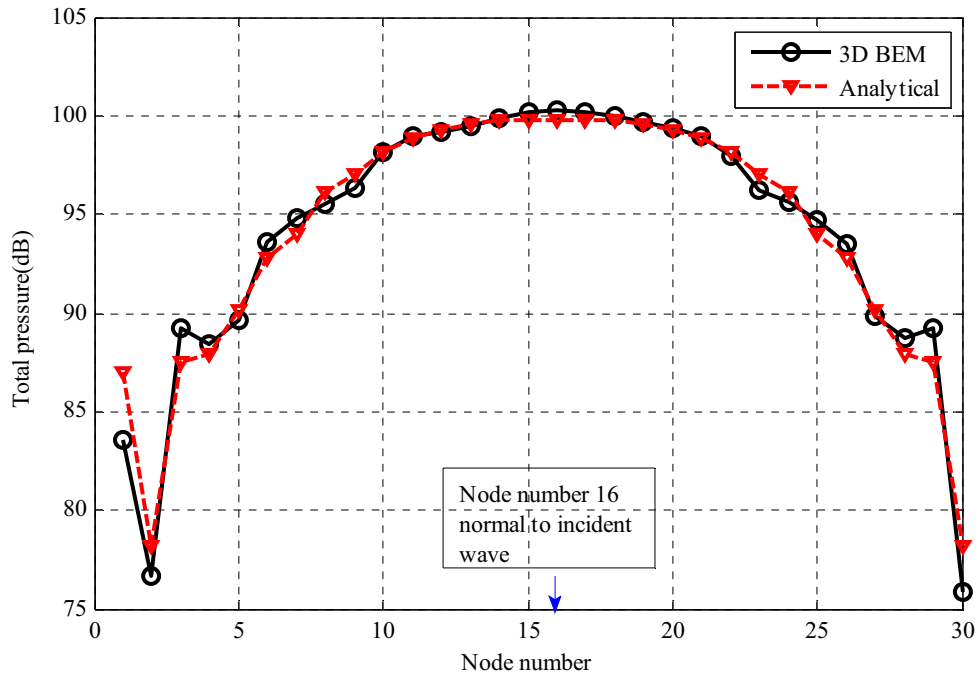
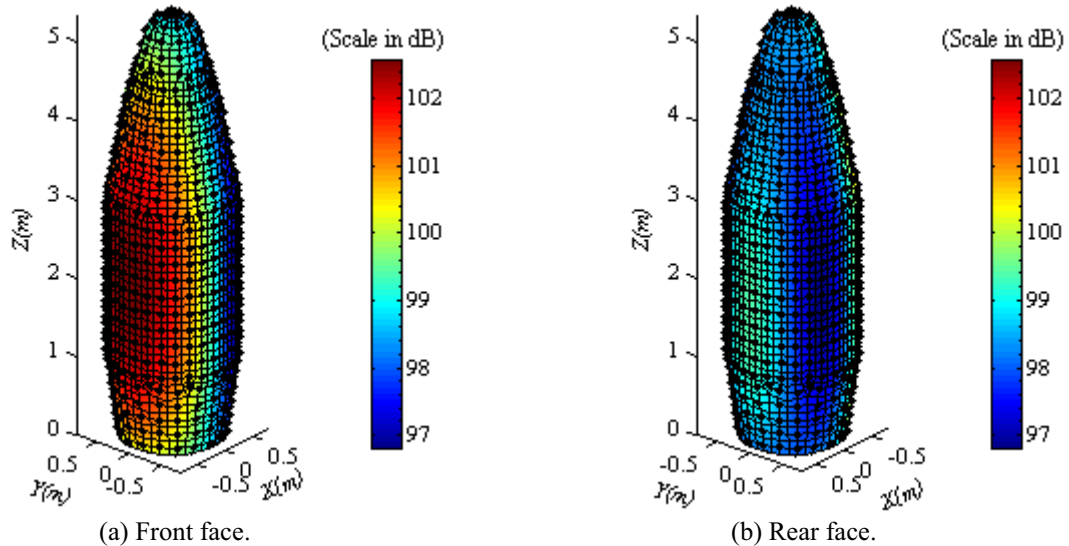


Figure 8.53: Total sound pressure comparison between the BEM and analytical results calculated on the circumferential nodes at a height of $z = 2.065\text{m}$ (see Figure 8.48) on the RSLVF, for plane waves incident on the front face, for 1/3-octave band centre frequency of 400Hz. [Reference pressure $20\mu\text{Pa}$ and incident pressure magnitude $P^O = 1\text{ Pa}$]

8.7.2 Sound Pressure Due to a Point Source

A point source of arbitrary amplitude $1 + i \text{ m}^3 / \text{s}$ was considered at $X = -20D \text{ m}$ (Diameter, $D = 1.266\text{m}$, see Figure 7.5), $Y = 0\text{m}$ and $Z = 0\text{m}$ (see Figure 7.1 for the source geometry) from the RSLVF axis. Excitation at a frequency 50Hz was applied and the total sound pressure loading at the surface of the RSLVF due to this point source is shown in the Figures 8.54(a-b). High sound pressure levels mostly occur at the front face of the RSLVF, where the sound wave impinges. The total sound pressure on the circumferential nodes at a height of $z = 2.065\text{m}$ (see Figure 8.48) was calculated using BEM and compared with the analytical result calculated using equation (7.6) and is shown in Figure 8.55. The comparison shows good agreement with the analytical result, with no significant difference between the pressure

patterns. However, the pressure amplitude between the results is different. This is because the BEM is able to consider the diffraction of sound waves from the edges of the RSLVF whereas the analytical model assumes an infinite length cylinder with no edges. From this investigation, it can be concluded that it is possible to determine the sound pressure loading on the RSLVF numerically by identifying the source positions for the launch case.



Figures 8.54(a-b): Numerical results for the sound pressure distribution at the surface of the RSLVF, due to a point source (see Figure 7.1 for the point source geometry) of 50Hz located at $X = -20D$ m (Diameter, $D = 1.266$ m, see Figure 7.5), $Y = 0$ m and $Z = 0$ m. [Reference pressure $20\mu\text{Pa}$]

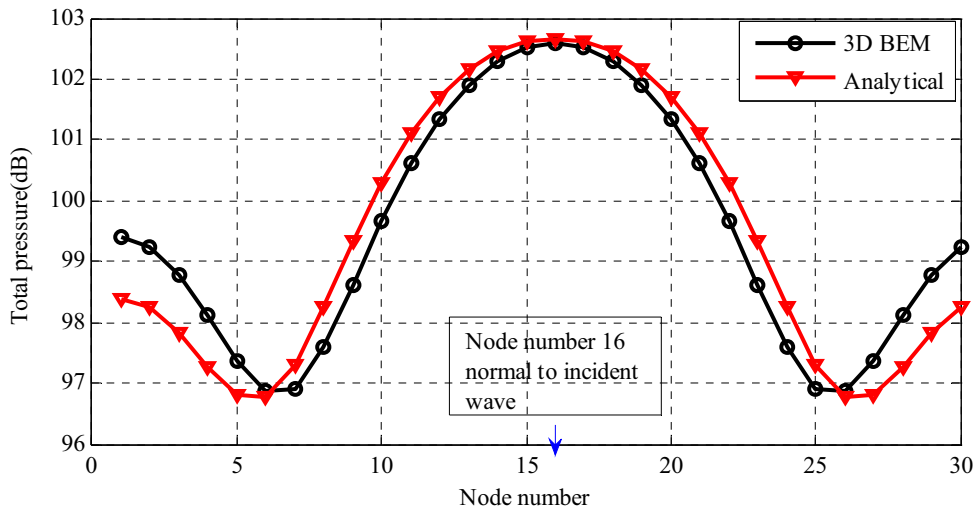
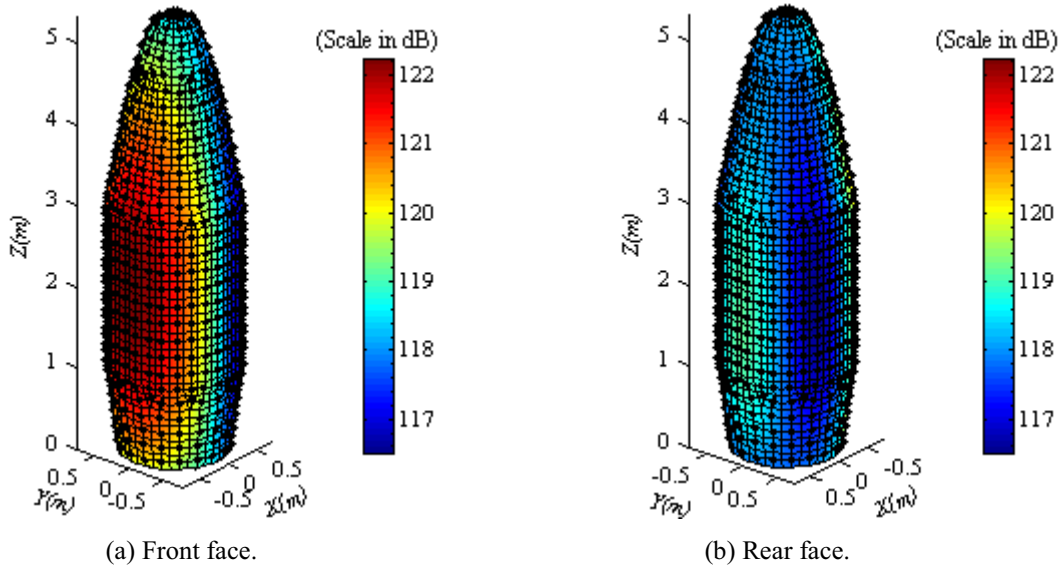


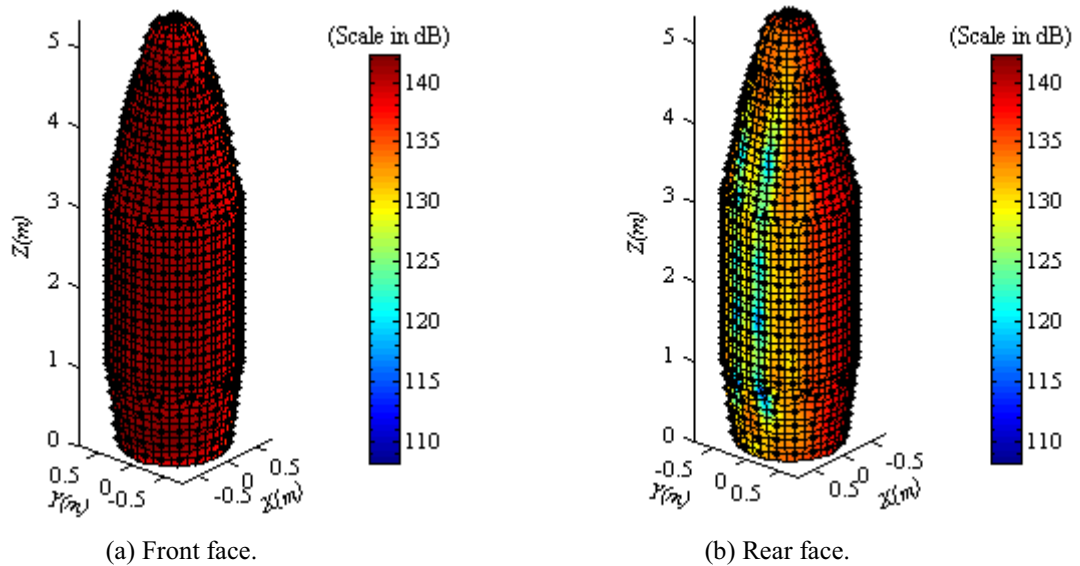
Figure 8.55: Total sound pressure comparison between the 3D BEM and analytical results calculated on the circumferential nodes at a height of $z = 2.065$ m (see Figure 8.48) on the RSLVF, for a point source of 50Hz located at $X = -20D$ m (Diameter, $D = 1.266$ m, see Figure 7.5), $Y = 0$ m and $Z = 0$ m. [Reference pressure $20\mu\text{Pa}$]

8.7.3 Sound Pressure Due to a Line Source

For the line source arrangement, fifteen point sources of arbitrary amplitudes and phases (see Table 5.1) were considered and placed on the negative X axis (see Figure 8.28 for the line source arrangement). The distance between the RSLVF axis and the first source was 1.633m and the distance between each source was 1.5m. The sound pressure excitation at the surface of the RSLVF due to this line source consisting of fifteen point sources, when all the point sources are generated same frequency 50Hz, is shown in Figures 8.56(a-b). Another case was investigated where each source generates a different frequency, similar to the arrangement discussed in Section 8.6.2.3 for the Boeing cylinder. For this case, the sound pressure distribution on the surface of the RSLVF for a line source of ten point sources with different frequencies from 50HZ to 400Hz is shown in Figures 8.57(a-b). For each case, the total sound pressure distribution on the circumferential nodes at the middle of section two (height, $z = 2.065\text{m}$, see Table 7.3 and Figure 7.5) is shown in Figures 8.58 and 8.59, respectively, and is also compared with the analytical result calculated using equation (7.6). The comparisons show good agreement between the two methods for a line source. However, there is difference in pressure magnitude between the results of the two methods, as the BEM is capable of taking into account the sound diffraction from the edges, whereas the analytical model assumes no effect due to the edges. This could be the subject of an extended investigation. However, from the results it can be concluded that it is possible to use the BEM analysis for evaluating the sound pressure at the surface of the RSLVF due to a line source for the launch case.



Figures 8.56(a-b): Numerical results for the total sound pressure distribution at the surface of the RSLVF, due to a line source of fifteen point sources (see Figure 8.28 for the line source geometry) of arbitrary amplitudes (see Table 5.1) placed on the negative X axis. Each source generated a frequency of 50Hz. [Reference pressure $20\mu\text{Pa}$]



Figures 8.57(a-b): Numerical results for the total sound pressure distribution at the surface of the RSLVF, due to a line source consisting of ten point sources of varying frequencies corresponding to one-third-octave band centre frequencies from 50Hz to 400Hz. Arbitrary strengths given in Table 5.1 were used for each point source. [Reference pressure $20\mu\text{Pa}$]

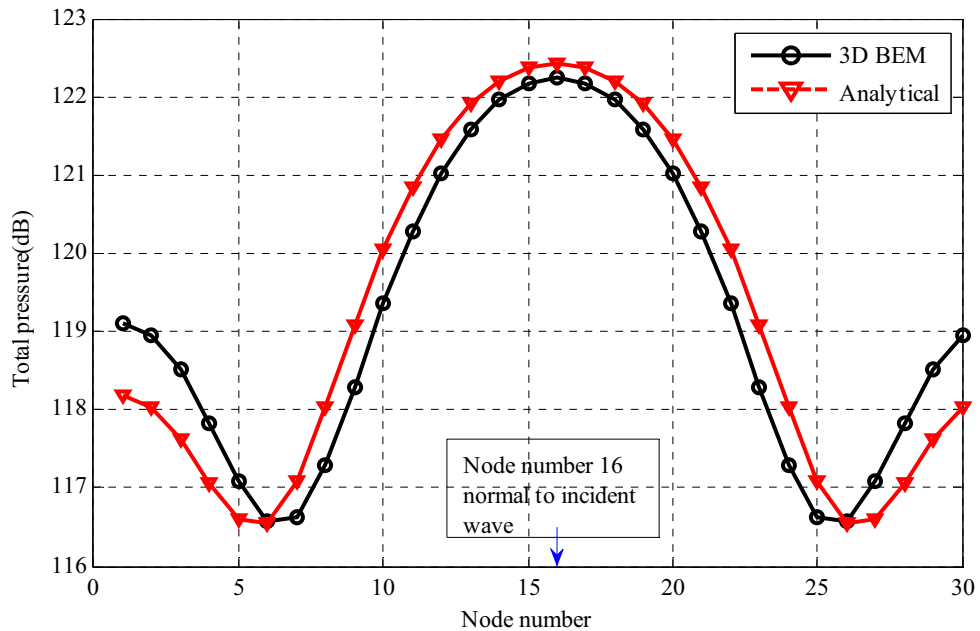


Figure 8.58: Total sound pressure comparison between the 3D BEM and analytical results calculated on the circumferential nodes at a height of $z = 2.065\text{m}$ (see Figure 8.48) on the RSLVF, for a line source consisting of fifteen point sources (see Figure 8.28 for the line source geometry) of arbitrary amplitudes (see Table 5.1) placed on the negative X axis. Each source generated a frequency of 50Hz. [Reference pressure $20\mu\text{Pa}$]

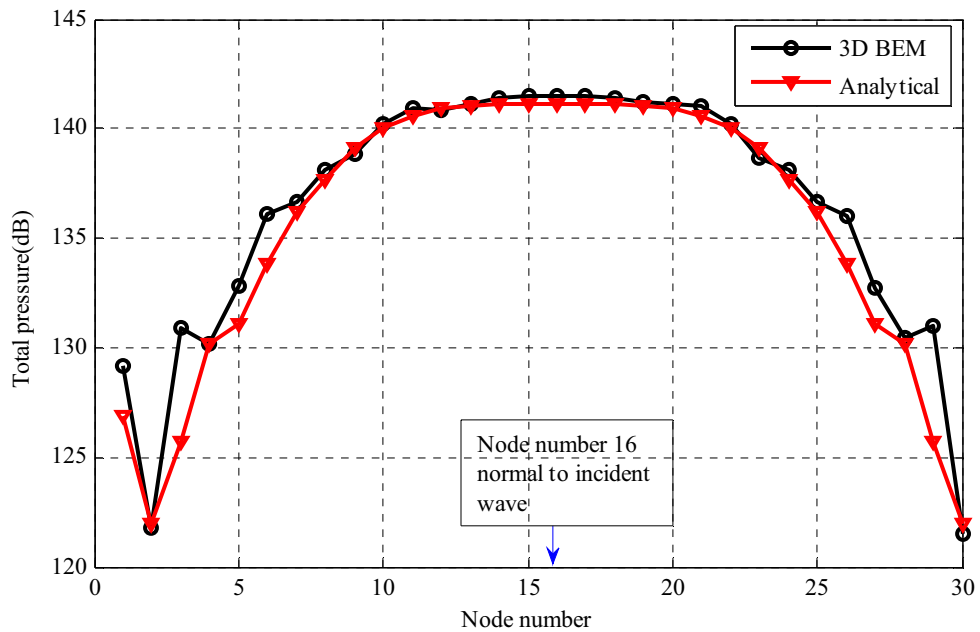


Figure 8.59: Total sound pressure comparison between the 3D BEM and analytical results calculated on the circumferential nodes at a height of $z = 2.065\text{m}$ on the RSLVF, due to a line source consisting of ten point sources (see Figure 8.28 for the line source geometry) of varying frequencies corresponding to one-third octave band centre frequencies from 50Hz to 400Hz, placed on the negative X axis at the bottom of the RSLVF. Arbitrary strengths given in Table 5.1 were used for each point source. [Reference pressure $20\mu\text{Pa}$]

8.8 Conclusions

The conclusions from the work reported in this chapter are:

- The Open BEM software package is suitable for determining the acoustic pressure excitation at the surface of the Boeing cylinder and RSLVF fairing.
- The 2D numerical results showed good agreement with the analytical and experimental results for values of ka up to $ka = 15$.
- The 2D numerical models for point and line sources produced similar results to the analytical results reported in Chapter 5 and 6, respectively.
- Another 2D numerical model, which determines the pressure fields on the field points away from the boundary surface, also gave good agreement with the analytical results. This model was extended to the Boeing cylinder, and the scattered and total sound pressure patterns in the sound fields were calculated for various values of ka . The sound pressure patterns satisfy the analytical results presented in Chapters 3, 4 and 5.
- The 3D numerical results also agree well with the analytical results, where quadratic eight node elements were used to build the geometries.
- The approach and analytical results presented in Chapter 7 are for an infinitely long cylinder and exclude diffraction around the ends of the cylinder. Diffraction around the ends of the cylinder has been considered numerically for finite length cylinders using the BEM approach in Chapter 8. Extensive comparisons between the theoretical and numerical results have been conducted considering two different aspect ratios; the experimental cylinder (aspect ratio is 12.7), and the extended cylinder (aspect ratio is 43.86). The results show that the analytical and numerical results match more accurately when the aspect ratio is high and the wave diffraction from the ends to the middle of the cylinder is reduced to an insignificant amount.

From these comparisons it is clear that the theory developed in Chapter 7 can accurately predict the pressure levels on the surface of the cylinder excluding the effects of diffraction around the ends.

For the extended cylinder the analysis and the associated nodal density produced reliable results compared with the analytical results for values of ka up to $ka = 5$ and breaks down when $ka > 5$.

The quarter-point technique was found to be reasonable way to solve for the edge effects. It was shown that diffraction resulted in an increase in the pressure magnitudes near the cylinder ends but did not significantly affect the overall sound pressure pattern.

- The 3D numerical analysis was validated compared with the analytical results for incident plane waves, a point source and a line source.
- Despite the Boeing cylinder aspect ratio being 1.13, the comparisons showed very good agreement between the analytical and numerical results. For the Boeing cylinder, the 3D numerical analysis was validated for values of $ka \leq 8$, which means the analysis was suitable in the low frequency range up to 355Hz.
- The 3D analysis of the RSLVF in the frequency range from 50Hz to 400Hz produced reliable results compared with the analytical results and showed the acoustic pressure excitations at the surface of the RSLVF for various types of acoustic loading.

The external acoustic pressure excitations of the RSLVF for various loading conditions were determined for arbitrary source strengths and locations. It has been demonstrated that the 3D numerical analysis can be used to predict the acoustic loads on the fairing given the source strengths and their locations. The next chapter investigates the launch acoustic environment to identify the source locations and strengths, and uses similar 3D numerical analysis as considered in this chapter.

Chapter 9

Prediction of Acoustic Loads on the Fairing During Lift-off of a Launch Vehicle

9.1 Introduction

In the previous chapter, it has been seen that theoretical and numerical models are able to predict the imposed acoustic loads on simple and complex structures for various source configurations. To determine an appropriate source model and configuration that will accurately represent the rocket motor sound, it is necessary to take into account various complicated parameters such as vehicle geometry, propulsion devices, flow configurations and launch pad configurations. The sound fields generated by large propulsion devices, mix with the exhaust flow, and are also deflected by the deflector below the vehicle and radiated back to the vehicle. The reflections and diffractions of the sound fields on the vehicle stand and other objects on or near the launch pad may increase the acoustic pressure fluctuations on the vehicle. However, when all the necessary parameters are known, it should be possible to predict the acoustic loads on the vehicle. Nevertheless, the prediction of the acoustic loading on launch vehicles faces tremendous theoretical and technological challenges due to the many complicated parameters and complex geometries involved.

In the past, the prediction of acoustic loads generated by the propulsion devices on the vehicle has been performed using semi-empirical analytical methods based on

experimental data (Franken *et al.*, 1960; Potter, 1966; Potter & Crocker, 1966; NASA-SP-8072, 1971). The prediction methods are outlined for chemical rockets in NASA-SP-8072 (1971), a space-vehicle design criteria document. The recommended methods predict the acoustic loads at a point on the vehicle using two different source allocation methods based on the experimental data of the sound power spectrum radiated by the propulsion devices, the lateral deflection of the jets exhausted by the rocket engines, and allocation of the noise generation sources along the exhaust stream. One is the unique source allocation method, which assumes that there is a single equivalent point source location along the exhaust flow axis for each frequency. The other one is the non-unique source allocation method, which assumes that there are a number of point source locations making a line source along the exhaust flow axis for each frequency. The scattering effects from the vehicle surface were completely omitted in these methods. Potter (1966) described an analytical method to implement the scattering effects from the surface, which involved the source allocation technique, and is based on the theoretical analyses for a simple cylinder presented by Morse (1936), Morse & Feshbach (1953b) and Morse & Ingard (1986). In particular, Potter's method is embodied in equation (3.26) (see Chapter 3 of this thesis). However, this is not appropriate for dealing with scattering from a hard launch vehicle surface, as already discussed previously. Malbeque *et al.* (1987), also considered the empirical source allocation technique to analyse the scattering of incident acoustic waves by the surface of the Ariane IV space launcher, using boundary integral methods. However, this analysis examined the sound field in the vicinity of the launcher rather than at the launcher surface.

This chapter investigates the acoustic loads, including the scattering effects on the RSLVF,

using two separate source allocation methods as suggested in NASA-SP-8072 (1971). The methods were used to allocate the source locations corresponding to one-third-octave band centre frequencies in the range from 50Hz to 400Hz, and the methods were extended using the analytical and numerical tools developed in this thesis, to examine the acoustic loads at the surface of the RSLVF.

9.2 Estimation of the Rocket Engine Exhaust Noise

Severe acoustic noise produced during the lift-off of a launch vehicle is related to the various physical and operating conditions of the engine and the exit conditions of the flow. Therefore, for prediction purposes, several parameters need to be taken into account. Operating and exit parameters for various chemical rocket engines are listed in Table 9.1, where engine ‘A’ has multiple nozzles (eight nozzles) and the rest have a single nozzle.

NOTE:

This table is included on page 198 of the print copy of the thesis held in the University of Adelaide Library.

Table 9.1: Rocket engine operating and exit parameters. [Data taken from Mayes *et al.* (1959)]

The acoustic power generated by the rocket engine is dependent on the mechanical power of the jet stream. This can be expressed by the following empirical equation as suggested

in NASA-SP-8072 (1971), a space-vehicle design criteria document:

$$W_{OA} = 0.005 n F U_e, \quad (9.1)$$

where

W_{OA} = overall acoustic power, W

n = number of nozzles

F = thrust of each engine, N

U_e = fully expanded exit velocity, m/s

The overall acoustic power level is (NASA-SP-8072, 1971),

$$L_w = 10 \log_{10} (0.005 n F U_e), \text{ dB.} \quad (9.2)$$

According to the referenced document, this equation assumes that the acoustic power is one percent of the total engine power. However, the equation clearly shows that the noise generation is 0.5%. Potter & Crocker (1966) have suggested the '*Gierke method*' to calculate the overall generated acoustic power, and there are discrepancies in results compared with the results obtained using equations (9.1) and (9.2). The '*Gierke method*' is discussed and compared with the results obtained using equations (9.1) and (9.2) for engine 'E' in *Appendix E*, where the difference between the two results is 6.47dB. For the current analysis the equations derived above were used and it is assumed that 0.5% of stream power is converted to acoustic power. The overall acoustic power levels for various engines are shown in Figure 9.1, where it can be seen that engine 'A' generates the highest and engine 'F' generates the lowest overall acoustic power level. The remaining engines generate almost the same amount of overall acoustic power level.

The length of the supersonic core generated by the engine is directly related to the fully expanded

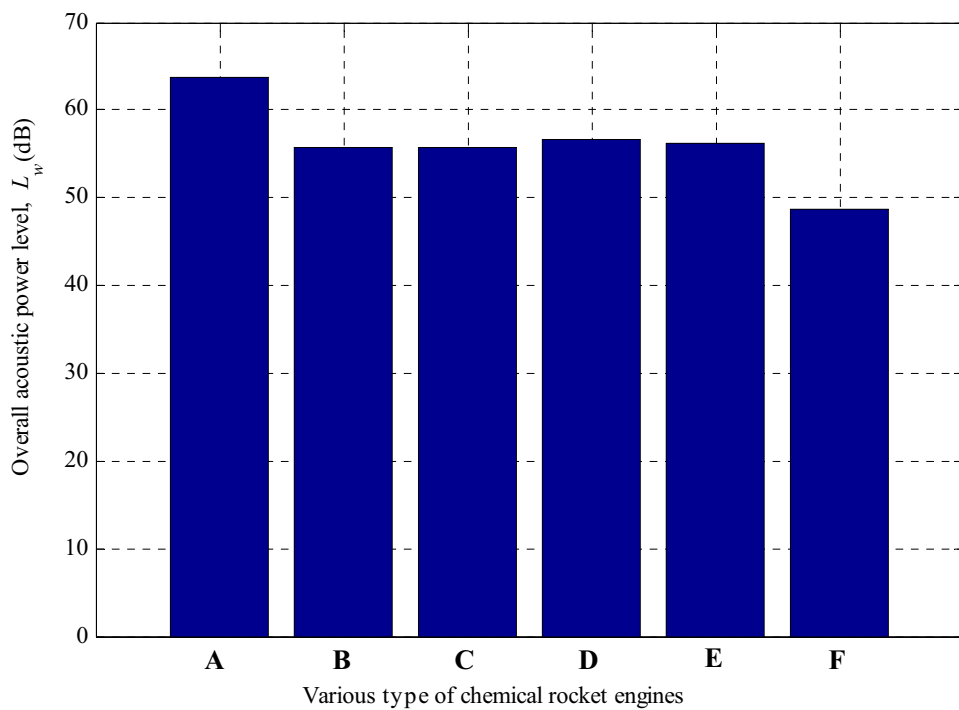


Figure 9.1: Overall acoustic power levels for various rocket engines ‘A’ to ‘F’.

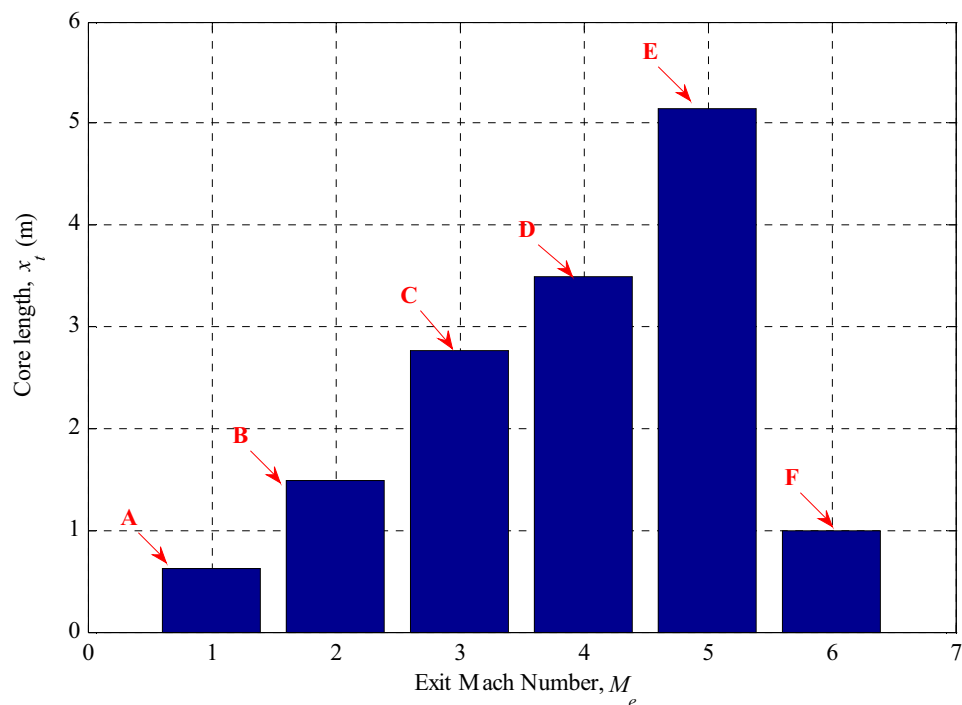


Figure 9.2: Core lengths for various chemical rocket engines ‘A’ to ‘F’.

exit Mach number. The length of the core can be determined as follows (NASA-SP-8072, 1971):

$$x_t = 3.45 \times (1 + 0.38M_e)^2 \times D_e , \quad (9.3)$$

where x_t is the length of the core, M_e is the Mach number and D_e is the nozzle exit diameter. If the vehicle has multiple nozzles, an exit nozzle diameter can be calculated as follows (NASA-SP-8072, 1971):

$$D_e = \sqrt{n} D_{ei} , \quad (9.4)$$

where D_{ei} is the exit diameter of the individual nozzle. The core lengths associated with the various chemical engines are shown in Figure 9.2. Engine ‘E’ generates the highest core length of 5.15m. Engine ‘A’, which has multiple nozzles, generates a core length of 0.62m. For the current work, engine ‘E’ was chosen for the prediction of acoustic loads on the rocket fairing because it has the highest core length.

9.3 Geometry Under Consideration to Predict the Acoustic Loads

For the current work, the geometry chosen for the acoustic loading calculations is shown in Figure 9.3. The rocket is launched vertically, with a 90° bucket deflector turning the exhaust stream horizontally. This means that the flow axis is perpendicular to the vehicle axis. For this particular case, it was assumed that all the sources are situated below the rocket along the exhaust flow axis so that all the incoming waves impinge obliquely on the rocket.

The present work is not focused on the interaction of the supersonic jet with the deflector as this is beyond the scope of this thesis. In the current work the 90° bucket deflector was

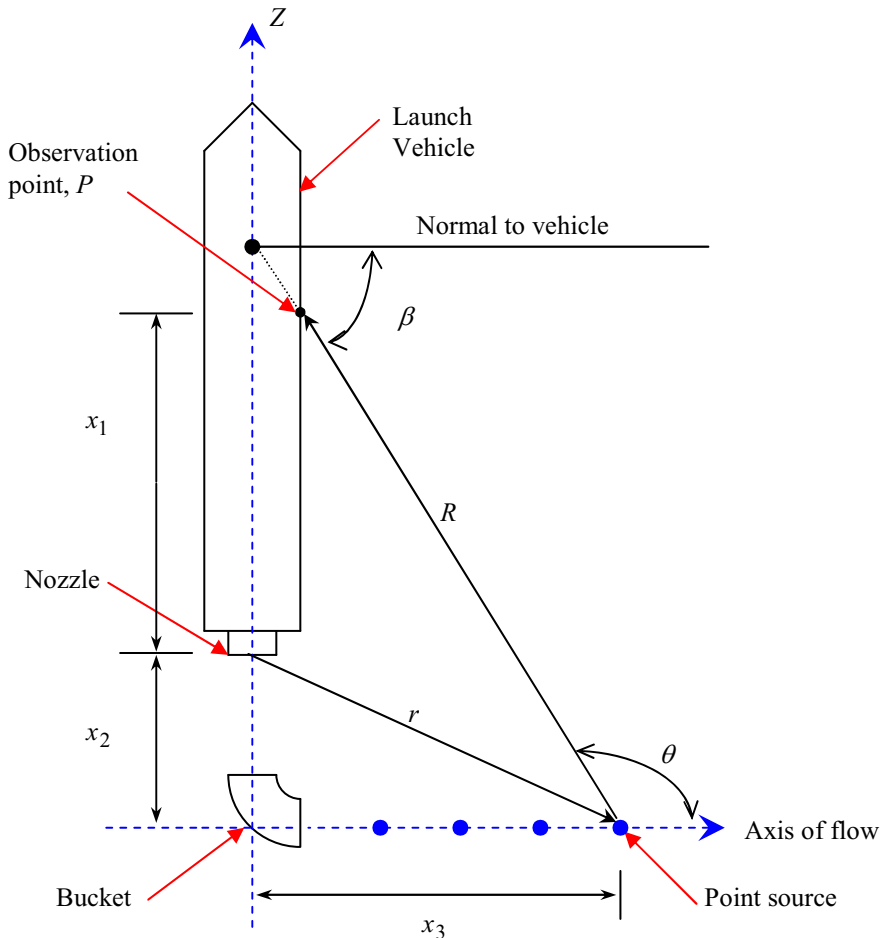


Figure 9.3: Geometry of source locations relative to the vehicle and flow axis.

considered and it has been assumed that the source allocation is along a line perpendicular to the vehicle axis.

The parameters shown in Figure 9.3 are defined as follows:

x_1 is the axial distance of the observation point P on the vehicle from the nozzle exit;

x_2 is the vertical distance from the nozzle exit of the sources along the flow axis;

x_3 is the distance of the source from the vehicle axis along the flow axis;

- r is the distance of the source from the nozzle exit;
- R is the distance between the source and a given point, P , on the vehicle;
- β is the incline angle between the line joining the observation point P to the source location, and the normal of the vehicle axis and
- θ is the angle from the horizontal axis of the noise radiation.

9.4 Prediction of Acoustic Loads Using the Unique Source Allocation Method

The methodology that used here for the prediction of acoustic loads on the vehicle is outlined in NASA-SP-8072 (1971). This technique assumes that the rocket exhaust noise can be modelled as originating from a single unique effective source location along the flow axis in each frequency band of interest. For the current analysis, one-third-octave band centre frequencies from 50Hz to 400Hz are used.

9.4.1 Prediction Formulations

In the document referenced above, the normalized relative sound power spectrum levels for various chemical rockets with single nozzles, which include a thrust range of 1.56 kN to 31,100 kN, are given in terms of Strouhal number, $\left(\frac{f D_e}{U_e} \right)$. The apparent axial distance of the source from the nozzle plane is also given in terms of Strouhal number. Both of these results were used to estimate the sound power level and effective unique source location for each frequency band of interest. The estimated results for the normalized relative sound power level and apparent source location for each 1/3 octave band centre

frequency of engine ‘E’ are given in Figures 9.4 and 9.5, respectively, as a function of Strouhal number (Data estimated from NASA-SP-8072, 1971). Figure 9.5 shows that in the low frequency range the sources are located much further downstream than at higher frequencies. However, the normalized relative sound power spectrum (shown in Figure 9.4) can be converted to any acoustic bandwidth as follows (NASA-SP-8072, 1971):

$$L_{w,b} = 10 \log_{10} \left[\frac{W(f)}{W_{OA}} \frac{U_e}{D_e} \right] + L_w - 10 \log_{10} \frac{U_e}{D_e} + 10 \log_{10} \Delta f_b , \quad (9.5)$$

where $W(f)$ is the sound power per Hz and Δf_b is the bandwidth of the frequency band, which was calculated for each 1/3 octave band centre frequency from 50Hz to 400Hz using Bies & Hansen (2003). Figure 9.6 shows the calculated sound power level for each 1/3 octave bandwidth for the current analysis.

The directional characteristic of the sound radiated back to the vehicle depend on Strouhal number, exit flow direction, effective source location of the rocket exhaust noise and observation position on the vehicle. Figure 9.7 shows the far-field directivity curve for chemical rockets, which was estimated from NASA-SP-8072 (1971). In the referenced document, there are many directivity curves presented in terms of Strouhal number, $\left(\frac{f D_e}{U_e} \right)$. For simplicity to estimate the data, only one directivity curve was chosen in the current analysis for engine ‘E’ for use with all the frequencies and source locations. To find the directivity index from Figure 9.7, the directivity angle θ relative to the exhaust axis needs to be calculated using the equivalent source position for each frequency and observation point on the vehicle.

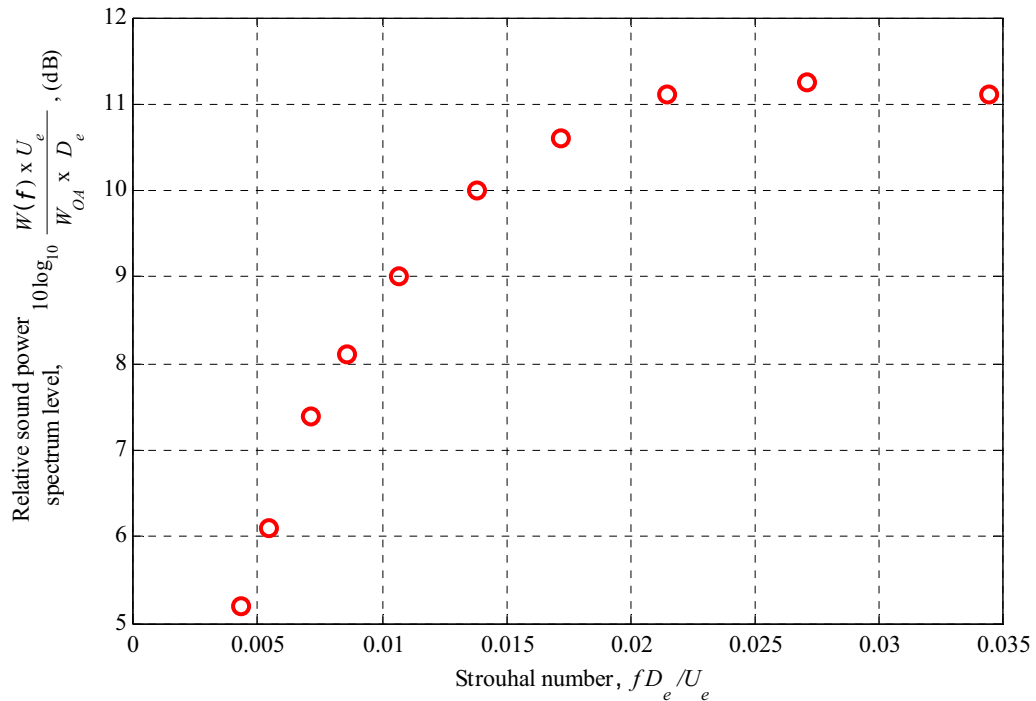


Figure 9.4: Estimated relative sound power levels for each one-third-octave band centre frequency from 50Hz to 400Hz. [Data estimated from Figure 5, presented in NASA-SP-8072 (1971)]

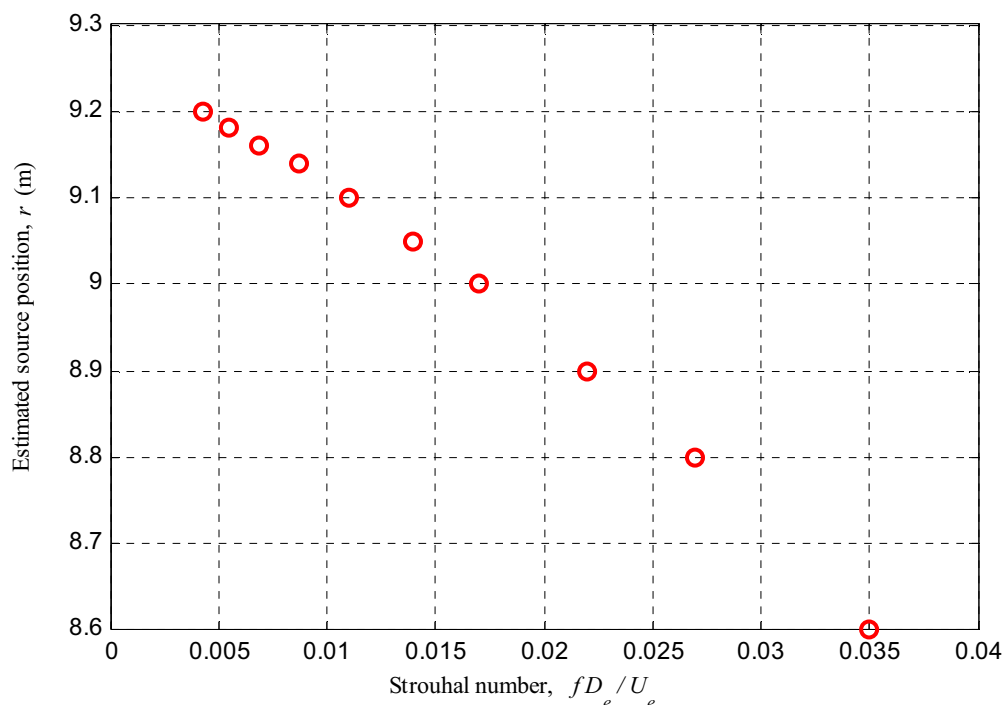


Figure 9.5: Estimated source locations for each one-third-octave band centre frequency from 50Hz to 400Hz. [Data estimated from Figure 14, presented in NASA-SP-8072 (1971)]

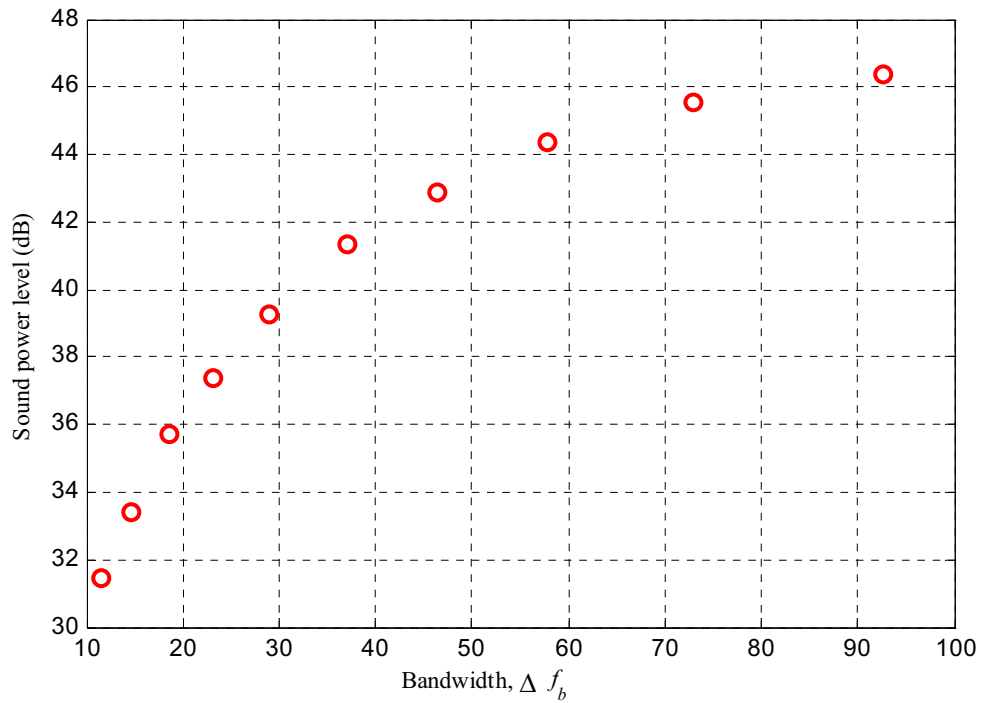


Figure 9.6: Calculated sound power levels at each one-third-octave bandwidth from 50Hz to 400Hz.

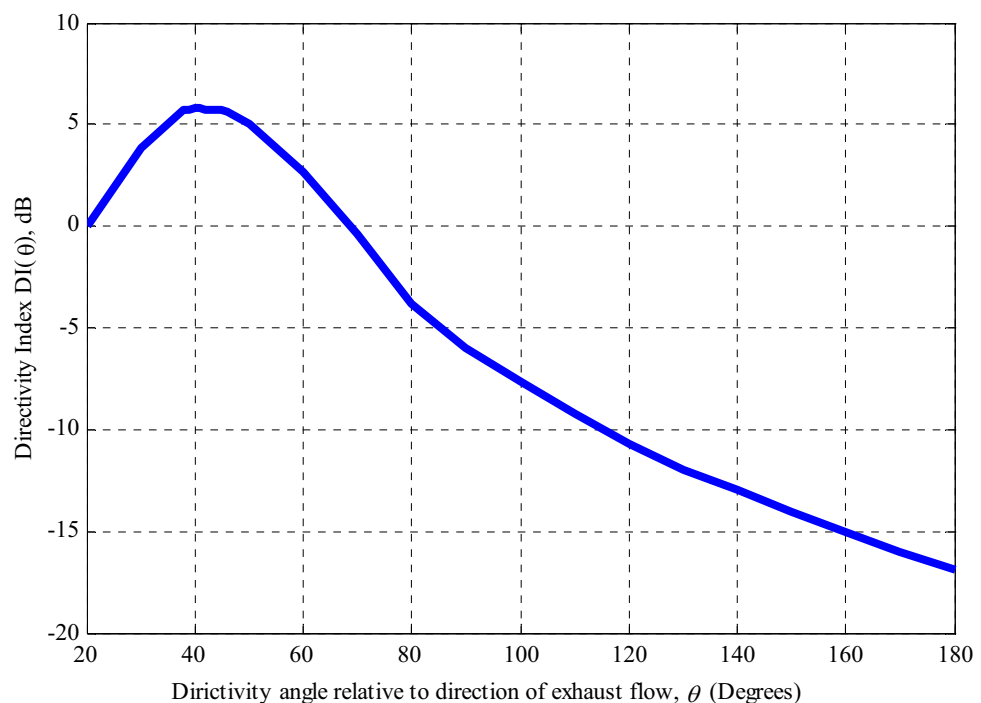


Figure 9.7: Simple directivity curve is used in calculations. [Data estimated from Figure 10, presented in NASA-SP-8072 (1971)]

The acoustic power of each source for each frequency band can be determined from the acoustic power level, $L_{w,b}$ presented in equation (9.5), as follows:

$$W_b = 10^{\left(\frac{L_{w,b}}{10}\right)}, \text{ Watts} \quad (9.6)$$

where the subscript b indicates the frequency band. The strength of each source corresponding to each frequency band can be determined as follows (Bies & Hansen, 2003):

$$Q_{s,b} = \sqrt{\frac{4\pi W_b}{k^2 \rho c}}, \text{ m}^3/\text{s} \quad (9.7)$$

where c and ρ are the speed and density of air in the exhaust flow, respectively, k is the wave number and Q_s indicates the strength of source. The sound pressure level on the circumference around the vehicle, including the effects due to the reflecting surface of the vehicle, for a band centred on any frequency can be expressed as

$$L_{p,b,\phi_i} = 10 \log_{10} \left\{ \left[P_a^t(R_i, k, a, z, \phi_i, Q_{s,b}) \right]^2 \right\} + \text{DI}(\theta), \text{ (re } 20 \mu\text{Pa}) \quad (9.8)$$

where the pressure quantity, P_a^t , represents the total sound pressure on the vehicle due to incident and scattered waves, and is a function of the distance R_i from the source to the observation point on the vehicle, wave number k , radius of the vehicle a , elevation height z , azimuthal angle ϕ_i and source strength $Q_{s,b}$, and the term $\text{DI}(\theta)$ is the directivity index determined from Figure 9.7. This pressure quantity can be determined using equation (7.6) presented in Chapter 7 and equations (8.13) and (8.21) presented in Chapter 8 for the analytical and numerical calculations respectively. The first summation presented in equation (7.6) and the summation presented in equation (8.21) need to be take into

account for all the sources that is for all the frequency bands, using logarithmic summation of L_{p,b,ϕ_i} over the entire spectrum. Then the overall sound pressure level calculated by the logarithmic summation of L_{p,b,ϕ_i} over the entire spectrum becomes (NASA-SP-8072, 1971)

$$L_{p,OA,\phi_i} = 10 \log_{10} \sum_{\text{All } b} 10^{L_{p,b,\phi_i}/10} . \text{ (re } 20\mu\text{Pa}) \quad (9.9)$$

In the above equations (9.8) and (9.9), the sound pressure due to scattering from the reflecting surface of the vehicle as well as the spreading due to distance, are included. The effect of the scattered sound field on the sound pressure on the surface of the vehicle was not considered in the previous analysis presented by NASA-SP-8072 (1971). It is also noticeable that in the above equations the 4π term has been used because the directivity index, $DI(\theta)$, of the sound radiation relative to the exhaust axis includes the effect of the sources being located on a hard surface.

9.4.2 Acoustic Loadings on the Fairing

In this section, the unique source allocation technique, which approximates the sound generation using an equivalent single point source for each frequency band of interest along the flow axis, was used to predict the acoustic loads on the RSLVF both analytically and numerically. Both calculations were conducted for each one-third-octave band centre frequency, from 50Hz to 400Hz. There are in total 10 equivalent point sources relative to these one-third-octave band centre frequencies. It was assumed that the fairing structure and the flow axis are situated at $x_1 = 15D_e$ upstream and $x_2 = 5D_e$ downstream of the

vehicle respectively. A reference point was chosen at $\phi_i = 0^\circ$, which is the front point on the vehicle facing the exhaust flow. Hence $\phi_i = 180^\circ$ is the rear point on the vehicle. For simplicity, it was assumed that the temperature along the flow axis is $T = 1000^\circ\text{C}$. At that temperature the speed of sound and density in air is 715.49 m/s and 0.28 kg/m³ respectively.

For comparison, both the analytical and numerical calculations were conducted around the circumference of section two (see Figure 7.5 in Chapter 7), at a height of $z = 2.17\text{m}$ from the bottom face of the RSLVF. This height was chosen because at that height there are sixty circumferential nodes, which are sufficient to achieve an accurate numerical estimation of the sound pressure pattern for comparison with the analytical result. The estimated and calculated values of all the parameters that were used in the calculations are given in Table 9.2 for each 1/3 octave band centre frequency, and the directivity index was assumed to be same for all the circumferential positions at the observation height on the fairing.

Source Number	One-Third-Octave Band Centre Frequency (Hz)	Estimated Source Distance, r (m)	Source Distance From the Vehicel Axis, x_3 (m)	Elevation Angle, β (Degrees)	Directivity Angle, θ (Degrees)	Estimated Directivity Index, $DI(\theta)$, (dB)	Calculated Acoustic Power Level in Each Band, $L_{w,b}$ (dB)	Source Strength, $Q_{s,b}$ (m ³ /s)
1	50	9.20	9.13	26.74	153.26	-13.6	31.47	21.36
2	63	9.18	9.11	26.79	153.21	-13.5	33.38	21.12
3	80	9.16	9.09	26.84	153.16	-13.4	35.72	21.78
4	100	9.14	9.07	26.89	153.11	-13.3	37.38	21.09
5	125	9.10	9.03	26.99	153.00	-13.2	39.25	20.93
6	160	9.05	8.98	27.12	152.87	-13.1	41.33	20.77
7	200	9.00	8.93	27.25	152.75	-13.0	42.89	19.89
8	250	8.90	8.83	27.52	152.48	-12.9	44.36	18.84
9	315	8.80	8.72	27.81	152.19	-12.8	45.52	17.09
10	400	8.60	8.52	28.36	151.63	-12.7	46.40	14.89

Table 9.2: Details of the 10 sources. (All the data given here for engine ‘E’; overall acoustic power level, $L_W = 56.28$ dB; speed of sound and density in air at $T = 1000^\circ\text{C}$ is 715.49 m/s and 0.28 kg/m³ respectively.)

9.4.2.1 Analytical Results

For the analytical acoustic loading on the RSLVF using the unique source allocation technique, which approximates the sound generation using an equivalent single point source for each frequency band of interest, the diameter of section two of the RSLVF (see Figure 7.5 and Table 7.3 in Chapter 7) was considered for evaluation of the sound pressure levels at its surface around the circumferential positions as a function of azimuthal angles ϕ_i . The scattering of sound from the surface was considered in the calculations as described in equations (9.8) and (9.9). Figures (9.8), (9.9) and (9.10) show the sound pressure levels at the surface of the RSLVF at each one-third-octave band centre frequency from 50 Hz to 400Hz, calculated using equation (9.8) at a height of $z = 2.17\text{m}$ from the bottom face of the RSLVF. The overall sound pressure level (OSPL) for ten equivalent point sources acting as a line source, for the entire spectrum of one-third-octave band centre frequency range from 50Hz to 400Hz, calculated using equation (9.9) at a height of $z = 2.17\text{m}$ from the bottom face of the RSLVF, is shown in Figure 9.11. The overall sound pressure level (OSPL) calculated using equation (9.9) at the forward ($\phi = 0^\circ$) and backward ($\phi = 180^\circ$) point of the RSLVF is 125.1 dB and 114.7 dB respectively. The directivity pattern of the overall sound pressure level (OSPL) is also shown in Figure 9.12. From these results, it can be seen that sound pressure amplitude varies relatively smoothly at the front of the RSLVF facing the exhaust flow and varies more aggressively at the back of the RSLVF, due to positive and/or negative interference of the two diffracted waves travelling around the two sides of the RSLVF. The sound pressure fluctuation increases at the back of the RSLVF as the frequency increases because the amount of interference of the two diffracted waves travelling around the two sides of the RSLVF increases.

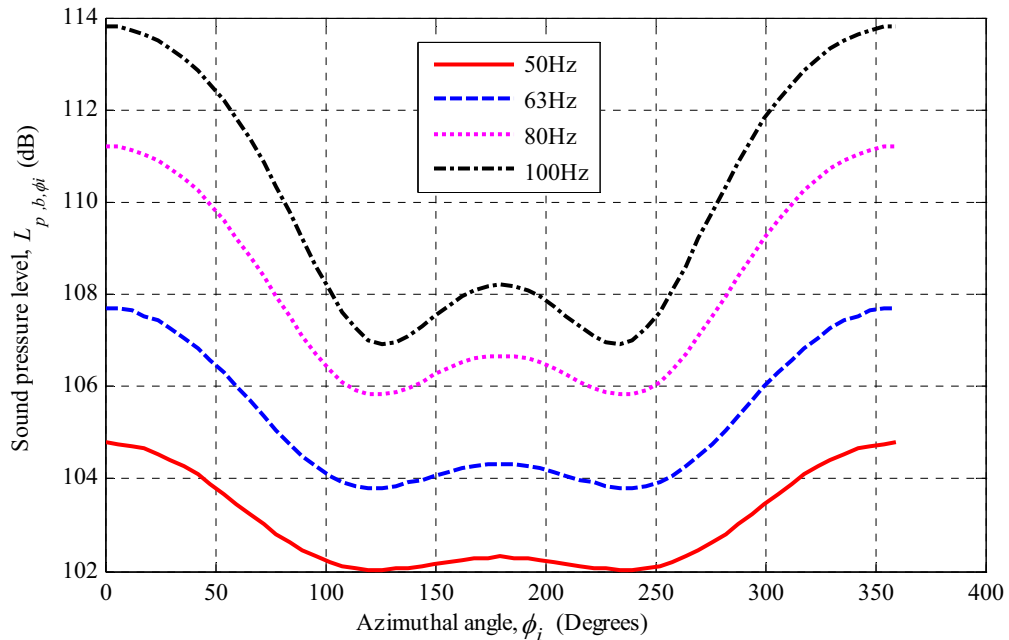


Figure 9.8: Analytically calculated sound pressure levels at the surface of section two (see Figure 7.5 in Chapter 7) at a height of $z = 2.17\text{m}$ from the bottom face of the RSLVF, using the unique source allocation method, for an equivalent single point source for each one-third-octave band centre frequency from 50Hz to 100Hz. For the equivalent point source location at each frequency see Table 9.2. [$x_1 = 15D_e$, $x_2 = 5D_e$ and reference pressure $20\mu\text{Pa}$]

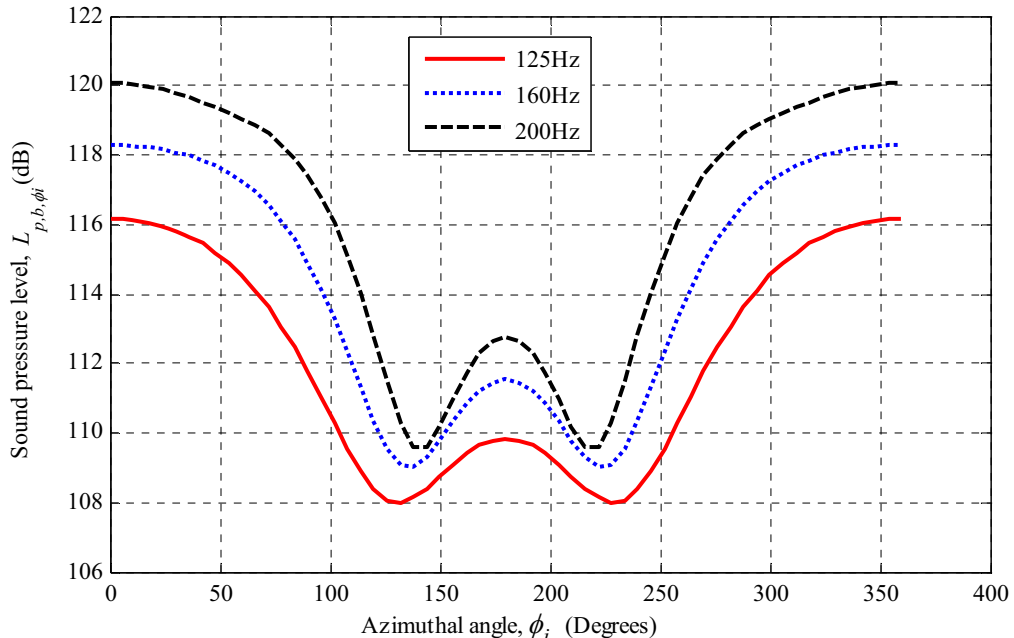


Figure 9.9: Analytically calculated sound pressure levels at the surface of section two (see Figure 7.5 in Chapter 7) at a height of $z = 2.17\text{m}$ from the bottom face of the RSLVF, using the unique source allocation method, for an equivalent single point source for each one-third-octave band centre frequency from 125Hz to 200Hz. For the equivalent point source location at each frequency see Table 9.2. [$x_1 = 15D_e$, $x_2 = 5D_e$ and reference pressure $20\mu\text{Pa}$]

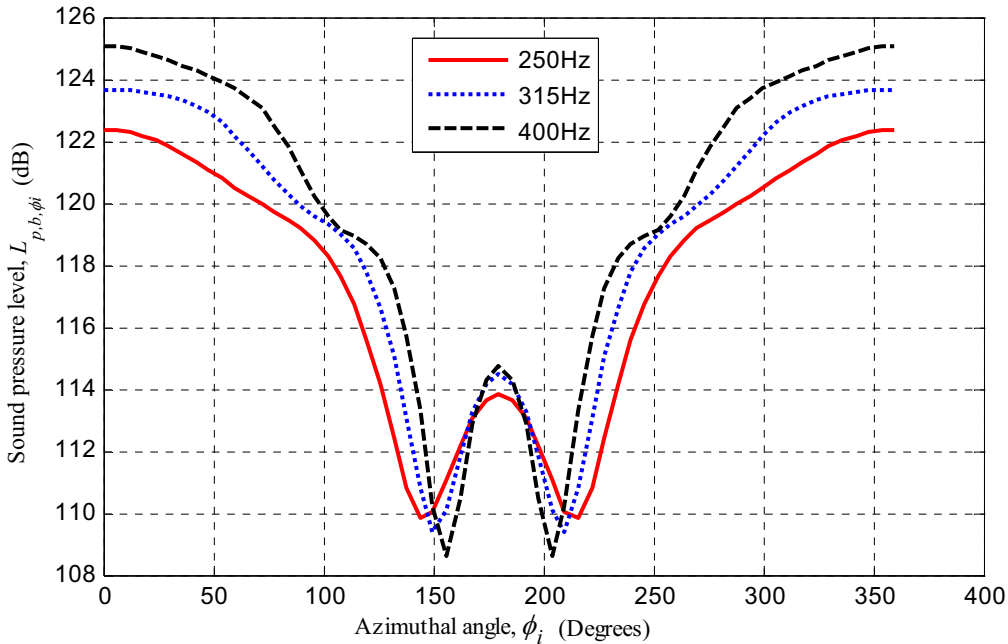


Figure 9.10: Analytically calculated sound pressure levels at the surface of section two (see Figure 7.5 in Chapter 7) at a height of $z = 2.17\text{m}$ from the bottom face of the RSLVF, using the unique source allocation method, for an equivalent single point source for each one-third-octave band centre frequency from 250Hz to 400Hz. For the equivalent point source location at each frequency see Table 9.2. [$x_1 = 15D_e$, $x_2 = 5D_e$ and reference pressure $20\mu\text{Pa}$]

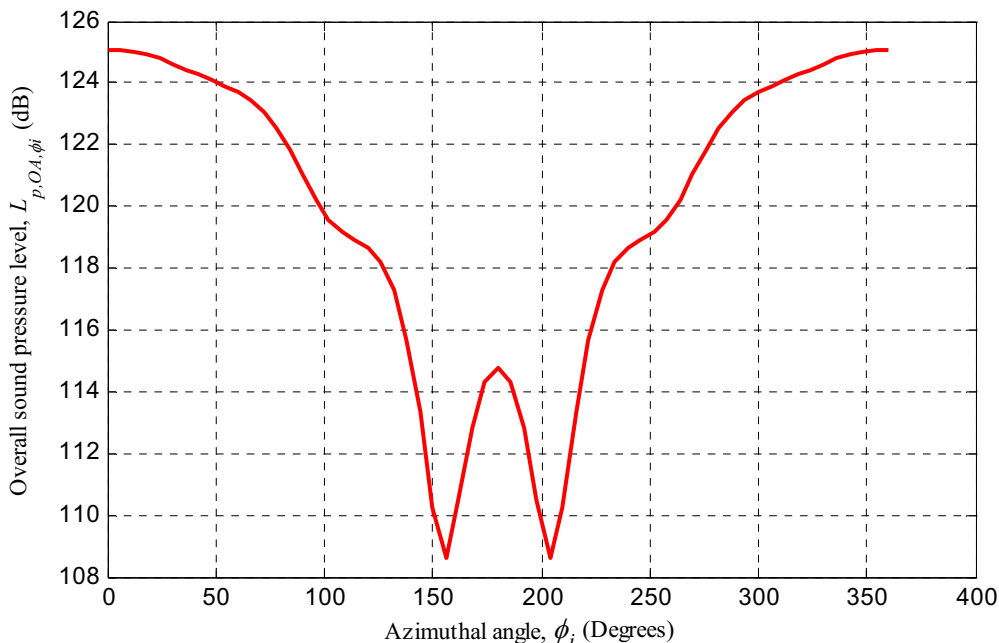


Figure 9.11: Analytically calculated overall sound pressure level at the surface of section two (see Figure 7.5 in Chapter 7) at a height of $z = 2.17\text{m}$ from the bottom face of the RSLVF, using the unique source allocation method, for the entire spectrum of one-third-octave band centre frequency range from 50Hz to 400Hz. For the equivalent point source location at each frequency see Table 9.2. [$x_1 = 15D_e$, $x_2 = 5D_e$ and reference pressure $20\mu\text{Pa}$]

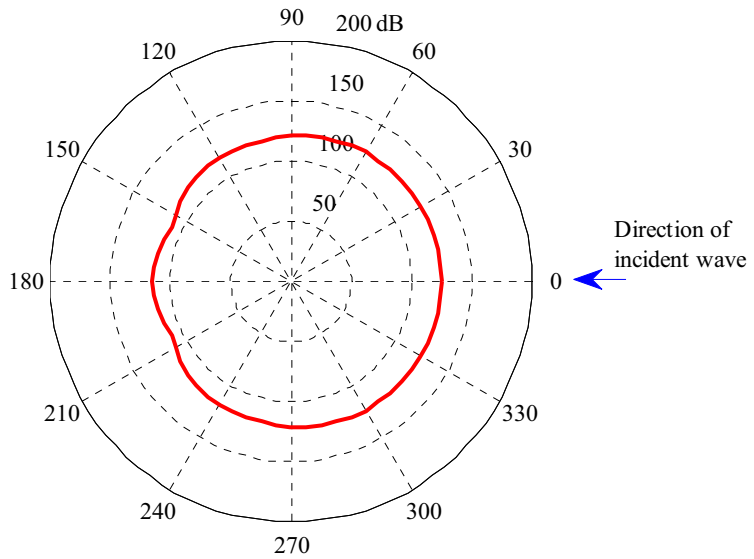


Figure 9.12: Analytically calculated directivity pattern of the overall sound pressure level at the surface of section two (see Figure 7.5 in Chapter 7) at a height of $z = 2.17\text{m}$ from the bottom face of the RSLVF, using the unique source allocation method, for the entire spectrum of one-third-octave band centre frequency range from 50Hz to 400Hz. For the equivalent point source location at each frequency see Table 9.2. [$x_1 = 15D_e$, $x_2 = 5D_e$ and reference pressure $20\mu\text{Pa}$]

9.4.2.2 Numerical Results

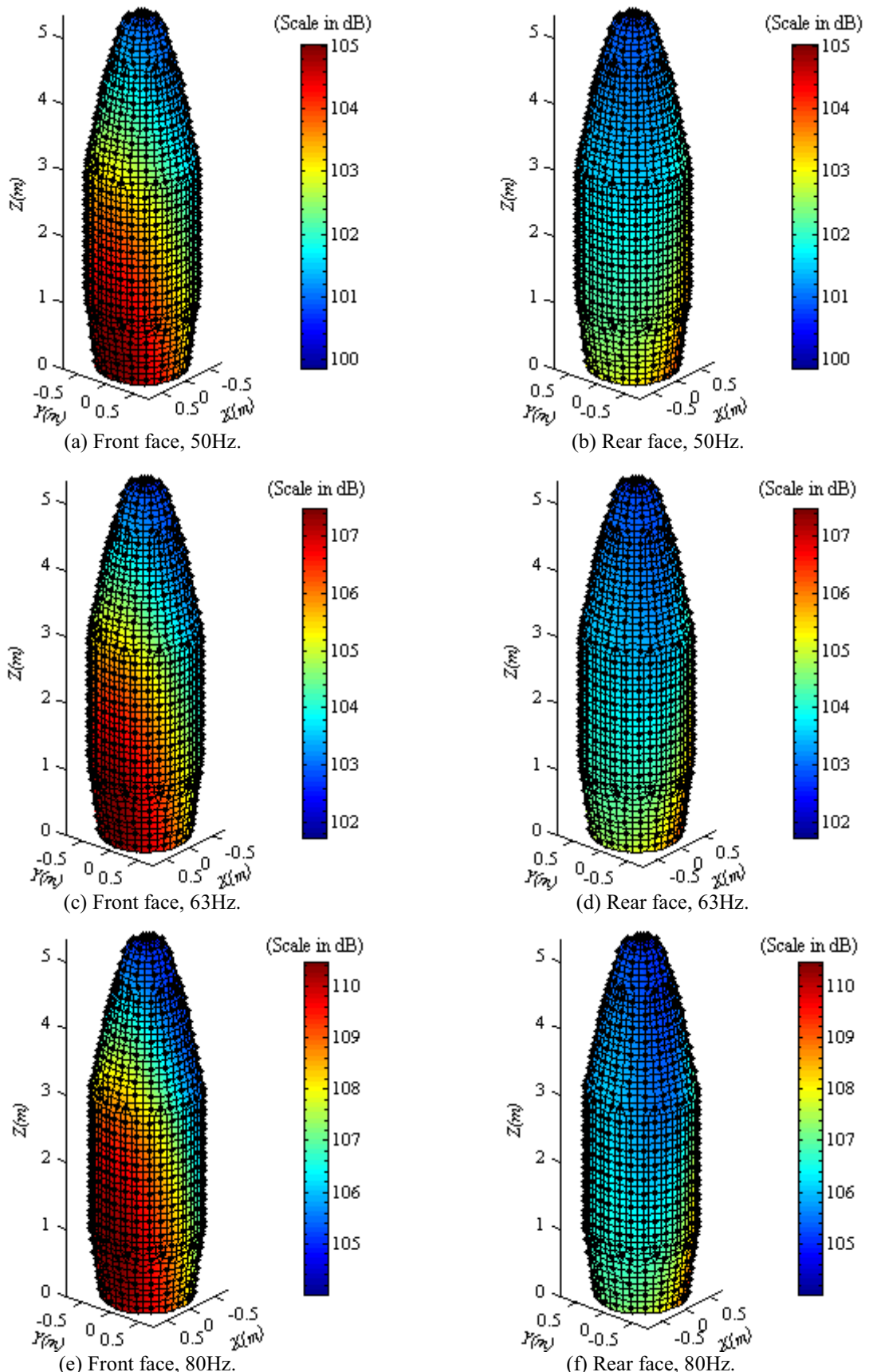
For the numerical analysis the Boundary Element Method (BEM) was used. The parameters used for the numerical calculations are given in Table 9.2, for each equivalent point source at each one-third-octave band centre frequency from 50Hz to 400Hz. The numerical results for each one-third-octave band centre frequency are presented in Figures 9.13 (a-t), calculated using equation (9.8). The numerical result of the overall sound pressure distribution for the entire spectrum over the frequency range from 50Hz to 400Hz is shown in Figures 9.14 (a-b), calculated using equation (9.9). The results show that for very low frequencies (50Hz to 100Hz), the highest acoustic pressures mostly occur on the surface of sections one and two (see Figure 7.5 in Chapter 7) of the RSLVF, as shown in Figures 9.13(a-h). The reasons for this are: (a) the sources are located below the RSLVF;

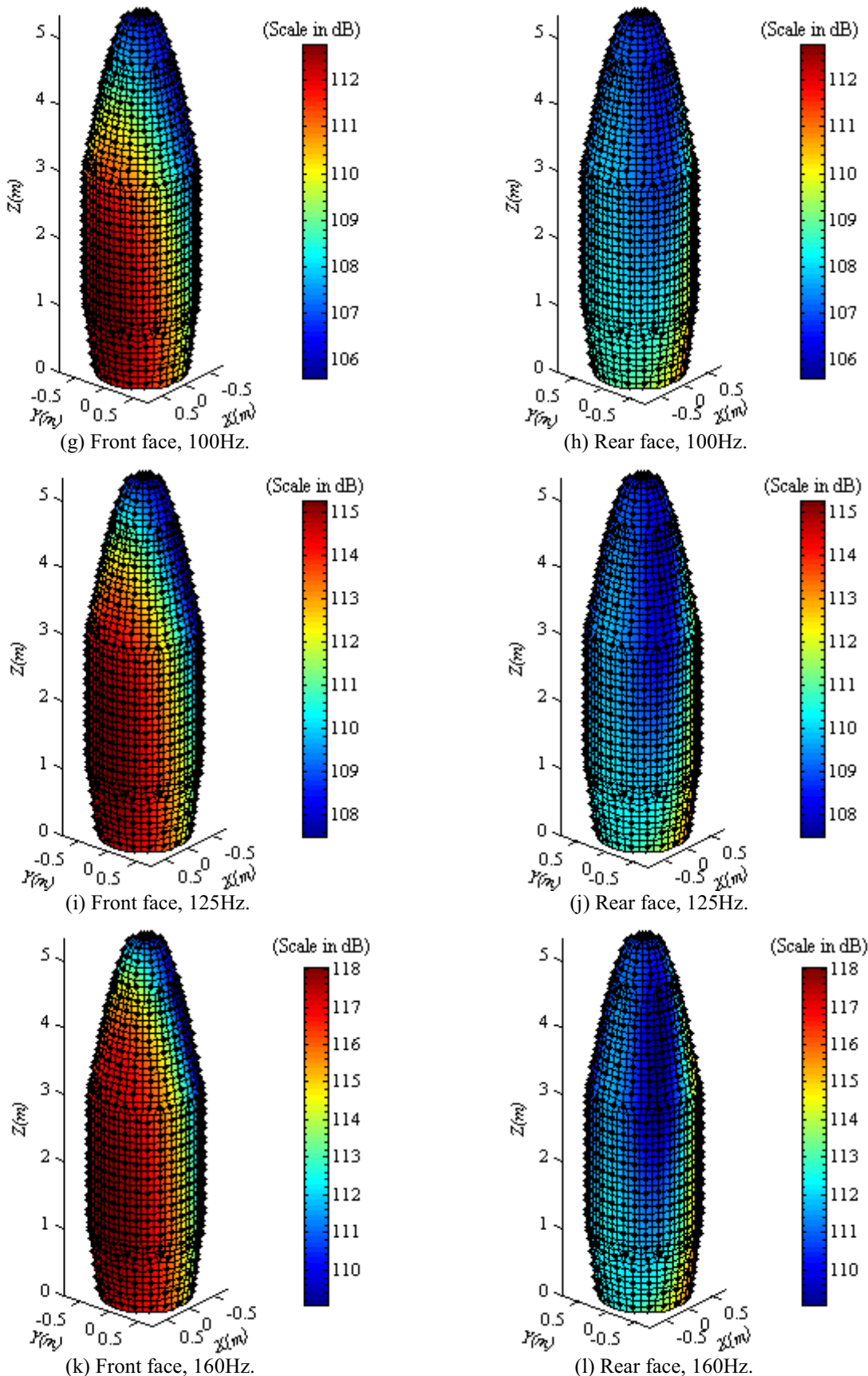
along the exhaust flow axis, and (b) the RSLVF dimension is relatively small compared to the wavelength of the very low frequency noise hence not much of the acoustic pressure incident on the RSLVF is absorbed. As the frequency increases much of the acoustic pressure incident on the RSLVF is absorbed and the high acoustic pressure become scattered over the entire RSLVF since the RSLVF dimension is no longer smaller than the acoustic wavelength, as shown in Figures 9.13(i-t). Since all the sources are point sources and are located below the RSLVF, along the exhaust flow axis, the results are not similar to those presented for plane waves in Figures 8.49 (a-t) in Chapter 8. The pressure magnitudes are different to the previous results because the source strength of each equivalent point source along the exhaust flow axis as well as the decay of sound pressure amplitude due to distance from the source to the RSLVF were considered for the following numerical calculations, whereas an unit incident sound pressure amplitude and an incident plane wavefront were assumed in the previous results. It appears that the overall sound pressure level reaches around 126dB for ten equivalent single point sources situated close to the vehicle, along the exhaust flow, as shown in Figures 9.14(a-b), for the entire spectrum over the frequency range from 50Hz to 400Hz.

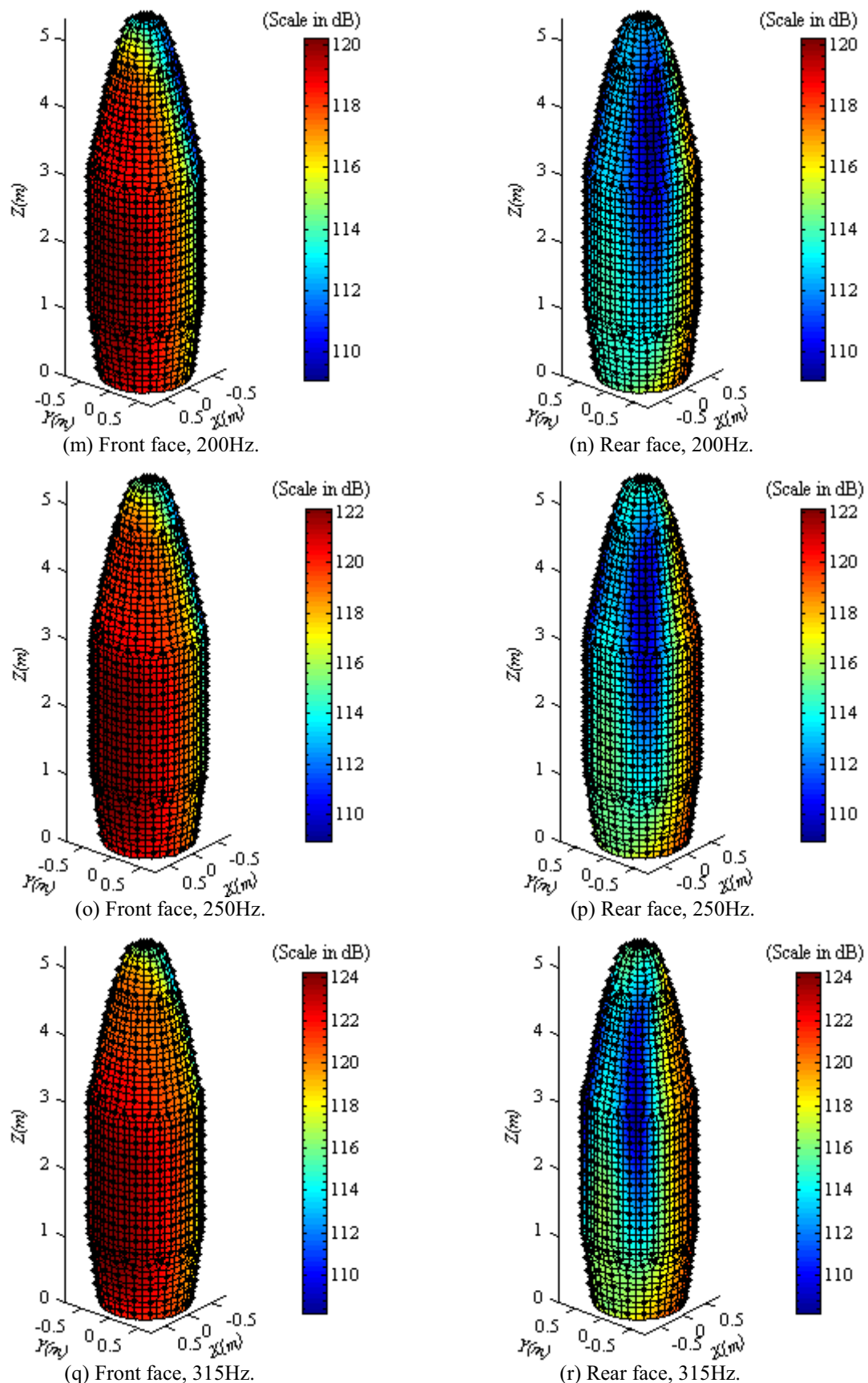
The sound pressure levels on the circumferential nodes at the surface of section two (see Figure 7.5 in Chapter 7) at a height of $z = 2.17\text{m}$ from the bottom face of the RSLVF were calculated using BEM for each one-third-octave band centre frequency and are shown in Figures 9.15, 9.16 and 9.17. The results show similar pressure fluctuations, at each band centre frequency, to the fluctuations in the analytical results shown in Figures 9.8, 9.9 and 9.10, which were obtained using the unique source allocation technique. There are slight differences between pressure amplitudes obtained using the numerical and analytical calculations, as shown in Figure 9.18, for the overall

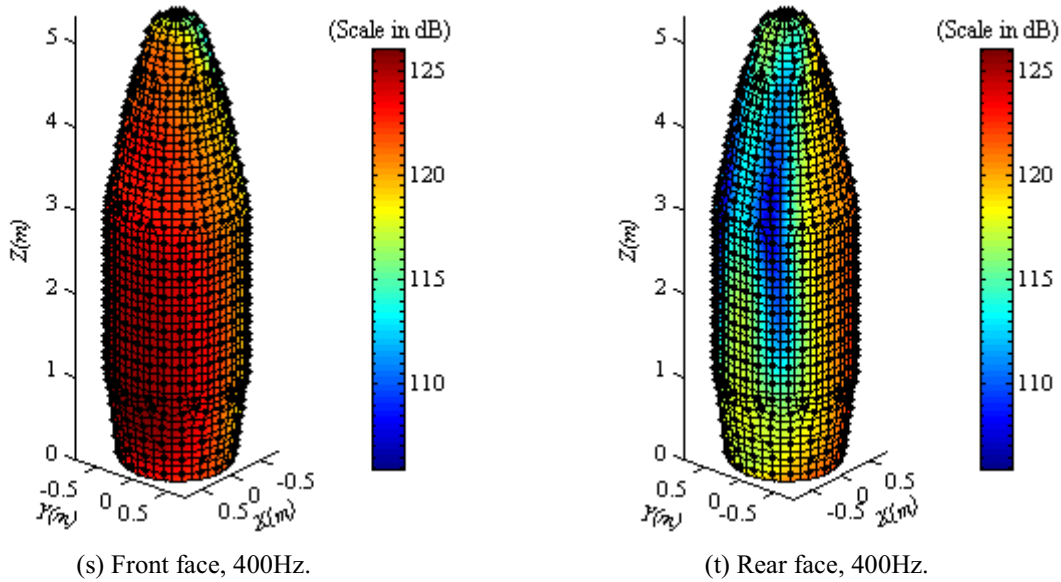
sound pressure level over the frequency range from 50Hz to 400Hz. The reason for this is that the diffraction of sound waves around the ends of the RSLVF was not considered analytically. In fact, the current work is not able to consider the diffraction of sound waves analytically for a complex three dimensional geometry such as the RSLVF.

It has been observed that the unique source allocation method is capable of predicting the acoustic loads on the surface of the RSLVF in the low frequency range from 50Hz to 400Hz, but it approximates the sound generation using an equivalent single point source for each frequency of interest only. In the next section, a non-unique source allocation method is investigated in the low frequency range from 50Hz to 400Hz, which assumes that there are a number of point source locations making a line source along the exhaust flow for each frequency of interest. This approach should yield more accurate results than the unique source allocation method discussed in this section.

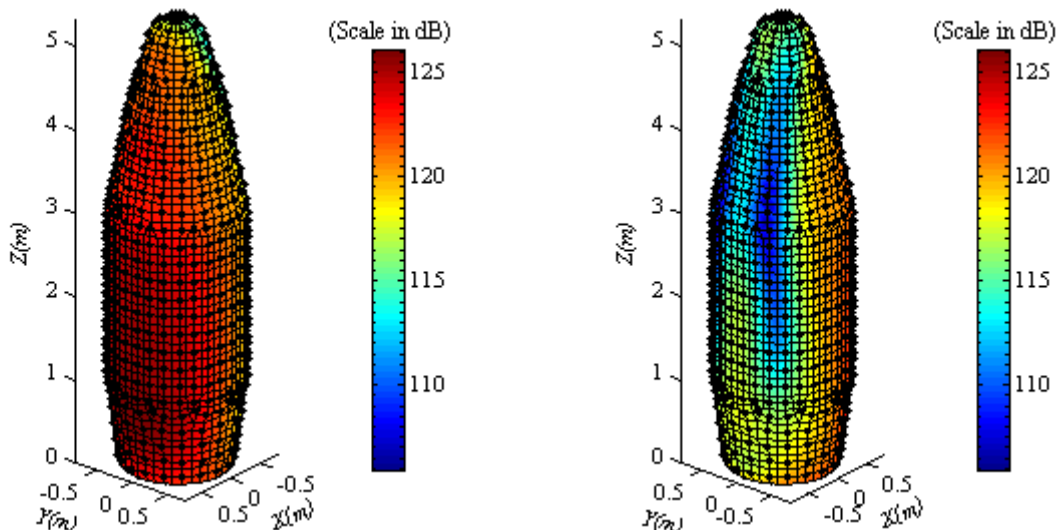








Figures 9.13 (a-t): Numerically calculated sound pressure excitation at the surface of the RSLVF using the unique source allocation method, for various one-third-octave band centre frequencies from 50Hz to 400Hz. For the equivalent point source location at each frequency see Table 9.2. [$x_1 = 15D_e$, $x_2 = 5D_e$ and reference pressure $20\mu\text{Pa}$]



Figures 9.14 (a-b): Numerically calculated overall sound pressure excitation at the surface of the RSLVF using the unique source allocation method, for the entire spectrum of one-third-octave band centre frequency range from 50Hz to 400Hz. For the equivalent point source location at each frequency see Table 9.2. [$x_1 = 15D_e$, $x_2 = 5D_e$ and reference pressure $20\mu\text{Pa}$]

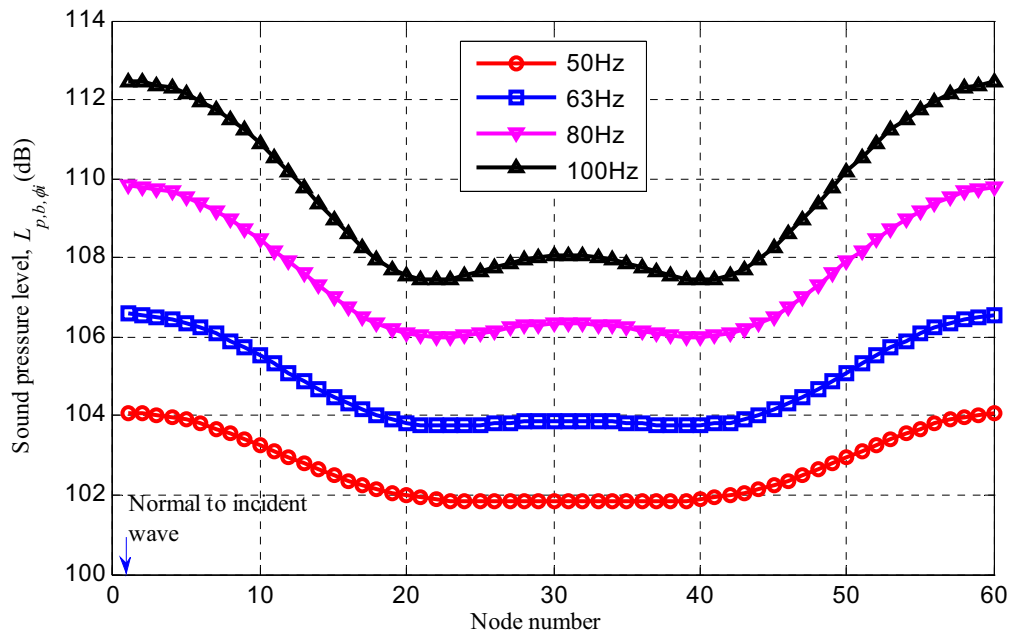


Figure 9.15: Numerically calculated sound pressure levels on the circumferential nodes at a height of $z = 2.17\text{m}$ from the bottom face of the RSLVF, using the unique source allocation method, for various one-third-octave centre frequencies from 50Hz to 100Hz. For the equivalent point source location at each frequency see Table 9.2. [$x_1 = 15D_e$, $x_2 = 5D_e$ and reference pressure $20\mu\text{Pa}$]

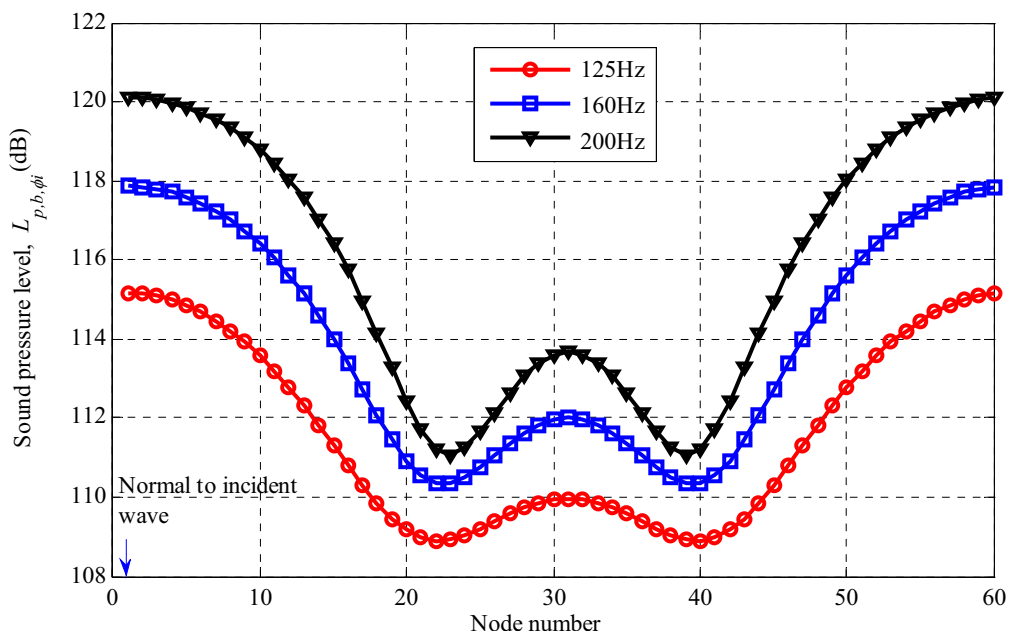


Figure 9.16: Numerically calculated sound pressure levels on the circumferential nodes at a height of $z = 2.17\text{m}$ from the bottom face of the RSLVF, using the unique source allocation method, for various one-third-octave centre frequencies from 125Hz to 200Hz. For the equivalent point source location at each frequency see Table 9.2. [$x_1 = 15D_e$, $x_2 = 5D_e$ and reference pressure $20\mu\text{Pa}$]

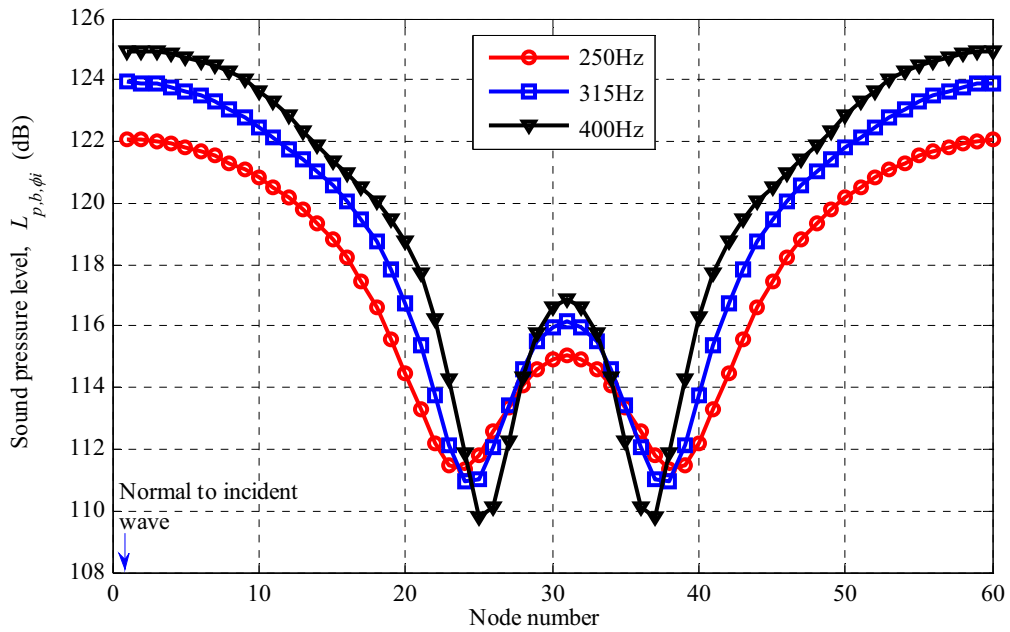


Figure 9.17: Numerically calculated sound pressure levels on the circumferential nodes at a height of $z = 2.17\text{m}$ from the bottom face of the RSLVF, using the unique source allocation method, for various one-third-octave centre frequencies from 250Hz to 400Hz. For the equivalent point source location at each frequency see Table 9.2. [$x_1 = 15D_e$, $x_2 = 5D_e$ and reference pressure $20\mu\text{Pa}$]

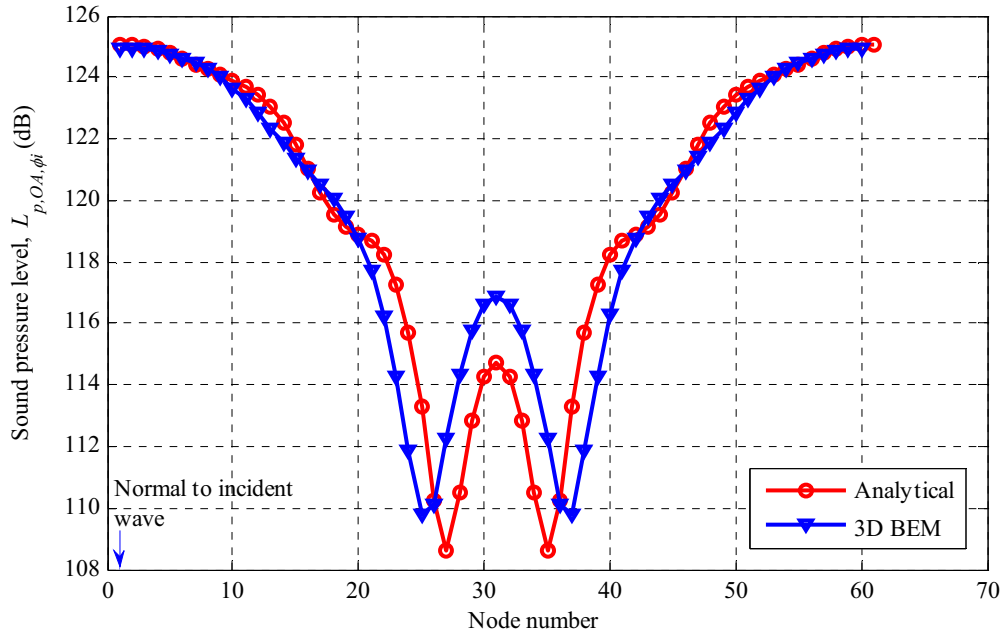


Figure 9.18: Comparison of the overall sound pressure level between the numerical and analytical results calculated on the circumferential nodes at a height of $z = 2.17\text{m}$ from the bottom of the RSLVF, using the unique source allocation method, for the entire spectrum of one-third-octave band centre frequency range from 50Hz to 400Hz. For the equivalent point source location at each frequency see Table 9.2. [$x_1 = 15D_e$, $x_2 = 5D_e$ and reference pressure $20\mu\text{Pa}$]

9.5 Prediction of Acoustic Loads Using the Non-Unique Source Allocation Method

The non-unique source allocation method is more complicated than the unique source allocation method described previously. The non-unique source allocation method recognizes that the rocket noise in each frequency band is generated throughout the exhaust flow, and a unique, single equivalent point source location along the flow axis is not assumed as in the previous method (NASA-SP-8072, 1971). The non-unique source allocation methodology is based on experimentally measured data and normalized results, and is described in detail in the above referenced document. Predictions can be made for sources located in the near-field as well as the far-field along the exhaust flow. In this section, the acoustic loadings on the RSLVF using the non-unique source allocation technique were observed only due to the sources closest to the vehicle. The reason is only ten point sources were used and positioned close to the vehicle, along the exhaust flow, to keep the computational time reasonable for the numerical calculations of acoustic loading. However, the non-unique source allocation technique could be further extended in future by using more acoustic sources.

9.5.1 Prediction Formulations

For the prediction of the acoustic loading on the vehicle, it is necessary to distribute the sources in relation to the core length along the exhaust flow. The core lengths of the various rocket engines have already been discussed and shown in Figure 9.2. The normalized overall sound power per unit core length for standard chemical rockets is reported in NASA-SP-8072 (1971) and was used in the current work to estimate the sound

power per unit core length for engine ‘E’. For noise prediction purposes the rocket flow can be divided into number of segments and the overall acoustic power for each segment can then be calculated using the estimated sound power per unit core length and the length of each segment as follows (NASA-SP-8072, 1971):

$$L_{w,seg} = 10 \log_{10} \left[\frac{x_t W(r)}{W_{OA}} \right] + L_w + 10 \log_{10} \frac{\Delta x}{x_t}, \quad (9.10)$$

where the term, $10 \log_{10} \left[\frac{x_t W(r)}{W_{OA}} \right]$, refers to the relative sound power per unit core length at location r (the values were estimated from NASA-SP-8072 (1971) for the current calculations and are provided in Table 9.3), $W(r)$ is the acoustic power as a function of distance between the nozzle exit and the source, W_{OA} is the overall acoustic power generated by the rocket engine, L_w is the overall acoustic power level of the rocket engine, Δx is the length of each segment, x_t is the total core length and the subscript ‘seg’ indicates the segments of exhaust flow.

The normalized relative sound power spectrum level with modified Strouhal number, $\left(\frac{f r a_e}{U_e a_o} \right)$, is given in the referenced document and was used to provide an acoustic output power estimate for engine ‘E’ in the current work. This sound power spectrum can then be converted to a conventional acoustic bandwidth as follows (NASA-SP-8072, 1971):

$$L_{w,seg,b} = 10 \log_{10} \left[\frac{W(f, r) U_e a_o}{W(r) r a_e} \right] + L_{w,seg} - 10 \log_{10} \frac{U_e a_o}{r a_e} + 10 \log_{10} \Delta f_b, \quad (9.11)$$

where the term, $10 \log_{10} \left[\frac{W(f, r) U_e a_o}{W(r) r a_e} \right]$, refers to the relative sound power spectrum level

(the values were estimated from NASA-SP-8072 (1971) for the current calculations and are provided in Table 9.4), U_e is the exhaust velocity, a_o is the speed of sound in air, a_e is the speed of sound in the exhaust flow at the nozzle exit, r is the distance from the nozzle to the centre of each segment along the flow axis and Δf_b is the bandwidth of the frequency band. For the current analysis, the acoustic power level, $L_{w,seg,b}$, corresponding to each segment was calculated for each 1/3 octave band centre frequency from 50Hz to 400Hz and are provided in Table 9.5.

The acoustic power of each source corresponding to each segment for a frequency band of interest can be determined from the acoustic power level, $L_{w,seg,b}$ presented in equation (9.11), as follows:

$$W_{seg,b} = 10^{\left(\frac{L_{w,seg,b}}{10}\right)}, \text{ Watts} \quad (9.12)$$

where the subscript b indicates the frequency band. The strength of each source corresponding to each segment for a frequency band of interest can be determined as follows (Bies & Hansen, 2003):

$$Q_{s,seg,b} = \sqrt{\frac{4\pi W_{seg,b}}{k^2 \rho c}}, \text{ m}^3/\text{s} \quad (9.13)$$

where c and ρ are the speed and density of air in the exhaust flow, respectively, k is the wave number. For the current analysis, the source strength, $Q_{s,seg,b}$, corresponding to the each segment was calculated for each 1/3 octave band centre frequency from 50Hz to 400Hz and are provided in Table 9.6.

The sound pressure level on the circumference around the vehicle, including the effects

due to the reflecting surface of the vehicle, for a band centred on any frequency can be expressed as

$$L_{p,seg,b,\phi_i} = 10 \log_{10} \left\{ \left[P_a^t(R_i, k, a, z, \phi_i, Q_{s,seg,b}) \right]^2 \right\} + \text{DI}(\theta) \quad (\text{re } 20 \mu\text{Pa}) \quad (9.14)$$

where the pressure quantity, P_a^t , represents the total sound pressure on the vehicle due to incident and scattered waves, and is a function of the distance R_i from the source to the observation point on the vehicle, wave number k , radius of the vehicle a , elevation height z , azimuthal angle ϕ_i and source strength $Q_{s,seg,b}$, and the term $\text{DI}(\theta)$ is the directivity index determined from Figure 9.7. As discussed in Section 9.4.1, this pressure quantity can be determined using equation (7.6) presented in Chapter 7 and equations (8.13) and (8.21) presented in Chapter 8 for the analytical and numerical calculations respectively. The first summation presented in equation (7.6) and the summation presented in equation (8.21) need to be taken into account for all the sources for a frequency band of interest, using logarithmic summation of L_{p,seg,b,ϕ_i} for all the segments. Then the overall sound pressure level calculated by the logarithmic summation of L_{p,seg,b,ϕ_i} over the entire segments of the exhaust flow for a frequency band of interest becomes (NASA-SP-8072, 1971)

$$L_{p,OA,seg,b,\phi_i} = 10 \log_{10} \sum_{\text{All seg}} 10^{L_{p,seg,b,\phi_i}/10} \quad (\text{re } 20 \mu\text{Pa}) \quad (9.15)$$

Again, in the above equations (9.14) and (9.15), the sound pressure due to scattering from the reflecting surface of the vehicle as well as the spreading due to distance, are included. The effect of the scattered sound field on the sound pressure on the surface of the vehicle was not considered in the previous analysis presented by NASA-SP-8072 (1971). It is also noticeable that in the above equations the 4π term has been used because the directivity

index, $DI(\theta)$, of the sound radiation relative to the exhaust axis includes the effect of the sources being located on a hard surface.

9.5.2 Acoustic Loadings on the Fairing

For the analytical and numerical prediction of acoustic loadings on the fairing, the non-unique source allocation method, which estimates that the rocket noise in each frequency band is generated throughout the exhaust flow, was used in the one-third-octave band centre frequency range from 50Hz to 400Hz. It was assumed that the fairing structure and the flow axis are situated at $x_1 = 15D_e$ upstream and $x_2 = 5D_e$ downstream of the vehicle respectively. A reference point was chosen at $\phi_i = 0^\circ$, which is the front point on the vehicle facing the exhaust flow. Hence $\phi_i = 180^\circ$ is the rear point on the vehicle. For simplicity, it was assumed that the temperature along the flow axis is $T = 1000^\circ\text{c}$. At that temperature the speed of sound and density in air is 715.49 m/s and 0.28 kg/m³ respectively. The flow axis was divided into 10 segments along the flow with an assumed length of 1m for each segment. At the centre of each of the 10 segments a point source completely uncorrelated with the other nine was assumed. The distances from the vehicle axis to the centre of each segment were estimated and used to determine the necessary parameters for each source. The specifications of each source, and the calculated and estimated values of all the parameters are reported in Tables 9.3 and 9.4. The calculated acoustic power level for each band of interest corresponding to each segment is reported in Table 9.5. The calculated source strength of each source corresponding to each segment also provided in Table 9.6. The source directivity index was assumed to be the same for

radiation to all the circumferential positions on the vehicle for any specified elevation angle from the source to launch vehicle.

For comparison, both the analytical and numerical calculations were conducted around the circumference of section two (see Figure 7.5 in Chapter 7), at a height of $z = 2.17\text{m}$ from the bottom face of the RSLVF. This height was chosen because at that height there are sixty circumferential nodes which are sufficient to achieve a better numerical estimation of the sound pressure pattern for comparison with the analytical result.

Source Number	Estimated Source Distance, $x_3(\text{m})$	Source Distance From the Nozzle, $r (\text{m})$	Distance per unit Core Length, r/x_t	Elevation Angle, β (Degrees)	Directivity Angle, θ (Degrees)	Estimated Directivity Index, DI (dB)	Estimated Sound Power per Unit Core Length, $10\log_{10}\left(\frac{x_t W(r)}{W_{\text{OA}}}\right)$ (dB)	Calculated Acoustic Power per Segment, $L_{w, \text{seg}}$ (dB)
1	1	1.52	0.194	77.73	102.27	-7.5	-12.7	36.46
2	2	2.31	0.388	66.50	113.50	-9.0	-10.0	39.16
3	3	3.21	0.582	56.88	123.12	-11.0	-8.0	41.16
4	4	4.16	0.776	48.99	131.01	-12.0	-7.0	42.16
5	5	5.13	0.970	42.61	137.39	-12.5	-5.1	44.06
6	6	6.11	1.164	37.48	142.52	-13.0	-5.0	44.16
7	7	7.09	1.358	33.31	146.69	-13.5	-4.5	44.66
8	8	8.08	1.552	29.89	150.11	-13.8	-3.6	45.56
9	9	9.07	1.746	27.07	152.93	-14.0	-3.1	46.06
10	10	10.06	1.940	24.70	155.30	-14.5	-3.4	45.76

Table 9.3: Details of 10 sources using the non-unique source allocation method (all the data presented here for engine 'E'). Core length, $x_t = 5.15\text{m}$; Overall acoustic power level of the rocket engine, $L_w = 56.28\text{ dB}$; Length of each segments, $\Delta x = 1\text{m}$. [Data estimated from Figure 12, presented in NASA-SP-8072 (1971)]

Source Number	Estimated relative sound power spectrum level, $10 \log_{10} \left[\frac{W(f, r) U_e a_o}{W(r) r a_e} \right]$, dB									
	50Hz	63Hz	80Hz	100Hz	125Hz	160Hz	200Hz	250Hz	315Hz	400Hz
1	-19.00	-18.00	-17.00	-16.00	-15.20	-14.10	-12.70	-12.60	-12.00	-10.60
2	-17.00	-16.10	-15.50	-15.50	-13.80	-12.60	-12.45	-10.75	-9.80	-8.65
3	-16.00	-15.00	-14.00	-12.65	-12.60	-12.45	-10.00	-9.70	-8.20	-7.00
4	-15.00	-14.00	-12.60	-12.55	-12.40	-9.90	-9.60	-7.90	-7.05	-6.75
5	-14.00	-12.65	-12.55	-12.45	-10.00	-9.65	-8.00	-7.00	-6.80	-6.57
6	-12.70	-12.57	-12.00	-10.50	-9.75	-8.60	-7.50	-6.85	-6.68	-6.80
7	-12.60	-12.50	-10.80	-9.81	-9.65	-7.90	-6.85	-6.70	-6.65	-7.48
8	-12.55	-12.48	-10.00	-9.70	-8.20	-7.10	-6.80	-6.61	-6.85	-7.65
9	-12.50	-11.00	-9.80	-8.70	-7.90	-6.90	-6.65	-6.70	-7.50	-8.60
10	-12.48	-10.00	-9.70	-8.50	-7.20	-6.80	-6.60	-6.80	-7.60	-8.70

Table 9.4: Estimated relative sound power level for ten sources for each 1/3 octave band centre frequency from 50Hz to 400Hz, using the non-unique source allocation method (all the data presented here for engine 'E'). Core length, $x_t = 5.15\text{m}$; Overall acoustic power level of the rocket engine, $L_w = 56.28\text{ dB}$; Speed of sound in the exhaust flow, $a_e = 715.49\text{ m/s}$; Length of each segments, $\Delta x = 1\text{m}$. [Data estimated from Figure 13, presented in NASA-SP-8072 (1971)]

Segment Number	Calculated acoustic power level in each band for each segment, $L_{w,s,b}$ (dB)									
	50Hz	63Hz	80Hz	100Hz	125Hz	160Hz	200Hz	250Hz	315Hz	400Hz
1	-1.1565	0.8472	2.8847	4.8538	6.6229	8.7950	11.1641	12.2332	13.8369	16.2744
2	5.3612	7.2649	8.9024	9.8715	12.5406	14.8127	15.9318	18.6009	20.5546	22.7421
3	9.7901	11.7938	13.8313	16.1504	17.1695	18.3916	21.8107	23.0798	25.5835	27.8210
4	12.9160	14.9197	17.3572	18.3763	19.4954	23.0675	24.3366	27.0057	28.8594	30.1969
5	16.7262	19.0799	20.2174	21.2865	24.7056	26.1277	28.7468	30.7159	31.9196	33.1871
6	18.8855	20.0192	21.6267	24.0985	25.8149	28.0370	30.1061	31.7252	32.8989	33.8164
7	20.1315	21.2352	23.9727	25.9318	27.0609	29.8830	31.9021	33.0212	34.0749	34.2824
8	21.6492	22.7229	26.2404	27.5095	29.9786	32.1507	33.4198	34.5789	35.3426	35.5801
9	22.7011	25.2048	27.4423	29.5114	31.2805	33.3526	34.5717	35.4908	35.6945	35.6320
10	22.8710	26.3548	27.6922	29.8613	32.1304	33.6025	34.7716	35.5407	35.7445	35.6819

Table 9.5: Calculated acoustic power level for 10 sources corresponding to 10 segments for each 1/3 octave band centre frequency from 50Hz to 400Hz, using the non-unique source allocation method (all the data presented here for engine 'E'). Core length, $x_t = 5.15\text{m}$; Overall acoustic power level, $L_w = 56.28\text{ dB}$; Speed of sound in the exhaust flow, $a_e = 715.49\text{ m/s}$; Length of each segments, $\Delta x = 1\text{m}$.

Segment Number	Source strength, $Q_{s,seg,b}$ (m ³ /s)									
	50Hz	63Hz	80Hz	100Hz	125Hz	160Hz	200Hz	250Hz	315Hz	400Hz
1	0.4993	0.4991	0.4969	0.4987	0.4891	0.4907	0.5156	0.4665	0.4453	0.4643
2	1.0574	1.0448	0.9935	0.8886	0.9666	0.9810	0.8927	0.9711	0.9651	0.9777
3	1.7607	1.7599	1.7524	1.8309	1.6471	1.4812	1.7565	1.6263	1.7219	1.7544
4	2.5234	2.5223	2.6298	2.3657	2.1528	2.5375	2.3494	2.5556	2.5108	2.3064
5	3.9128	4.0720	3.6554	3.3073	3.9221	3.6092	3.9036	3.9175	3.5712	3.2542
6	5.0171	4.5370	4.2992	4.5702	4.4564	4.4965	4.5648	4.4001	3.9974	3.4987
7	5.7910	5.2188	5.6324	5.6460	5.1438	5.5613	5.6134	5.1082	4.5770	3.6916
8	6.8966	6.1937	7.3127	6.7705	7.1973	7.2204	6.6851	6.1116	5.2962	4.2864
9	7.7846	8.2423	8.3980	8.5255	8.3611	8.2920	7.6332	6.7881	5.5152	4.3121
10	7.9383	9.4090	8.6431	8.8760	9.2206	8.5341	7.8109	6.8272	5.5470	4.3370

Table 9.6: Calculated source strength for 10 sources corresponding to 10 segments for each 1/3 octave band centre frequency from 50Hz to 400Hz ,using the non-unique source allocation method (all the data presented here for engine 'E'). Core length, $x_t = 5.15\text{m}$; Overall acoustic power level, $L_w = 56.28 \text{ dB}$; Length of each segments, $\Delta x = 1\text{m}$; speed of sound and density in air at $T = 1000^\circ\text{C}$ is 715.49 m/s and 0.28 kg/m^3 respectively.

9.5.2.1 Analytical Results

For the acoustic loading calculated analytically, using the non-unique source allocation method, which estimates that the rocket noise in each frequency band of interest is generated throughout the exhaust flow, the diameter of section two of the RSLVF (see Figure 7.5 and Table 7.3 in Chapter 7) was used, assuming that the RSLVF and the flow axis are situated at $x_1 = 15D_e$ upstream and $x_2 = 5D_e$ downstream of the vehicle respectively. The calculations were conducted considering the impacts of the scattered waves using equations (9.14) and (9.15), of the acoustic loading on the RSLVF from ten point sources acting as a line source, as shown in Figure 9.3, at each 1/3 octave band centre

frequency from 50Hz to 400Hz. Figures 9.19, 9.20 and 9.21 show the overall sound pressure levels at the circumferential surface of the RSLVF, at each one-third-octave band centre frequency from 50Hz to 400Hz, for ten point sources acting as a line source, calculated using equation (9.15) at a height of $z = 2.17\text{m}$ from the bottom face of the RSLVF. The results show that for the small chemical rocket engine ‘E’ the sound pressure level reaches around 111.6dB at the front of the RSLVF facing the exhaust flow, for ten point sources located close to the vehicle. It is noticeable that the non-unique source allocation method results in a lesser acoustic pressure magnitude compared with the results presented in Figures 9.8 to 9.12, using the unique source allocation method. The reason for this is that for each frequency band of interest, the source strength of each source calculated using the non-unique source allocation method was less compared with the source strength of a single equivalent point source calculated using the unique source allocation method (see Tables 9.2 and 9.6 for source strengths). The results also indicate that for each frequency band of interest, sound pressure amplitude varies relatively smoothly at the front face of the RSLVF facing the exhaust flow and varies aggressively at the back of the RSLVF, due to the reinforcement and cancellation that occurs between the diffracted waves passing around each side of the RSLVF. The sound pressure fluctuation increases as the frequency band of interest increases because the amount of interference of the two diffracted waves passing around the two sides of the RSLVF increases.

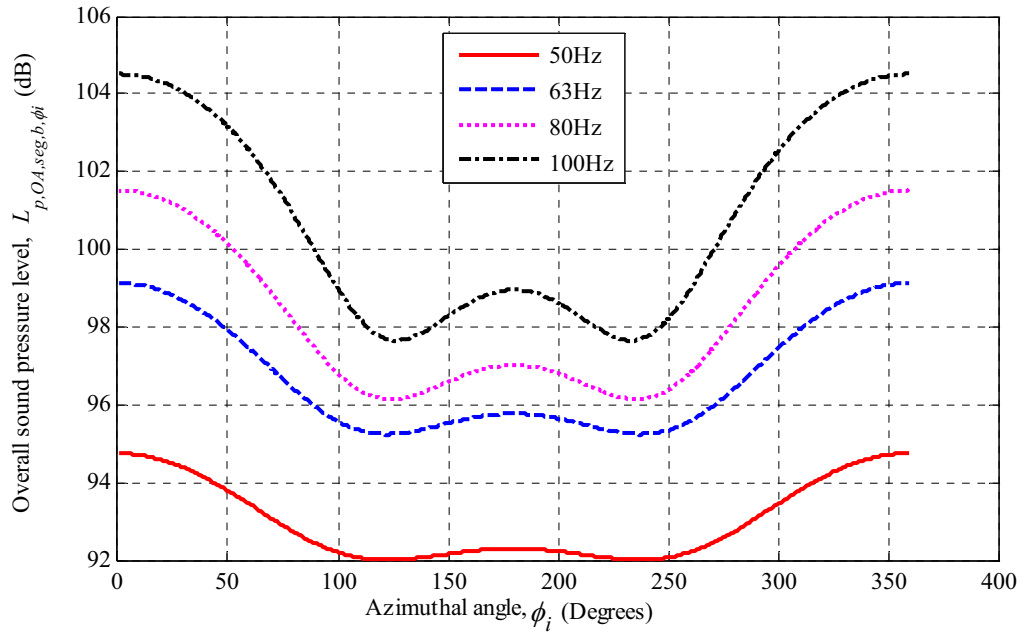


Figure 9.19: Analytically calculated overall sound pressure level at the circumferential surface of section two (see Figure 7.5) at a height of $z = 2.17\text{m}$ from the bottom face of the RSLVF, using the non-unique source allocation method, for a line source of 10 individual point sources along the exhaust flow (see Figure 9.3), for each one-third-octave band centre frequency from 50Hz to 100Hz. The data used for the analytical calculation for each point source are given in Tables 9.3, 9.4, 9.5 and 9.6. [$x_1 = 15D_e$, $x_2 = 5D_e$ and reference pressure $20\mu\text{Pa}$]

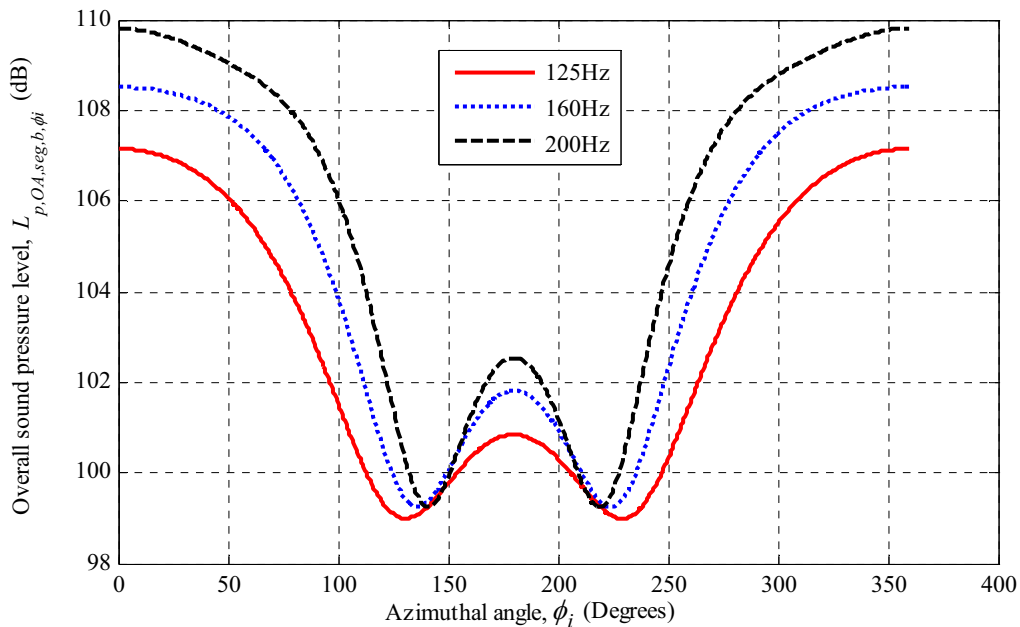


Figure 9.20: Analytically calculated overall sound pressure level at the circumferential surface of section two (see Figure 7.5) at a height of $z = 2.17\text{m}$ from the bottom face of the RSLVF, using the non-unique source allocation method, for a line source of 10 individual point sources along the exhaust flow (see Figure 9.3), for each one-third-octave band centre frequency from 125Hz to 200Hz. The data used for the analytical calculation for each point source are given in Tables 9.3, 9.4, 9.5 and 9.6. [$x_1 = 15D_e$, $x_2 = 5D_e$ and reference pressure $20\mu\text{Pa}$]

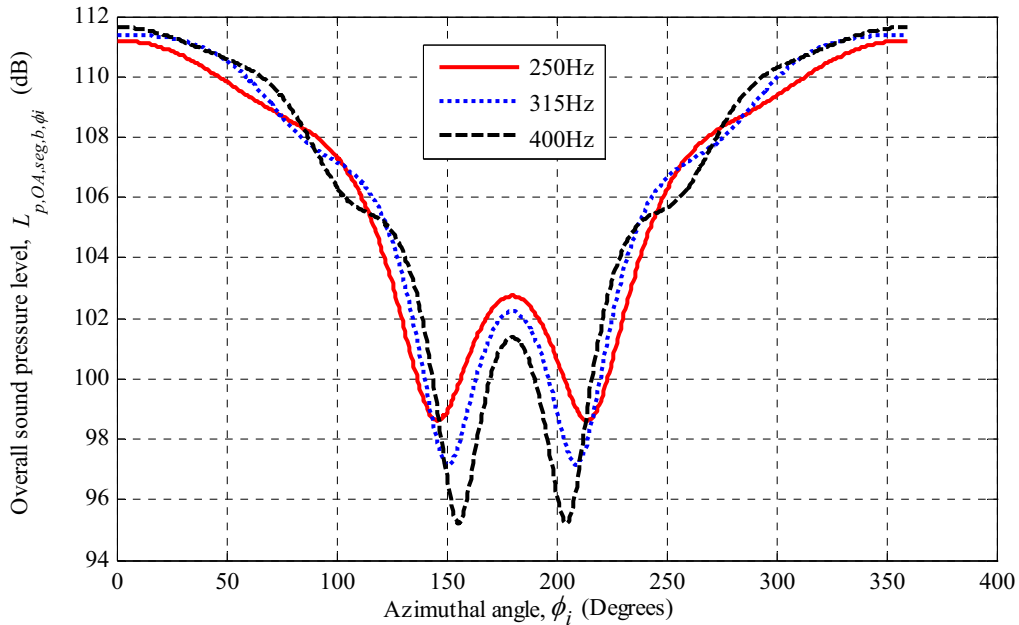


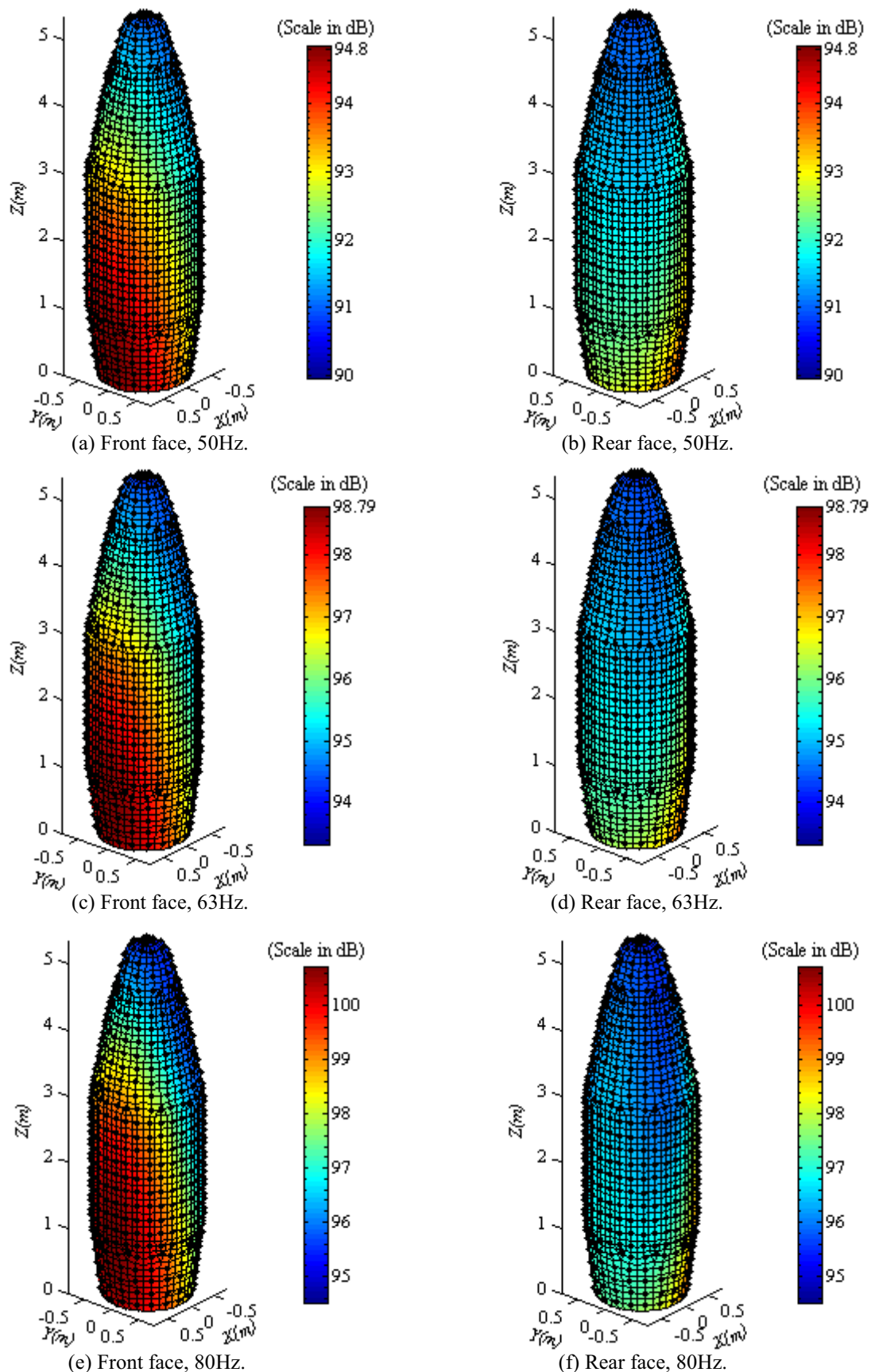
Figure 9.21: Analytically calculated overall sound pressure level at the circumferential surface of section two (see Figure 7.5) at a height of $z = 2.17\text{m}$ from the bottom face of the RSLVF, using the non-unique source allocation method, for a line source of 10 individual point sources along the exhaust flow (see Figure 9.3), for each one-third-octave band centre frequency from 250Hz to 400Hz. The data used for the analytical calculation for each point source are given in Tables 9.3, 9.4, 9.5 and 9.6. [$x_1 = 15D_e$, $x_2 = 5D_e$ and reference pressure $20\mu\text{Pa}$]

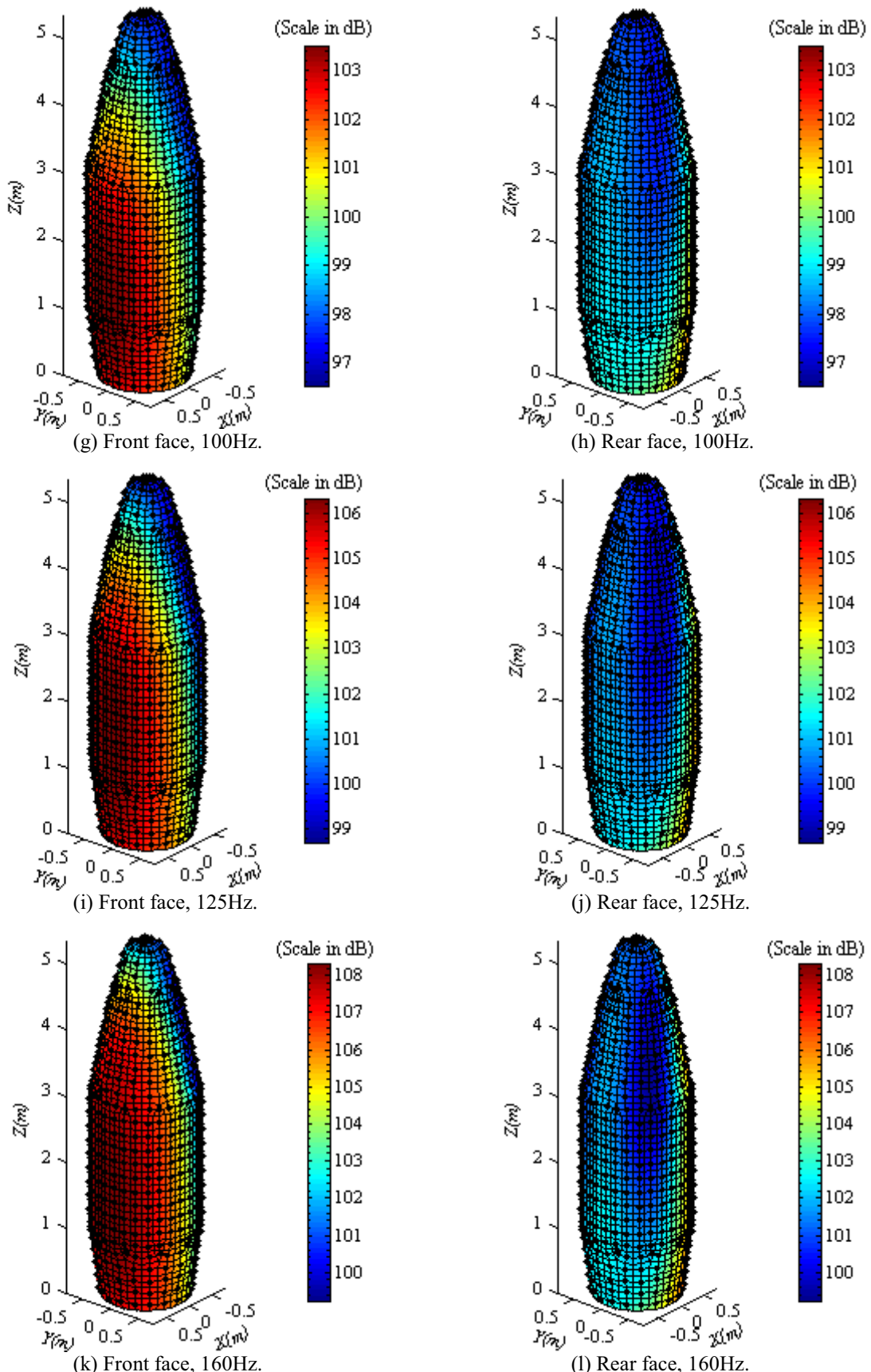
9.5.2.2 Numerical Results

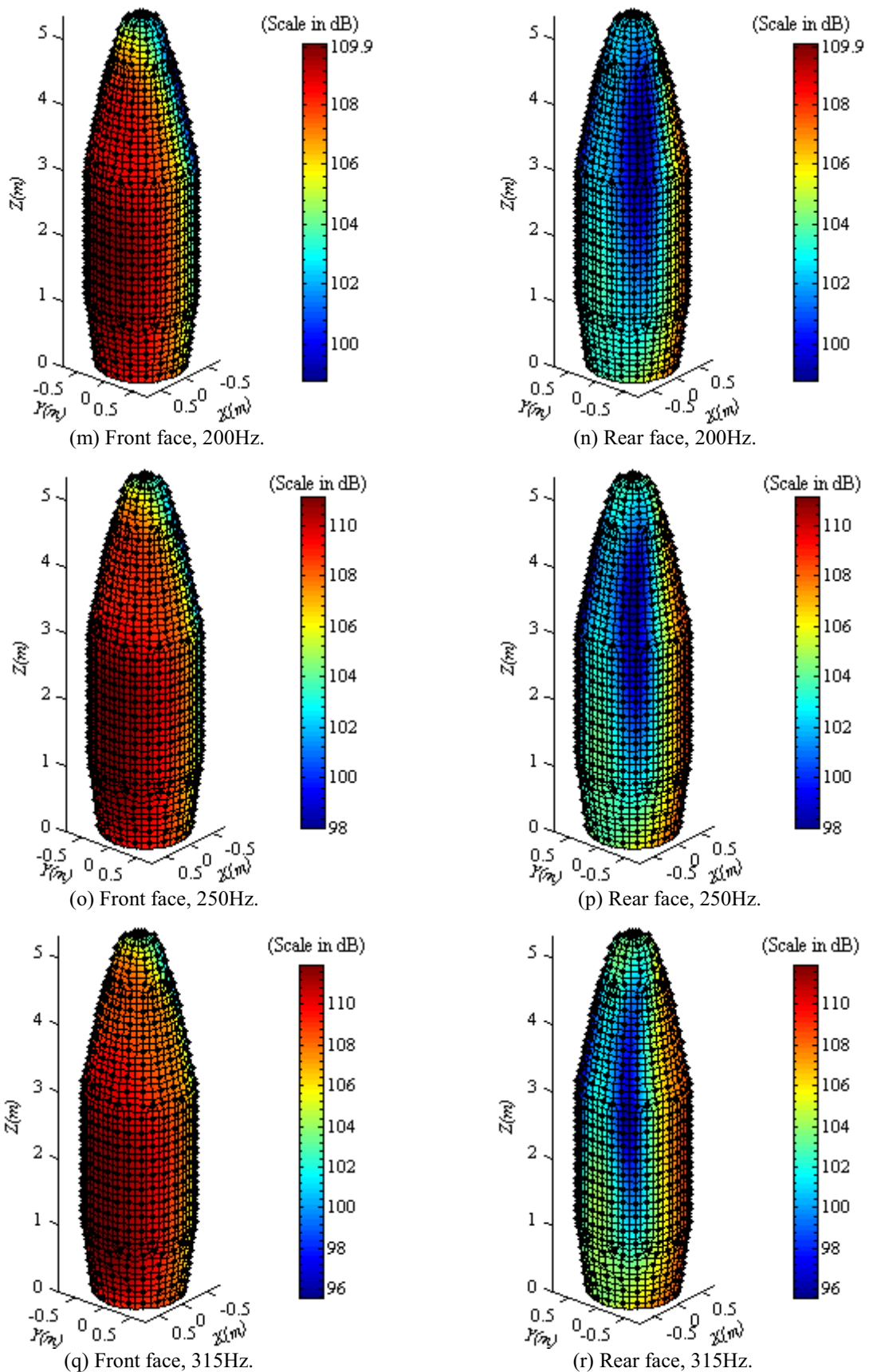
For the numerical analyses, using the non-unique source allocation method, ten point sources were used to constitute a line source along the exhaust flow (see Figure 9.3), for frequencies corresponding to one-third-octave band centre frequencies from 50Hz to 400Hz. The specifications for each source given in Tables 9.3, 9.4, 9.5 and 9.6 were used in the calculations for acoustic loading on the RSLVF, assuming that the RSLVF and the flow axis are situated at $x_1 = 15D_e$ upstream and $x_2 = 5D_e$ downstream of the vehicle respectively. The numerical results for each band centre frequency are shown in Figures 9.22(a-t), calculated using equation (9.15). The results show that for very low frequencies (50Hz to 100Hz), the highest acoustic pressures mostly occur on the surface of sections one and two (see Figure 7.5 in Chapter 7) of the RSLVF, as shown in Figures 9.22(a-h).

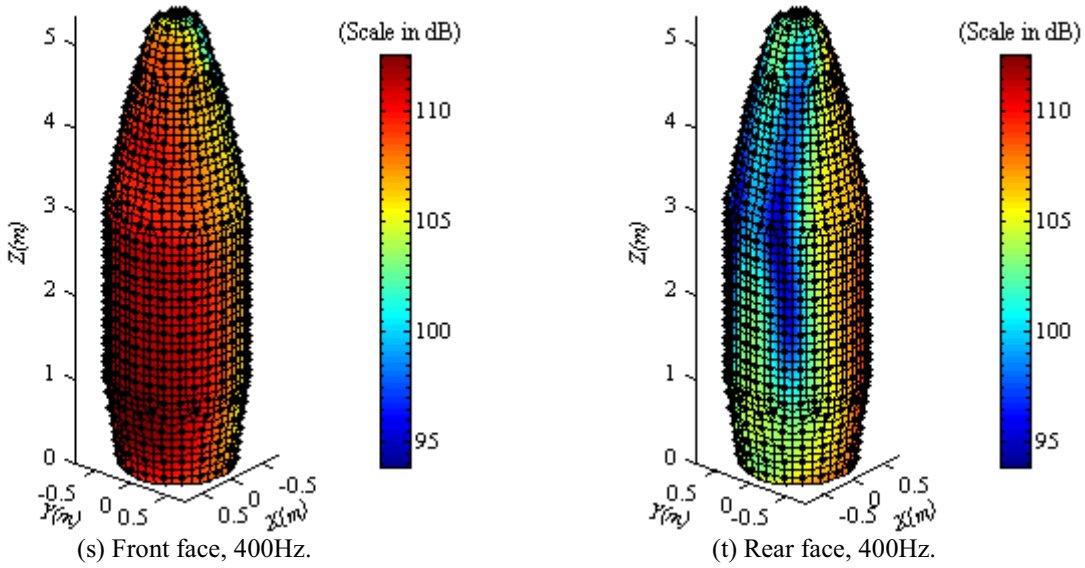
The reasons for this are discussed in Section 9.4.2.2. As the frequency increases much of the acoustic pressure incident on the vehicle is absorbed and the high acoustic pressure become scattered over the entire RSLVF since the RSLVF dimension is no longer smaller than the acoustic wavelength, as shown in Figures 9.22(h-t). It appears that the overall sound pressure level reaches around 112.6dB for ten individual point sources situated close to the vehicle acting as a line source, along the exhaust flow, as shown in Figures 9.22(s-t) for the frequency of 400Hz. The results show that the non-unique source allocation method results in a lesser acoustic pressure magnitude compared with the results presented in Figures 9.13 to 9.18, using the unique source allocation method. The reason, discussed previously in section 9.5.2.1, is for each frequency band of interest, the source strength of each source calculated using the non-unique source allocation method was less compared with the source strength of a single equivalent point source calculated using the unique source allocation method (see Tables 9.2 and 9.6 for source strengths). However, if greater computer resources were available, more sources could be considered in the calculations along the exhaust flow. Nevertheless, ten sources were considered to be sufficient for the purpose of the work in this thesis.

The sound pressure levels on the circumferential nodes at a height of $z = 2.17\text{m}$ around section two (see Figure 7.5 in Chapter 7) of the RSLVF were calculated using the 3D BEM for each one-third-octave band centre frequency and are shown in Figures 9.23, 9.24 and 9.25. The results show similar pressure fluctuations to the analytical results shown in Figures 9.19, 9.20 and 9.21, which were calculated using the non-unique source allocation method. The small differences in pressure magnitude are a result of diffraction around the ends of the cylinder which is taken into account in the BEM analysis but not in the analytical model.









Figures 9.22 (a-t): Numerically calculated sound pressure excitation at the surface of the RSLVF at various one-third-octave band centre frequencies from 50Hz to 400Hz, using the non-unique source allocation method. The data used for the numerical calculation for each point source are given in Tables 9.3, 9.4, 9.5 and 9.6. [$x_1 = 15D_e$, $x_2 = 5D_e$ and reference pressure $20\mu\text{Pa}$]

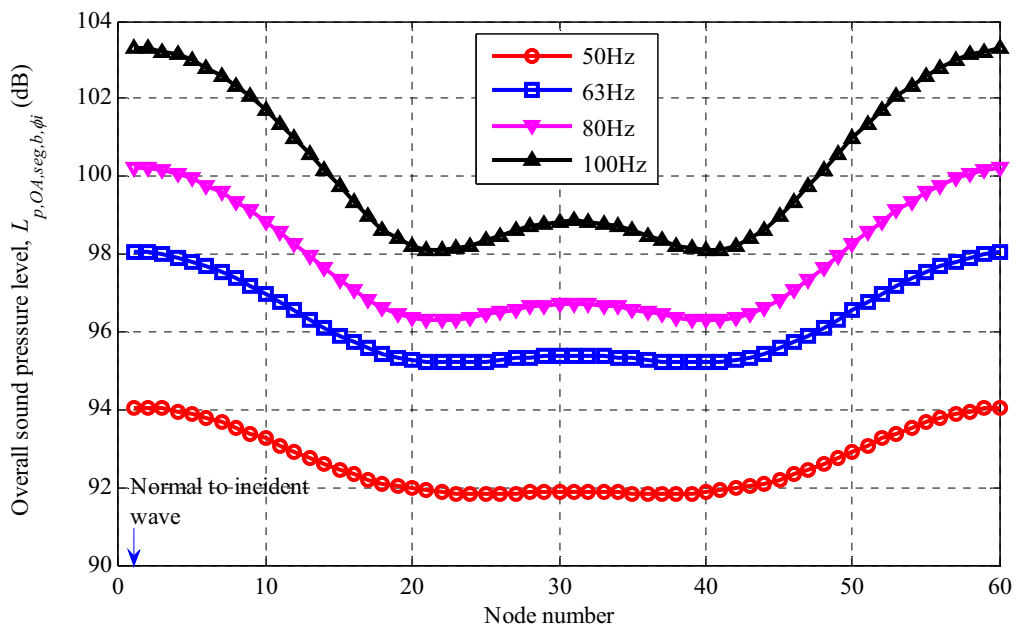


Figure 9.23: Numerically calculated sound pressure levels on the circumferential nodes at a height of $z = 2.17\text{m}$ from the bottom face of the RSLVF at various one-third-octave centre frequencies from 50Hz to 100Hz, using the non-unique source allocation method. The data used for the numerical calculation for each point source are given in Tables 9.3, 9.4, 9.5 and 9.6. [$x_1 = 15D_e$, $x_2 = 5D_e$ and reference pressure $20\mu\text{Pa}$]

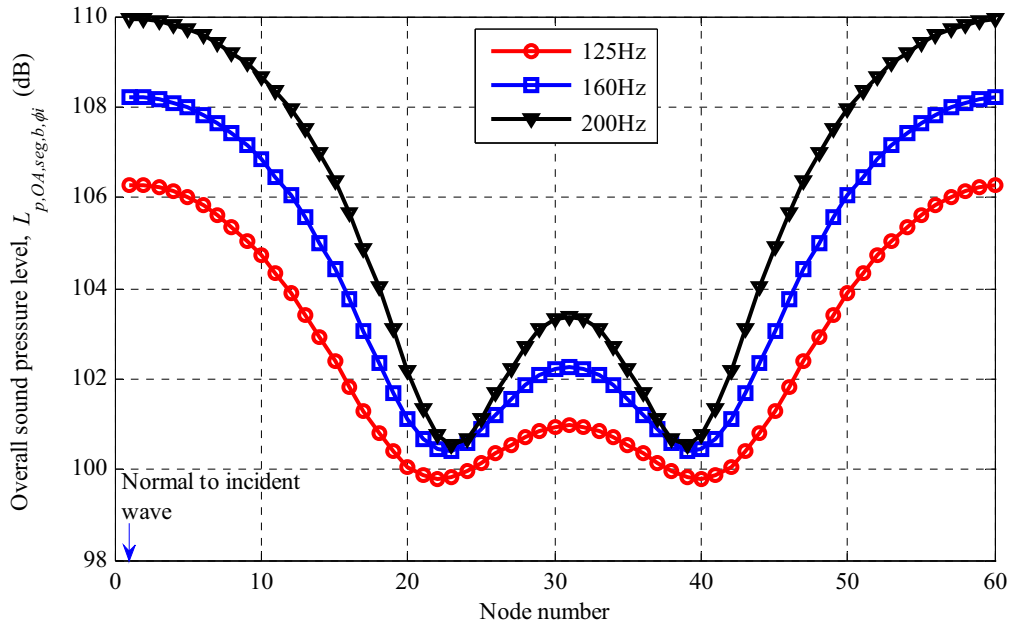


Figure 9.24: Numerically calculated sound pressure levels on the circumferential nodes at a height of $z = 2.17\text{m}$ from the bottom face of the RSLVF at various one-third-octave centre frequencies from 125Hz to 200Hz, using the non-unique source allocation method. The data used for the numerical calculation for each point source are given in Tables 9.3, 9.4, 9.5 and 9.6. [$x_1 = 15D_e$, $x_2 = 5D_e$ and reference pressure $20\mu\text{Pa}$]

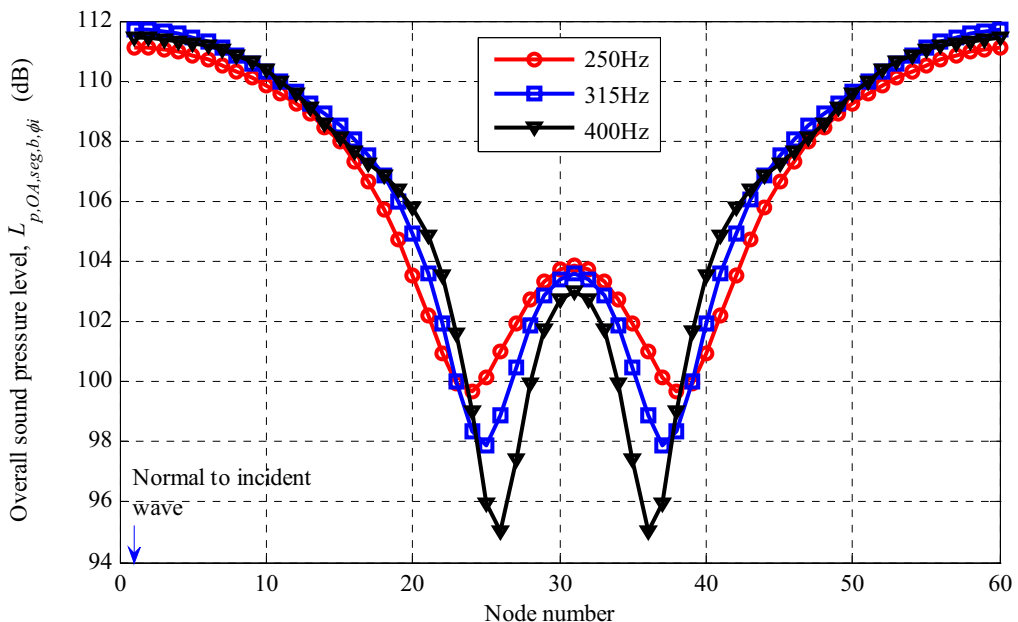


Figure 9.25: Numerically calculated sound pressure levels on the circumferential nodes at a height of $z = 2.17\text{m}$ from the bottom face of the RSLVF at various one-third-octave centre frequencies from 250Hz to 400Hz, using the non-unique source allocation method. The data used for the numerical calculation for each point source are given in Tables 9.3, 9.4, 9.5 and 9.6. [$x_1 = 15D_e$, $x_2 = 5D_e$ and reference pressure $20\mu\text{Pa}$]

9.6 Conclusions

The acoustic noise generated due to the launch of a launch vehicle has been estimated for a chemical rocket engine ‘E’. A geometry that assumes the engine exhaust noise to be originating along the exhaust flow, perpendicular to the vehicle axis, has been used for the determination of the acoustic pressure loading at the surface of the RSLVF.

Two separate source allocation methods have been used to determine the source positions and strengths along the exhaust flow axis for each one-third-octave band centre frequency in the range from 50Hz to 400Hz. The first method assumed that the rocket noise could be modelled using a single unique source location along the flow axis for each one-third-octave frequency band. The numerical results obtained using this method showed that the overall sound pressure level reaches around 126dB for ten equivalent single point sources situated close to the vehicle acting as a line source, along the exhaust flow, for the entire spectrum over the frequency range from 50Hz to 400Hz.

The second source allocation method assumed that the exhaust flow could be represented by a number of point sources distributed through the flow for each frequency band of interest. Using this method, ten individual point sources were arbitrarily positioned close to the vehicle. The numerical results showed that the overall sound pressure level reaches around 112.6dB for the frequency of 400Hz, for ten individual point sources situated close to the vehicle acting as a line source, along the exhaust flow.

Both cases, the numerical results produced similar pressure fluctuations, at each band centre frequency, to the fluctuations in the analytical results, which were obtained using the unique and

non-unique source allocation methods. There were small differences in pressure magnitude between the results obtained analytically and numerically because of diffraction around the edges of the RSLVF which was taken into account in the BEM analysis but not in the analytical model.

It has been observed that the non-unique source allocation method results in a lesser acoustic pressure magnitude compared with the unique source allocation method. The reason is, for each frequency band of interest, the strength of each source calculated using the non-unique source allocation method was less compared with the strength of a single equivalent point source calculated using the unique source allocation method.

The method described in Chapter 7 for oblique waves was used to obtain the analytical results presented in this chapter, which showed good agreement with the numerical results. However, the diffraction of sound waves was not taken into account in the analytical calculations in contrast to the results calculated using the BEM technique. Therefore, the pressure magnitude of the results obtained analytically was slightly smaller or greater than the results obtained using BEM.

Chapter 10

Summary and Conclusions

10.1 Summary

In this thesis, theories to calculate the incident, scattered and total sound pressure fields at the surface of a cylinder due to incident plane waves that strike normal to the circumference of the cylinder have been described in detail. For the theoretical analyses, the cylinder was assumed infinite in length to avoid the effects of diffraction of sound waves from the ends of the cylinder. For the total sound pressure calculations, a suitable mathematical expression was derived using mathematical descriptions for the incident and scattered sound pressure fields, which is suitable for any argument of ka (k is wave number and a is radius of the cylinder) and does not require any type of limitation or restriction, such as short or long wavelengths. The present work was compared with the previous work (Morse, 1936; Morse & Feshbech, 1953b; Morse & Ingard, 1986; Junger & Feit, 1993) and the comparisons revealed that for the sound pressure field at the surface of the cylinder, the mathematical derivations presented in this thesis agree well with mathematical derivations presented by Junger & Feit (1993), but not with the derivations for total sound pressure field presented by Morse (1936), Morse & Feshbech (1953b) and Morse & Ingard (1986).

From the results of sound pressure distribution at the surface of the cylinder, it was observed that the sound pressure amplitude varies relatively smoothly in the region from approximately 100° to 260° at the front face of the cylinder where the sound waves

directly impinge at 180° . The sound pressure amplitude varies aggressively in the regions from approximately 0° to 100° and 260° to 360° at the rear face of the cylinder. The reason for this variation in amplitude is that waves are diffracted around two sides of the cylinder in the clockwise and anti-clockwise directions. When one wave travels a distance which is an odd number of half wavelengths more than the distance travelled by the other, there is destructive interference. When they travel the same distance or an integer number of wavelengths, there is reinforcement and a peak results.

Although it was not the primary focus of this thesis, the theoretical analysis was extended to predict the sound pressure field at locations in the acoustic field surrounding the cylinder, due to incident plane waves that strike normal to the circumference of the cylinder. It was shown that the present theoretical approach produces results that converge to a solution for the scattered and total sound pressure fields at any location in the sound field from the cylinder. It was also shown that the mathematical expressions derived in this thesis do not require asymptotic forms or limits of the argument, kr (k is wave number and r is radial distance of the observation point in the sound field from the cylinder) for convergence. In comparison, the derivations presented by Morse (1936), Morse & Feshbach (1953b) and Morse & Ingard (1986) all require asymptotic limits. It was also observed that for determining the sound pressure field at locations *not* on the surface of the cylinder, there is no significant difference between the results obtained using the analysis derived in this thesis and the analysis presented by Junger & Feit (1993).

It was found that the aforementioned theoretical approaches, including the theoretical framework used in this thesis, for predicting the sound pressure field at the surface of the

cylinder, are only suitable for incident plane waves from a source assumed to be located at an infinite distance from the cylinder so that plane waves are incident on the cylinder. Therefore, a theoretical method was developed in this thesis, which is able to predict the sound pressure field at the surface of the cylinder due to a point source and a line source located at a finite distance from the cylinder. The results using the theoretical method presented here show that it is possible to predict the sound pressure field at the surface of the cylinder by identifying the source position and strength, which was not possible using results from previous work by Morse (1936), Morse & Feshbech (1953b), Morse & Ingard (1986) and Junger & Feit (1993).

An experiment was conducted in an anechoic chamber to measure the sound pressure field at the surface of an experimental cylinder due to a point source positioned at a finite distance from the cylinder for the purpose of verifying the theoretical model developed for a point source. The intention of this experiment was to obtain the sound pressure pattern on the surface of the cylinder only for comparison with the analytical results. Hence the source strength was not taken in to account. The experimentally measured and analytically predicted sound pressures were normalised to be equal on the front face of the cylinder closest to incident wave. The experimentally measured sound pressure field verified the analytically predicted normalised sound pressure field on the surface of the cylinder due to a point source and the results agreed well. It was observed that at the lower frequencies the experimental results show approximately 1dB higher pressure amplitudes at certain locations of minimum pressure at the rear of the cylinder compared with the analytical results. The reason for this is that at the lower frequencies a small amount of sound energy was reflected by the walls of the anechoic chamber and hit the surface of the cylinder,

which added with the total amount of reinforcement and cancellation that occurs between the two diffracted waves travelling around each side of the cylinder. For higher frequencies almost no energy was reflected by the walls of the anechoic chamber and the experimental results showed very good agreement with the analytical results, even at the locations of pressure minima at the rear of the cylinder.

Another method was developed to predict the sound pressure field at the surface of a cylinder due to oblique incident waves from a point source and a line source. The methodology was applied to a Boeing cylinder and an RSLVF (Representative Small Launch Vehicle Fairing) and the results are presented in this thesis. For acoustic loading, the RSLVF was divided into four sections. For each section an individual thin slice was used and the circumferential sound pressure was estimated at the surface of each slice at different heights. The results presented for each slice indicate that the sound pressure pattern at a particular frequency on each slice is similar, but the sound pressure amplitude decreases as the height increases because the sound pressure decays due to increasing distance from the source.

The Boundary Element Method (BEM) was investigated and used to build numerical models to predict the sound pressure field as a result of normal and oblique incident waves from various idealised sources (plane waves, point source and line source) incident on a Boeing cylinder and an RSLVF. The BEM was able to take into account sound diffraction around the ends of the Boeing cylinder and the RSLVF, which was a limitation of the purely theoretical methodologies developed in this thesis. The BEM was implemented for both two and three dimensional geometries of the Boeing cylinder and the RSLVF, and the

results were compared with the analytical results for various idealised sources. The comparisons showed that using an analytical model that excludes diffraction around the ends was sufficiently accurate to act as a check on the validity of the BEM model and it was concluded that the BEM can be used for calculating the acoustic loading on the RSLVF during launch.

A detailed examination of the characteristics of the noise sources for an exhaust plume at launch is beyond the scope of the current examination. However, the empirical methods which are outlined for chemical rockets in NASA-SP-8072 (1971), a space vehicle design criteria document, were used for predicting the acoustic loads on the RSLVF for one-third-octave band centre frequencies ranging from 50Hz to 400Hz. Two different source allocation methods were used to predict the acoustic loads on the RSLVF, based on the experimental data of the sound power spectrum radiated by the propulsion devices, the lateral deflection of the jets exhausted by the rocket engines and the allocation of noise generation sources along the exhaust stream, provided in NASA-SP-8072 (1971). One is the unique source allocation method, which assumed a single equivalent point source location along the flow axis for each frequency of interest. It has been observed that using the unique source allocation method it is not possible to predict the acoustic loading for a number of point sources acting as a line source along the exhaust flow axis for each frequency of interest. Therefore, the acoustic loading was also calculated using the non-unique source allocation method, which assumed that there are ten point source locations acting as a line source along the flow axis close to the vehicle for each frequency of interest. Both methodologies were conducted numerically and analytically, and the results agreed well. It was found that the non-unique source allocation method results in a lesser acoustic pressure magnitude

compared with the unique source allocation method. The reason for this is, for each frequency band of interest, the strength of each source calculated using the non-unique source allocation method was less compared with the strength of a single equivalent point source calculated using the unique source allocation method.

10.2 Conclusions

The analysis and results presented in this thesis demonstrate that it is theoretically possible to predict the sound pressure field as a result of normal and oblique incident waves from various idealised sources, such as plane waves, a point source and a line source, incident on a Boeing cylinder and an RSLVF. Although the experimental results were affected by a small amount of sound energy that was reflected by the walls of the anechoic chamber in the lower frequencies, the results were sufficiently accurate to validate the point source theory developed in this thesis. The theory was further developed for oblique incident waves and a line source, and compared with the numerical results obtained using the Boundary Element Method (BEM), which was used in this thesis for the numerical calculations for various idealised sources (plane waves, oblique waves, point source and line source). The comparisons between the analytical and numerical results showed that using an analytical model that excluded diffraction around the ends was sufficiently accurate to check the validity of the BEM models. It was also concluded that the BEM can be used to model the acoustic loading on the RSLVF during launch.

It was shown that for determining the acoustic loading on the RSLVF during launch, the launch environment can be modelled using two empirical methods, which are outlined for chemical rockets in NASA-SP-8072 (1971), a space vehicle design criteria document. It was

found that the recommended methods are based on the experimental data of the sound power spectrum radiated by the propulsion devices, the lateral deflection of the jets exhausted by the rocket engines and allocation of the noise generation sources along the exhaust stream. Also, the accuracy of these empirical methods fully relies on the existence of sufficient and accurate experimental data. However, both empirical methods have been applied in this thesis to calculate the acoustic loading on the RSLVF, using the experimental data provided in NASA-SP-8072 (1971), which were sufficient for the initial investigation calculated in this thesis. For the current analyses, the effect on the sound pressure due to the reflecting surface of the vehicle has been considered, which was not considered in the previous analyses presented by NASA-SP-8072 (1971). Both empirical methods were investigated numerically and analytically for determining the acoustic loads on the RSLVF, and it was shown that it is possible to accurately predict the acoustic loading on the RSLVF.

The overall contributions of this study are outlined as follows

- A suitable analytical form has been developed to calculate the total circumferential sound pressure field at the surface of a cylinder, as a result of incident plane waves that strike normal to the circumference of the cylinder. This form has the advantage that it can consider both incident and scattered sound pressure fields at the same time, with no need to calculate them separately, thus reducing the calculation time. Also, the analytical form developed in this thesis converges for all values of the argument ka (k is wave number and a is radius of a cylinder).
- An analytical model has been developed to calculate the scattered and total sound pressure fields at any position relative to a cylinder in a sound field, resulting from incident plane waves that strike normal to the circumference of the cylinder. This

new model has overcome the near-field and far-field limitations of previous models, and is applicable for any position in the sound field for any frequency of interest.

- A theoretical method has been developed that can take into account the type of noise source and its position at a finite distance from a cylinder, to calculate the circumferential sound pressure field at the cylinder surface. This method has been developed further for a line source.
- A theoretical method has been developed that predicts the circumferential sound pressure field at the surface of a cylinder; due to oblique incident waves from a point source and line source.
- A full investigation has been conducted for the external acoustic loading of an RSLVF using the Boundary Element Method (BEM) approach. Various acoustic loading conditions have been investigated, including the effect due to the reflecting surface of the RSLVF.

10.3 Recommendations for Future Work

The following are recommendations for future work:

1. The theoretical developments conducted in this thesis represent only an initial investigation, and as such the cylinder and fairing walls were modelled as rigid for the purpose of determining the external acoustic loading. Hence, the effect of secondary radiation due to vibration of the flexible cylinder and fairing walls or absorption of energy due to their damping behaviour has not been taken into account. This could be the main focus of an extended investigation.
2. The effects due to the diffraction around the ends of the cylinder, which has been

avoided in the analytical modelling work of this thesis, could be included in a future investigation to develop the full theoretical model of acoustic loading on finite length cylinders such as the Boeing cylinder and an RSLVF.

3. The non-linear features of sound on acoustic loading, which has been ignored in this study for simplicity, could be included in a future investigation to develop more realistic theoretical model of acoustic loading during launch.
4. One simple experiment could be conducted in future to measure the sound directivity on the cylinder surface for a smaller distance between the speaker and cylinder. This could be useful to check the validity of the theoretical model developed in Chapter 5 for sources closer to the cylinder.